Author's note: Two pages have deliberately been left blank in this electronic open-access version of the thesis. The copyright status of the following publications could not be determined, and as such only the citation is included.

- H.P. Panopoulos, K.P. Wootton, M.J. Boland and R.P. Rassool (2010), Electron Beam Energy Measurement by Resonant Spin Depolarisation at the Australian Synchrotron, *Proc. 19$^{\text{th}}$ AIP Congress*, Melbourne, December 2010.

- R. Dowd, M.J. Boland, R.P. Rassool and K.P. Wootton (2010), Damping Ring Studies for Future Linear Colliders, *Proc. 19$^{\text{th}}$ AIP Congress*, Melbourne, December 2010.

The original pages have been supplied for archival purposes to The University of Melbourne in a separate document.

Demonstrating Beams for a Future Linear Collider using Electron Storage Rings

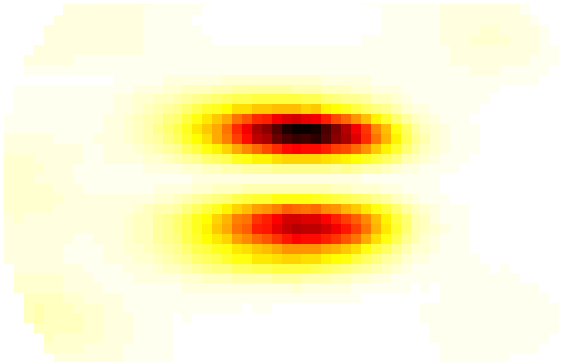

Kent Peter Wootton

BSc (Hons), BE (Hons)

Submitted in total fulfilment of the requirements of the degree of

Doctor of Philosophy

February 2014

School of Physics

The University of Melbourne

Produced on archival quality paper

Abstract

The Compact Linear Collider (CLIC) is a proposed electron-positron collider at the energy frontier. Achieving the required design luminosity requires the creation and preservation of beams of unprecedented low horizontal and vertical emittance. These beams will be provided by damping rings, which are storage ring accelerators designed to damp beam emittances by the emission of synchrotron radiation.

This thesis describes contributions to the simulation of low emittance beams in the CLIC main damping rings, and measurements of beams at the Australian Synchrotron (AS) and SPEAR3 electron storage rings to demonstrate feasibility of lowest emittance beams.

The equilibrium horizontal emittance of a storage ring lattice is a design parameter critical for brightest beams, and will be minimised for the CLIC damping ring lattice by the inclusion of a defocussing gradient in the main bending magnets. Measurements of the electron beam in the SPEAR3 storage ring are presented, using the highest precision beam energy measurement technique available. These measurements demonstrated that numerical modelling of gradient magnets was better than the usual hyperbolic cosine trajectory approximation.

The equilibrium vertical emittance in storage rings is governed principally by the vertical alignment of accelerator magnets. Using simulation, a sensitivity analysis of the CLIC main damping ring lattice to magnet misalignments is presented. Misalignments considered included quadrupole vertical offsets and rolls, sextupole vertical offsets, and main dipole rolls. The vertical emittance was found to be most sensitive to betatron coupling induced by vertical misalignment of sextupole magnets.

The world-record low vertical emittance of the AS storage ring makes the facility an important test bed for future collider damping rings. A new vertical emittance measurement technique was developed, utilising diffraction-limited radiation from a vertical undulator. This counter-intuitive technique has been used to observe picometre vertical electron beam emittances at the AS storage ring. Future improvements to the technique are discussed.

Finally, opportunities of low vertical emittance beams are summarised in the contexts of storage ring particle physics experiments and user light sources.

Declaration

This is to certify that

i. the thesis comprises only my original work towards the PhD except where indicated in the Preface,

ii. due acknowledgement has been made in the text to all other material used,

iii. the thesis is fewer than 100 000 words in length, exclusive of tables, maps, bibliographies and appendices. The thesis is 32 230 words.

Kent Peter Wootton
February 2014

Preface

> *"Tapestries are made by many artisans working together. The contributions of separate workers cannot be discerned in the completed work, and the loose and false threads have been covered over. So it is in our picture of particle physics."* – Prof. S. L. Glashow, Harvard, Nobel Lecture, 8$^{\text{th}}$ December, 1979.

The principal original contribution of this work is the development of a new technique for the measurement of vertical emittance in a storage ring, using a vertical undulator.

Chapter 5 on the calibration of straight rectangular gradient bending magnets presents measurements of beam energy and momentum compaction factor at the SPEAR3 storage ring, which are all entirely the work of the author. The measurement of momentum compaction factor at the Australian Synchrotron was made by Harris P. Panopoulos (The University of Melbourne, now at Austin Hospital, Heidelberg, VIC, Australia), and presented as the subject of his Masters thesis in November 2010. The author offers interpretation of experimental results, using the combination of datasets.

The modelling of the trajectory through bending magnets was undertaken by Y.–R. Eugene Tan (Australian Synchrotron) who constructed the model of the AS storage ring, and Xiaobiao Huang (SLAC National Accelerator Laboratory) who constructed the lattice model of the SPEAR3 storage ring. The modelling approaches are included for reference in Appendix D.

Acknowledgements

"[This accelerator] has to do with: Are we good painters, good sculptors, great poets? I mean all the things that we really venerate and honor in our country and are patriotic about." – Dr. R. R. Wilson, Fermilab, Congressional Testimony, 17$^{\text{th}}$ April 1969.

It gives me great pleasure to acknowledge the many pivotal contributions to my postgraduate research.

If this thesis tells a story, the story is one of opportunity. During my candidature, I have enjoyed tremendous research autonomy from my supervisors, and first and foremost I want to sincerely thank Dr Mark Boland, Dr Roger Rassool and Dr Ioannis Papaphilippou for their supervision and guidance. I will always fondly remember the group celebrations in the basement, at Papa Gino's, and at Easter and Christmas.

The previous and current students of accelerator and detector physics at Melbourne and Monash deserve special thanks. In particular, thanks to David Peake, Bryn Sobott, Vivien Lee, Stefanie Elbracht-Leong, Tessa Charles, Anja Schubert, Harris Panopoulos, Evelyne Meier, Anna Phan, T'Mir Julius, Andrew Cole, Thomas Lucas, Sophie Dawson and Paul Giansiracusa.

Several friends and colleagues deserve special thanks for helping and encouraging my research. Thank-you to James Shanks, for all the useful discussions about vertical emittance. I am indebted to Jeff Corbett, Toshiyuki Mitsuhashi, and Ralph Steinhagen for the many constructive discussions and experiments on synchrotron light diagnostics. Bruce Cowie deserves to be thanked mostly for the jelly snakes and digestive biscuits, but really for encouraging and supporting me in the use of the soft X-ray beamline for so many experiments. I'd especially like to thank Kathryn Spiers for the conversation about undulators in the lead-up to one of the synchrotron open days – that conversation changed my thesis so much for the better.

The University of Melbourne has supported several of my overseas trips to accelerator schools, for which I am very grateful. I want to thank the Australian Synchrotron, for supporting me during my study, particularly hosting me at the lab and funding overseas trips to accelerator schools and conferences. I hope some of

my teaching at our Australian accelerator schools has helped return the favour. I am also very grateful to Ioannis Papaphilippou of CERN, for hosting me on several visits. For hosting my stay at SLAC, I want to thank James Safranek, Kai Tian, Xiaobiao Huang, and John Schmerge for the loan of his bicycle. While there, I had the pleasure of meeting Christine Petit Jean Genaz whom I want to thank for JACoW, which is such an indispensable resource for the accelerator physics community.

It is no understatement to say that the main reason I chose to do this PhD project was the accelerator physics group of the Australian Synchrotron. To Greg LeBlanc, Rohan Dowd, Yaw-Ren Eugene Tan, Martin Spencer, Elsa van Garderen and David Zhu, thank-you sincerely. The accelerator operators can never be thanked enough, especially for the friendship, but also for helping with machine studies at any hour of the night. I also want to thank the operators for maintaining an excellent barricade of the control room: confining me to my office for several months to write this thesis. I want to thank Don McGilvery, Cameron Rodda, Joel Trewhella, Robbie Clarken, Rod King, Peter Jones, Stephen Martin, Louise Hearder, Mark Atkinson, Simon Cunningham, Eleanor Dryley, Steven MacDonald, Michel ten Have and Viliami Takau.

I am particularly grateful to Yaw-Ren Eugene Tan, David Peake, Simon Cunningham and Mark Atkinson for proofreading earlier drafts of this thesis.

When I thought at the end of Honours that my family could take no more, they have endured, supported and championed me through my PhD. I'd especially like to thank my parents Peter and Anne Wootton, who have supported me wholeheartedly in my education. Thank-you also to Matthew Wootton, Belinda Williams and Michael Wootton: science and art are similar in so many respects.

Finally, it takes a lot of love to support your partner through postgraduate study. It is a great deal harder when it keeps them at the other end of the planet for many consecutive years. So many of these achievements are the product of your understanding, inquisitiveness, love and patience. There are no words that can express my thanks to you enough, my dear fiancée Laura Boon.

For my parents, Peter and Anne.

Table of Contents

List of Figures

List of Tables

Chapter 1

Introduction

The realm of particle physics is the very small, seeking to explain the fundamental composition and interactions of matter. One of the biggest unanswered questions in the fields of cosmology and particle physics is "What is the universe made of?"

Our present model of fundamental particles and their interactions is called the Standard Model. At times, this model has been developed by theoretical predictions of new particles, and at times by the discovery of new particles using collider experiments. Recently discovered Standard Model particles include the top quark [1, 2] and Higgs boson.

On the 4^{th} of July 2012, experiments at the Large Hadron Collider (LHC) at the European Organization for Nuclear Research (CERN) announced the discovery of a new standard model Higgs boson of mass 125 GeV [3, 4]. The Nobel Prize in Physics in 2013 was awarded for the theory predicting this massive boson [5,6]. The recent discovery of a Standard Model Higgs boson is a strong motivation for the construction of a new electron-positron collider at the energy frontier.

In spite of the successes of the Standard Model, luminous matter accounts for a mere 4.9% of energy in the universe: the remaining 95% is composed of 26.8% dark matter, and 68.3% the more mysterious dark energy [7]. New physics is required to explain the composition and interactions of both. At present, little is known about either dark matter or dark energy, except that their interaction with luminous matter must be very weak.

Various experiments have been used in dark matter and dark energy searches [8]. Cosmological surveys demonstrate that the distribution of dark matter throughout the universe is uneven [9]. One experiment claims discovery of a dark matter candidate through direct detection of dark matter particles travelling through laboratory scintillator detectors [10]. However, this result has not been observed at other similar

experiments [11, 12]. The small exclusion limits of cross-sections between dark matter and ordinary matter set by these experiments of the order 10^{-44} cm^2 are evident of the very low event statistics expected of such cosmological experiments [13].

High energy particle collider experiments seek to directly create new particles in the laboratory, in sufficient numbers to measure their properties [14]. In addition to the LHC, future colliders are proposed for the discovery of new physics, and also to investigate the known Standard Model particles.

1.1 Statement of Problem

The Compact Linear Collider (CLIC) is a proposed electron-positron collider for high energy particle physics experiments. Achieving a design luminosity exceeding 10^{34} cm^{-2} s^{-1} at a centre of mass energy up to 3 TeV requires the creation and preservation of electron and positron beams of unprecedented low horizontal and vertical emittance.

Conventional electron and positron sources are unable to provide beams of sufficiently low emittance. Instead, low emittance beams will be produced and then damped in electron and positron storage rings called damping rings. Although constructed with a different purpose, modern electron storage ring light sources can be used to test the physics of electron and positron beams in damping rings[1].

1.2 Contention

Through experiments using ultralow vertical emittance beams in electron storage rings – in particular the Australian Synchrotron (AS) storage ring – the contention of this thesis is to demonstrate the feasibility of the single-particle vertical emittance for the main electron and positron damping rings of CLIC.

1.3 Outline of this Thesis

This thesis presents new diagnostic techniques for the calibration of electron storage rings optimised for low horizontal emittance, and direct measurement of ultralow vertical emittance.

[1]The single-particle motion of electrons and positrons in storage rings is identical except for the sign of the charge. Unless explicitly stated, in this thesis, beams of electron and positron species in storage rings are treated identically and referred to only as electron beams.

Chapter 2 presents the motivation of this thesis: linear colliders as future energy frontier electron-positron colliders.

The physics of electron storage rings is presented in **Chapter 3**. This chapter emphasises beam physics concepts critical to the optimisation of storage ring lattices for low horizontal and vertical emittance.

Chapter 4 introduces the AS and Stanford Positron Electron Accelerating Ring (SPEAR)3 electron storage rings, used in these studies as test accelerators for the proposed CLIC damping ring. Common properties of proposed collider damping rings and electron storage ring light sources are summarised.

The equilibrium horizontal emittance of a storage ring lattice is a design parameter critical for brightest beams, and would be minimised for the CLIC damping ring lattice by the inclusion of a defocussing gradient in the main bending magnets. In spite of the high precision fabrication of rectangular gradient bending magnets, these magnets are seldom used in storage rings because of the additional difficulty in modelling the beam trajectory. Measurements are presented in **Chapter 5** of the SPEAR3 storage ring, using the highest precision beam energy measurement technique available.

The equilibrium vertical emittance in storage rings is governed principally by the vertical alignment of accelerator magnets. Using simulation, a sensitivity analysis of the CLIC main damping ring lattice to magnet misalignments is presented in **Chapter 6**. Misalignments considered included quadrupole vertical offsets and rolls, sextupole vertical offsets, and main dipole rolls.

The world-record low vertical emittance of the AS storage ring makes the facility an important test accelerator for future linear collider damping rings. A new vertical emittance measurement technique was developed, utilising a diffraction-limited vertical undulator. This counter-intuitive technique described in **Chapter 7** has been used at the AS storage ring to observe picometre vertical electron beam emittances. These first measurements are presented in **Chapter 8**. Potential future improvements to the technique are outlined.

Finally, opportunities of low vertical emittance beams are summarised in **Chapter 9** in the contexts of storage ring particle physics experiments and user light sources.

Chapter 2

Motivating Linear Colliders

To understand the need for electron-positron linear colliders in future high energy physics experiments, it helps to understand the history of colliders. Important historical accelerator developments motivating linear electron-positron colliders are summarised.

2.1 Particle Accelerators for High Energy Physics

Our everyday experience is with matter composed principally of protons, neutrons and electrons. These are some of the low energy states of matter. High energy particles with rest mass m can be created by exploiting Einstein's principle of mass-energy equivalence [15],

$$E = mc^2, \tag{2.1}$$

where E is energy, and c the speed of light in a vacuum.

To make high mass particles, an amount of energy equal to or greater than the mass of the products needs to be supplied. One way of supplying this energy is to accelerate a stable particle such as an electron to high energy. In a collision with another particle, the kinetic energy can be converted into massive particles. The total energy E of an accelerated particle is expressed by [16],

$$E = \sqrt{(mc^2)^2 + \vec{p}^2c^2}, \tag{2.2}$$

where $\vec{p}$ is the momentum of the particle.

2.1.1 Fixed-Target Experiments

Fixed-target experiments collide a beam of energetic, moving particles with stationary particles (an example of this is Rutherford scattering [17]). Firing a beam of positrons in collision with target electrons at rest, the energy available for particle production E^* in the centre of mass frame is given by [18],

$$E^* = \sqrt{2E_1 m_e c^2}, \tag{2.3}$$

where E_1 is the energy of the incoming positron (given by Equation 2.2), and m_e the rest mass of electrons and positrons. Equation 2.3 demonstrates that the energy available for particle production in fixed-target experiments is proportional to the square root of the beam energy. These beams can come from radioactive sources or cosmic rays, but particle accelerators are used to achieve high flux beams.

Circular accelerators – in particular the synchrotron – are useful sources of high flux, high energy beams. Historically, to achieve increased beam energy, circular machines of increasing circumference have been constructed [19]. In jest, Enrico Fermi proffered that this approach would eventually necessitate the construction of an accelerator encircling the world [20, 21]. A more sustainable collision technique was needed to affordably continue high energy physics experiments.

2.1.2 Synchrotron and Storage Ring Colliders

The revolution came with colliding beam storage rings [22]. For colliding beams of positrons and electrons of equal energy E, the energy available for particle production E^* is given by [18],

$$E^* = 2E, \tag{2.4}$$

that is, the full beam energy is available for particle production. The construction of energy frontier electron and proton colliders is summarised in Figure 2.1.

Apparatus for colliding beams were first patented by Wideröe [25], and independently published in scientific literature [26, 27]. The first collider was the electron-positron storage ring Anello di Accumulazione (AdA) [24, 28, 29]. At present, the LHC is the highest energy proton-proton collider. At 8 TeV centre of mass energy, the energy reach is significantly above the previous highest energy proton-antiproton collider – the Tevatron at Fermilab, at 1.96 TeV [30].

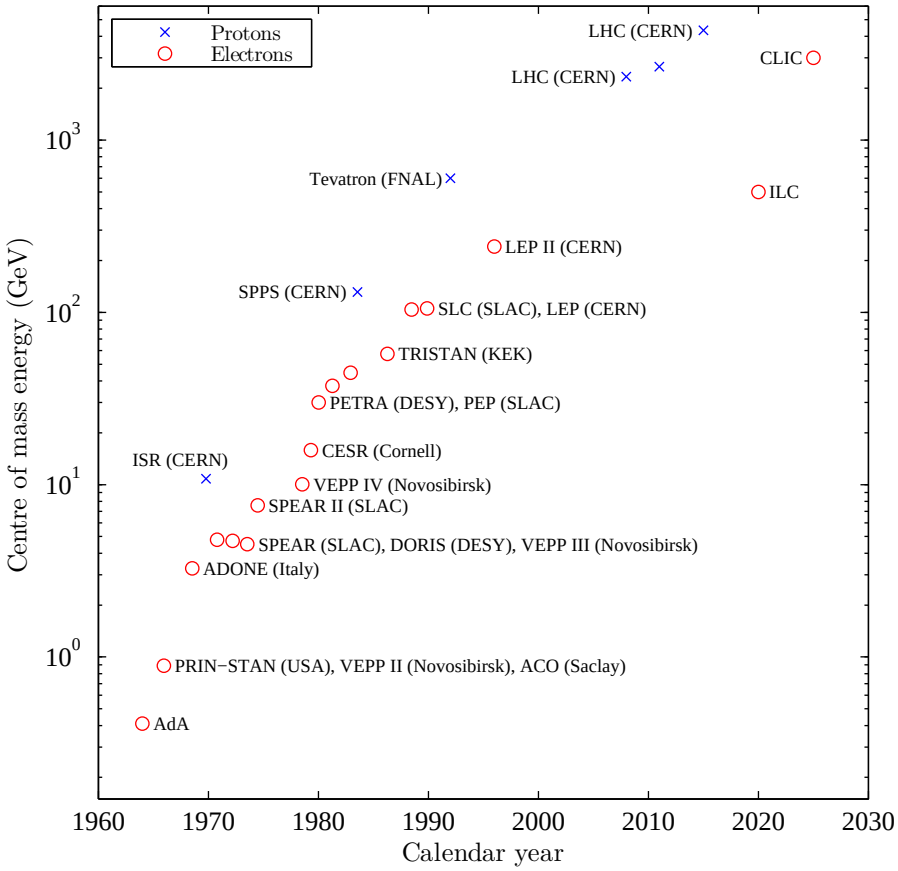

Figure 2.1: Livingston plot of proton and electron colliders: progression of centre of mass energy with calendar year [23, 24]. For proton colliders, the maximum centre of mass-energy of the colliding partons is shown. The proposed CLIC and ILC electron-positron colliders are indicated.

2.1.3 Electron-Positron Circular Colliders

As outlined in Figure 2.1, the construction of electron-positron colliders of increasing energy reach is complementary to hadron colliders. With hadron colliders such as the LHC as discovery machines, lepton colliders are required for precision measurements.

With the notable exception of the SLAC Linear Collider (SLC) [31], previous electron-positron colliders have been rings. In order to increase the beam energy of electron-positron circular colliders, rings of increasing circumference were constructed. This was to overcome the beam energy loss to synchrotron radiation, which is proportional to the fourth power of the beam energy, and inversely proportional to the circumference [32]. The largest electron-positron ring constructed was the Large Electron Positron Collider (LEP), of 27 km circumference reaching centre of mass energies of 207 GeV [33]. Construction of a circular electron-positron

collider of higher energy than LEP would necessitate the construction of a ring of significantly greater circumference.

2.1.4 Electron-Positron Linear Colliders

To keep future high energy colliders to an acceptable civil engineering footprint of approximately 50 km tunnel length, linear colliders are proposed. At present, two major projects are in design.

The International Linear Collider (ILC) is an electron-positron linear collider designed for a centre of mass energy of 500 GeV, with an option to upgrade to 1 TeV. The proposed ILC accelerator complex is illustrated schematically in Figure 2.2. Superconducting radio frequency (rf) cavities are used for the main linacs, with rf power supplied from klystrons. Using this technology, accelerating gradients of 35 MV m^{-1} are expected. With the publication of a Reference Design Report (RDR) in 2007 [34] and Technical Design Report (TDR) in 2013 [35], this is a mature accelerator and detector design.

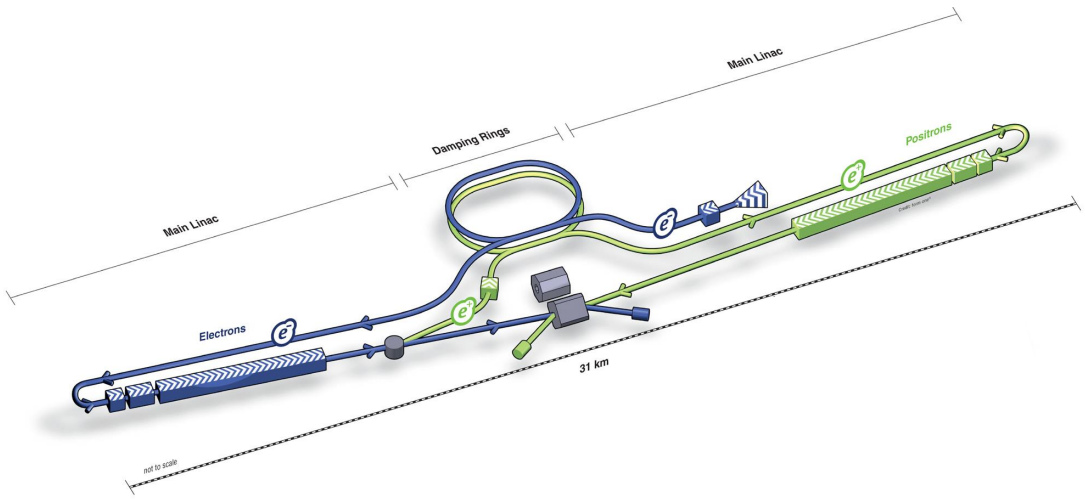

Figure 2.2: Schematic of International Linear Collider accelerator complex [35].

CLIC is the other proposal for an energy frontier electron-positron linear collider. The proposed accelerator complex is illustrated schematically in Figure 2.3. With a design centre of mass energy of 3 TeV, CLIC has a higher energy reach than the ILC. The project aims to achieve an accelerating gradient of 100 MV m^{-1}, using high frequency X-band (12 GHz) normal conducting accelerating cavities. Effectively, the project calls for two accelerator complexes: for the acceleration of the main beam, by the novel deceleration of the drive beam. The efficient provision of high-frequency rf power is possible with the centralised production of high-current, low-energy drive

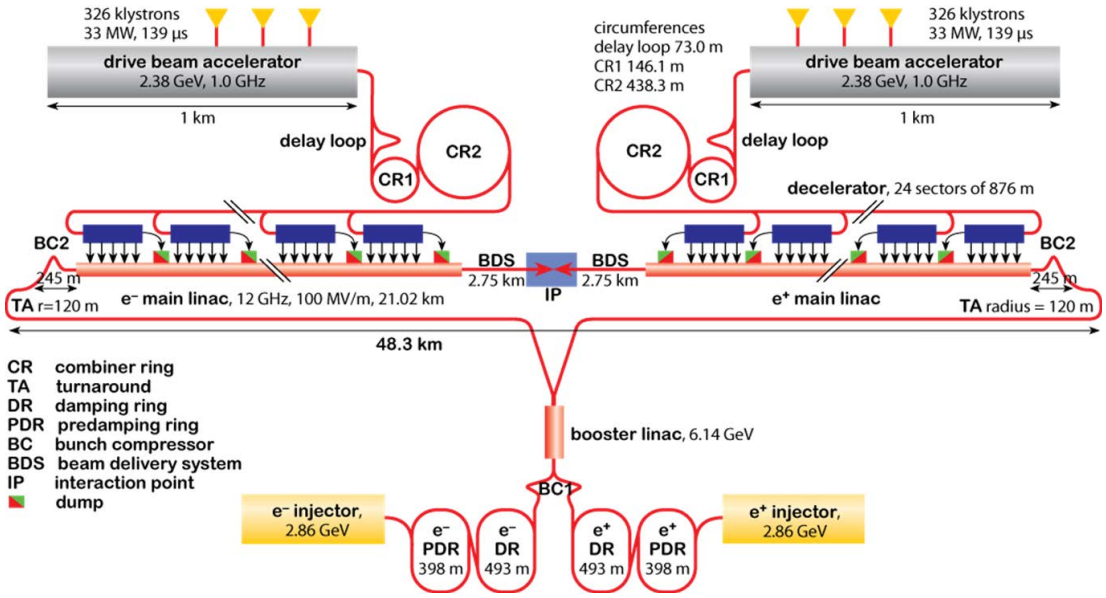

Figure 2.3: Schematic of Compact Linear Collider accelerator complex [36].

beams. The Conceptual Design Report (CDR) was published in 2013 [36–38].

Both the ILC and CLIC accelerator complexes follow a similar sequence of components. High brightness beams are created at electron and positron sources, the emittance phase-space volume is damped in damping rings, and the beams are accelerated to the centre of mass energy in the main linacs. Both projects incorporate damping rings to define the minimum emittance of the accelerated beams. The emission of synchrotron radiation serves to damp the six-dimensional emittance of stored electron and positron beams towards a minimum equilibrium value.

2.2 Summary

For future high energy particle physics experiments, linear colliders are proposed as more cost effective than storage rings of equivalent energy. For such colliders, low horizontal and vertical emittance beams will be essential. It is the physics and measurement of electron beams in low emittance storage and damping rings that is considered in this thesis.

Chapter 3

Electron Storage Ring Accelerator Physics

3.1 Motivation

This chapter presents a review of physics pertinent to the design of electron beams in circular particle accelerators. Particle accelerators are designed to provide a narrow beam of high-energy charged particles. This implies particles with high longitudinal momentum, and a narrow spread of momentum and position in longitudinal and transverse directions. This concept is quantified by emittance, and the physics of electron rings providing low emittance beams is the subject of this chapter.

The design of electron storage rings of increasingly low emittance is motivated by two communities, with similar figures of merit. In particle physics, the study of rare particle decays calls for colliders with the maximum affordable design luminosity. The luminosity $\mathcal{L}$ is given by Equation 3.1 [39],

$$\mathcal{L} = f\frac{n^2}{4\pi\sqrt{\varepsilon_x\beta_x^*\varepsilon_y\beta_y^*}}, \tag{3.1}$$

where f is the collision frequency, and n the number of colliding particles in each bunch. The minimisation of the horizontal and vertical emittances $\varepsilon_x, \varepsilon_y$, and the betatron functions at the interaction point β_x^*, β_y^*, maximises the collider luminosity. The equilibrium emittance and betatron functions of storage ring particle accelerators will be defined in this chapter.

The second application of low emittance beams are synchrotron radiation sources,

optimised for maximum brilliance described by Equation 3.2 [40],

$$\begin{aligned}\mathcal{B}(\omega) &= \frac{\dot{N}_{ph}(\omega)}{4\pi^2\sigma_x\sigma_{x'}\sigma_y\sigma_{y'}(\mathrm{d}\omega/\omega)} \\ &\equiv \frac{\dot{N}_{ph}(\omega)}{4\pi^2\varepsilon_x\varepsilon_y(\mathrm{d}\omega/\omega)},\end{aligned} \tag{3.2}$$

where for the photon angular frequency of interest ω and within the spectral range $(\mathrm{d}\omega/\omega)$, the brilliance $\mathcal{B}$ is given in terms of the number of photons per second $\dot{N}_{ph}(\omega)$, and beam sizes and divergences $\sigma_i, \sigma_{i'}$ respectively.

One approach to maximise the luminosity or brilliance of a storage ring is to minimise the transverse emittance of a beam.

3.2 Charged Particle Motion in Electromagnetic Fields

The motion of individual charged particles in electromagnetic fields is governed by the Lorentz force. For a particle with electric charge q and velocity $\vec{v}$, the force $\vec{F}$ on the particle is given by [41, 42]

$$\vec{F} = q\left(\vec{E} + \vec{v} \times \vec{B}\right), \tag{3.3}$$

where electric and magnetic fields are denoted respectively by $\vec{E}$ and $\vec{B}$.

Inspection of Equation 3.3 succinctly elucidates the design philosophy of high-energy accelerators. To increase the energy of a charged particle, an electric field is applied in the particles' direction of motion, denoted as the longitudinal direction. Transverse acceleration of particles can be achieved either by electric or magnetic fields, but at high energy ($|\vec{v}| \approx c$) is efficiently accomplished using magnetic fields.

Hence, rings are designed using rf cavities (electric fields) for acceleration, and magnetic fields for deflection of charged particle beams.

3.2.1 Notation for Relativistic Beams

High energy particle beams are accelerated to velocities $\vec{v}$ approaching the speed of light c, with the relativistic velocity $\vec{\beta}$ given by,

$$\vec{\beta} = \frac{\vec{v}}{c}. \tag{3.4}$$

Particles accelerated to a total energy E can be described equivalently by the Lorentz factor γ,

$$\gamma = \frac{E}{m_0 c^2}, \tag{3.5}$$

$$E = m_0 c^2 + E_k,$$

$$E = \sqrt{(m_0^2 c^2)^2 + (\vec{p}c)^2}. \tag{3.6}$$

where m_0 is the rest mass of the particle, E_k the kinetic energy and $\vec{p} = \gamma m_0 \vec{\beta} c$ is the momentum of the particle. For high energy electron accelerators, $\gamma \gg 1$ and $\vec{\beta} \approx 1$. Hence, the total energy is dominated by the momentum.

As described by Equation 3.3, high-energy charged particles are efficiently deflected by magnetic fields. Charged particles in a homogeneous magnetic field are deflected in a circular orbit of radius ρ. This radius can be determined by equating the Lorentz force (Equation 3.3), with the centripetal force,

$$q\left(\vec{E} + \vec{v} \times \vec{B}\right) = \frac{\gamma m_0 \vec{v}^2}{\rho},$$

$$\vec{B}\rho = \frac{\vec{p}}{q}.$$

The product $(\vec{B}\rho)$ is the magnetic rigidity of the beam. For singly charged electrons $(q = 1)$,

$$\vec{B}\ [\mathrm{T}]\rho\ [\mathrm{m}] = \frac{10^9}{2.998 \times 10^8}\vec{p}\ [\mathrm{GeV\ c^{-1}}],$$

$$\vec{B}\ [\mathrm{T}]\rho\ [\mathrm{m}] = 3.336\ \vec{p}\ [\mathrm{GeV\ c^{-1}}]. \tag{3.7}$$

For example, an electron beam with momentum $\vec{p} = 3$ GeV c^{-1} has a beam rigidity $B\rho = 10$ T m.

3.2.2 Coordinate System

The conventional coordinate system in accelerator design is a right-handed Frenet-Serret curvilinear system [43, 44]. This is illustrated in Figure 3.1.

Magnetic fields are defined with respect to the curvilinear trajectory s. This curvilinear system is convenient when describing deviations of beams from a design orbit. In some sections of this thesis, the trajectory of beams will be expressed in a local Cartesian coordinate system, with z as the longitudinal coordinate.

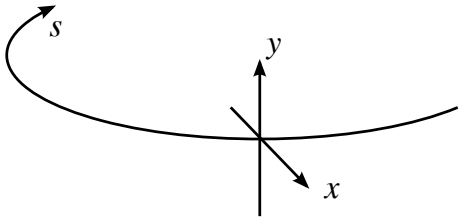

Figure 3.1: Frenet-Serret curvilinear coordinate system. The $x-y$ coordinates follow the curvilinear design trajectory s.

3.2.3 Charged Particle Optics

The focussing strength of magnetic multipole elements can be usefully defined in terms of the beam rigidity. Multipoles of increasing order are illustrated in Figure 3.2.

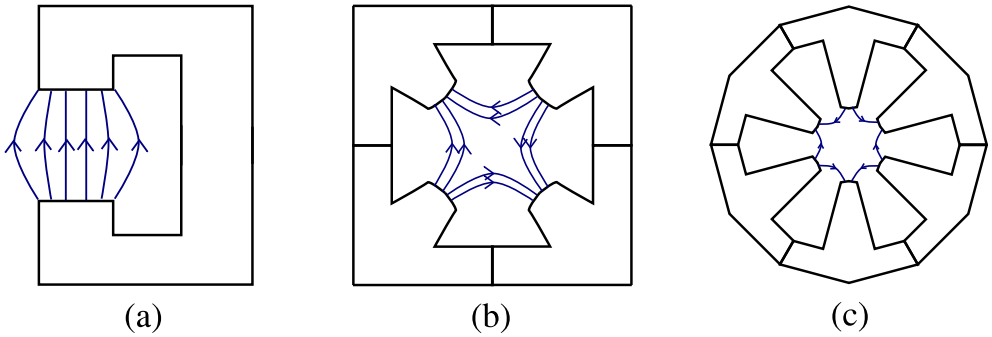

Figure 3.2: Laminations of magnetic multipoles, showing magnetic field lines. (a) Dipole; (b) Quadrupole; (c) Sextupole.

Solenoid magnets (with magnetic field in the longitudinal direction s) are commonly included in accelerators for particle physics, but seldom in storage ring light sources. As indicated in Equation 3.3, the focussing force provided is very weak because $(\vec{v} \times \vec{B}) \approx 0$, even for $|\vec{v}| \approx c$. The storage rings used in simulations and experiments in the present work do not include solenoid magnets.

Dipole magnets are used to bend charged particle beams in a circular trajectory. The strength of a dipole magnet G is denoted by

$$G = \frac{1}{\rho} = \frac{1}{B\rho} B_y. \tag{3.8}$$

Quadrupole magnets act as focussing lenses – focussing in one plane while simultaneously defocussing in the other. The gradient of a quadrupole magnet k_1 is denoted by

$$k_1 = \frac{1}{B\rho} \frac{\partial B_y}{\partial x}. \tag{3.9}$$

Hence particles travelling through the centreline of a quadrupole ($x = 0$) experience zero magnetic field.

Sextupole magnets can be used to provide the correct focussing strength to off-energy particles. The gradient of a sextupole magnet k_2 is denoted by

$$k_2 = \frac{1}{B\rho}\frac{\partial^2 B_y}{\partial x^2}. \tag{3.10}$$

As for a quadrupole, particles travelling through the centreline of a sextupole magnet ($x = 0$) experience zero magnetic field.

Multipoles of arbitrary higher order can be defined with gradients k_n [45],

$$k_n = \frac{1}{B\rho}\frac{\partial^n B_y}{\partial x^n}. \tag{3.11}$$

For reference, a description of these definitions is included in Appendix C.

3.3 Machine Functions

A storage ring lattice is an arrangement of multipole magnets to store a circulating beam of a given energy. Storage ring accelerators composed of separated function dipoles and quadrupoles described in Section 3.2.3 are defined as strong-focussing machines [46]. This section describes the linear motion of charged particles in circular storage rings, which is defined from the dipoles and quadrupoles.

3.3.1 Hill's Equations

Particle motion about the equilibrium orbit may be written in a form very similar to expressions for simple harmonic motion. In terms of the curvilinear coordinate s, the particle motion is given by the Hill's equations [47],

$$\frac{d^2x}{ds^2} = -\frac{1-n(s)}{\rho^2(s)}x, \tag{3.12}$$

$$\frac{d^2y}{ds^2} = -\frac{n(s)}{\rho^2(s)}y, \tag{3.13}$$

where $\rho(s)$ is the bending radius, and

$$n(s) = -\frac{\rho(s)^2}{(B\rho)}\frac{\partial B_y}{\partial x} \equiv -\rho(s)^2 k_1(s). \tag{3.14}$$

Equation 3.12 and 3.13 have solutions uniquely determined from the position y and angle $y' = dy/ds$ of a particle at the position s_0, given in the form [47],

$$y(s) = ay(s_0) + by'(s_0), \tag{3.15}$$

$$y'(s) = cy(s_0) + dy'(s_0), \tag{3.16}$$

which can be expressed in matrix notation by,

$$\begin{pmatrix} y(s) \\ y'(s) \end{pmatrix} = \begin{bmatrix} a & b \\ c & d \end{bmatrix} \begin{pmatrix} y(s_0) \\ y'(s_0) \end{pmatrix} = \mathbf{M} \begin{pmatrix} y(s_0) \\ y'(s_0) \end{pmatrix}. \tag{3.17}$$

This transfer matrix notation is convenient for accelerators. Individual elements such as drift lengths, dipoles, and quadrupoles can be described mathematically by transfer matrices [39]. The motion of a particle through a sequence of elements can be expressed by the product of individual transfer matrices.

3.3.2 Betatron Functions and Tunes

Beams in storage ring accelerators need to be stored for many revolutions, usually much greater than 10^9 turns. For this reason, stable solutions must exist for the equations describing particle motion in a ring: the amplitude must not continue to grow with subsequent turns [47]. Hence solving for the eigenvalues of the one-turn transfer matrix $\mathbf{M}(s)$ [47],

$$|\mathbf{M} - \lambda \mathbf{I}| = 0, \tag{3.18}$$

where $\mathbf{I}$ is the identity matrix. Choosing a phase advance μ,

$$\cos\mu = \tfrac{1}{2}\mathrm{Trace}(\mathbf{M}) = \tfrac{1}{2}(a + d), \tag{3.19}$$

the eigenvalues of Equation 3.18 can be expressed as [47]

$$\lambda = \cos\mu \pm i \sin\mu = e^{\pm i\mu}. \tag{3.20}$$

The phase advance μ is a constant of the ring lattice, and hence independent of s [47]. However the machine parameters $\alpha(s)$, $\beta(s)$ and $\gamma(s)$ (often called the Twiss [48] or Courant-Snyder [47, 49] parameters) do in general vary around the machine, and

can be defined as [47],

$$a(s) - d(s) = 2\alpha(s)\sin\mu, \tag{3.21}$$

$$b = \beta(s)\sin\mu, \tag{3.22}$$

$$c = -\gamma(s)\sin\mu, \tag{3.23}$$

The transfer matrix $\mathbf{M}$ of Equation 3.17 can be expressed in terms of these parameters by [47]

$$\mathbf{M} = \begin{bmatrix} \cos\mu + \alpha(s)\sin\mu & \beta(s)\sin\mu \\ -\gamma(s)\sin\mu & \cos\mu - \alpha(s)\sin\mu \end{bmatrix} \tag{3.24}$$

For detailed derivations of these functions, the reader is referred to recent literature [18, 39, 45]. The betatron function (sometimes abbreviated to beta function) $\beta(s)$ defines the amplitude function of the beam [18]. In each of the horizontal and vertical planes, the betatron tunes are defined as

$$\nu_x = \frac{\mu_x}{2\pi} = \frac{1}{2\pi}\oint \frac{ds}{\beta_x(s)}, \tag{3.25}$$

$$\nu_y = \frac{\mu_y}{2\pi} = \frac{1}{2\pi}\oint \frac{ds}{\beta_y(s)}. \tag{3.26}$$

It is unfortunate that literature uses the Greek symbols $\alpha(s)$, $\beta(s)$ and $\gamma(s)$ to denote the machine functions. This can cause confusion with the momentum compaction factor α_c and the relativistic velocity $\vec{\beta} = \vec{v}/c$ and Lorentz factor γ. Often in this thesis, these symbols are unavoidably used even within the same equation, and where necessary the distinction will be made in words.

3.3.3 Dispersion Function

An ensemble of particles in an accelerator has some finite energy spread about the energy of the nominal particle. As a result of this energy spread, electrons of higher (lower) energy will be deflected by bending magnets through a smaller (greater) bending angle than the design particle. The position of an off-energy particle with energy $(E + \delta E)$ is given by [50],

$$x_E(s) = \eta_x(s)\frac{\delta E}{E}, \tag{3.27}$$

where $\eta_x(s)$ is the dispersion function, and represents a chromatic aberration of the magnetic elements of the lattice [45]. Storage rings are usually defined with

deflection in a single horizontal plane (no vertical bends), leading to $\eta_y(s) = 0$ for most storage ring designs.

3.3.4 Phase Stability

The dispersion function $\eta_x(s)$ couples horizontal oscillations with energy oscillations. Stability of the beam energy in a storage ring is defined as phase stability, with respect to the rf accelerating potential. The term 'phase stability' was first defined by McMillan [51], but the concept was independently co-discovered [51–56].

In the same manner that quadrupole magnetic field gradients provide transverse focussing to beams, the sinusoidal rf gradient provides energy focussing to bunches in storage rings. The important parameters are the beam energy loss per turn U_0 and the rf cavity accelerating potential V. This is illustrated in Figure 3.3.

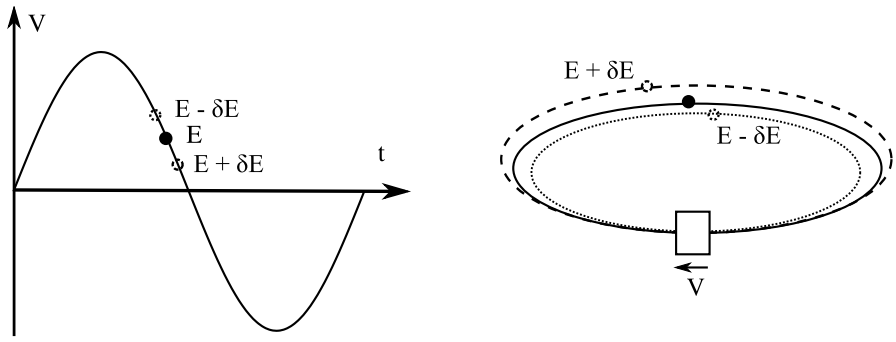

Figure 3.3: Principle of phase stability. Particles with energy greater than E arrive later, and receive a lower accelerating potential V than the synchronous particle, and vice versa for lower energy particles.

Electron storage rings at energies above transition energy[1] are considered in this thesis [46]. Above transition, the velocity of the electron beam in the storage ring is effectively constant, asymptotically close to the speed of light. Consider that an electron on the design energy makes one revolution of the machine on the synchronous orbit. Hence according to the beam rigidity ($B\rho$), an electron with greater energy is deflected less by bending magnets and traverses an orbit of greater circumference, arriving some time later at the rf cavity. By the same argument, electrons of energy less than the synchronous particle arrive earlier, and so receive a greater accelerating potential.

[1]The transition energy $\gamma_{\rm tr} = 1/\sqrt{\alpha_c}$, where the momentum compaction factor is $\alpha_c = (\Delta C/C)/(\Delta p/p)$ [47]. For the AS storage ring, $\gamma = 5871$ is much greater than $\gamma_{\rm tr} = 22$, and the storage ring is above transition.

This design results in phase stable acceleration of particle beams in discrete bunches.

3.3.5 Emittance

The ensemble of particles in a beam occupies a volume of position-momentum phase space. The phase space can be described conveniently in terms of the horizontal, vertical and longitudinal spatial dimensions. Conventions differ, but in this work the axes are defined in a right-handed coordinate system with horizontal $(x, \Delta\vec{p_x})$, vertical $(y, \Delta\vec{p_y})$ and longitudinal $(s, \Delta\vec{p_s})$ dimensions and momenta. The transverse phase space occupied by a beam is illustrated in Figure 3.4.

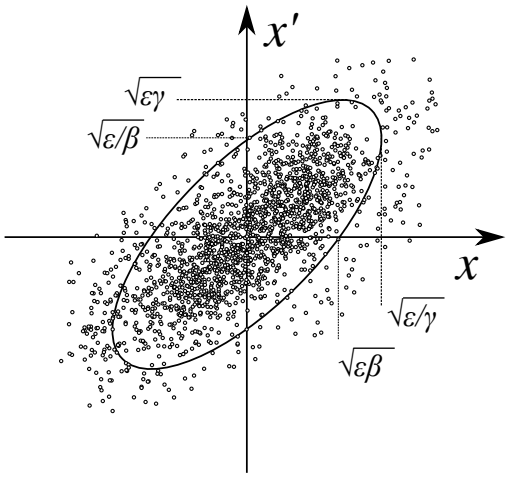

Figure 3.4: Horizontal emittance phase ellipse in terms of the machine parameters α, β and γ [45].

The area in phase space $\pi\varepsilon$ of the electron bunch is defined as the emittance. Beam emittances are typically approximated as Gaussian with tails of diminishing electron density, and defined as the beam distribution ellipse at one standard deviation. The equation for the beam ellipse in phase space is given by [47]

$$\varepsilon_x = \gamma_x(s)x^2 + 2\alpha_x(s)xx' + \beta_x(s)x'^2. \tag{3.28}$$

As shown in Equation 3.1 and 3.2, accelerators providing brightest beams are optimised for lowest transverse emittances.

Liouville's theorem is applied to particle accelerators to postulate that in the absence of damping, the six-dimensional emittance volume of a beam is conserved [45, 57]. This is the best case, and any mismatch of the beam phase ellipse with the

machine betatron phase advance results in the dilution of the emittance volume [45]. This is especially important for proton and ion machines, which have no significant damping mechanism. However this is qualitatively different for electron machines which have strong damping by synchrotron radiation.

3.4 Synchrotron Radiation

In this section, bending magnet and Insertion Device (ID) synchrotron radiation sources are described. The action of emission of synchrotron radiation provides a transverse damping force to electron bunches in a storage ring. Electrons performing betatron oscillations about a reference orbit emit synchrotron radiation in a cone tangential to the particle's direction of motion. Hence the emitted photon carries away both transverse and longitudinal momentum from the electron, while only the longitudinal momentum is recovered by the rf cavity [40]. In this way, the action of synchrotron radiation emission serves to cool the amplitude of transverse momenta of particles in the bunch. This is illustrated for the transverse dimensions in Figure 3.5.

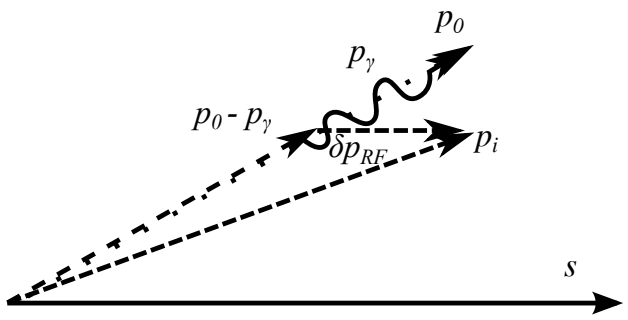

Figure 3.5: Damping of electron beam emittances by synchrotron radiation. An electron of initial momentum $\vec{p}_0$ emits a synchrotron radiation photon of momentum $\vec{p}_\gamma$. On passing through an rf cavity, the electron gains $\delta\vec{p}_{\mathrm{RF}}$ in the direction of s only. Hence the final momentum $\vec{p}_i$ has the same longitudinal momentum, but reduced transverse momentum. [58].

3.4.1 Bending Magnet Radiation

The emission of radiation by a single electron traversing a bending magnet results in a large instantaneous energy loss, given by [32, 45, 59]

$$P_\gamma = \frac{c}{2\pi} C_\gamma \frac{E^4}{\rho^2}, \tag{3.29}$$

$$\begin{aligned} C_\gamma &= \frac{4\pi}{3} \frac{r_e}{(m_e c^2)^3} \\ &\equiv \frac{1}{4\pi\varepsilon_0} \frac{4\pi}{3} \frac{q_e^2}{(m_e c^2)^4}, \end{aligned} \tag{3.30}$$

where r_e is the classical radius, q_e the electric charge and m_e the mass of an electron. Following the conventions of electromagnetism rather than accelerator physics, here ε_0 denotes the permittivity of free space (not an emittance). The average energy loss per turn of an electron in an isomagnetic lattice due to synchrotron radiation is given by [32, 45, 59, 60]

$$U_0 = C_\gamma \frac{E^4}{\rho}. \tag{3.31}$$

Pessimistically classified as a "radiative energy loss" [32], synchrotron radiation was so named because of its first observation in an electron synchrotron [61]. A practical consequence of the emission of synchrotron radiation is that high rf fields are required each turn to maintain the energy of an electron beam in a storage ring.

3.4.2 Synchrotron Radiation Integrals

The equilibrium properties of an electron beam in a flat storage ring are defined in terms of five synchrotron radiation integrals, summarised in Equation 3.32 – 3.36 [62–64]. These integrals are made around the closed orbit.

$$I_{1x} = \oint \frac{\eta_x(s)}{\rho_x(s)} ds, \tag{3.32}$$

$$I_{2x} = \oint \frac{1}{\rho_x(s)^2} ds, \tag{3.33}$$

$$I_{3x} = \oint \frac{1}{|\rho_x(s)^3|} ds, \tag{3.34}$$

$$I_{4x} = \oint \left(\frac{\eta_x(s)}{\rho_x(s)} \right) \left(\frac{1}{\rho_x(s)^2} + 2k_1(s) \right) ds, \tag{3.35}$$

$$I_{5x} = \oint \frac{\mathcal{H}_x(s)}{|\rho_x(s)^3|} ds, \tag{3.36}$$

where ρ is the bending radius, $\eta_x(s)$ the horizontal dispersion function and $\eta'_x(s) = d\eta_x(s)/ds$, $k_1(s)$ the quadrupole gradient and $\mathcal{H}_x(s)$ defined as [62]

$$\begin{aligned}\mathcal{H}_x(s) &= \gamma_x(s)\eta_x(s)^2 + 2\alpha_x(s)\eta_x(s)\eta'_x(s) + \gamma_x(s)\eta'_x(s)^2 \\ &\equiv \frac{1}{\beta_x(s)}\left[\eta_x(s)^2 + \left(\beta_x(s)\eta'_x(s) - \frac{1}{2}\beta'_x(s)\eta_x(s)\right)^2\right],\end{aligned} \tag{3.37}$$

expressed either in terms of the machine functions $\gamma_x(s)$ and $\alpha_x(s)$, or betatron and dispersion functions. All lattice and dispersion parameters are defined in terms of position s around the circumference.

3.4.3 Damping Partition Numbers and the Robinson Criterion

The equilibrium energy loss per turn of synchrotron radiation serves to damp particle motion in all three planes, but not necessarily equally. To determine the damping rates in each plane, damping partition numbers $\mathcal{J}$ defined for a planar storage ring are defined as [39]

$$\mathcal{J}_x = 1 - \frac{I_4}{I_2}, \tag{3.38}$$

$$\mathcal{J}_y = 1, \tag{3.39}$$

$$\mathcal{J}_s = 2 + \frac{I_4}{I_2}. \tag{3.40}$$

These damping partition numbers are distributed within an invariant, the Robinson criterion [58],

$$\mathcal{J}_x + \mathcal{J}_y + \mathcal{J}_s = 4. \tag{3.41}$$

Similarly, the damping decrement $\alpha_x, \alpha_y, \alpha_s$ can be defined by [40, 58],

$$\alpha_x = \mathcal{J}_x \frac{\langle P_\gamma \rangle}{E}, \tag{3.42}$$

$$\alpha_y = \mathcal{J}_y \frac{\langle P_\gamma \rangle}{E}, \tag{3.43}$$

$$\alpha_s = \mathcal{J}_s \frac{\langle P_\gamma \rangle}{E}, \tag{3.44}$$

with P_γ given by Equation 3.29, and E the beam energy.

3.4.4 Horizontal Emittance

The horizontal emittance is an equilibrium between the transverse cooling of synchrotron radiation, and the heating from the quantised emission of photons [45]. It can be defined in terms of the synchrotron radiation integrals as [39]

$$\varepsilon_x = C_q \gamma^2 \frac{I_5}{I_2 - I_4}, \tag{3.45}$$

$$C_q = \frac{55\hbar}{32\sqrt{3}mc}, \tag{3.46}$$

where γ is the Lorentz factor.

The equilibrium horizontal emittance depends upon the lattice design. Importantly, the horizontal emittance is proportional to the third power of the deflected angle of the main bending magnet [40]. Hence an important factor in minimising the horizontal emittance is maximising the number of arc unit cells.

3.4.5 Insertion Device Magnets

IDs (wigglers or undulators) are periodic arrays of magnets of alternating polarity [65, 66]. An electron beam passing through an ID is wiggled periodically, producing a very bright photon source. An ID is illustrated in Figure 3.6.

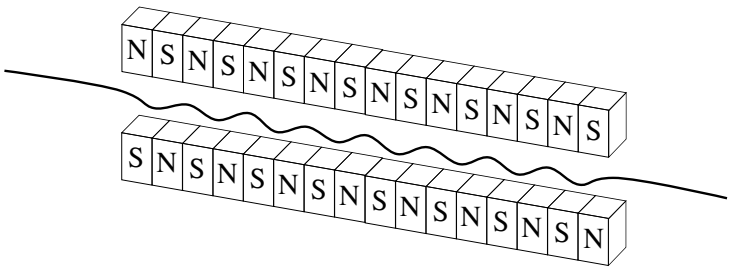

Figure 3.6: Wiggler or undulator insertion device as a synchrotron light source. A planar insertion device is shown, resulting in transverse oscillations of the charged particle beam.

The strength of an ID is typically classified by the deflection parameter K_u given by [45, 64],

$$K_u = \frac{eB_0}{\beta m_0 c k_p} \equiv 93.4 B_0[\mathrm{T}]\lambda_p[\mathrm{m}], \tag{3.47}$$

where B_0 is the peak magnetic field, λ_p the ID period and $k_p = 2\pi/\lambda_p$. Physically, the deflection parameter K_u represents the amplitude of oscillations with respect to the $1/\gamma$ opening angle of radiation. IDs of low deflection parameter ($K_u < 1$)

are typically classified as undulators [67–72], while devices with high deflection parameter ($K_u \gg 1$) are typically classified as wigglers. There are practical, but no fundamental distinctions between wigglers and undulators.

3.4.6 Influence of Wigglers on the Horizontal Emittance

Wiggler magnets are central to the horizontal emittance reduction strategy of proposed electron colliders [73], damping rings [37, 74–76] and storage ring light sources [77–80].

A planar wiggler ID is a periodic array of short bending magnets of alternating polarity. With each bend of the beam, synchrotron radiation is emitted, and can be used as a very intense light source [81, 82]. Wigglers can be used to increase the energy loss per turn to synchrotron radiation, and when positioned in zero-dispersion insertions, increase the damping rate to reduce the equilibrium horizontal emittance below that of the bare lattice. Even positioned in zero-dispersion insertions, the wiggler introduces self-dispersion and hence can increase the emittance [45].

To determine the effect of introducing wigglers to a storage ring lattice, the increase in emittance arising from a wiggler is considered. Consider a wiggler magnetic field oriented vertically, and sinusoidal in amplitude with the wiggler period λ_p, $k_p = 2\pi/\lambda_p$ and full length $L_w = N_u\lambda_p$, where N_u is the number of wiggler periods. The radiation integrals for the wiggler are given by [83],

$$I_{1w} = \frac{L_w}{2\rho_w^2 k_p^2}, \tag{3.48}$$

$$I_{2w} = \frac{L_w}{2\rho_w^2}, \tag{3.49}$$

$$I_{3w} = \frac{4L_w}{3\pi\rho_w^3}, \tag{3.50}$$

$$I_{4w} = -\frac{L_w}{8\rho_w^4 k_p^2}, \tag{3.51}$$

$$I_{5w} \approx \frac{4}{15\pi}\frac{\langle\beta_x(s)\rangle L_w}{\rho_w^5 k_p^2}, \tag{3.52}$$

where in Equation 3.52 it is assumed that $\mathcal{H}_x \approx \beta_x(s)\eta_x'(s)^2$ in the wiggler, and ρ_w is the bending radius of the wiggler poles [39]. The equilibrium horizontal emittance

and energy spread for the ring become [39],

$$\varepsilon_x = \varepsilon_{x0}\left(1+\frac{I_{5w}}{I_5}\right)\left(1+\frac{I_{2w}-I_{4w}}{I_2-I_4}\right)^{-1}, \tag{3.53}$$

$$\sigma_E^2 = \sigma_{E0}^2\left(1+\frac{I_{3w}}{I_3}\right)\left(1+\frac{2I_{2w}+I_{4w}}{2I_2+I_4}\right)^{-1}, \tag{3.54}$$

where ε_{x0} is the emittance of the bare lattice defined in Equation 3.45, σ_{E0} the energy spread of the bare lattice, given by [39],

$$\left(\frac{\sigma_{E0}}{E}\right)^2 = C_q\gamma^2\frac{I_3}{2I_2+I_4}, \tag{3.55}$$

with I_{1-5} defined as per Equation 3.32 – 3.36. The consequence of Equation 3.53 is that wigglers can reduce the equilibrium horizontal emittance. For a planar wiggler ($I_{4w}=0$), in a dispersion-free insertion ($\eta_x(s)=0$) of a separated function storage ring ($I_4=0$), the condition for emittance increase due to wiggler self dispersion is given by [83]

$$\frac{4}{3\pi}\frac{\langle\mathcal{H}_w\rangle L_w}{\rho_w^3}\frac{\rho^3}{2\pi\rho} > \frac{L_w}{2\rho_w^2}\frac{\rho^2}{2\pi\rho}. \tag{3.56}$$

3.4.7 Vertical Emittance

In a fashion similar to the horizontal emittance, synchrotron radiation integrals can be defined for the vertical emittance.

$$I_{1y} = \oint \frac{\eta_y(s)}{\rho_y(s)}ds, \tag{3.57}$$

$$I_{2y} = \oint \frac{1}{\rho_y(s)^2}ds, \tag{3.58}$$

$$I_{3y} = \oint \frac{1}{|\rho_y(s)^3|}ds, \tag{3.59}$$

$$I_{4y} = \oint \left(\frac{\eta_y(s)}{\rho_y(s)}\right)\left(\frac{1}{\rho_y(s)^2}+2k_1(s)\right)ds, \tag{3.60}$$

$$I_{5y} = \oint \frac{\mathcal{H}_y(s)}{|\rho_y(s)^3|}ds. \tag{3.61}$$

In the limit of zero lattice alignment errors, and in the absence of skew fields, the horizontal electron or positron storage ring exhibits a vanishingly small vertical emittance. This quantum limit of vertical emittance is governed by the stochastic emission of synchrotron radiation photons, in a narrow cone of opening angle $\sim 1/\gamma$ tangential to the deflected trajectory of the electron. The quantum limit of vertical

emittance limit is given by [50, 84],

$$\varepsilon_y = \frac{13}{55}\frac{C_q}{\mathcal{J}_y}\frac{\oint \beta_y(s)|G^3(s)|ds}{\oint |G^2(s)|ds}. \tag{3.62}$$

Making use of the average vertical betatron function $\overline{\beta_y}$, and the Root Mean Square (RMS) energy spread σ_E, this expression can be simplified for the normalised vertical emittance around the ring [84],

$$\gamma\varepsilon_y \approx 0.24\mathcal{J}_s\overline{\beta_y}\frac{\sigma_E^2}{\gamma}. \tag{3.63}$$

For the CLIC damping ring lattice considered, this limit is,

$$\gamma\varepsilon_y \approx 7.5 \times 10^{-10}[\text{m rad}],$$
$$\varepsilon_y \approx 1.3 \times 10^{-13}[\text{m rad}].$$

The design vertical emittance is only approximately an order of magnitude greater than this quantum limit. The equilibrium vertical emittance is typically observed to significantly exceed this quantum limit. The limit of vertical emittance for constructed machines is defined by the ability to steer through randomly misaligned centres of lattice magnetic elements. The increase in emittance arises as a result of coupling large magnitude betatron oscillations from the horizontal into the vertical plane, as well as spurious vertical dispersion.

3.5 Transverse Beam Size

To optimise the luminosity of a collider given in Equation 3.1, the beam size at the interaction point should be minimised. Beam sizes vary with the longitudinal position s around a storage ring. The beam size at the position s in a storage ring in either the horizontal or vertical planes is given by [50],

$$\sigma_x(s) = \sqrt{\beta_x(s)\varepsilon_x + \eta_x(s)^2\left(\frac{\sigma_E}{E}\right)^2}, \tag{3.64}$$

$$\sigma_y(s) = \sqrt{\beta_y(s)\varepsilon_y + \eta_y(s)^2\left(\frac{\sigma_E}{E}\right)^2}. \tag{3.65}$$

Typically, storage rings are designed with $\eta_y = 0$ for all s, but for ultralow vertical emittances the spurious dispersion is a non-negligible contribution to the beam size σ_y. Hence, direct observation of vertical beam size $\sigma_y(s)$ is expected in

order to conservatively claim observation of ultralow vertical emittance.

3.6 Summary

So as to achieve the design luminosity, the CLIC main damping rings need to operate routinely at ambitious transverse emittances. The tight design 1 pm rad vertical emittance is only a factor of 8 larger than the quantum limit of vertical emittance. The development of techniques to control and measure ultralow vertical emittance beams can be successfully tested using existing electron storage rings.

Chapter 4

Storage Ring Light Sources as Damping Ring Test Accelerators

4.1 Motivation

High energy colliders are not the only use of high energy particle accelerators. In parallel, high energy accelerators were also developed as synchrotron radiation sources [85]. The challenges of designing low emittance storage ring synchrotron radiation sources [86] are very similar to the requirements of electron damping rings for linear colliders [87].

In order to demonstrate the feasibility of design extracted emittances for the CLIC main damping rings, the few proposed linear collider projects are keen to leverage the expertise and experience of the many constructed storage ring light sources. Illustrated in Figure 4.1 are the horizontal and vertical emittances for a selection of constructed and proposed electron and positron storage and damping rings.

The design horizontal emittance for the CLIC main damping rings is ambitious, but has almost been demonstrated at PETRA III, with the recent reported observation of a record low horizontal emittance of $\varepsilon_x = 160$ pm rad [94]. The design vertical emittance $\varepsilon_y \approx 1$ pm rad has been demonstrated at the AS and Swiss Light Source (SLS) [92, 95].

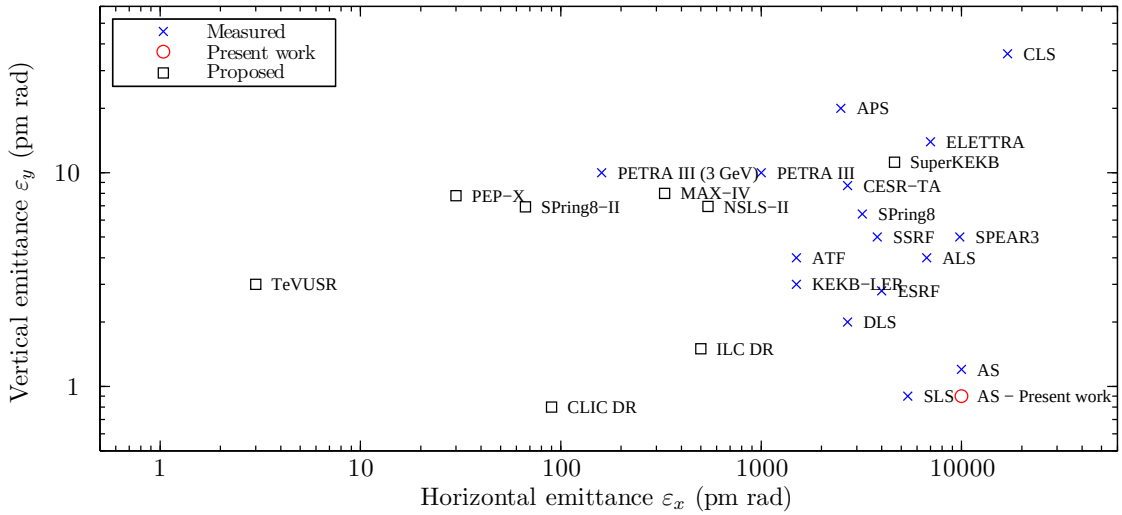

Figure 4.1: Geometric emittances of existing and proposed electron-positron rings. Minimum measured emittances of constructed rings are denoted by ×, and design emittances of proposed rings denoted by □ [88–94]. The present work of Chapter 8 measured at the AS is denoted by ○.

4.2 Australian Synchrotron Electron Storage Ring

The AS is a third generation electron storage ring light source of beam energy $E = 3$ GeV, serving photon beamlines around the storage ring circumference [96–98]. The accelerator complex is illustrated in Figure 4.2.

Design parameters of the AS ring are summarised in Appendix A. As a modern storage ring light source, the AS has qualities desirable for testing damping ring physics. The electron beam energy of $E = 3$ GeV is comparable to that of proposed linear collider damping rings. The storage ring is designed to accommodate many long insertions for synchrotron radiation insertion devices, including superconducting wigglers. Principally though, the AS storage ring is important to damping rings because of the ultralow vertical emittance achieved in this ring [95].

4.3 SPEAR3 Electron Storage Ring

The SPEAR laboratory has a rich history in high-energy physics, with Nobel prizes for the co-discovery of the J/ψ (charmonium meson) [100] and τ lepton [101]. Since its inception, an important aspect of science at SPEAR has been synchrotron radiation photons [81], initially with the parasitic use of synchrotron radiation X-rays

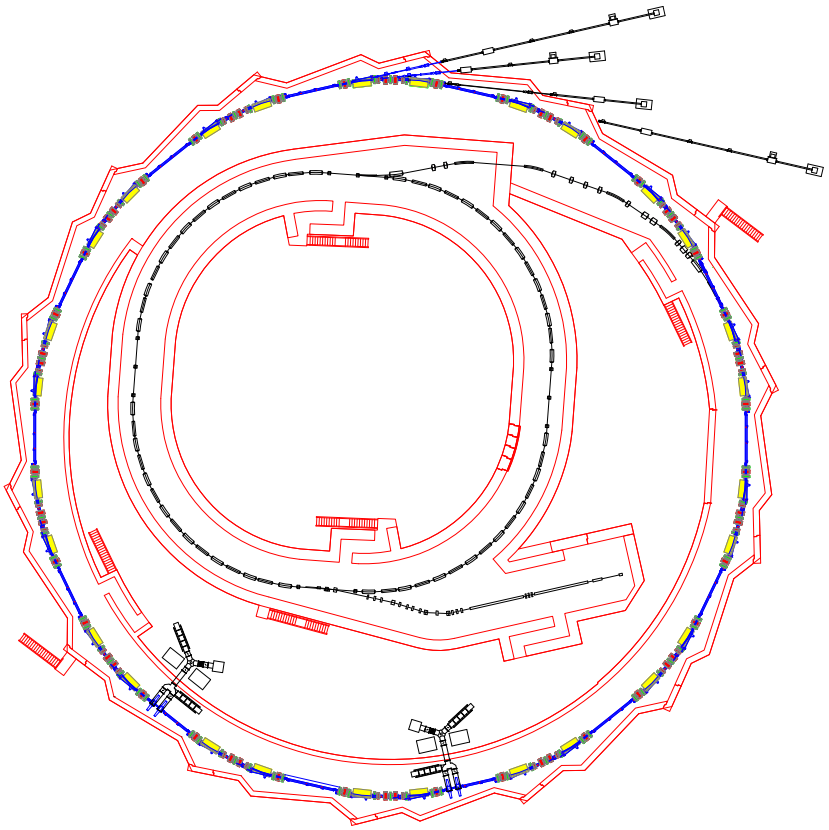

Figure 4.2: Schematic of AS accelerator complex [99].

for photon science experiments [102].

With the removal of the original electron-positron storage ring collider, the new SPEAR3 storage ring is a third-generation electron storage ring of $E = 3$ GeV beam energy dedicated to synchrotron radiation experiments [103]. The SPEAR3 ring is illustrated in Figure 4.3.

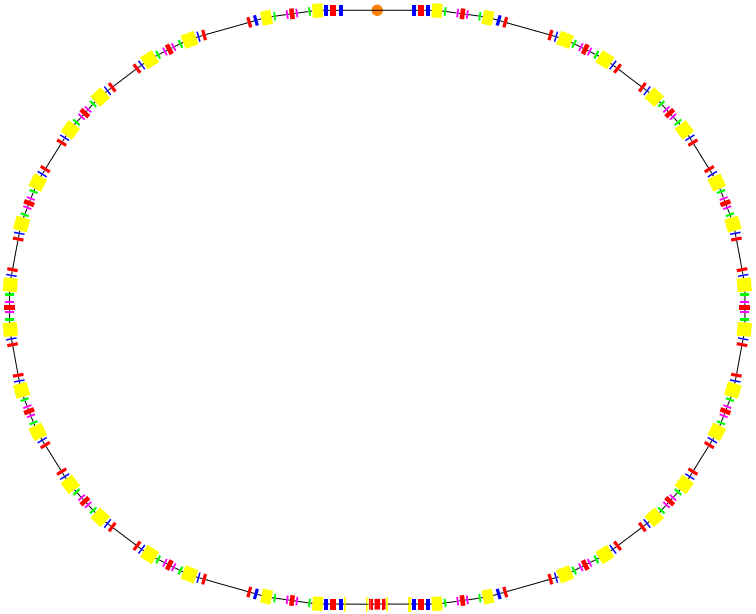

Figure 4.3: Schematic of SPEAR3 storage ring, racetrack lattice.

Because of the heritage of SPEAR as a collider, the SPEAR3 storage ring is a racetrack lattice with two-fold symmetry. This closely approximates the racetrack lattice for the CLIC damping rings, with low horizontal emittance arc cells, and matching cells for the wiggler insertions.

Parameters of the SPEAR3 ring are summarised in Appendix A. Both the SPEAR3 and AS storage rings incorporate a defocussing gradient in the bending magnets, as part of a strategy of minimising horizontal emittance through damping partition number exchange [96, 103, 104]. A defocussing gradient is planned to be included in bending magnets of the CLIC damping rings for this purpose, in addition to minimising vertical emittance growth due to Intra-Beam Scattering (IBS) [37].

4.4 CLIC Electron Damping Ring

Since early designs [105], the CLIC main damping ring proposal has called for a compact racetrack lattice [76,106,107]. The damping ring is illustrated schematically in Figure 4.4.

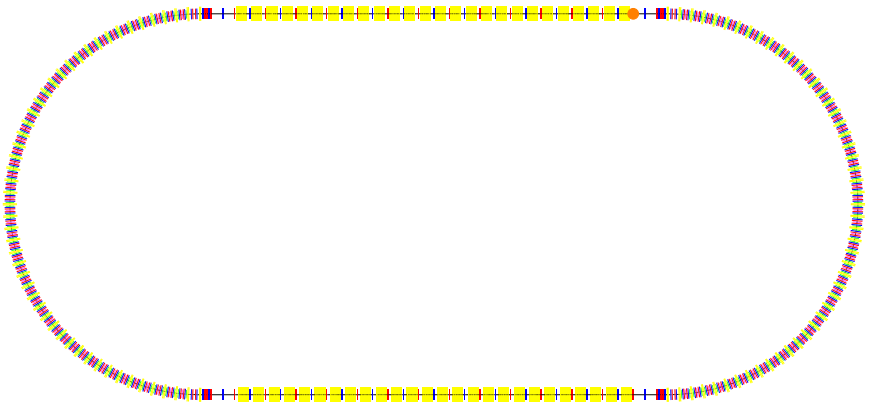

Figure 4.4: Schematic of CLIC damping ring, racetrack lattice.

The emittance is dominated by two wiggler insertions [108]. The acceptance of the main damping ring is relaxed compared to the ILC damping ring (especially for the positron ring), by the inclusion of pre-damping rings [109]. A compact lattice was developed [110–113], and from that non-linear optimisation performed [114]. It was later deemed that this lattice was too ambitious, and with a larger circumference the present design considers an arc cell of slightly higher equilibrium horizontal emittance [37, 107].

With the change in main linac rf frequency [106], the ring energy was revised up from $E = 2.42$ to 2.86 GeV [115], bringing the lattice closer in energy to many existing storage ring light sources.

4.5 Summary

The transverse emittances of the proposed CLIC damping rings are ambitious. Using existing storage ring light sources as test accelerators, it is possible to test and develop the required emittance optimisation routines and diagnostic techniques.

In particular, the AS storage ring is important as a damping ring test accelerator because of the low vertical emittance achieved in this ring.

Chapter 5

Measuring Combined-Function Magnets used for Low Horizontal Emittance

5.1 Motivation

The principal optimisation in low emittance storage ring lattice design is horizontal emittance minimisation. To this end, lattice cells of the AS and SPEAR3 light source storage rings were designed with defocussing gradient magnets.

Defocussing gradient bending magnets are a design choice that minimises the horizontal emittance of a lattice. The trajectory through rectangular gradient magnets does not follow a circular arc as in the case of pure dipole magnets, leading to a crucial point of difference between straight gradient magnets and pure dipole magnets: how can these magnets be aligned to produce the design bending and gradient fields?

A familiar description of storage ring accelerators is that particle beams are deflected according to their electrical charge, mass and energy using electric and magnetic fields. These fields are arranged such that beams perform stable, oscillatory motion over many thousands of turns, which can be measured to high precision as a frequency spectrum. Measurement and control of resonances at the revolution and rf frequencies, betatron and synchrotron tunes, informs the global properties of the linear lattice [47]. Here, another property of the electron is exploited – its spin – to inform and calibrate the dipole lattice model of storage rings.

In literature, there are very few measurements of the momentum compaction factor with straight rectangular gradient bending magnets. The momentum com-

paction factor was measured at the Advanced Light Source (ALS), with only a small departure from the model [116], however no details of the lattice model used in that study are available. At the time of measurement, the bending magnets of the ALS lattice were all rectangular defocussing gradient magnets: the lattice has since been changed to incorporate superbends [117].

To calibrate the model of horizontal defocussing straight rectangular gradient bending magnets (presented for reference in Appendix D), here experimental results are presented in the storage rings of light sources SPEAR3 [103] and AS [98], which are modern light sources of intermediate-energy with straight rectangular defocussing gradient dipoles in the Double-Bend Achromat (DBA) lattices [118].

5.2 Bending Magnet Choice for Low Horizontal Emittance Rings

A reduction in the equilibrium horizontal emittance can be achieved by the inclusion of a transverse gradient in the bending magnets. As a strategy, horizontal emittance minimisation using gradient bending magnets is well-established for storage ring light sources [119]. As given in Section 3.4.4, the equilibrium horizontal emittance of an electron storage ring is given by [39, 62],

$$\varepsilon_x = C_q \gamma^2 \frac{I_5}{(I_2 - I_4)} \equiv C_q \gamma^2 \frac{\langle \mathcal{H}_x / |\rho|^3 \rangle}{\mathcal{J}_x \langle 1/\rho^2 \rangle} \tag{5.1}$$

Inspection of Equation 5.1 illustrates that one strategy to minimise the horizontal equilibrium emittance is to maximise the horizontal damping number $\mathcal{J}_x$ [119]. This is achieved through exchange of the horizontal and longitudinal damping numbers $\mathcal{J}_x,\ \mathcal{J}_s$ [58]. The horizontal damping partition number $\mathcal{J}_x$ is given by [63, 64, 119],

$$\mathcal{J}_x = 1 - \frac{I_4}{I_2} \equiv 1 - \frac{\oint \frac{\eta_x}{\rho^3} \left(1 + 2\rho^2 k_1\right) ds}{\oint \frac{1}{\rho^2} ds}, \tag{5.2}$$

$$k_1 = \frac{1}{B\rho} \frac{dB_y}{dx}. \tag{5.3}$$

For a separated function lattice (pure dipole field bending magnets), the focussing gradient $dB_y(s)/dx = 0$ at longitudinal positions s where $\rho(s) \neq 0$. Therefore in a separated function lattice, the product $(2\rho^2 k) = 0$. In general, the horizontal dispersion function $\eta_x(s)$ is much smaller than the bending radius ρ, hence $I_4 \ll I_2$ [63], and $\mathcal{J}_x \approx 1$.

However for combined-function bending magnets (both dipole field and transverse gradient), the product $(2\rho^2 k) \neq 0$. Using a significant defocussing gradient, I_4 can be made negative resulting in $\mathcal{J}_x > 1,\ \mathcal{J}_s < 2$.

This strategy of exchanging between the horizontal and longitudinal damping partitions has been demonstrated to give a lower horizontal emittance than the Theoretical Minimum Emittance (TME) lattice [120, 121], which was calculated using pure dipole bending magnets [122,123]. This is the motivation for defocussing gradient bending magnets in many proposed low emittance rings, including the CLIC damping rings.

5.2.1 Dipole Bending Magnets

The conventional approach in the design of strong focussing lattices is to separate the functions of magnets into individual multipoles. This gives the greatest flexibility in lattice tuning. The profile of a dipole bending magnet is presented in Figure 5.1.

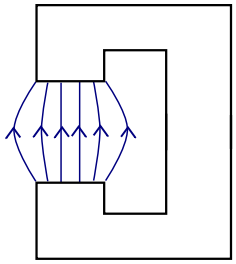

Figure 5.1: Profile of dipole bending magnet, C-style laminations [124]. The important quality is that the pole faces are parallel, producing a uniform dipole field.

The advantage of dipole magnets as bending magnets is that within the region of good field [124], the bending field is uniform. This results in a uniform, identically circular beam trajectory through the magnet, with very large mechanical tolerances on positioning alignment. There are good reasons to choose sector bending magnets against straight, principally the minimisation of iron in construction by optimisation of the region of good field [124].

5.2.2 Curved Rectangular Combined-Function Magnets

Many existing [125–128] and new lattices propose to use curved combined-function magnets [79, 80, 129–132]. A curved combined-function magnet is illustrated in Figure 5.2.

An advantage of this geometry is that the design bending field is equal along the beam trajectory, resulting in a circular trajectory for the design orbit. In addition,

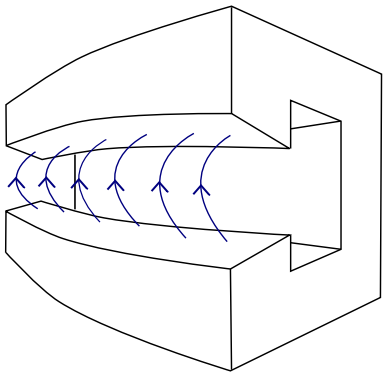

Figure 5.2: Curved rectangular bending magnet, with a transverse defocussing gradient. Magnet laminations are typically stacked in a circular arrangement, following the design curvilinear trajectory of the beam.

the transverse gradient is equal along the beam trajectory. A disadvantage is that it is more difficult to assemble magnet laminations to the required alignment tolerance.

5.2.3 Straight Rectangular Combined-Function Magnets

Very few rings use straight combined-function magnets [98, 103, 104, 133–135]. The AS and SPEAR3 storage rings are among these few, and are the subject of this study. A straight combined-function magnet is illustrated in Figure 5.2.

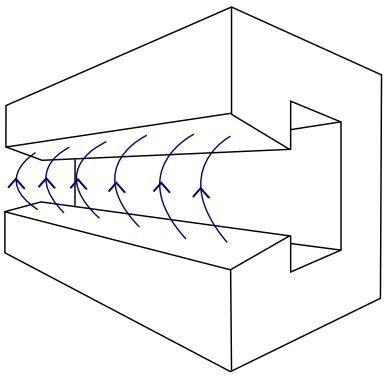

Figure 5.3: Straight rectangular bending magnet, with a transverse defocussing gradient. Unlike a curved magnet (Figure 5.3), magnet laminations are stacked straight.

As opposed to curved combined-function bending magnets, straight magnets are comparatively easy to fabricate as the laminations are assembled in a straight line [124]. However as shown in Section D.2, the design bending field changes along the beam trajectory resulting in a design trajectory significantly different to a circular trajectory.

For pure dipole bending magnets, the difference between rectangular and sector bending magnets is typically assumed to be edge focussing [136]. However straight gradient magnets feature a longitudinal variation in the main bending field, arising from the curved trajectory of the electron beam. This is significantly different to a curved gradient bending magnet, and is expanded upon in Appendix D.

5.3 Beam Energy Measurements using Electron Spin

Electron beam energy measurements using resonant spin depolarisation have been performed at storage rings for calibrating many aspects of the machine [116, 137–142], most notably the absolute beam energy, beam energy stability and momentum compaction factor. Pioneering work on polarisation was performed on e^+–e^- collider rings such as ACO [143,144], VEPP-2M [145,146], SPEAR [147], and LEP [139]. The technique is used because it is the highest precision energy measurement presently available, with typical measurement accuracy of order $\Delta E/E = 10^{-5} - 10^{-6}$.

5.3.1 Radiative Polarisation

A beam of electrons in a storage ring with an initial random distribution of spin orientations (unpolarised) develops polarisation over time, by the Sokolov-Ternov effect [148]. A concise summary of the important physics underpinning spin-flip radiation is given by Jackson [149], with some errata corrected [150]. Under the action of emission of spin-flip photons, the population of beam electron spins aligns anti-parallel with the main guide field of the bending magnets. The population of spin-up and spin-down particles is biased by the asymmetry of transition probabilities of spin-flip radiation [148]. This is illustrated in Figure 5.4 using separately normalised spectra of synchrotron radiation and spin flip radiation.

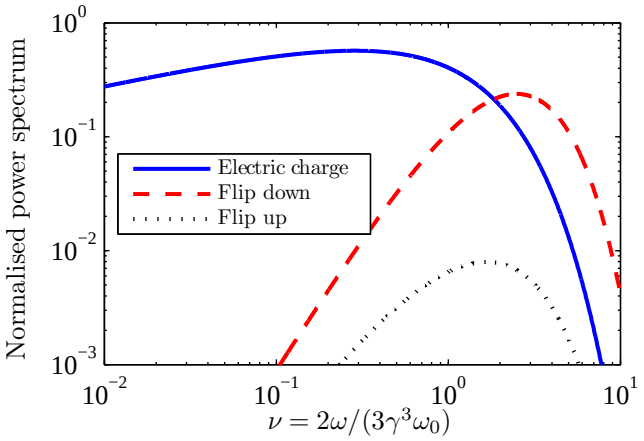

Figure 5.4: Separately normalised synchrotron non-flip (electric charge) and magnetic moment spin-flip radiation power spectrum [149].

The equilibrium distribution of spins is determined by considering the transition probabilities of the up and down spin states. This is given by [149],

$$\frac{dw(\nu,\theta_0)}{d\nu} = \frac{9}{10\pi}\frac{\nu^2}{\tau_0}\left[\frac{1}{2}\sin^2\theta_0\int_\nu^\infty K_{1/3}(s)ds + \frac{1}{2}\left(1+\cos^2\theta_0\right)K_{2/3}(\nu) + \cos\theta_0 K_{1/3}(\nu)\right]. \tag{5.4}$$

This number spectrum is illustrated in Figure 5.5, where flip-down denotes $\theta_0 = 0$ and flip-up denotes $\theta_0 = \pi$.

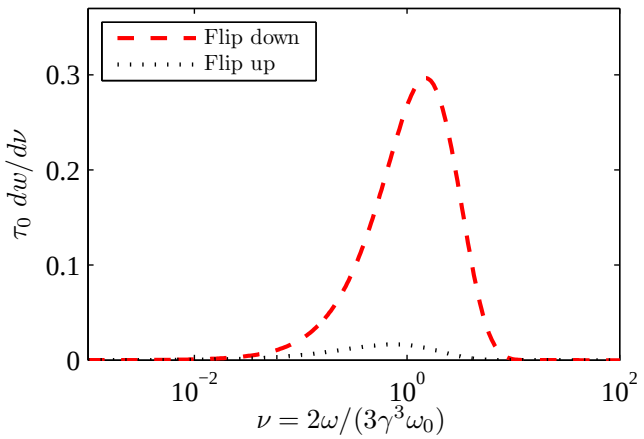

Figure 5.5: Normalised photon number spectrum of flip-up and flip-down radiation given by Equation 5.4 [149].

Integrating over all photon energies ν for both the flip-up and flip-down transi-

tions, the equilibrium Sokolov-Ternov polarisation P_{ST} is given by,

$$\begin{aligned} P_{\mathrm{ST}} &= \frac{\int_0^\infty \frac{dw(\nu,0)}{d\nu}d\nu - \int_0^\infty \frac{dw(\nu,\pi)}{d\nu}d\nu}{\int_0^\infty \frac{dw(\nu,0)}{d\nu}d\nu + \int_0^\infty \frac{dw(\nu,\pi)}{d\nu}d\nu} \\ &= \frac{\left(1+8/\left(5\sqrt{3}\right)\right) - \left(1-8/\left(5\sqrt{3}\right)\right)}{\left(1+8/\left(5\sqrt{3}\right)\right) + \left(1-8/\left(5\sqrt{3}\right)\right)} \\ &= \frac{8}{5\sqrt{3}} \approx 0.9238. \end{aligned} \tag{5.5}$$

The polarisation $P(t)$ of the beam develops by [150]

$$P(t) \approx P_{\mathrm{ST}}\left(1 - e^{-t/\tau_{\mathrm{ST}}}\right), \tag{5.6}$$

where time is denoted by t.

Magnetic fields B are considered in the directions perpendicular ($B_\perp$) and parallel ($B_\parallel$) to the curvilinear beam trajectory s. In a storage ring, both vertical and radial magnetic fields are denoted here by $B_\perp$. To accommodate reverse bends and wiggler insertion devices, we integrate both $B_\perp$ and its absolute value $|B_\perp|$ around the trajectory s. For a ring with reverse bending magnets or wigglers, the polarisation $P\left(t\right)$ approaches an equilibrium [140],

$$P_0 = P_{\mathrm{ST}}\frac{\oint B_\perp^3 ds}{\oint |B_\perp^3| ds}. \tag{5.7}$$

By inspection of Equation 5.7, P_0 approaches a maximum for a storage ring without reverse bends or wiggler insertion devices. For a beam of electron species with gyromagnetic factor $g_e \approx 2$ in an isomagnetic, planar ring, the theoretical maximum of polarisation is $P_0 = 0.9238$ [148]. The characteristic Sokolov-Ternov polarisation time τ_{ST} is given in Système International d'Unités (SI) units by [148],

$$\tau_{\mathrm{ST}}^{-1} = \frac{1}{4\pi\epsilon_0}\frac{5\sqrt{3}}{8}\frac{\hbar q_e^2 \gamma^5}{m_e^2 c^2}\frac{1}{\rho^3}, \tag{5.8}$$

where ρ is the local bending radius, m_e, q_e the electron mass and electric charge, ϵ_0 the permittivity of free space, $\hbar$ the reduced Planck's constant, and γ is the Lorentz factor of this relativistic electron beam. If the bending radius $\rho(s)$ varies around the ring circumference, rather than use the average value ρ, the third synchrotron

radiation integral is substituted [62, 150],

$$\frac{1}{\rho^3} \rightarrow I_3 = \frac{1}{2\pi R} \oint \frac{1}{|\rho(s)|^3} ds, \tag{5.9}$$

where R denotes the mean storage ring radius. For the SPEAR3 storage ring at a beam energy of 3 GeV, the Sokolov-Ternov polarisation time is $\tau_{\mathrm{ST}} = 1003$ s.

5.3.2 Resonant Spin Depolarisation

Spin transport is described by the Thomas–BMT equation [151]. The electron spin precesses about the polarisation axis at the spin precession frequency [139],

$$\vec{\Omega}_{\mathrm{BMT}} = -\frac{q_e}{\gamma m_e} \left[(1 + a_e\gamma)\, B_\perp + (1 + a_e)\, B_\parallel - \left(a_e\gamma + \frac{\gamma}{1+\gamma} \right) \frac{\vec{\beta} \times \vec{E}}{c} \right], \tag{5.10}$$

where q_e is the electric charge and $a_e = (g_e - 2)/2$ the anomalous magnetic moment of the electron, and c the speed of light in vacuum. As defined for Equation 5.7, the direction of electric fields $\vec{E}$ are considered with respect to the relativistic velocity of the electron $\vec{\beta} = \vec{v}/c$. Normally the storage rings of light sources do not include any significant solenoid magnetic fields nor transverse electric fields, that is $B_\parallel = 0$, $\vec{\beta} \times \vec{E} = 0$. Hence the simplifying assumption can be made that the electron spin precesses about a polarisation axis which is anti-parallel to $B_\perp$. For bending magnets of a ring, $B_\perp$ is a vertical magnetic field. The precession frequency given by Equation 5.10 can be simplified to the spin tune ν_{spin} [139],

$$\nu_{\mathrm{spin}} = a_e\gamma \equiv \left(\frac{g_e - 2}{2} \right) \frac{E}{m_e c^2}, \tag{5.11}$$

where E is the beam energy. If the beam is excited by a radial magnetic field f_{kick} resonant at any harmonic to the spin tune, the polarisation axis of the beam can be coherently rotated away from its equilibrium vertical orientation. The beam is hence resonantly depolarised at the frequency $f_{\mathrm{kick}} = f_{\mathrm{dep}}$ [137],

$$f_{\mathrm{dep}} = f_{\mathrm{rev}} \left(|\nu_{\mathrm{spin}}| \pm n \right) \tag{5.12}$$

where f_{rev} is the revolution frequency of the beam, and n is any integer.

Equation 5.12 highlights the quantities to be measured in a resonant depolarisation experiment. In order to determine the spin tune ν_{spin} and corresponding beam energy, both the depolarisation frequency f_{dep} and revolution frequency f_{rev} are

measured. The uncertainty in the measurement of the spin tune is then dependent upon the uncertainty in the measurement of $f_{\text{rev}}, f_{\text{dep}}$.

5.3.3 Present Fundamental and Experimental Uncertainties

The gyromagnetic factor g_e for electrons has been measured to precision within the 12^{th} significant figure [152]. The NIST CODATA accepted values for the electron anomalous magnetic moment and mass are used [153],

$$a_e \;=\; 0.001\,159\,652\,180\,76\;(27), \tag{5.13}$$

$$m_e \;=\; 0.510\,998\,928\;(11)\;\text{MeV}. \tag{5.14}$$

As a point of interest, with a relative uncertainty of $\Delta a_e/a_e \;=\; 2.3 \times 10^{-10}$, $\Delta m_e/m_e \;=\; 2.2 \times 10^{-8}$, the uncertainty in the accepted value of the electron mass has improved by almost an order of magnitude since the LEP energy measurements in 1994 [139]. Hence the theoretical fundamental limit of uncertainty in the resonant depolarisation technique is reduced to approximately $\Delta E/E = 2.2 \times 10^{-8}$. In practice, this limit remains orders of magnitude lower than other experimental uncertainties, as detailed for these experiments in Table 5.1.

Table 5.1: Relative experimental uncertainties for SPEAR3 experiments

Parameter	Relative uncertainty
a_e	2.3×10^{-10}
m_e	2.2×10^{-8}
f_{RF}	1×10^{-10}
f_{kick}	1×10^{-7}
f_{dep}	1×10^{-6}

As outlined in Table 5.1, the rf frequency f_{RF} is calibrated to high precision and the excitation frequency f_{kick} can be calibrated against a reference clock. Hence from Equation 5.11, measurement of the spin tune ν_{spin} gives a direct measurement of the beam energy, with experimental uncertainty dominated by uncertainty in fitting the depolarising frequency f_{dep}.

5.3.4 Depolarising Effects

The effective polarisation time τ_{eff} is given by [64, 154],

$$\frac{1}{\tau_{\text{eff}}} = \frac{1}{\tau_{\text{ST}}} + \frac{1}{\tau_{\text{dep}}}, \tag{5.15}$$

where τ_{ST} represents the Sokolov-Ternov polarisation time (Equation 5.8), and τ_{dep} a depolarisation time governed by radial magnetic field errors [154]. Storage rings of several GeV achieve Sokolov-Ternov polarisation times on the order of 15-20 minutes, with depolarisation times exceeding several hours [155]. Because the depolarisation effects have a much longer characteristic time, the effective polarisation time is dominated by the Sokolov-Ternov polarisation time.

A strong depolarising resonance to be avoided is the choice of stored beam energy corresponding to integer spin tune (Equation 5.11) [144]. Also depolarising is the overlap of the spin tune with betatron or synchrotron tunes. The vertical betatron tune has been usefully employed for resonant spin depolarisation [147]. In that experiment, the vertical betatron tune was swept as the depolariser. The width of the vertical betatron tune resonance limited the uncertainty in the beam energy measurement to approximately $\Delta E/E = 10^{-4}$. In this experiment at the AS and SPEAR3, a feedback kicker is excited with a sinusoidal oscillation, because it can have a narrower frequency spread than the betatron tune.

5.3.5 Møller Scattering Polarimetry

Møller scattering is electron-electron scattering and occurs within a bunch in the storage ring. The polarimetry observable is the Møller scattering cross-section of Touschek scattered electrons [156–159]: the intra-bunch cross-section resulting from betatron oscillations. The particle loss rate dN/dt is described in terms of the polarisation $P(t)$ by [145, 150, 155],

$$\frac{dN}{dt} = -\frac{N(t)^2 c}{\sqrt{2}\gamma^2 \sigma_x \sigma_{x'} \sigma_y \sigma_{y'} \sigma_z} \left(f_1 + f_2 P(t)^2\right), \tag{5.16}$$

where $N(t)$ is the number of electrons per bunch at a time t. For a stored beam of current $I(t)$ with equal current in several bunches, the bunch population $N(t) \propto I(t)$. The horizontal, vertical and longitudinal beam dimensions are denoted by $\sigma_x, \sigma_y, \sigma_z$, and divergences denoted $\sigma_{x'}, \sigma_{y'}$ in the horizontal and vertical directions respectively. The functions f_1 and f_2 have very complicated dependencies upon beam properties [145, 155], but can be treated for a given measurement as constants. Importantly, because $N(t) \propto I(t)$, an instantaneous normalised loss rate R_{norm} can be defined as

$$R_{\mathrm{norm}} = \frac{1}{I(t)^2}\frac{dN}{dt} \propto f_1 + f_2 P(t)^2. \tag{5.17}$$

The normalised loss rate is the figure of merit used to evaluate changes in the

level of beam polarisation.

5.4 Apparatus

For these experiments, the method selected for polarising and depolarising an electron beam follows the technique used at BESSY I [138], BESSY II [140, 160, 161], ALS [116], SLS [141], and ANKA [142]. Independent recent measurements at Diamond [162] and SOLEIL [154, 163] use the same technique, and achieve the same high precision. However, of the above storage rings, the ALS alone employs straight rectangular gradient bending magnets.

5.4.1 Storage Ring Setup

The SPEAR3 lattice was configured for maximum equilibrium polarisation. The pertinent design parameters of the SPEAR3 ring are summarised in Table 5.2.

Table 5.2: SPEAR3 storage ring design parameters [164].

Parameter		Value	Units
Beam energy	E	3.00	GeV
Lattice periodicity	...	18	...
Lorentz factor	γ	5871	...
Spin tune	ν_{spin}	6.8081	...
Betatron tunes	ν_x	14.130	...
	ν_y	6.194	...
Bending radius	ρ	7.86	m
Circumference	C	234.144	m
RF frequency	f_{RF}	476.300	MHz
Harmonic number	h	372	...
Polarisation time	τ_{ST}	1003	s

Using Equation 5.11, the spin tune of a 3 GeV electron beam was calculated as $\nu_{\mathrm{spin}} = 6.8081$, corresponding to a Lorentz factor $\gamma = 5871$. A significant spin tune depolarising resonance is the vertical betatron tune. To avoid this resonance, lattice quadrupole strengths were changed to reduce the fractional vertical tune to $\nu_y \approx 0.1$.

5.4.2 Depolarisation Kicker

Resonant depolarisation of the beam is achieved with a magnetic field which is radial in orientation (perpendicular to both the beam trajectory and main bending

field), and oscillating sinusoidally in time. The transverse kick field is provided by rf striplines, which are illustrated in Figure 5.6.

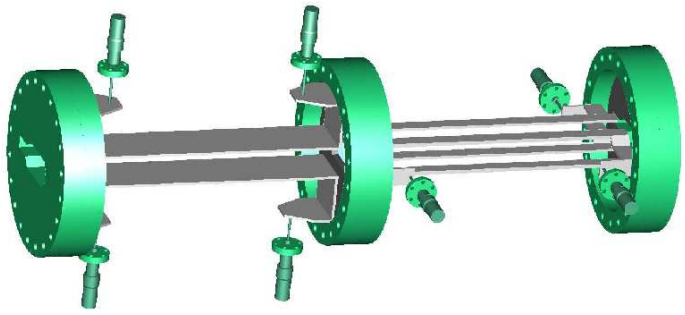

Figure 5.6: Radiofrequency kickers.

Exciting the beam at a betatron resonance results in a decreased loss rate (increased electron beam lifetime) since the bunch vertical size increases, hence the Touschek scattering rate decreases. Crossing a spin resonance, the count rate increases since the Møller scattering cross section increases when the polarisation is reduced.

The excitation frequency f_{kick} was swept at a rate of 10 Hz s^{-1}. Depolarisation is a resonant effect – it is particularly important to scan slowly [140].

5.4.3 Polarimeter

Exploiting the polarisation asymmetry of the Møller scattering cross section (Section 5.3.5), the electron beam polarimeter was a beam loss monitor. Doped sodium iodide crystals are efficient scintillators of gamma ray fluxes [165]. A 50 mm diameter NaI scintillator and photomultiplier tube were used. Touschek scattered beam electrons are detected after striking the storage ring vacuum chamber at a glancing angle of incidence, producing an electromagnetic cascade in the many radiation lengths of iron [166, 167]. The detector is used to observe bremsstrahlung of the order 1-10 MeV [168]. The scintillator was installed in the orbit plane of the ring, on the inner side of the vacuum chamber.

To maximise the normalised count rate, the detector was installed adjacent to the scraper defining the minimum energy aperture of the SPEAR3 storage ring. This is immediately downstream of the central focussing quadrupole, which is the point of maximum horizontal dispersion in one of the DBA arc cells.

5.4.4 Detector Choice

The change in beam polarisation is observed in the normalised loss rate R_{norm}, given by Equation 5.17. To measure this quantity, two main approaches are considered in literature: evaluation of the Touschek lifetime from the Direct-Current Current Transformer (DCCT), and detection of the electromagnetic shower from Touschek scattered beam particles striking the vacuum chamber when lost [138, 169]. Figure 5.7 presents measurements of a depolarisation using each of these techniques.

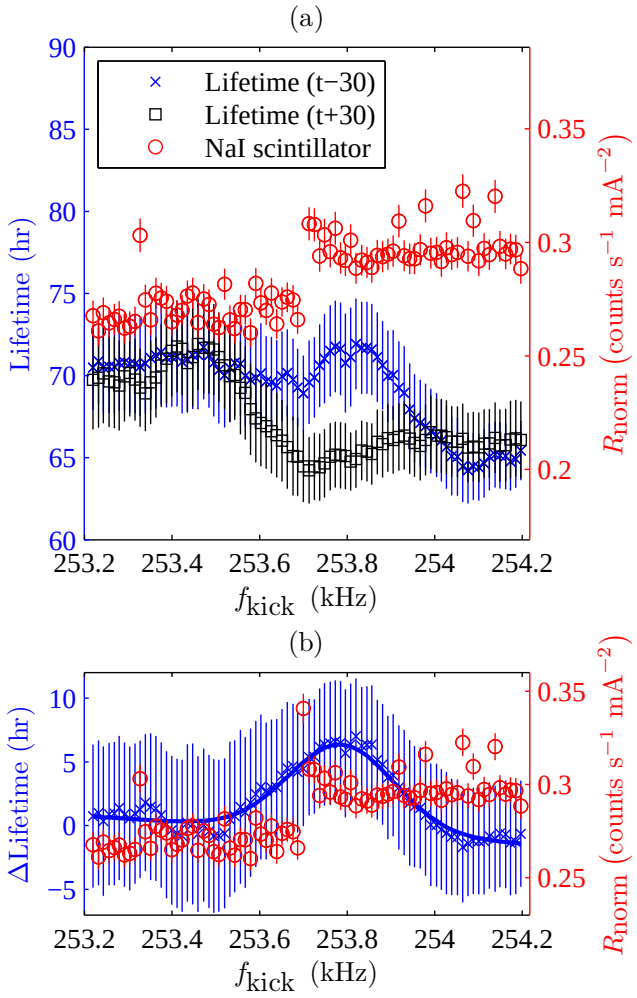

Figure 5.7: Choice of resonant depolarisation detector for SPEAR3. (a) Measured using NaI scintillator and DCCT, increasing the excitation frequency in time. The lifetime is calculated from 30 samples of the DCCT, comparing both 30 seconds before and after the scan frequency. (b) Comparison in resonance width using NaI scintillator, and (ΔLifetime). [K.P. Wootton, et al., *Phys. Rev. ST – Accel. Beams*, **16**, 074001 (2013). Published by the American Physical Society under the terms of the Creative Commons Attribution 3.0 License.]

Figure 5.7 shows that both approaches can be used to identify depolarisation

of an electron beam. The measured NaI loss monitor count rate responds to the resonant depolarisation within 1 s, while calculation of the lifetime with small uncertainty requires approximately 30 s of measurements of the stored beam current and the drop in lifetime is observed approximately 30 s after the depolarisation. The beam lifetime is calculated from the time derivative of the stored beam current, while the loss monitor measures the absolute loss rate, which is the derivative of the beam current with respect to time.

Here two lifetime calculations are presented, evaluating the lifetime using the previous 30 s of DCCT measurements $(t - 30)$, and using the following 30 s of DCCT measurements $(t - 30)$. This ΔLifetime is presented in Figure 5.7 (b). The change in polarisation needs to be quite large to observe the depolarisation using the beam lifetime. From a beam physics perspective, large changes of polarisation are not necessary to measure the beam energy: one is interested in the precession frequency at which depolarisation occurs. The time delay of 20-30 s observed in the beam lifetime measurement compromises the precision measurement of depolarisation frequency.

5.5 Experimental Results

Results of experiments performed at SPEAR3 are presented and analysed in this section.

5.5.1 Polarisation Time

As described in Section 5.3.1, the development of electron beam polarisation was observed through the Touschek cross-section. The development of polarisation of the stored electron beam was measured using the Touschek polarimeter, and presented in Figure 5.8.

The normalised loss rate was observed to be dependent upon the beam polarisation. As the polarisation developed, the normalised loss rate decreased, in agreement with the Sokolov-Ternov theory described in Section 5.3.1. Fitting Equation 5.17 to this data, the effective polarisation time was measured to be 840 ± 19 s.

As given in Section 5.3.1, the theoretical Sokolov-Ternov polarisation time was calculated for the SPEAR3 storage ring. Assuming a beam energy of 3 GeV and using Equation 5.8 with the substitution for the third synchrotron radiation integral given by Equation 5.9, gave a polarisation time of 1003 s.

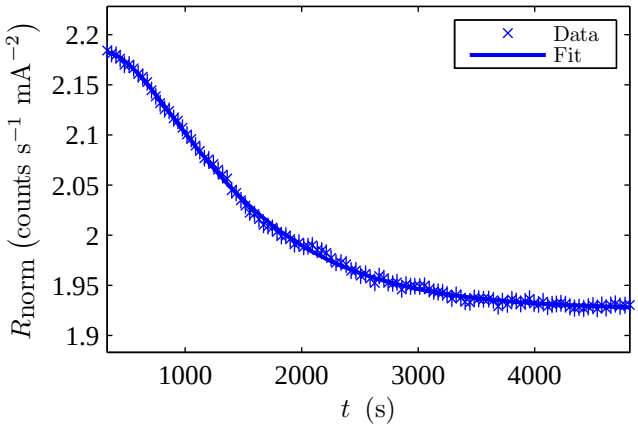

Figure 5.8: Development of electron beam radiative polarisation measured for the SPEAR3 storage ring. A polarisation time of $\tau_{\mathrm{eff}} = 840 \pm 19$ s was fitted. [K.P. Wootton, et al., *Phys. Rev. ST – Accel. Beams*, **16**, 074001 (2013). Published by the American Physical Society under the terms of the Creative Commons Attribution 3.0 License.]

For the purposes of resonant spin depolarisation experiments, it is not important that there is a difference between the measured and theoretical Sokolov-Ternov polarisation time. It is not necessary to use fully-polarised beams – it is sufficient to observe a change in polarisation.

Why is the measured polarisation time less than the theoretical Sokolov-Ternov polarisation time? The measured rate of polarisation – the effective polarisation time – is an equilibrium between polarising and depolarising effects, and given by Equation 5.15. One of the strongest depolarising resonances is the vertical betatron tune, and as outlined in Section 5.4.1 the vertical betatron tune was deliberately moved away from the spin tune for this experiment.

However, in spite of the high periodicity of the SPEAR3 lattice of 18 DBA cells, the racetrack lattice has superperiodicity of only 2 (and with the undulator chicane, this is reduced to mirror symmetry). Higher-order betatron resonances are cancelled by high lattice superperiodicity [45], which the SPEAR3 lattice does not exhibit. The original SPEAR lattice had many narrow depolarising spin resonances in tune space [147, 170]. It is possible that for these experiments with the SPEAR3 lattice the spin tune overlapped with one such resonance, reducing both the equilibrium polarisation and the effective polarisation time [171].

5.5.2 Electron Beam Energy

A sinusoidal radial magnetic field was applied to the electron beam through rf stripline kickers. The excitation frequency f_{kick} was swept around a value estimated by Equation 5.12 for a beam energy corresponding to 3 GeV. Resonant depolarisation of the electron beam spins was observed at the frequency f_{dep}, and this measurement is presented in Figure 5.9 for the SPEAR3 storage ring.

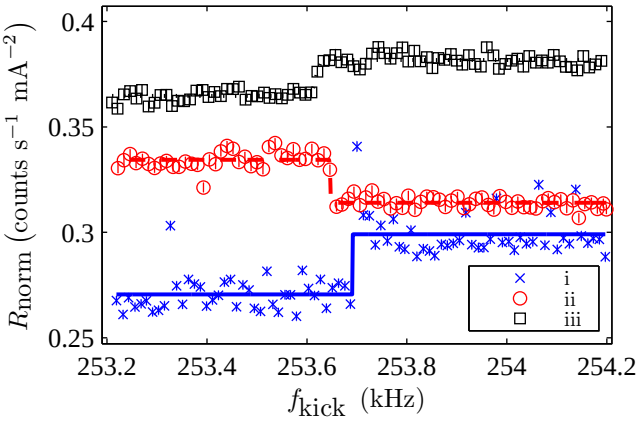

Figure 5.9: Resonant depolarisation at spin tune of the SPEAR3 storage ring [172].

The beam energy can be determined for any single resonant spin depolarisation measurement. For an rf frequency of $f_{\text{rf}} = 476,310,497$ Hz and harmonic number 372, the resonant depolarisation shown in Figure 5.9 (iii) had a fitted mean depolarising frequency $f_{\text{dep}} = 253{,}620 \pm 20$ Hz. Using Equation 5.12, this corresponded to a spin tune of $\nu_{\text{spin}} = 6.801{,}92 \pm 0.000{,}02$, a beam energy of $E = 2{,}997{,}251 \pm 7$ eV [164].

During the measurement presented in Figure 5.9, the fast-orbit feedback system was operating. Changes in the sum of horizontal corrector magnets resulted in the real changes in beam energy between Figure 5.9 (i-iii) [172]. With fast-orbit feedback running, the beam energy was observed to fluctuate within the range $E = 2.9972 - 2.9973$ GeV during these measurements [172].

The measured beam energy agreed with the beam energy predicted in previous modelling of the bending magnet magnetic field [173]. In that work, using a numerical model for the bending magnet described in Section D.2, the beam energy was predicted to be 0.1% lower than the design $E = 3.0$ GeV.

5.5.3 Synchrotron Tune Sidebands

Resonant depolarisation of an electron beam is possible at excitation frequencies which are synchrotron sidebands to the spin tune. In locating the spin tune by

scanning the excitation frequency f_{kick}, the electron beam can be depolarised at synchrotron sidebands to the spin tune, $f_{\text{dep}} = f_{\text{spin}} \pm f_s$. This depolarising resonance can be mistaken for the spin tune ν_{spin}. This is quite common in resonant depolarisation experiments – indeed, the initial resonant depolarisation in these experiments at SPEAR3 was observed to be a synchrotron sideband to the spin tune ν_{spin}.

To test whether the spin resonance corresponded to the spin tune or a synchrotron sideband, the beam energy was measured at SPEAR3 for different gap voltages V_{gap}, as illustrated in Figure 5.10.

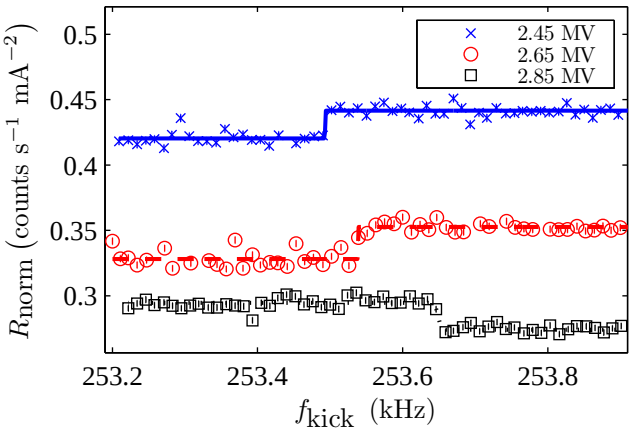

Figure 5.10: Resonant depolarisation for SPEAR3, at various RF gap voltages [172].

Illustrated in Figure 5.10 are excitation sweeps across the real spin tune at gap voltages between 2.45 and 2.85 MV. For these different gap voltages, there is a corresponding change in the synchrotron frequency. The synchrotron frequency f_s is given by [47],

$$f_s = f_{\text{rev}} \sqrt{-\frac{\eta_x h e V_{\text{gap}}}{2\pi E} \cos\phi_s}, \tag{5.18}$$

where η_x is the slip factor, h is the harmonic number, (eV_{gap}) is the cavity gap voltage, E is the beam energy, ϕ_s is the synchronous phase and f_{rev} is the revolution frequency. For gap voltages between 2.45 and 2.85 MV, the synchrotron frequency f_s was calculated for the SPEAR3 ring, using the parameters in Table 5.3 and Table 5.4.

This reduction in gap voltage reduces the synchrotron frequency from 11.3 kHz to 10.4 kHz. As the measured depolarisation frequency does not change by 900 Hz with the change in gap voltage, this is a depolarisation of the spin tune and not a synchrotron sideband. As with measurements of the beam energy presented in Section 5.5.2, the change in depolarisation frequency observed in Figure 5.10 is

Table 5.3: Calculation of synchrotron frequency – SPEAR3 model values.

Parameter		SPEAR3 model value	Units
Revolution frequency	f_{rev}	1.280	MHz
Slip factor	η_x	-0.00146	...
Harmonic number	h	372	...
Energy loss per turn	U_0	0.8812	MeV $(\mathrm{turn})^{-1}$
Beam energy	E	3000.0	MeV

Table 5.4: Synchrotron tune for gap voltages corresponding to Fig. 5.10.

Gap voltage V_{gap} (MV)	Synchronous phase ϕ_s (rad)	Synchrotron frequency f_s (kHz)
2.85	2.83	11.3
2.65	2.80	10.9
2.45	2.77	10.4

interpreted as a real change in beam energy arising from the operation of the fast global orbit feedback during this measurement.

5.5.4 Momentum Compaction Factor

Resonant spin depolarisation is one of very few methods for measurement of the momentum compaction factor of an electron storage ring. The momentum compaction factor can be calculated from measurements of the synchrotron frequency [174], to limited accuracy. The momentum compaction factor α_c of a storage ring lattice can be calculated by integrating around the curvilinear trajectory s as [45]

$$\alpha_c = \frac{1}{C} \oint_0^C \frac{\eta_x(s)}{\rho(s)} ds, \tag{5.19}$$

where C is the circumference, $\eta_x(s)$ the horizontal dispersion and $\rho(s)$ the local bending radius. The meaning of the momentum compaction factor expressed in Equation 5.19 is the fractional change in the orbit circumference for a given change in beam energy. Hence the strategy adopted in the measurement of the momentum compaction factor is to measure [46],

$$\alpha_c = \frac{\Delta C/C}{\Delta E/E}. \tag{5.20}$$

In principle, one could change the beam energy and measure the change in orbit

circumference. In practice, changing the frequency of the rf cavities forces a change in the revolution frequency of the electron beam. This forces the stored beam onto a dispersive orbit (ΔC) of different energy (ΔE).

The momentum compaction factor of the SPEAR3 lattice was measured. Small changes to the rf frequency resulted in small changes to the beam energy, which were measurable using the resonant depolarisation technique. The measured momentum compaction factor is presented in Figure 5.11.

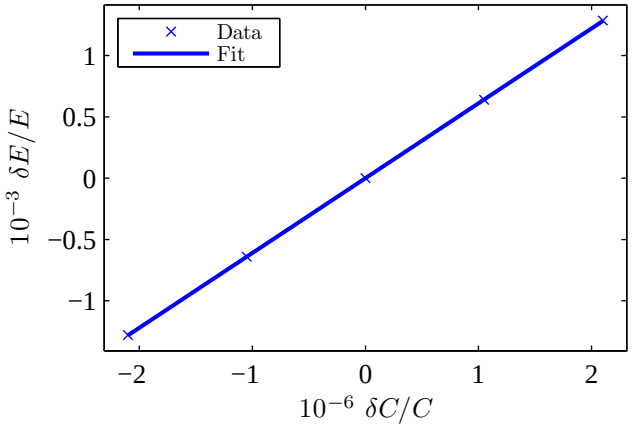

Figure 5.11: Measurement of the momentum compaction factor of the SPEAR3 storage ring [172].

The momentum compaction factor for the SPEAR3 storage ring lattice was measured as $\alpha_c = 0.00164 \pm 0.00001$ [164].

5.6 Discussion

The main result of this experiment was the direct measurement of the momentum compaction factor of the SPEAR3 storage ring. This measurement was used to evaluate various models of the bending magnets of the AS and SPEAR3 storage rings.

Several models of the trajectory of an electron beam through straight rectangular defocussing gradient bending magnets are given in Appendix D. Defocussing gradient bending magnets are used in both the AS and SPEAR3 storage rings: the AS bending magnet is scaled from the SPEAR3 bending magnet [124]. Similar modelling was undertaken for the SPEAR3 bending magnet [173].

To evaluate these different modelling approaches, the measured and modelled values of the momentum compaction factor were compared for the AS and SPEAR3

bending magnets. As defined in Equation 5.19, the momentum compaction factor depends upon both the bending radius $\rho(s)$ and the horizontal dispersion $\eta_x(s)$. In relation to the momentum compaction factor, both of these are discussed.

5.6.1 Bending Radius

The bending field $B_0(z)$ of the gradient bending magnet is described by a virtual quadrupole of transverse quadrupole gradient B_1. This is basically a thick quadrupole model, where the transverse position of the electron beam changes along the magnet length. Hence the dipole field varies in the longitudinal coordinate z by $B_0(z) = B_1 x(z)$. As a result, the local bending radius $\rho(z)$ is given by,

$$\rho(z) = p/(q_e B_0) = p/(q_e B_1 x(z)), \tag{5.21}$$

where p is the magnitude of the beam electron momentum. The local bending radii of each of the four models described in Section D.2 are plotted in Figure 5.12.

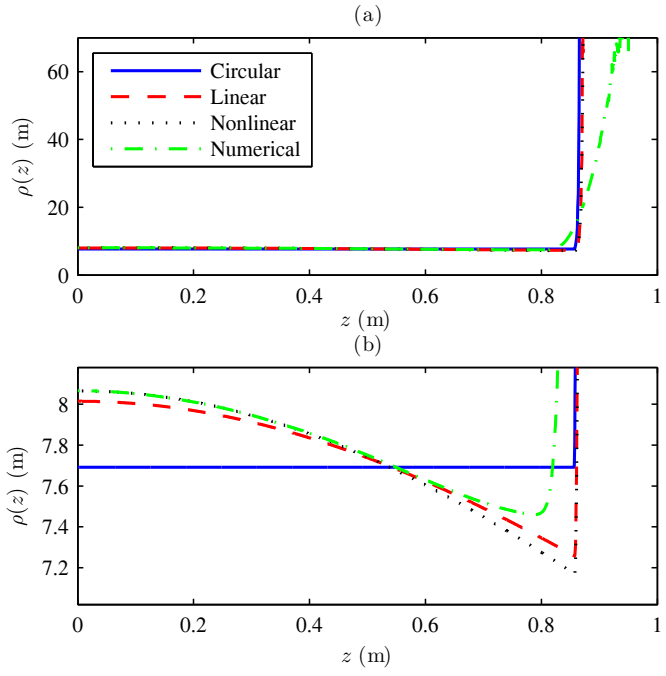

Figure 5.12: Bending radius ρ as a function of the longitudinal coordinate z, for each of the four models described in Section D.2 for the AS bending magnet. (a) Bending radius $\rho(z)$ with longitudinal position z, highlighting the longitudinal extent of the fringe field in the numerical model. (b) Magnification of (a), highlighting variation of bending radius within the iron length of the magnet. [K.P. Wootton, et al., *Phys. Rev. ST – Accel. Beams*, **16**, 074001 (2013). Published by the American Physical Society under the terms of the Creative Commons Attribution 3.0 License.]

The bending radius $\rho(z)$ varies longitudinally within the bending magnet. The highest bending fields correspond to lower bending radii at large z, as highlighted in Figure 5.12 (b). This results in a trajectory with greatest bending near the extrema of the bending magnet (the entrance and exit), and less bending in the centre.

5.6.2 Dispersion Function

The storage ring linear lattice parameters (Section 3.3) can also be compared for lattices with bending magnets modelled by the linear hyperbolic and numerical trajectories. The AS storage ring was simulated using the Accelerator Toolbox (AT) code [175] for both the analytical linear model given by Equation D.4, and numerically evaluated bending magnet fields given by Equation D.9. Linear hyperbolic cosine and numerical models of the trajectory were specifically compared, as the linear method is commonly implemented in accelerator tracking codes, and elements commonly included in accelerator tracking codes (sector bending magnets with multipole components) can be used to construct the magnetic field profile along the numerically evaluated trajectory.

For each modelling technique, the three families of storage ring quadrupoles were matched to give the same betatron tunes and horizontal dispersion in the straights. Figure 5.13 shows the betatron and dispersion functions for the AS lattice, and the difference between these solutions for the linear hyperbolic and numerical models of the bending magnet.

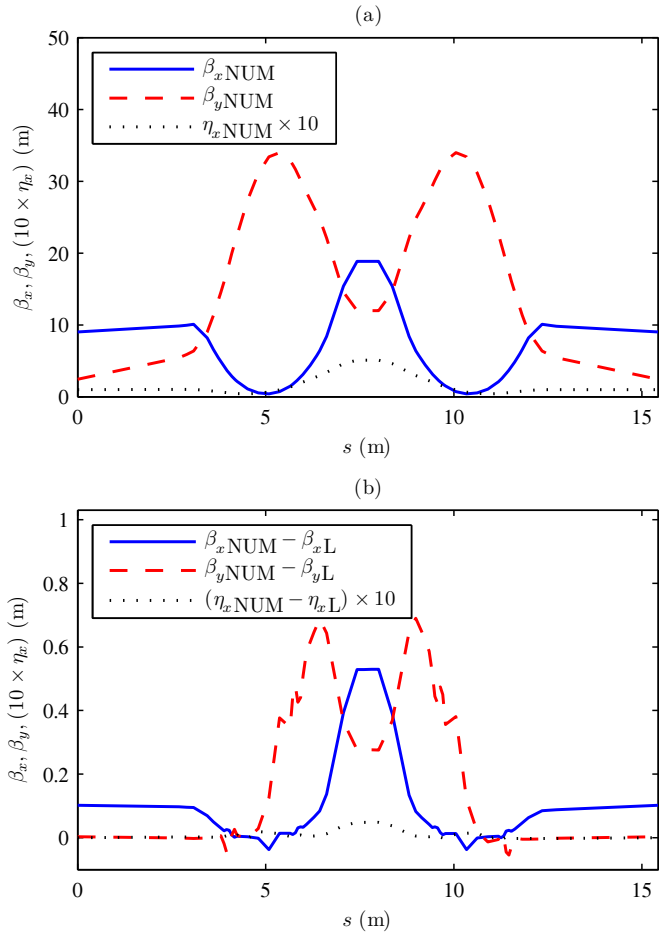

Figure 5.13: (a) Lattice functions evaluated using numerical model for trajectory, fitting quadrupoles for the 0.1 m dispersion lattice of the AS [98]. (b) Difference between lattice functions of numerical and linear hyperbolic cosine trajectory. [K.P. Wootton, et al., *Phys. Rev. ST – Accel. Beams*, **16**, 074001 (2013). Published by the American Physical Society under the terms of the Creative Commons Attribution 3.0 License.]

Figure 5.13 (b) demonstrates that the solution of quadrupole strengths for matched tunes and dispersion in the centre of the straights yields a significant difference in the dispersion and betatron functions across the arc cell. The horizontal dispersion $\eta_x(s)$ is an input to the momentum compaction factor. At the Beam Position Monitor (BPM) in the centre of the arc, the peak difference between the model dispersion functions is $\eta_{x\mathrm{NUM}} - \eta_{x\mathrm{L}} = 4.8$ mm. The measured dispersion function $\eta_{x\mathrm{MEAS}}$ is compared to numerical and linear models in Figure 5.14.

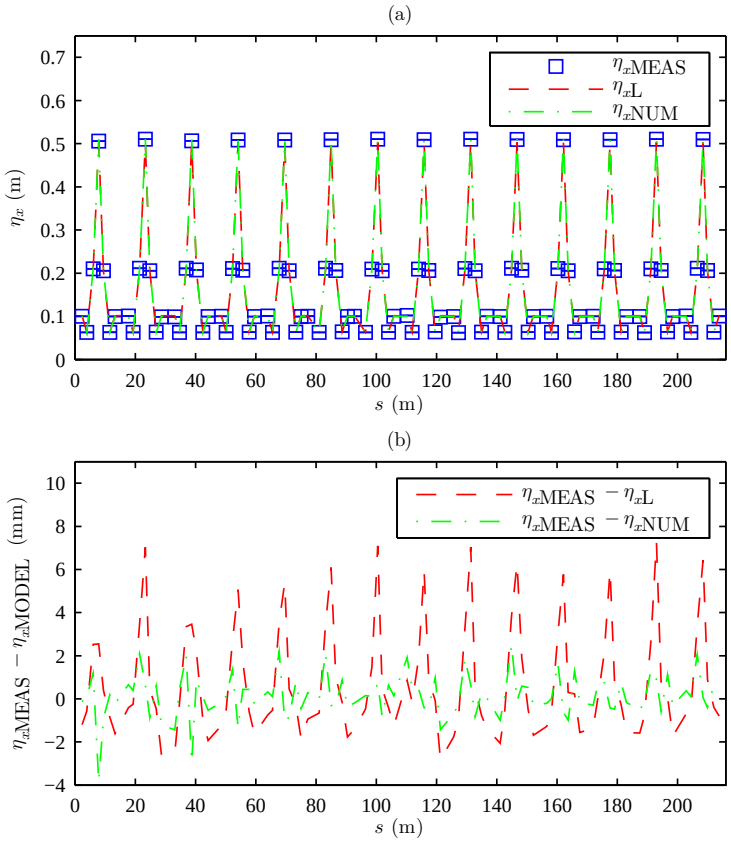

Figure 5.14: Measurement and modelling of AS storage ring dispersion. (a) Measured (with uncertainties), linear hyperbolic, and numerical models of horizontal dispersion; (b) Difference between measured and modelled dispersion for both models at all BPMs of the storage ring. The numerical model better fits the measured horizontal dispersion of the AS storage ring. [K.P. Wootton, et al., *Phys. Rev. ST – Accel. Beams*, **16**, 074001 (2013). Published by the American Physical Society under the terms of the Creative Commons Attribution 3.0 License.]

For the horizontal dispersion shown in Figure 5.14, the mean and standard deviation of the difference between the measured and model dispersion of the BPMs in the centre of the arcs is for the linear model $\eta_{x\mathrm{MEAS}} - \eta_{x\mathrm{L}} = 5.8 \pm 1.4$ mm, and for the numerical model $\eta_{x\mathrm{MEAS}} - \eta_{x\mathrm{NUM}} = -0.6 \pm 1.4$ mm.

Hence, the measured dispersion function agrees with the numerical model to within the limits of this lattice calibration, that is $\eta_{x\mathrm{MEAS}} \equiv \eta_{x\mathrm{NUM}}$. The difference between the measured dispersion and linear model is attributed to the difference between the linear and numerical models, that is $\eta_{x\mathrm{MEAS}} - \eta_{x\mathrm{L}} \equiv \eta_{x\mathrm{NUM}} - \eta_{x\mathrm{L}}$.

5.6.3 Momentum Compaction Factor

To evaluate which is a more accurate representation of the beam trajectory within the bending magnet, the momentum compaction factor was measured to high precision using resonant spin depolarisation. Measured and modelled values of the momentum compaction factors of both the AS and SPEAR3 lattices are compared in Table 5.5.

Table 5.5: Momentum compaction factor – measured and modelled [164].

	AS	SPEAR3
Linear hyperbolic cosine model	0.00205	0.00162
Numerical model	0.00211	0.00165
Measured	0.00211 ± 0.00005	0.00164 ± 0.00001

Within the uncertainty of the measurement, the measured momentum compaction factor agreed with the numerical model of the trajectory within the bending magnet, and disagreed with the usual linear hyperbolic cosine approximation. The accuracy of the numerical model comes from using the correct distribution of the dipole field component as illustrated in Figure 5.12 (see also Figure D.3).

5.6.4 Numerical Modelling of Trajectory

The principal advantage of the numerical modelling technique employed is the generality of the solution, which is given for reference in Appendix D. In this work, numerical modelling of the electron beam trajectory through a field map has been applied to a straight, rectangular defocussing gradient bending magnet. However, this modelling technique can just as easily be applied to other non-conventional magnet assemblies for various proposed accelerators, including low-emittance electron lattices.

Present and future third-generation storage ring light source lattices already consider defocussing magnets and damping partition exchange as part of a low emittance strategy [128,176]. Ultimate Storage Ring (USR) light sources [79,80,129–131] plan to employ transverse and longitudinal gradient dipole magnets as part of a strategy to reduce the equilibrium horizontal emittance.

Fixed-Field, Alternating Gradient (FFAG) accelerators have enjoyed a recent resurgence in interest [177]. In particular, scaling lattices employing gradient dipoles [178, 179] could realise benefits to trajectory and focusing modelling using these numerical techniques. The modelling technique could also be useful for non-scaling lattices with real quadrupoles at large transverse offsets [180,181]. Also, with beams

of antiproton species, this modelling approach could prove useful to the Recycler ring at Fermilab [135].

Blending both FFAG and low emittance electron lattices, reverse-bend lattices have been proposed for storage rings [182], using curved magnets present in usual accelerator tracking codes [183]. The fabrication of straight magnets could be significantly simpler, with models for arbitrary beam trajectories obtained using numerical integration.

5.7 Summary

The aim of this chapter was the characterisation of a straight rectangular defocussing gradient bending magnet. Defocussing gradient bending magnets are commonly used as part of a strategy to minimise horizontal emittance, and will be used for this purpose in the CLIC damping rings. In spite of the easy fabrication of straight magnets, at present these are employed at very few storage rings because of the concomitant difficulty in modelling the beam trajectory.

Measurements were made at the SPEAR3 storage ring which employs gradient bending magnets, using the high-precision technique of resonant spin depolarisation. To measure the momentum compaction factor, the rf frequency provided an accurate constraint on the circumference of the closed orbit, and resonant spin depolarisation an accurate measurement of stored beam energy. The momentum compaction factor of the SPEAR3 storage ring was measured as $\eta_c = 0.00164 \pm 0.00001$.

Within the uncertainty of the measurement, the momentum compaction factor was shown to agree with the numerical model of the trajectory within the bending magnet, and disagree with the hyperbolic cosine approximation. Linear and numerical models of the trajectory were specifically compared, as the linear method is commonly implemented in accelerator tracking codes, and elements commonly included in accelerator tracking codes can be used to yield the numerically evaluated trajectory.

Chapter 6

Modelling Ultralow Vertical Emittance Damping Rings

6.1 Motivation

Historically, the principal goal of low-emittance storage ring design has been the minimisation of horizontal beam emittance. For constructed rings, the equilibrium horizontal emittance can be sensibly varied by a factor of approximately two. However the equilibrium vertical emittance can be varied by several orders of magnitude, offering the opportunity to maximise design luminosities by minimising damping ring equilibrium vertical emittance – designing damping rings for flat beams.

Storage ring accelerators are typically designed for a beam orbit in a single, horizontal plane. At the *in silico* design stage of accelerators, lattice magnetic elements (dipoles, quadrupoles, sextupoles) are aligned perfectly with respect to the design beam orbit – in particular neither vertically into nor out of this horizontal plane. Hence with no bending and no dispersion in the vertical direction, the vertical emittance evaluated from synchrotron radiation integrals (Equation 3.57 – Equation 3.61) is identically zero, as stated in Section 3.4.7. Notwithstanding the contribution from the quantum limit of vertical emittance, this ideal scenario is never achieved in practice.

At the time of construction, real storage ring accelerator magnets depart from this ideal alignment. The aim of this work was to determine the sensitivity of the achievable electron beam vertical emittance to magnet alignment tolerances for the CLIC damping rings. The lattice used was the CLIC damping ring lattice for the CLIC CDR [37], simulated in Methodical Accelerator Design (version 10) (MAD-X) with alignment offsets. A theoretical expectation value for the vertical emittance is

also given [84].

6.2 The CLIC Damping Rings: A Challenge

The goal of this work was to investigate of the sensitivity of the vertical emittance to magnet misalignments for the CLIC main damping rings. Table 6.1 presents a summary of beam parameters at extraction from the CLIC main damping rings [37].

Table 6.1: Main damping ring extracted beam requirements [37].

Parameter		Value	units
Energy	E	2.86	GeV
Bunch population	N	4.1	10^9
Normalised emittance, horizontal	$\gamma\varepsilon_x$	480	nm rad
Normalised emittance, vertical	$\gamma\varepsilon_y$	4.5	nm rad

The design extracted beam emittances include growth due to collective effects, particularly IBS. It has been demonstrated that a zero-population equilibrium vertical emittance, $\gamma\varepsilon_y = 3.7$ nm rad will be required to allow for growth due to IBS [184]. Constraining the vertical emittance to only a factor of five larger than the quantum limit of vertical emittance of $\gamma\varepsilon_{y\mathrm{QLOVE}} = 0.7$ nm rad is demanding.

A similar analysis was made for an earlier CLIC damping ring lattice [113]. A similar analysis was also made for this lattice using the resonant driving terms formalism [185].

6.3 Sources of Vertical Emittance

The equilibrium vertical emittance of beams in present storage rings is governed by residual vertical dispersion, and betatron coupling resulting from magnet alignment offsets. Magnet misalignments considered included:

- Quadrupole vertical offsets;
- Quadrupole transverse rolls;
- Sextupole vertical offsets;
- Dipole transverse rolls.

Expectation values for the vertical emittance resulting from various magnet misalignments were calculated [84,186]. Analytical estimates of vertical emittance arising from misalignments typically assume the machine (either storage or damping ring) is an approximately circular lattice composed of many equivalent lattice cells, with errors distributed randomly around the machine. The horizontal emittance is assumed to be dominated by main dipole radiation. Damping rings of future electron linear colliders (ILC, CLIC, KEK Accelerator Test Facility (KEK-ATF)) are proposed as wiggler-dominated racetrack lattices. An example is the CLIC main damping ring lattice, as shown in Figure 4.4. The racetrack lattice is composed of many TME arc cells arranged in two arcs, connected by two Focussing–Open–Defocussing–Open (FODO) cell wiggler straights.

The entire lattice is very compact, with minimum spacings between adjacent magnets. This is especially evident in the arc cells, where some elements are longitudinally separated by only $ds = 0.08$ m. The FODO wiggler cells are tighter still, requiring space for a transition between the superconducting wiggler within a cryochamber vessel, to room-temperature synchrotron radiation absorbers and quadrupoles.

6.4 Vertical Emittance Arising from Vertical Dispersion

In the absence of orbit correction, much of the vertical emittance growth can be attributed to the closed orbit error, giving rise to vertical dispersion. In a storage ring with sextupoles as the highest order multipole elements, the mean square vertical dispersion arises from five main contributions [84],

- Quadrupole transverse rolls (Θ_Q);
- Sextupole vertical offsets (Y_S);
- Vertical dipole kicks (ΔG);
  - Main dipole rolls (Θ_B);
  - Quadrupole vertical offsets (Y_Q);
- Function of the errors giving rise to a non-zero closed orbit;
- Dependence upon the orbit correlation function.

Each of these five items will be addressed in the sections that follow. The expected value of the emittance arising from the mean vertical dispersion can be expressed in the form [84],

$$\langle \varepsilon_y \rangle = 2\mathcal{J}_s \frac{\langle \eta_y^2 \rangle}{\overline{\beta_y}} \sigma_E^2. \tag{6.1}$$

Hence, in the subsections that follow, the individual contributions to

$$\frac{\langle \eta_y^2 \rangle}{\overline{\beta_y}} \tag{6.2}$$

are evaluated. These analytical estimates for the vertical emittance arising from vertical dispersion assume a ring before correcting orbit, betatron functions and chromaticity. It is envisaged that the constructed lattice arc cells will necessarily include orbit corrector windings, as well as skew quadrupole correctors.

6.4.1 Quadrupole Roll Misalignment

The contribution to vertical dispersion from an RMS roll misalignment of main quadrupoles is given by [84],

$$\left(\frac{\langle \eta_y^2 \rangle_{\Delta\Theta_Q}}{\overline{\beta_y}} \right)_1 = \frac{1}{8 \sin^2 \pi\nu_y} \sum_{\text{quads}} (k_1 L)^2 \, 4\Theta_Q^2 \beta_y(s) \eta_x(s)^2, \tag{6.3}$$

where Θ_Q is the RMS roll of the main quadrupoles.

In the roll misalignment of the combined-function bending magnets of the CLIC damping ring lattice, Equation 6.3 is used to account for the roll of the k_1 quadrupole gradient. The dispersion generated is small when compared to the roll of the corresponding main dipole field.

6.4.2 Sextupole Vertical Misalignment

The contribution to vertical dispersion from an RMS vertical misalignment of main sextupoles is given by [84],

$$\left(\frac{\langle \eta_y^2 \rangle_{\Delta Y_S}}{\overline{\beta_y}} \right)_2 = \frac{1}{8 \sin^2 \pi\nu_y} \sum_{\text{sexts}} (k_2 L)^2 \, Y_S^2 \beta_y(s) \eta_x(s)^2, \tag{6.4}$$

where Y_S is the RMS vertical misalignment of the main sextupoles.

6.4.3 Dipole Kicks

The contribution to vertical dispersion from dipole kicks distributed around the circumference is given by [84],

$$\left(\frac{\langle \eta_y^2 \rangle_{\Delta G}}{\overline{\beta_y}}\right)_3 = \frac{\langle y_c^2 \rangle}{\overline{\beta_y}}, \tag{6.5}$$

where $\langle y_c^2 \rangle$ is the RMS vertical closed orbit. The RMS magnitude of the Closed Orbit Distortion (COD) for Gaussian distributed, random dipole errors is given by [84],

$$\frac{\langle y_c^2 \rangle}{\overline{\beta_y}} = \frac{1}{8 \sin^2 \pi\nu_y} \sum_{\text{kicks}} \langle G(s)^2 L(s)^2 \rangle \beta_y(s), \tag{6.6}$$

where $G(s) = G_{yc} + G\Theta_B + k_1 Y_Q$, G_{yc} the kick from a vertical corrector, $G \equiv 1/\rho$ the main dipole gradient, Θ_B the RMS rotational misalignment of main dipoles, k_1 the main quadrupole gradient, Y_Q the RMS vertical misalignment of the main quadrupoles, and $L(s)$ the magnet length. For a corrected orbit, the vertical alignment Y_Q could be approximated by the BPM resolution.

The uncorrected orbit arising from the dipoles introduces dispersion in two mechanisms. The first is given by Equation 6.6. For main dipole rolls this gives [84],

$$\begin{aligned} \frac{\langle y_c^2 \rangle}{\overline{\beta_y}} &= \frac{1}{8 \sin^2 \pi\nu_y} \sum_{\text{all dip}} \langle G(s)^2 \Theta_B^2 L(s)^2 \rangle \beta_y(s) \\ &\equiv \frac{1}{8 \sin^2 \pi\nu_y} \sum_{\text{all dip}} \left(\frac{L}{\rho}\right)^2 \Theta_B^2 \beta_y(s), \end{aligned} \tag{6.7}$$

with G the main dipole gradient, and Θ_B the rotation about the longitudinal axis. The sum is taken over all the arc dipoles.

The dispersion generated by the vertical misalignment of quadrupoles is treated in a similar fashion to dipole rolls. For quadrupoles offset by RMS offsets Y_Q [84],

$$\frac{\langle y_c^2 \rangle}{\overline{\beta_y}} = \frac{1}{8 \sin^2 \pi\nu_y} \sum_{\text{all quads}} (k_1 L)^2 Y_Q^2 \beta_y(s). \tag{6.8}$$

The sum is taken over all main quadrupoles.

6.4.4 Closed Orbit

Considering a lattice without (or prior to) orbit correction, misalignments of the main magnets result in uncorrected vertical orbits. The closed orbit function hence gives a large contribution to the vertical dispersion. The contribution to the vertical dispersion is given by [84],

$$\overline{\left(\frac{\langle\eta_y^2\rangle}{\overline{\beta_y}}\right)_4} = 2\xi_y \frac{\langle y_c^2\rangle}{\overline{\beta_y}} \sum_{n=1}^{\infty} \sum_{\pm} \frac{c_n}{\nu_y \pm n}, \tag{6.9}$$

where the overbar denotes evaluation of the mean dispersion around the ring. The coefficients of the closed orbit c_n are given by [84],

$$c_n = \frac{\left(n^2+\nu_y^2\right)\left(1-\cos 2\pi\nu_y\right)}{\pi^2\left(n^2-\nu_y^2\right)^2}. \tag{6.10}$$

It can be seen that c_n is large only for integer values just above and below the vertical tune. The sum may be approximated with only these terms, though this approximation is not made in this work. The local vertical chromaticity ξ_y is given by [187],

$$\xi_y \equiv \frac{d\nu_y}{dp/p_0} = -\frac{1}{4\pi}\oint \left(k_1 + k_2\eta_x\right)\beta_y(s)ds. \tag{6.11}$$

6.4.5 Orbit Correlation Function

Solving again for an uncorrected vertical closed orbit and assuming the vertical fractional tune $\Delta\nu_y$ to be small, the term pertaining to the closed orbit correlation function can be approximated by [84],

$$\overline{\left(\frac{\langle\eta_y^2\rangle}{\overline{\beta_y}}\right)_5} \approx \frac{1}{16\sin^2\pi\Delta\nu_y}\frac{\langle y_c^2\rangle}{\overline{\beta_y}}\mathrm{sinc}^4\pi\Delta\nu_y\left[\left(4\pi\xi_y\right)^2+\left(4\pi\Delta_{SB}\right)^2\right], \tag{6.12}$$

$$\Delta_{SB} = \frac{1}{4\pi}\left|\int_0^C f(z)\beta_y(z)e^{i2\phi(z)}dz\right|,$$

$$f = k_1 + k_2\eta_x,$$

$$\phi(z) \equiv \int_0^z \frac{ds}{\beta_y(s)\nu_y}.$$

The phase advance ϕ is defined such that $\phi(C)-\phi(0)=2\pi$, and f is proportional to the local chromaticity given by Equation 6.11 [187].

6.5 Betatron Coupling

Vertical emittance arising from the coupling of betatron oscillations is calculated from several main misalignments,

- Main quadrupole rolls;
- Main sextupole vertical displacements;
- Orbit errors.

These misalignments introduce spurious skew quadrupole gradients, coupling betatron oscillations from the horizontal into the vertical plane. In this analysis, only terms linear in coupling have been considered.

6.5.1 Quadrupole Roll Misalignment

The roll misalignment of a main normal (upright) quadrupole field k_1 by an angle of Θ_Q can be described as a small skew quadrupole field,

$$k_{1S} = k_1 \Theta_Q. \tag{6.13}$$

The emittance growth from this misalignment is given by [84],

$$\langle \varepsilon_y \rangle = \frac{\varepsilon_x}{4} \frac{\alpha_x}{\alpha_y} \frac{(1 - \cos 2\pi\nu_x \cos 2\pi\nu_y)}{(\cos 2\pi\nu_x - \cos 2\pi\nu_y)^2} \sum_{\text{all quads}} (k_1 L)^2 \, 4\Theta_Q^2 \beta_x(s) \beta_y(s), \tag{6.14}$$

where α_x, α_y are the horizontal and vertical damping decrements of the lattice, defined in Equation 3.42 – Equation 3.43.

6.5.2 Sextupole Vertical Misalignment

The misalignment of a main normal (upright) sextupole field k_2 by a vertical displacement of Y_S can be described as a small skew quadrupole field,

$$k_{1S} = k_2 Y_S. \tag{6.15}$$

The emittance growth from this misalignment is given by [84],

$$\langle \varepsilon_y \rangle = \frac{\varepsilon_x}{4} \frac{\alpha_x}{\alpha_y} \frac{(1 - \cos 2\pi\nu_x \cos 2\pi\nu_y)}{(\cos 2\pi\nu_x - \cos 2\pi\nu_y)^2} \sum_{\text{all sexts}} (k_2 L)^2 \, Y_S^2 \beta_x(s) \beta_y(s), \tag{6.16}$$

where α_x, α_y are the horizontal and vertical damping decrements of the lattice, defined in Equation 3.42 and 3.43.

6.5.3 Orbit Errors

The magnitude of the vertical closed orbit error resulting from quadrupole rolls and sextupole vertical offsets is considered negligible. However for dipole kick errors (quadrupole vertical offsets and main dipole rolls), the coupling introduced by the closed orbit resulting from misalignment errors is significant.

The betatron coupling described here arises from the orbit error in the sextupoles giving rise to a net skew quadrupole field. The emittance growth is given by [84],

$$\langle \varepsilon_y \rangle \approx \sum_n \sum_{\Delta\nu} \sum_{\psi_n} \frac{\varepsilon_x}{32 \sin^2 \pi\Delta\nu} \frac{\langle y_c^2 \rangle}{\beta_y} c_n \left| \int_s^{s+C} k_2(z) \beta_y(z) \sqrt{\beta_x(z)} e^{i\psi_n(z)} dz \right|^2, \quad (6.17)$$

where

$$c_n = \frac{\left(n^2 + \nu_y^2\right)\left(1 - \cos 2\pi\nu_y\right)}{\pi^2 \left(n^2 - \nu_y^2\right)}, \quad (6.18)$$

$$n = 1, 2, 3, \ldots, \quad (6.19)$$

$$\Delta\nu = \nu_x \pm \nu_y, \quad (6.20)$$

$$\psi_n(z) = \psi_x + \begin{cases} \left(1 + \frac{n}{\nu_y}\right)\psi_y \quad \text{and} \quad \left(1 - \frac{n}{\nu_y}\right)\psi_y, & \Delta\nu = \nu_x + \nu_y \\ -\left(1 + \frac{n}{\nu_y}\right)\psi_y \quad \text{and} \quad -\left(1 - \frac{n}{\nu_y}\right)\psi_y, & \Delta\nu = \nu_x - \nu_y \end{cases} \quad (6.21)$$

6.6 Simulations

To evaluate the deleterious effect of misalignments on vertical emittance in the CLIC damping ring lattice, beam dynamics simulations were made.

6.6.1 Lattice

The lattice used was the CLIC damping ring lattice for the CDR [37]. The lattice was composed of combined-function bending magnets, quadrupoles, sextupoles and damping wigglers with a wiggling field oriented in the normal vertical orientation. This racetrack lattice includes 100 TME-like arc cells, and 26 zero-dispersion, FODO wiggler cells. The TME-like arc cell is illustrated in Figure 6.1.

A scheme of orbit correction magnets and beam position monitors was selected. The compact lattice design necessitates the use of extra windings as orbit correctors.

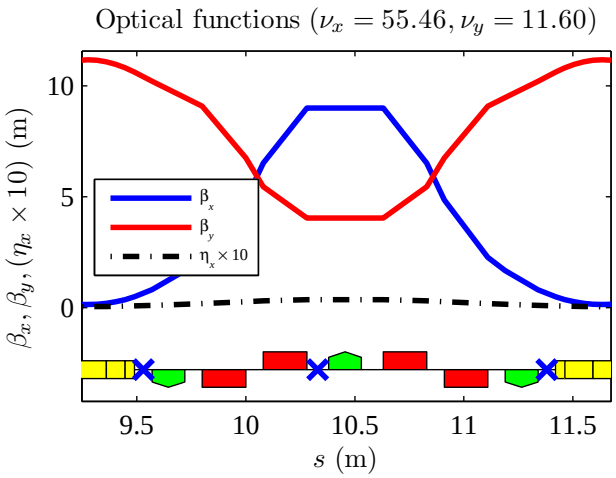

Figure 6.1: CLIC damping ring arc cell, proposed correctors and BPMs [188]. Lattice elements are indicated schematically on the lower axis. BPMs are indicated at positions marked by ×. Bending magnets are indicated by yellow rectangles, quadrupoles by red rectangles above and below the axis, and sextupoles indicated by green irregular pentagons. Orbit correctors are considered at the sextupole magnets.

The most conservative corrector pattern was considered: horizontal and vertical orbit correctors on each arc sextupole (three per TME cell), as well as alternating horizontal and vertical steering correctors adjacent to wiggler straight quadrupoles (two per FODO cell). To preserve the compact lattice, these correctors were considered as additional windings on the sextupole magnets. These steering (dipole) and skew quadrupole fields are identically orthogonal to the sextupole field, and so can be superimposed [124].

BPMs were positioned in arc cells at points of alternating high and low dispersion, as well as high and low beta functions. Button BPMs with both horizontal and vertical position measurement were assumed.

6.6.2 Misalignments Considered

Misalignments were made for all main quadrupoles, sextupoles and bending magnets. Misalignments were not considered for the damping wigglers. Magnet misalignments considered included:

- Quadrupole vertical offsets;
- Quadrupole transverse rolls;
- Sextupole vertical offsets;

- Dipole transverse rolls.

6.6.3 Description of Code

Random misalignments of magnet families were defined from Gaussian distributions of an RMS offset, truncated at 2.5 standard deviations. For each misalignment magnitude considered, 200 machines were seeded. Simulations were conducted using MAD-X, version 4.01.00.

6.6.4 Lattice Corrections

Orbit correction was undertaken using the MAD-X module. The correction algorithm used was singular value decomposition (SVD) [189]. All singular values were included in the correction.

Global corrections of tunes, chromaticity and energy were made. Beta-beating was uncorrected.

6.6.5 Emittance Estimates with Subdivided Magnet Elements

The main arc bending magnets were each subdivided into ten equal segments. The MAD-X EMIT module calculates the emittances based upon the method of Chao [190], and gives a more accurate evaluation of the curly-H function $(\mathcal{H}_x, \mathcal{H}_y)$ given by Equation 3.37 with the bending magnets subdivided [191].

The expectation value of dispersion given by dipole rolls is given by Equation 6.7. Consider the dispersion introduced from the roll of a single dipole of length L:

$$\begin{aligned} \frac{\langle y_c^2 \rangle}{\overline{\beta_y}} &\propto \sum_{\text{single dipole}} \left(\frac{L}{\rho}\right)^2 \Theta_B^2 \beta_y. \\ &= \left(\frac{L}{\rho}\right)^2 \Theta_B^2 \beta_y. \end{aligned} \tag{6.22}$$

For the same single dipole, subdivided into n segments of equal length $L_i = L/n$,

$$\begin{aligned}\frac{\langle y_c^2\rangle}{\overline{\beta_y}} &\propto \sum_{i=1}^{n}\left(\frac{L_i}{\rho}\right)^2\Theta_B^2\beta_y \\ &= \sum_{i=1}^{n}\left(\frac{L}{n\rho}\right)^2\Theta_B^2\beta_y \\ &= n\frac{1}{n^2}\left(\frac{L}{\rho}\right)^2\Theta_B^2\beta_y = \frac{1}{n}\left(\frac{L}{\rho}\right)^2\Theta_B^2\beta_y.\end{aligned} \tag{6.23}$$

Hence, for calculation of the expectation value of dispersion in misaligned, subdivided magnets, taking the sum over the subdivided lattice elements the dispersion introduced should be multiplied by the number of subdivisions, n.

6.7 Results

Emittances were calculated using the method of Chao [190]. Vertical emittance growth was considered for both the uncorrected and corrected lattice. Results from the uncorrected lattice can represent the lattice sensitivity to misalignments.

6.7.1 Analytical Estimates

The expectation value for the vertical emittance from each RMS misalignment was calculated for each of the sources in Section 6.3, using the theory of Section 6.4 and Section 6.5. In the limit of flat beams, the calculated vertical emittance scales with the square of the RMS misalignment. A summary of the sources of vertical emittance for the uncorrected lattice is given in Table 6.2.

Table 6.2: Analytical estimates of geometric vertical emittance growth in the CLIC damping ring lattice. Uncorrected lattice, by source.

Source	Quadrupole vertical 15 µm		Quadrupole roll 100 µrad		Sextupole vertical 100 µm		Dipole roll 100 µrad	
	ε_y (m rad)	%	ε_y (m rad)	%	ε_y (m rad)	%	ε_y (m rad)	%
Dipole kick	5.4×10^{-13}	0.4	7.7×10^{-14}	39	3.2×10^{-11}	39	2.8×10^{-14}	0.4
Closed orbit	1.2×10^{-10}	96	0	0	0	0	6.3×10^{-12}	96
Orbit correlation	1.1×10^{-15}	0	0	0	0	0	5.8×10^{-17}	0
Skew quadrupole	0	0	1.2×10^{-13}	61	5.0×10^{-11}	61	3.4×10^{-16}	0
Orbit errors	4.6×10^{-12}	3.6	0	0	0	0	2.4×10^{-13}	3.6

Table 6.2 highlights the dominant sources of geometric vertical emittance for each of the misalignment categories. In the uncorrected lattice, the vertical emittance produced by quadrupole vertical and dipole roll misalignments is dominated by orbit errors. Quadrupole roll and sextupole vertical misalignments introduce vertical emittance through betatron coupling from skew quadrupoles.

These sources and the effectiveness of proposed correction schemes are considered in the following sections.

6.7.2 Closed Orbit Error

Figure 6.2 shows the RMS vertical COD resulting from the four families of misalignments considered.

Figure 6.2 demonstrates that orbit correction is effective for minimising the COD for quadrupole vertical and dipole roll misalignments, which represent vertical dipole kicks. The closed orbit from quadrupole vertical misalignments is seen to be orders of magnitude greater than the next leading contribution of dipole roll misalignments. The uncorrected orbit amplification factor of 50 as shown in Figure 6.2 for quadrupole vertical misalignments, reduces to approximately 1 on orbit correction, as illustrated in Figure 6.3.

The quadrupole vertical misalignments illustrated in Figure 6.3 are not representative of the target storage ring magnet alignment – it is not deemed feasible to mechanically align quadrupoles to within $Y_Q = 10$ μm, RMS. However it is not necessary to achieve this using mechanical alignment techniques, due to the availability of algorithms for beam-based alignment of quadrupole centres [192–194].

Orbit correction is ineffective for reducing the COD arising from quadrupole roll and sextupole vertical misalignments. Fortunately, the COD is orders of magnitude smaller for these misalignments.

6.7.3 Emittance Simulations Before and After Corrections

The vertical emittance for RMS misalignments was evaluated analytically and using simulations in MAD-X, both before and after lattice corrections. Figure 6.4 shows the vertical emittance growth for misalignments of the main magnets, as well as the analytical expectation value. Figure 6.5 additionally shows the vertical emittance after corrections. For each RMS misalignment amplitude, the emittance was calculated for 200 seeded random misalignments of the accelerator magnets. The results of these simulations are represented in Figure 6.4 – 6.5 by the mean (μ) vertical

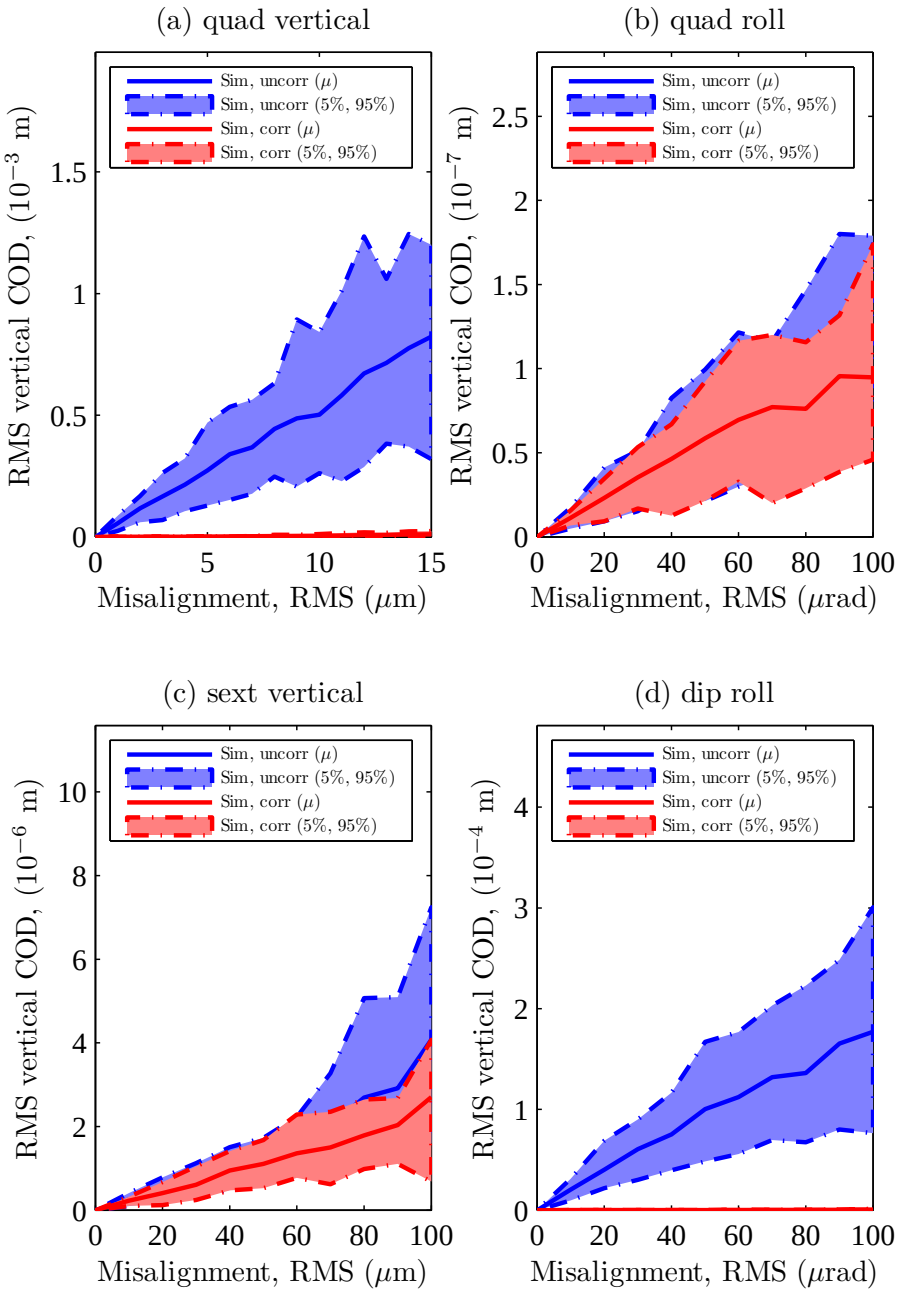

Figure 6.2: Vertical closed orbit distortion arising from magnet misalignments, before and after corrections [188].

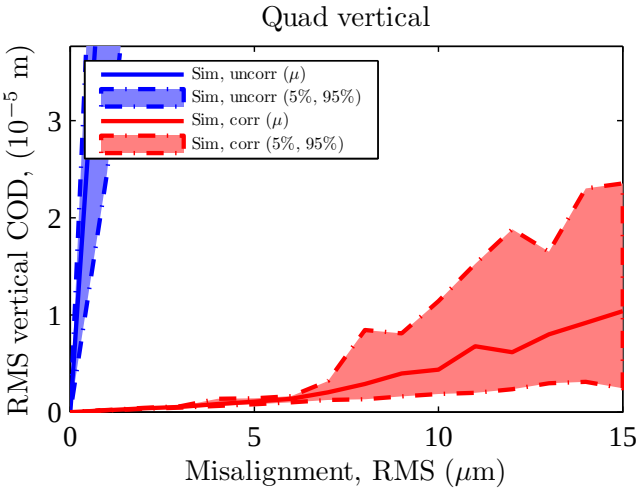

Figure 6.3: Vertical closed orbit distortion for quadrupole vertical displacements, after corrections [188].

emittance, as well as the 5^{th} and 95^{th} percentile vertical emittances, approximately $(\mu \pm 2\sigma)$. For comparison, all four misalignments are plotted all on the same axes in Figure 6.6.

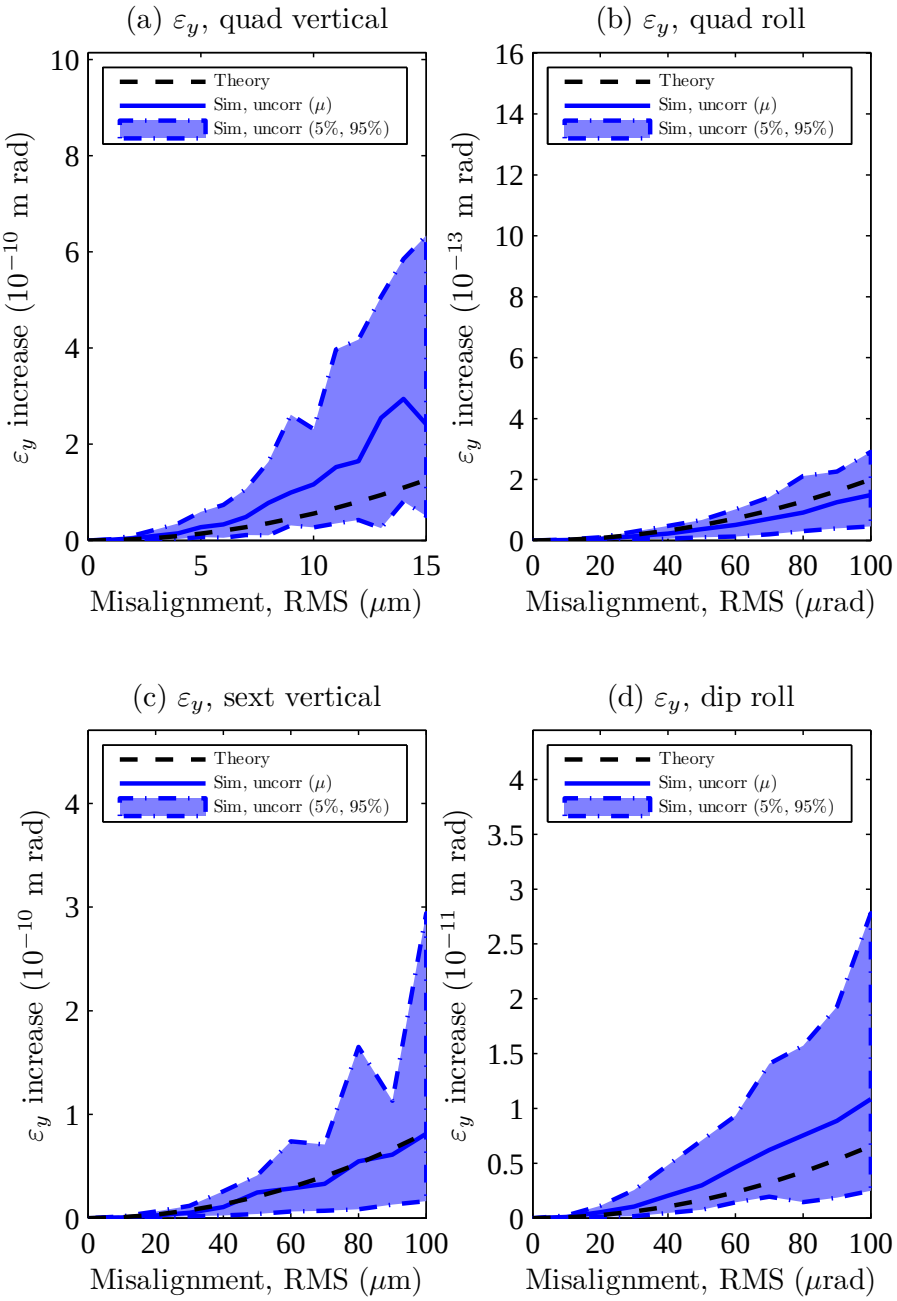

Figure 6.4: Geometric vertical emittance for magnet family misalignments. The vertical emittance is given for the uncorrected lattice in blue, and the analytical expectation value of the uncorrected lattice given by a black dashed line [188].

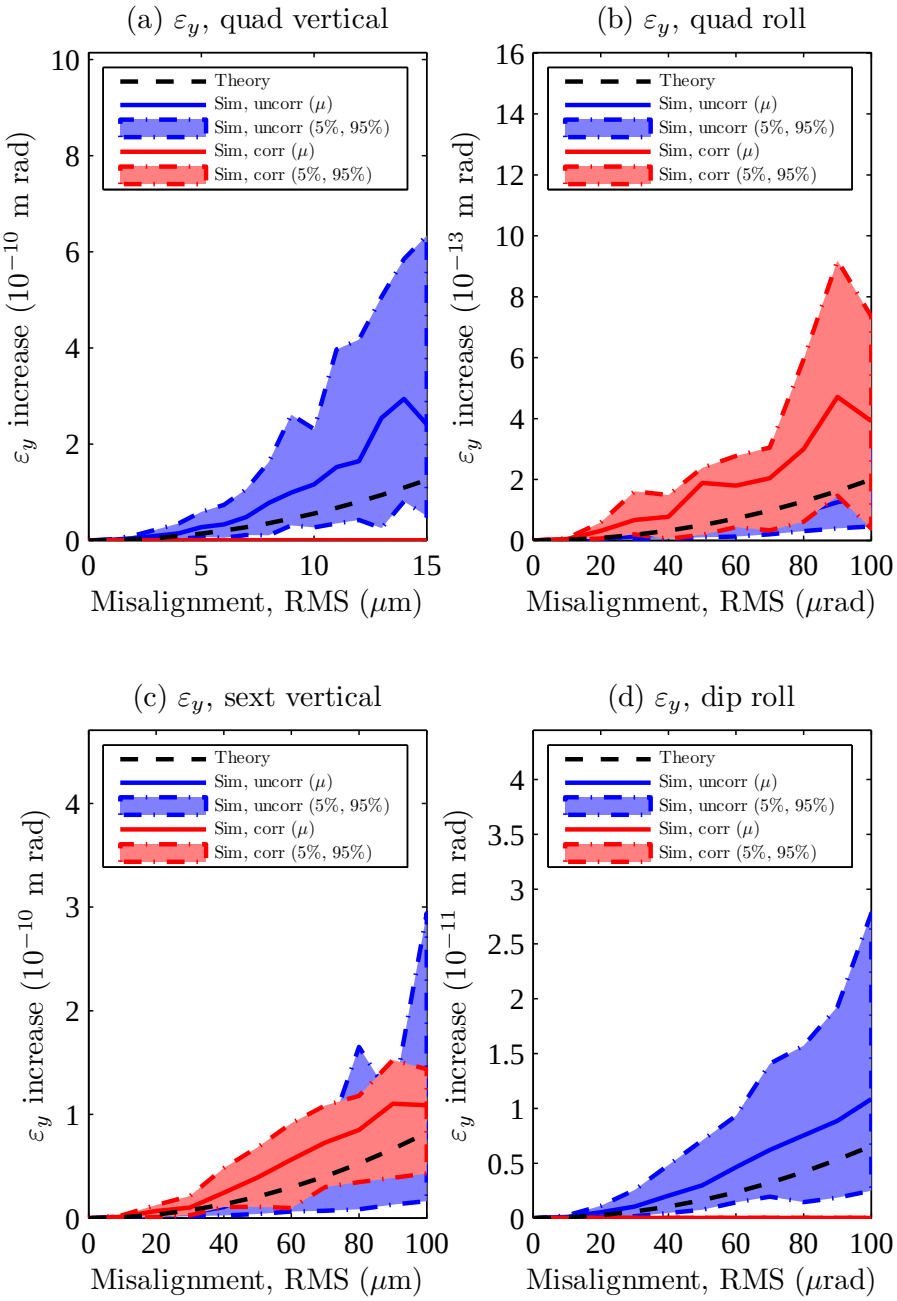

Figure 6.5: Geometric vertical emittance for magnet family misalignments. In addition to uncorrected vertical emittance of Figure 6.4, vertical emittance following lattice correction is plotted in red [188].

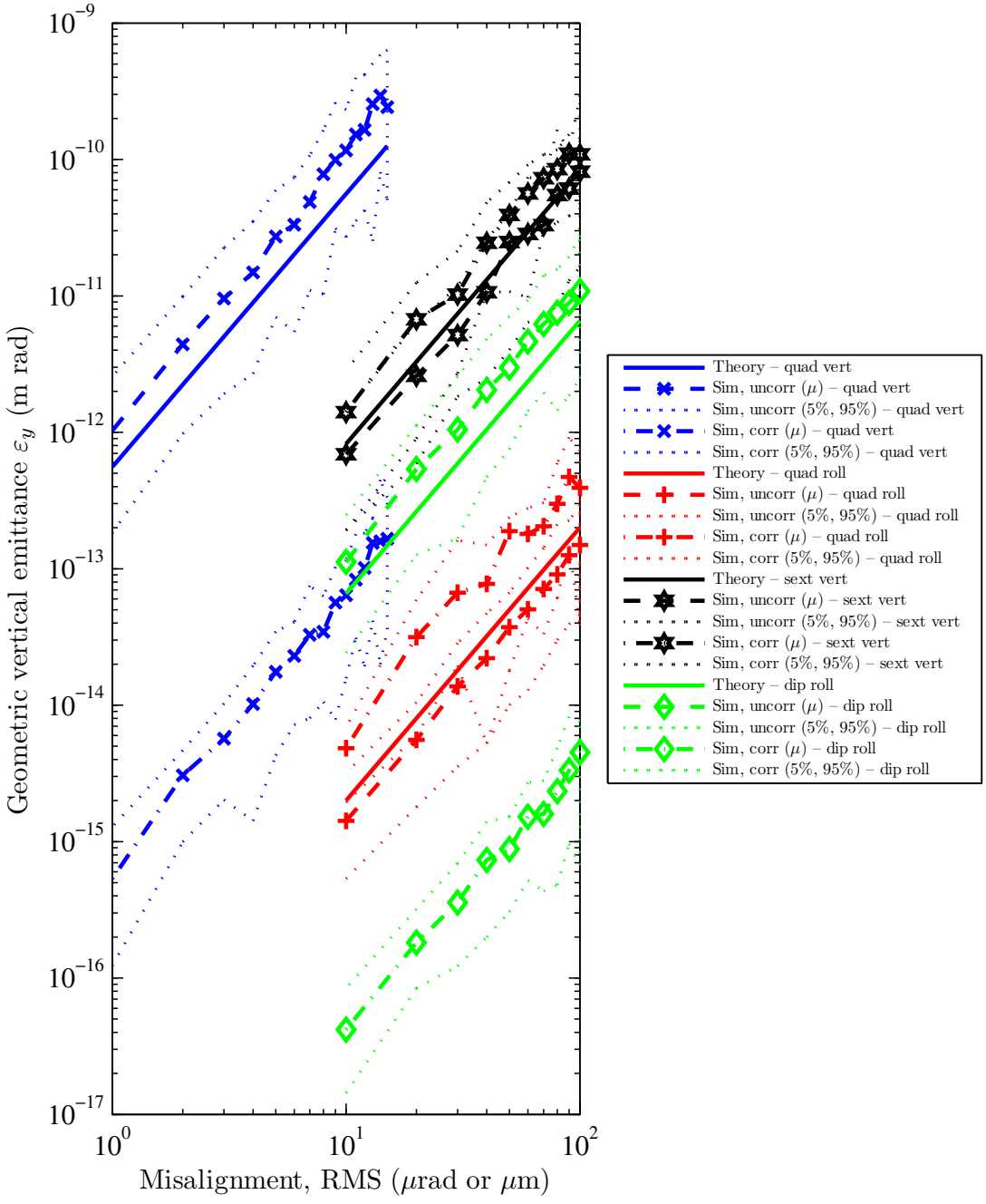

Figure 6.6: Comparison of all sources of geometric vertical emittance for magnet family misalignments. The goal geometric vertical emittance is $\varepsilon_y = 5\times10^{-13}$ m rad.

6.8 Discussion

The proposed usual orbit, tune and chromaticity corrections are insufficient for the design of an ultralow vertical emittance damping ring. As presented in Section 6.7.2 and illustrated in Figure 6.6, these corrections are sufficient for quadrupole vertical, quadrupole roll and bending magnet roll misalignments. However, they are not satisfactory for sextupole vertical misalignments. In the absence of a skew quadrupole corrector scheme, a vertical emittance of $\varepsilon_y = 0.9$ pm rad was achieved with an RMS sextupole vertical misalignment of $Y_S = 6$ μm.

For comparison, using beam-based alignment and individual shimming of the vertical offsets of sextupole magnets, sextupoles of the AS storage ring were aligned within tolerances of $Y_S = 25$ μm [195]. To allow realistic mechanical prealignment tolerances of approximately $\sigma_y = 50$ μm, skew quadrupole correctors and an individual correction scheme will be required.

6.8.1 Skew Quadrupole Correction

Only relatively recently has low vertical emittance become a design specification of damping and storage rings. Whilst many beam dynamics codes provide analysis of emittance growth arising from lattice imperfections, few codes provide a tool suitable for low vertical emittance correction. The MAD-X code features many useful modules for ring design and analysis, but as yet lacks a module for correction of linear optics or betatron coupling.

The Courant-Snyder optical functions are the closed orbit solutions to the equation of motion in a storage ring. These functions can be determined by measurement of orbit response matrices, which represent the change in orbit for a change in magnet strengths [196]. This is presently the highest precision technique for measuring and calibrating the linear lattice of a storage ring [197]. The benchmark code for storage ring light source lattice correction is Linear Optics from Closed Orbits (LOCO) [198–200], fitting orbit response matrices using a multi-parameter model of the storage ring lattice. A measured orbit response matrix of the AS is presented in Figure 6.7.

The principal advantage of fitting orbit response matrices such as Figure 6.7 is the large number of data points sampled during the measurement. Hence, an overconstrained model of the storage ring multipole elements can be fitted. Beta-beating can be corrected by fitting for upright quadrupole gradients [199, 201], and vertical emittance can be minimised by fitting skew quadrupole gradients at quadrupole and

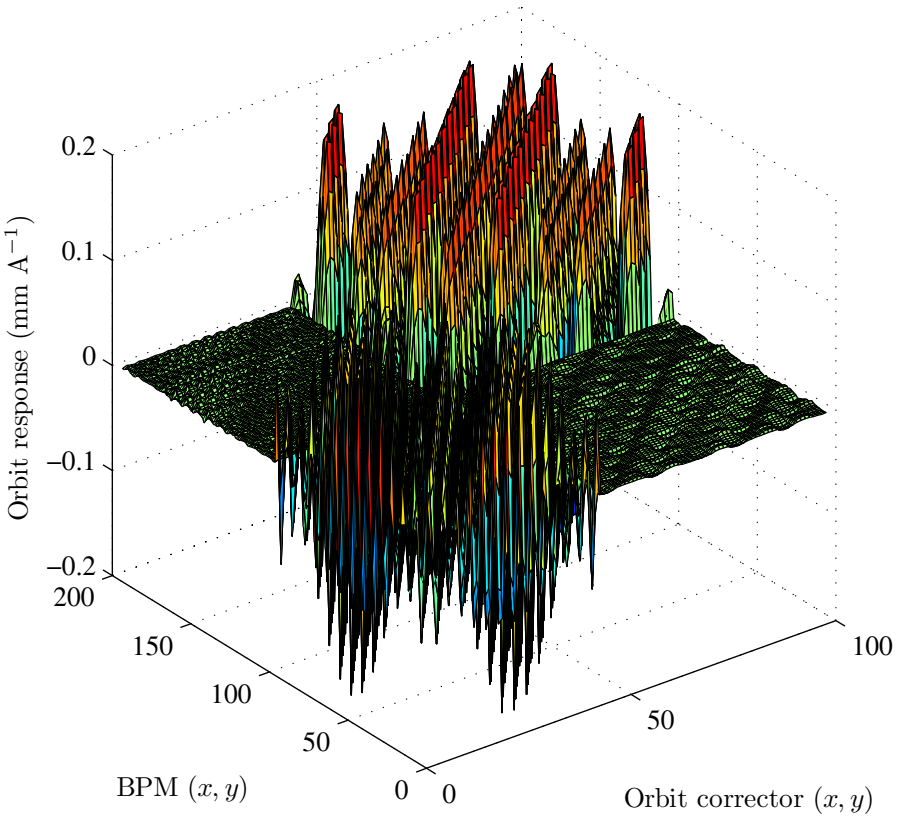

Figure 6.7: Measured orbit response matrix for minimum transverse emittance ratio for AS storage ring.

sextupole magnets [202, 203].

There was not time in the thesis to re-write the LOCO code as a module for MAD-X. Rather than performing simulations, it was decided to test this vertical emittance minimisation on an existing machine. As an ultralow vertical emittance storage ring, the AS storage ring was used to test ultralow vertical emittance optimisation and measurement.

6.9 Summary

The aim of this work was to determine the influence of magnet alignment on the single-particle vertical emittance of the electron beam in the CLIC main damping rings.

The expectation value for the vertical emittance was calculated. This analytical estimate demonstrated that the simulations of uncorrected lattices with magnet misalignments were reasonable. For the quadrupole vertical and bending magnet roll offsets, the vertical emittance growth was dominated by the vertical closed

orbit. The quadrupole roll and sextupole vertical offsets had equal contributions from dispersion resulting from dipole kicks, and betatron coupling arising from skew quadrupole terms.

The correction of orbit, tune and chromaticity is sufficient for quadrupole vertical, quadrupole roll and bending magnet roll misalignments. However these corrections are not satisfactory for sextupole vertical misalignments. In the absence of a skew quadrupole corrector scheme, a vertical emittance of $\varepsilon_y = 0.9$ pm rad was achieved with an RMS sextupole vertical misalignment of $Y_S = 6$ μm.

For comparison, using beam-based alignment and individual shimming of the vertical offsets of sextupole magnets, sextupoles of the AS storage ring were aligned within tolerances of $Y_S = 25$ μm [195]. To allow realistic mechanical prealignment tolerances of approximately $\sigma_y = 50$ μm, skew quadrupole correctors and an individual correction scheme would be required. Such a correction scheme can be tested at existing ultralow vertical emittance electron storage rings.

Chapter 7

Techniques to Measure Vertical Emittance of Beams in Storage Rings

7.1 Motivation

Beams of unprecedented small size are demanded for energy [204] and intensity frontier [205] electron-positron colliders. In order to achieve their design luminosities, next generation storage and damping rings are designed for vertical emittances in the range $\varepsilon_y = 0.5$ to 2.0 pm rad. In recent years, storage ring light sources and damping rings have produced electron beams achieving these ambitious vertical emittance targets [92, 206]. For the period 2011-2012 the AS storage ring held the world-record for lowest vertical emittance in a storage ring [95], currently held by SLS [92]. Hence electron storage ring light sources are important testbeds for linear collider damping rings.

Of the longitudinal, horizontal and vertical dimensions of electron beams, the vertical beam size (given by Equation 3.65) is the smallest – by orders of magnitude – and hence most difficult to measure. With dimensions of only several μm, the direct measurement of electron beam vertical size is made impossible by diffraction limits of visible light and hard X-ray diagnostics [207]. Ultimate proof of low vertical emittance is only demonstrated by direct observation of the vertical electron beam size.

This chapter presents a summary of techniques used to measure vertical emittance in storage rings. With particular emphasis on the AS storage ring, existing and new techniques are presented.

7.2 Existing Techniques

Vertical emittance measurements can be classified as belonging to one of two categories: indirect and direct. Direct measurement techniques observe the transverse size of the electron beam. Indirect techniques infer beam size from measurements of global properties of the beam or ring lattice.

7.2.1 Indirect Techniques

Several techniques exist for determining global properties of the electron beam in a storage ring. As presented in Section 6.8.1, orbit response matrices and in particular the LOCO algorithm are a high precision technique for measuring and correcting a storage ring linear lattice.

As an alternative to measurement of the equilibrium closed-orbit, strengths of multipole lattice elements can be measured using fast turn-by-turn measurements of an oscillating electron beam [197, 208]. By fitting the betatron phase advance, the storage ring lattice functions can be determined. With the lattice parameters fitted at every element of a ring, the emittance can be evaluated from synchrotron radiation integrals (Equation 3.57 – 3.61), and the beam size evaluated using Equation 3.65. At present, the precision of the technique is limited by the decoherence of betatron tunes at the high positive chromaticities at which many storage rings routinely operate. This includes the AS storage ring, which operates at high positive chromaticities of $(\xi_x, \xi_y) = (3.5, 13)$.

The charge density of an electron bunch can be inferred from the rate of intrabeam scattering. In strong-focussing storage rings, beam electrons perform betatron oscillations (high transverse momentum), and synchrotron oscillations (low longitudinal momentum). Elastic scattering of beam electrons within a bunch resulting from large transverse momentum scattering is called Touschek scattering [159]. It is a single scattering event with a large change in transverse momentum leading to the direct loss of two scattering beam particles [209], and is an important contribution to the beam lifetime for modern low emittance rings. Touschek scattering has been used to fit for ultralow vertical emittance beam size in the AS storage ring [95].

7.2.2 Direct Techniques

Direct measurement techniques observe the transverse size of the electron beam. These include techniques which interact directly with the beam such as wire scanners, or observe products of the beam such as synchrotron light.

Wire scanners are used as profile monitors of proton beams, but such devices are not feasible for electron machines due to melting by rf wakefields [210] and the large wire diameter compared to the small electron beam size [211]. Instead, a narrow laser-wire has been used as an emittance monitor at electron rings [211–213]. With a low-emittance tuning method, the technique has been used to successfully measure emittance ratios of order 1% [214]. The laser-wire technique is limited by the transverse size of the laser waist, and to measure smallest beam sizes one can instead use an interferogram of two beams. This Shintake monitor technique [215–217] has demonstrated measurement of beams with transverse dimensions $\sigma_y < 100$ nm [218]. This particular measurement was of beam size demagnified in a transfer line, not stored in a ring.

The measurement of beam emittance using synchrotron light is desirable because it is a non-destructive and minimally perturbing method of observation: a stored electron beam emits synchrotron radiation whether or not the physicist chooses to measure it. A typical synchrotron radiation diagnostic device is a hard X-ray pinhole camera, to image the profile of an electron beam passing through a bending magnet [219,220]. Hard X-ray Fresnel zone plates have also been used as the imaging optic instead of a pinhole [221]. As an alternative to imaging, the angular profile of bending magnet radiation has been measured using hard X-ray, in-air profile monitors [222], which is an especially cost-efficient vertical emittance monitor.

Working in the visible light part of the synchrotron radiation spectrum is convenient for the construction and operation of diagnostic equipment. Pioneered at the SLS, the π-polarisation technique was used to demonstrate record low vertical emittance in 2008 and again in 2012 [92, 223]. Observing the π (vertical) polarisation of bending magnet radiation, there is a phase shift of π radians between the wavefronts above and below the orbit plane [223]. Forming an image results in a null radiation field on-axis (phase shift of π radians), and any light observed is from the convolution of this radiation null with the electron beam vertical size. This technique cannot be implemented with the AS Optical Diagnostic Beamline (ODB) because it requires light from above and below the orbit plane, and the present configuration accepts light only above the orbit plane. The SLS diagnostic beamline is presently being upgraded to additionally enable synchrotron radiation interferometry [224, 225].

A standard visible light technique is synchrotron radiation optical interferometry [226–228]. The technique is based on Michelson's stellar interferometer, which was used to measure the angular diameter and separation of stars [229]. The angular size of objects is resolved by measuring the partial degree of spatial coherence, which is quantified by van Cittert-Zernike theory [230–232]. Synchrotron radiation

interferometry has been used for measurement of record low vertical emittance at KEK-ATF in 2004 [91]. The intensity imbalance technique has been demonstrated to improve the measurement sensitivity to smallest emittance beams, where the beam size approaches the diffraction-limited size of $\sigma_y \approx 1\mu$m [233–236].

7.3 Direct Measurement Techniques at the Australian Synchrotron

The synchrotron light emittance diagnostics available at the AS storage ring include a hard X-ray Diagnostic Beamline (XDB), and an ODB [237]. Both beamlines image the stored electron beam passing through a bending magnet.

7.3.1 X-ray Pinhole Camera

The XDB is a hard X-ray pinhole camera, which forms an image of the electron beam in the AS storage ring. To serve the user beamlines, the principal purpose of the XDB was the direct measurement of horizontal emittance. For the usual 0.1 m dispersion user lattice of the AS storage ring [98], the equilibrium horizontal beam size at the bending magnet source is $\sigma_x = 87$ μm [238].

With the beginning of experiments to minimise vertical emittance, the XDB was characterised as a vertical emittance monitor. The image formed by the pinhole camera was a convolution of the electron beam transverse size with the Point-Spread Function (PSF) of the imaging apparatus with a 20 μm pinhole mask.

Analysis of the XDB geometry demonstrated the sensitivity to imaging beams of vertical emittance down to several picometre radians [239]. Due to the uncertainty in deconvolving the PSF, the X-ray pinhole camera was unable to resolve vertical emittances smaller than this value. This frustrated the direct measurement of low vertical emittance beams created at the AS storage ring [95].

While the direct imaging of picometre electron beam vertical emittance using the XDB was frustrated, the apparatus was used in an indirect measurement of vertical emittance. Instead of the direct measurement of the vertical beam size, the XDB was used to measure the local transverse (x, y) tilt of the beam profile. As the betatron coupling of the lattice was lowered, the tilt of the beam ellipse at the pinhole camera was observed to minimise. This supported other indirect measurements of low vertical emittance in the AS storage ring [95], but was not direct proof of low vertical emittance.

7.3.2 Visible Light Synchrotron Radiation Interferometry

The ODB is a beamline dedicated to visible light diagnostics of the electron beam in the storage ring. It was designed to serve a suite of optical diagnostics, to measure the intensity, transverse and longitudinal dimensions of the electron beam in the storage ring [237].

An optical synchrotron radiation interferometer is one technique for direct observation of vertical emittance. Construction and commissioning of an interferometer at the AS storage ring can be found in Refs. [240,241]. Wavefronts from the electron beam source passing through an aperture of finite dimensions can be focussed using either a lens or diffracting optic. It was identified in that work that the vertical angular aperture of the present ODB was not large enough to pass highest spatial frequencies needed to resolve smallest vertical emittance electron beams. The beamline front end has several apertures, with an opening in the crotch absorber being the limiting (smallest) vertical angular aperture. The aperture is 5 mm (2.8 mrad) in the vertical direction and 10 mm (5.6 mrad) in the horizontal. This crotch absorber was designed for AS bending magnet X-ray beamlines. For reasons of cost and simplicity, this aperture was also used for the ODB – a visible light beamline.

Even at the Vacuum Ultra-Violet (VUV) limit of photon wavelength $\lambda = 200$ nm, this vertical opening is too narrow to pass the entire vertical fan of optical synchrotron radiation. Simulations in Synchrotron Radiation Workshop (SRW) [242] demonstrated that passing the full vertical distribution of bending magnet radiation (3σ, 99.8% power) at a wavelength of $\lambda = 532$ nm required a vertical opening aperture of 15 mm (8.4 mrad), three times larger than the present 2.8 mrad [241]. For synchrotron radiation interferometry a much larger vertical opening angle of synchrotron radiation was required.

The infrared beamline at the AS has a much larger vertical opening angle than the ODB. Bending magnet and edge radiation are extracted using a slotted mirror of transverse dimensions 17.3 mrad (vertical) $\times$ 60.2 mrad (horizontal) [243]. A centrally positioned slot of 2.3 mrad (3 mm) passed the central X-ray fan, to minimise the thermal load and subsequent distortion of the planar mirror surface.

The greatest experimental limitation was that the infrared beamline was designed for transmittance and reflectance of infrared rather than visible light. In particular, many of the infrared-transparent vacuum windows in the beamline were not optically flat surfaces, which significantly distorted visible-light synchrotron radiation wavefronts.

Using optical synchrotron radiation interferometry at this beamline, the smallest

vertical beam size measured at the bending magnet leading edge was $\sigma_y = 47^{+13}_{-3}$ μm. This corresponded to an emittance ratio of $\varepsilon_y/\varepsilon_x = 0.0067^{+0.004}_{-0.0007}$ [241].

Subsequently, the smallest electron beam size measured using intensity imbalance optical interferometry on the ODB at the AS was $\sigma_y = 40$ μm [235, 236]. This measured vertical electron beam size is much larger than the beam size expected at the dipole centre of $\sigma_y = 6$ μm for a vertical emittance of $\varepsilon_y = 1$ pm rad.

7.4 Undulator Radiation and Emittance

Third-generation storage ring light sources were designed with long insertions, specifically for wiggler and undulator ID magnets. Present synchrotron light experiments principally use undulators as their photon sources, exploiting the low horizontal emittance lattices optimised for such insertion devices. As the spectral and spatial profile of undulator radiation is especially sensitive to the transverse emittance [244], undulators have been used as emittance monitors at electron storage rings.

Projections of the spatial profile of undulator harmonics can be used to characterise the beam emittance. This has been demonstrated using a soft X-ray undulator producing a vertical field [245], referred to as a horizontal undulator because the beam is deflected in that transverse direction.

At high energy electron rings, undulator radiation has been used to image electron beams [246, 247]. The absolute brilliance of the undulator radiation spectrum has also been fitted to determine electron beam emittances [248]. In all of these attempts, relatively large vertical emittances were measured using horizontal undulators.

7.4.1 Spontaneous Undulator Radiation

To characterise the sensitivity of undulator radiation to electron beam emittance, a description is given of the single electron angular distribution of undulator radiation. The angular distribution of spontaneous radiation from a planar undulator is theoretically described [45, 70, 249]. Following the prescription employed in the SPECTRA program [250], the calculation of undulator radiation is given following the prescription of Alferov, *et al.* [251].

Radiation produced by an ID arises from the transverse oscillation of beam electrons by a periodic magnetic field. A planar device is considered, with a magnetic

field oscillating sinusoidally in the vertical direction y given by [45, 64],

$$\begin{aligned}\vec{B}(z) &= B_x(z)\hat{i} + B_y(z)\hat{j} + B_z(z)\hat{k}, \\ B_x(z) &= 0, \\ B_y(z) &= B_0 \cosh(k_p y)\cos(k_p z), \\ B_z(z) &= -B_0 \sinh(k_p y)\sin(k_p z),\end{aligned} \tag{7.1}$$

where the undulator period is given by $\lambda_p = 2\pi/k_p$. A usual horizontal ID is a magnetic field oscillating in the vertical orientation, resulting in horizontal oscillations of an electron beam passing through. The strength of IDs is typically classified by the deflection parameter K_u given by Equation 3.47 [45, 64],

$$K_u = \frac{eB_0}{\beta m_0 c k_p} \equiv 93.4 B_0[\mathrm{T}]\lambda_p[\mathrm{m}]. \tag{7.2}$$

For an undulator of ideal sinusoidal field distribution, the spectral and spatial distribution of flux is given in terms of linear polarisations $\sigma(\hat{i})$ and $\pi(\hat{j})$ at the photon frequency ω for the n^{th} harmonic by [45, 64]

$$\frac{d\dot{N}_{\mathrm{ph}}(\omega)}{d\Omega} = \alpha\gamma^2 N_p^2 \frac{\Delta\omega}{\omega}\frac{I}{q_e}\sum_{n=1}^{\infty} n^2 \left(\frac{\sin\left(\pi N_p \Delta\omega_n/\omega_1\right)}{\pi N_p \Delta\omega_n/\omega_1}\right)^2 \left(F_\sigma^2\hat{i} + F_\pi^2\hat{j}\right), \tag{7.3}$$

$$F_\sigma = \frac{2\gamma\theta\Sigma_1(n)\cos\phi - K_u\Sigma_2(n)}{1 + \frac{1}{2}K_u^2 + \gamma^2\theta^2}, \tag{7.4}$$

$$F_\pi = \frac{2\gamma\theta\Sigma_1(n)\sin\phi}{1 + \frac{1}{2}K_u^2 + \gamma^2\theta^2}, \tag{7.5}$$

where α is the fine-structure constant, N_p is the number of undulator periods, I the stored electron beam current, q_e the electronic charge, ω_n the photon frequency of the n^{th} undulator harmonic (ω_1 for the fundamental), and $\Delta\omega_n = \omega - \omega_n$. The distributions are expressed in the polar angle θ and azimuthal angle ϕ. The sums $\Sigma_1(n)$ and $\Sigma_2(n)$ are given by

$$\Sigma_1(n) = \sum_{m=-\infty}^{\infty} J_{-m}(u)J_{n-2m}(v), \tag{7.6}$$

$$\Sigma_2(n) = \sum_{m=-\infty}^{\infty} J_{-m}(u)[J_{n-2m-1}(v) + J_{n-2m+1}(v)], \tag{7.7}$$

where J are Bessel functions of the first-kind, with arguments of

$$u = \frac{\omega}{\omega_1} \frac{\vec{\beta} K_u^2}{4\left(1 + \frac{1}{2}K_u^2 + \gamma^2\theta^2\right)}, \tag{7.8}$$

$$v = \frac{\omega}{\omega_1} \frac{2\vec{\beta} K_u \gamma\theta \cos\phi}{1 + \frac{1}{2}K_u^2 + \gamma^2\theta^2}. \tag{7.9}$$

This single-electron angular distribution of undulator radiation is illustrated in Figure 7.1. Consider undulator radiation from a high deflection parameter undulator ($K_u = 5$), at high harmonics of the undulator fundamental ($n = 14, 15$). These are unusual parameter choices. Figure 7.1 highlights that at these unusually high deflection parameters and high harmonics, the angular distribution of undulator radiation resembles an interference pattern significantly narrower than the usual $1/\gamma$ cone of undulator radiation. The convolution of this single-electron distribution with the electron beam becomes a probe sensitive to the electron beam size.

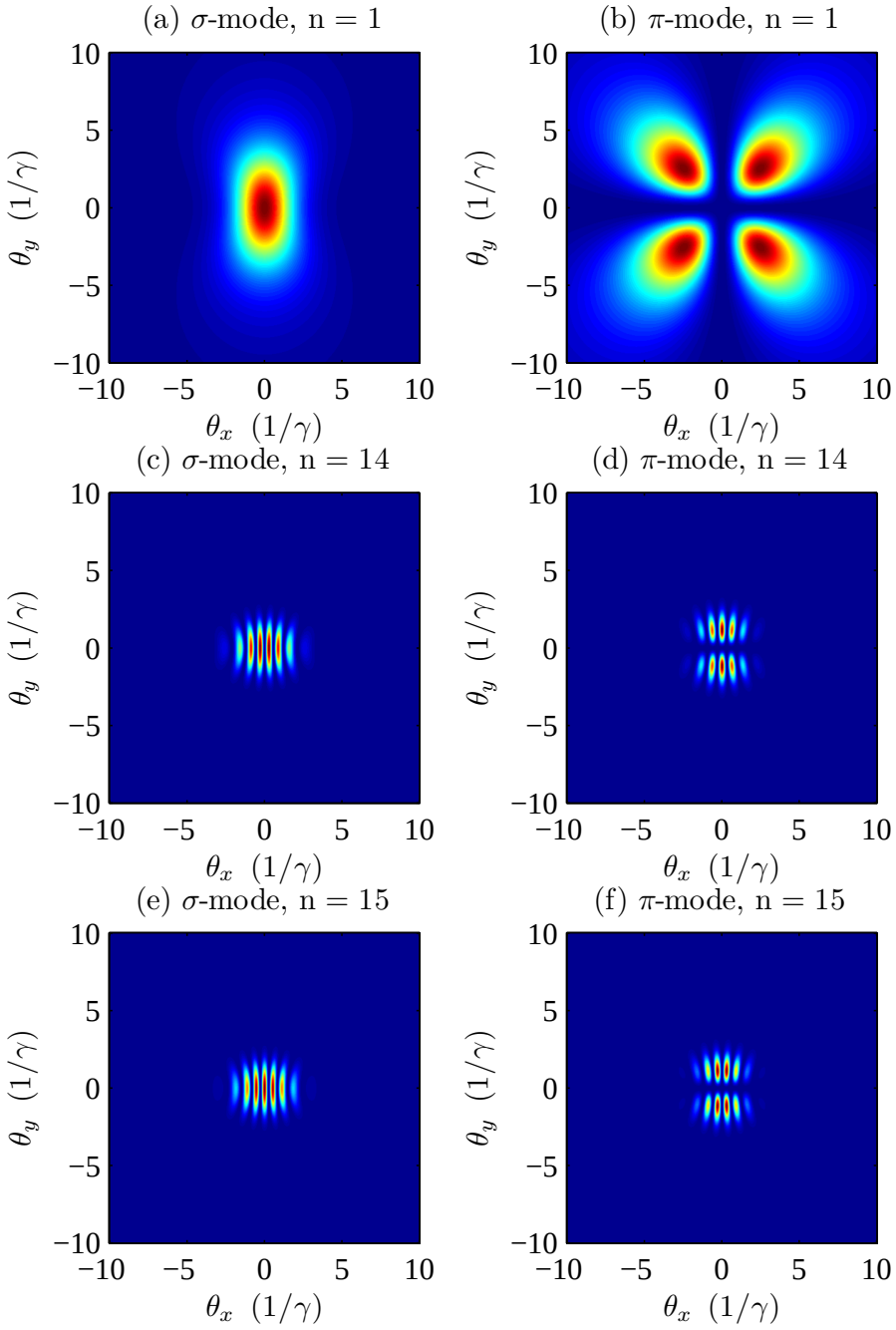

Figure 7.1: Single-electron angular distribution of undulator radiation, for an electron in a horizontal, planar undulator. The angular distribution is plotted in terms of horizontal and vertical opening angles θ_x, θ_y, for linear polarisation modes σ and π. Plot of analytical Equation 7.4, Equation 7.5 for undulator harmonics $n = 1, 14, 15$. For high undulator harmonics, the undulator radiation distribution resembles a narrow interference pattern [45].

7.4.2 Vertical Undulator Technique

The idea to use a vertical undulator to measure vertical emittance came out of a conversation about the on-axis radiation spectrum of horizontal undulators. To investigate this, simulations of an electron beam passing through an undulator were performed with the synchrotron radiation code SPECTRA [250], as illustrated in Figure 7.2.

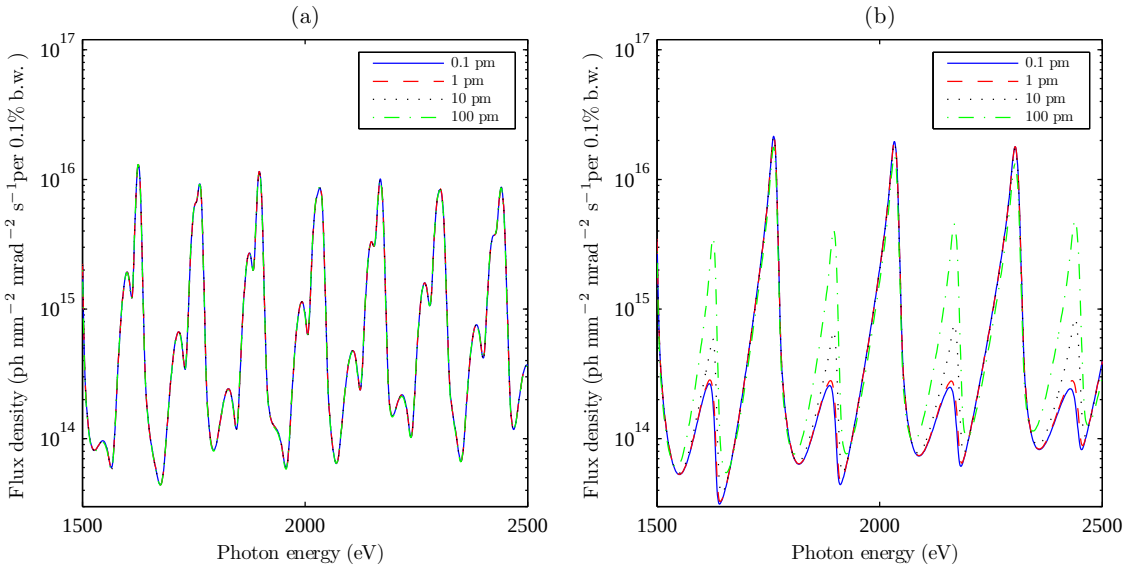

Figure 7.2: Undulator brilliance spectra for various vertical emittances ε_y, simulated in SPECTRA [250]. The photon energy of the undulator fundamental is 138 eV. (a) Horizontal undulator with peak field $B_y = 0.55$ T. (b) Vertical undulator with peak field $B_x = 0.55$ T. With a vertical undulator, the different vertical emittances can be resolved in the undulator spectrum [252].

The spectrum of undulator radiation in Figure 7.2 (a) from a horizontal undulator departs significantly from the single electron spectrum of undulator radiation. The finite horizontal emittance of $\varepsilon_x = 10$ nm rad contributes intensity to the even harmonics, in addition to changing the width and shape of the odd and even harmonics. So if the horizontal emittance appeared in the radiation spectrum of a horizontal undulator, could the same hold for a vertical undulator?

For the same electron beam and undulator strength parameters, the undulator spectrum was evaluated for an undulator oscillating the beam up and down – a vertical undulator. Simulation results are presented in Figure 7.2 (b), for various vertical emittances. This spectrum closely approximates the single-electron undulator radiation spectrum, with bright odd harmonics and suppressed even harmonics. It can be seen that the high, even undulator harmonics are sensitive to picometre

vertical emittances. Hence the brilliance of high undulator harmonics from a high deflection parameter undulator could be used as a vertical emittance diagnostic.

7.4.3 Vertical Undulator Theory

The theory of the technique is built upon two main ideas: vertical (as opposed to horizontal) undulators, and the measurement of ratios of photon beam brilliance rather than absolute values.

The orientation of insertion devices at storage ring light sources is governed by the need for a large momentum aperture at injection. Typically, storage rings are constructed with the orbit in the horizontal plane. To facilitate this aperture, the beam stay-clear in insertion straights of the AS storage ring was designed with $|x| \geq 15$ mm, $|y| \geq 5$ mm [97]. This stay-clear accommodates usual horizontal wiggler and undulator insertion devices, with arrays of magnetic poles above and below the orbit plane of the ring.

Horizontal undulators – undulators that deflect the electron beam in the orbit plane of the ring – have been proposed [253–257] and demonstrated [258–260] to give excellent measurement of the horizontal beam size and energy spread. Where the electron beam transverse emittance is close to fully-coupled ($\varepsilon_y \approx \varepsilon_x$), the brilliance of horizontal undulators exhibits some sensitivity to the vertical emittance [259]. Electron storage rings typically design for transverse emittance ratios less than a few percent ($\varepsilon_y \ll \varepsilon_x$), with damping ring designs aiming for minimum vertical emittance. In this low vertical emittance limit, horizontal undulators are insensitive to vertical emittance, limited by the single-electron opening angle of undulator radiation [258].

In contrast to horizontal undulators being largely insensitive to picometre vertical emittance, vertical undulators become especially sensitive. This was first identified by Shiro Takano [261, 262][1].

The second element of this technique is the evaluation of ratios of brilliance as opposed to the absolute photon beam brilliance, which is difficult to measure quantitatively. Previous analytical descriptions and modelling of horizontal undulator brilliance focussed on determination of the absolute photon beam brilliance [244, 264], and identified the brilliance of even harmonics as especially sensitive to the transverse emittance [265]. Instead, here the ratio of intensities of adjacent odd and even

[1] At the time of publication of K.P. Wootton's Refs. [252, 263], S. Takano's previous presentation of Ref. [261] was unknown. Ref. [261] was communicated by S. Takano [262] following K.P. Wootton's presentation at the International Beams Instrumentation Conference, 2012 [252].

undulator harmonics are measured and compared with simulations of photon brilliance. This approach was proposed for vertical undulator measurement of vertical emittance [261], and for measurement of horizontal emittance of electron beams accelerated by plasma wakefield accelerators [253–256]. In both of these studies, the first and second harmonics of the undulator spectrum were evaluated.

Modelled in SPECTRA [250], the sensitivity of horizontal and vertical undulators of equal deflection parameter to vertical emittance is illustrated in Figure 7.2. Over a range of operational vertical emittances there is no measurable change in brilliance for a horizontal undulator. However, for a vertical undulator, at high even undulator harmonics the photon beam brilliance changes by orders of magnitude. Hence, measurements of the photon beam brilliance at the even harmonics exhibit a strong dependence upon the electron beam emittance [265]. Greatest sensitivity to the lowest vertical emittance is observed at high undulator harmonics.

This technique shares similarities with another projection measurement of vertical emittance (the π-polarisation technique of Section 7.2.2) [92, 223], but differs by passing, as opposed to masking, the on-axis null radiation field. Illustrated in Figure 7.3 are simulated transverse profiles of the undulator radiation intensity. Instead of trying to measure the absolute photon flux of the on-axis null-field of the even harmonics, F_{n-1}, this low flux is calibrated against the high-flux peaks of the odd harmonics passing the same aperture, F_n. The ratio of fluxes of adjacent undulator harmonics F_{n-1}/F_n is evaluated. For Figure 7.3, the ratio of flux passing for the even 14^{th} to odd 15^{th} harmonics is $F_{n-1}/F_n = 0.42$ for a beam of 100 pm rad geometric vertical emittance shown in Figure 7.3 (e) & (g), and 0.17 for 1 pm rad shown in Figure 7.3 (f) & (h).

The ratio of fluxes is optimised by minimising the vertical offset of the pinhole. This is achieved experimentally by scanning the pinhole vertically through the interference pattern for the unambiguous intensity maximum of an odd undulator harmonic, as illustrated in Figure 7.3 (h).

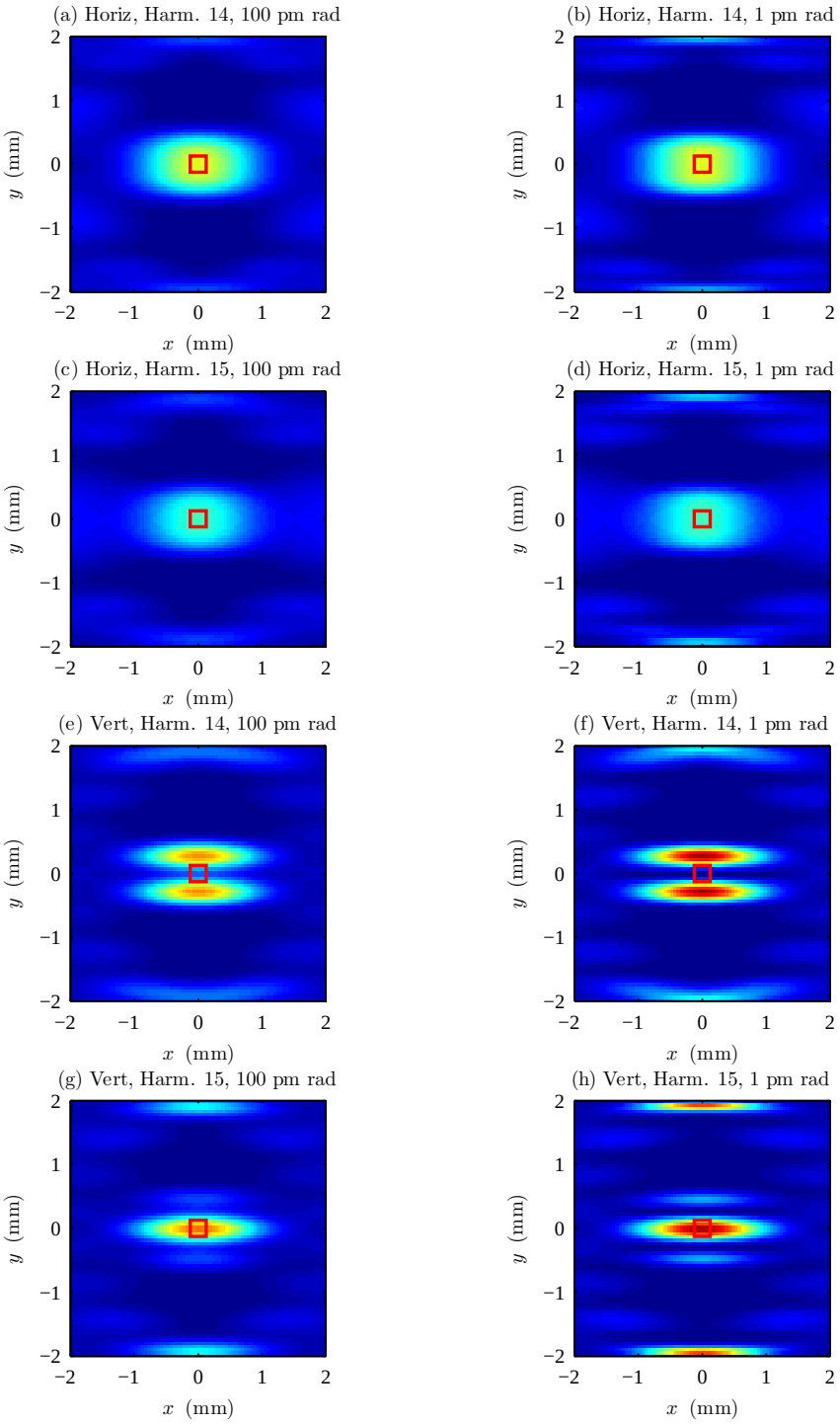

Figure 7.3: SPECTRA [250] simulation of profile of undulator radiation 15 m from the undulator centre, with 250×250 µm rectangular pinhole aperture outline marked in red. (a)-(d) Horizontal undulator. (a) Harmonic 14, $\varepsilon_y = 100$ pm. (b) Harmonic 14, $\varepsilon_y = 1$ pm. (c) Harmonic 15, $\varepsilon_y = 100$ pm. (d) Harmonic 15, $\varepsilon_y = 1$ pm. (e)-(g) Vertical undulator. (e) Harmonic 14, $\varepsilon_y = 100$ pm. (f) Harmonic 14, $\varepsilon_y = 1$ pm. (g) Harmonic 15, $\varepsilon_y = 100$ pm. (h) Harmonic 15, $\varepsilon_y = 1$ pm. [K.P. Wootton, et al., *Phys. Rev. Lett.*, **109** (19), 194801 (2012). © 2012 American Physical Society.]

7.5 Soft X-ray Beamline at the Australian Synchrotron

Vertical undulators are rare [264, 266–268] – typically beams are deflected in the horizontal plane. As outlined in Section 7.4.3, for reasons of maintaining a large injection aperture, vertical undulators are only selected when there is a compelling technical need. In this work, an elliptically polarised undulator was phased as a vertical undulator. Experiments in this chapter were performed on the AS storage ring. The Advanced Planar Polarised Light Emitter–II (APPLE-II) undulator serves the soft X-ray user beamline of the AS [269]. Components of this apparatus are illustrated in Figure 7.4.

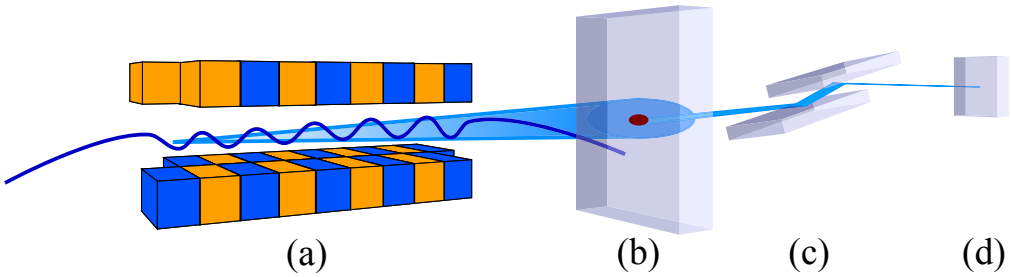

Figure 7.4: Schematic of vertical undulator emittance measurement apparatus. (a) APPLE-II undulator in storage ring; (b) Pinhole aperture formed to spatially filter undulator radiation; (c) Grating monochromator to bandpass photon energy; (d) Silicon photodiode to measure photon beam intensity.

The central components of this apparatus are an electron beam passing through a vertical undulator. This creates undulator radiation propagating in the forward direction of the electron beam. Undulator radiation was measured by closing four blades of the white-beam slits to form a narrow pinhole. Intensity at different energies was measured using a diffraction grating monochromator and photodiode.

This section outlines how these components were configured for the measurement and simulation of photon flux. The pinhole photon flux was calculated and presented on an absolute scale, however arbitrary units would suffice. This is because as outlined in Section 7.4.3, one of the benefits of this approach is that the relative rather than absolute spectral brilliance is used to determine the vertical beam emittance.

7.5.1 Advanced Planar Polarised Light Emitter–II Undulator

The undulator used was an APPLE-II type undulator [270, 271]. A render of the APPLE-II undulator is presented in Figure 7.5.

Properties of the electron beam and undulator are summarised in Table 7.1 below. The magnet arrays of the undulator were phased to produce a horizontal field, deflecting the electron beam in the vertical plane. A gap of 17.1 mm was selected – close to the minimum gap of 17.0 mm – producing a peak horizontal field of 0.55 T. Magnetic measurements of the undulator during manufacture demonstrate that in the configuration for vertical polarisation at minimum gap, the axis of the undulator field is within -6 ± 30 mrad of the nominal horizontal orientation [271].

Figure 7.5: Render of the APPLE-II undulator for the AS [271].

Table 7.1: Electron beam and undulator properties used in simulation.

Parameter		Value	Units
Beam			
Energy	E_0	3.0	GeV
Energy spread	σ_E	0.11	%
Horizontal emittance	ε_x	10	nm rad
Undulator			
Period length	λ_u	75	mm
Peak field	B_u	0.55	T
Deflection parameter	K_u	3.8	...
Number of full periods	N_u	25	...

7.5.2 White-Beam Slits as a Pinhole Aperture

The beamline used for these experiments does not have a pinhole to characterise the spatial profile of radiation [269]. Beamlines at other facilities do, for this specific purpose [272]. Instead, four blades of the white-beam slits were closed to form a rectangular pinhole aperture. The upper and lower blades which define the vertical height of the pinhole are illustrated schematically in Figure 7.6.

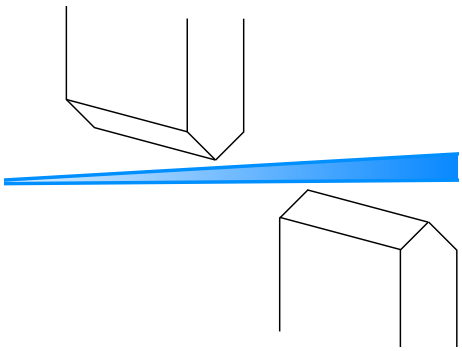

Figure 7.6: Upper and lower white beam slits, with an illustration of the photon beam passing. A similar pair of slits also were also closed in the horizontal direction, to define a rectangular pinhole.

This aperture was the first optical element of the photon beamline. The monochromator spectrometer and all focussing mirrors are positioned downstream of the slits.

7.5.3 Beamline Optical Elements

The existing soft X-ray beamline optics were used for the photon beam spectrometer. The beamline optics are illustrated in Figure 7.7.

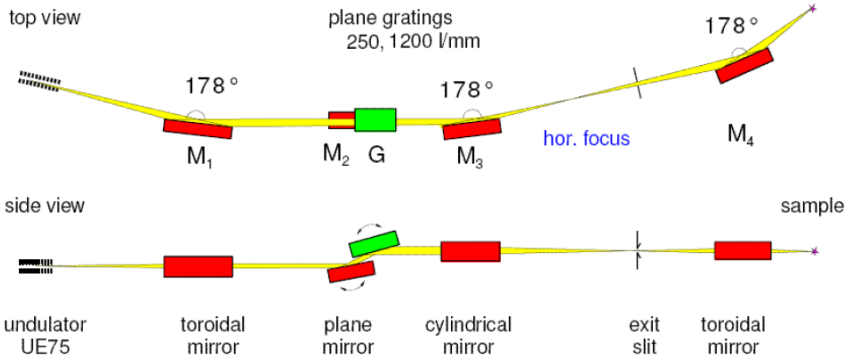

Figure 7.7: Soft X-ray beamline optical elements [269].

The beamline employs a linear grating for the monochromator, and several gold-coated toroidal mirrors to focus the beam. The calculated net reflectivity of these beamline elements is presented in Figure 7.8 [269, 273]. The M absorption edges of the gold coatings restrict our experiments to photon energies below 2200 eV.

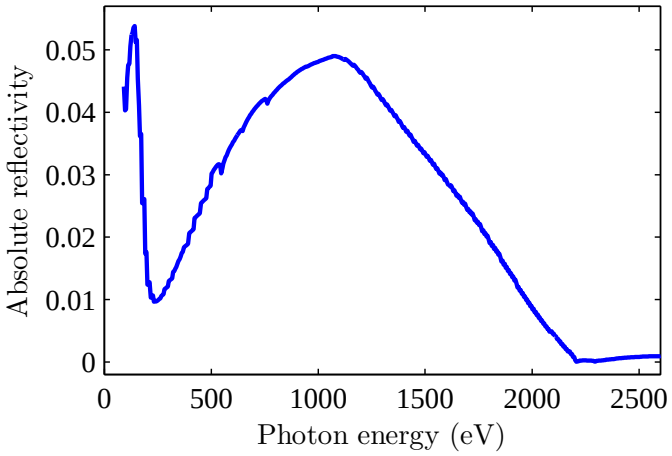

Figure 7.8: Absolute reflectivity of soft X-ray beamline optical elements with photon energy [269, 273]. There is a dramatic decrease in photon flux for photon energies above the M-absorption edges of Au at approximately 2150 eV.

7.5.4 Photodiode Detector

The intensity of light was measured using a single pixel photodiode. Two photodiodes are installed on the beamline as standard diagnostics of photon flux. Both photodiodes are square and approximately 10 mm × 10 mm in transverse extent. This large dimension was used to intercept the full photon beam. The spectral responsivity $s\left(\hbar\omega\right)$ of a diode can be modelled by [274],

$$s\left(\hbar\omega\right) = \frac{q_e}{E_{e-h}} \exp\left[-\mu_d\left(\hbar\omega\right) t_d\right] \left(1 - \frac{\exp\left[-\mu_s\left(\hbar\omega\right) t_s\right]}{\mu_s\left(\hbar\omega\right) L_{\text{diff}} + 1}\right), \tag{7.10}$$

where, q_e is the electronic charge, E_{e-h} is the electron-hole pair creation energy of the active material, $\mu_d(\hbar\omega)$ the dead layer absorption length, t_d the dead layer thickness, $\mu_s(\hbar\omega)$ the active layer absorption length, t_s the active layer thickness, and L_{diff} the diffusion length. Accepted values of the absorption lengths $\mu_d(\hbar\omega), \mu_s(\hbar\omega)$ were used, corresponding to the different diode materials [275]. Using the properties in Table 7.2, the responsivities of the two photodiodes were calculated over the relevant range of photon energies [274]. This is presented in Figure 7.9.

Table 7.2: GaP and Si photodiode properties.

Parameter	Symbol	GaP/Au	Ref.	Si/SiO_2	Ref.	Units
Dead layer material	...	Au	...	SiO_2	...	...
Dead layer thickness	t_d	9	[274]	7	[276]	nm
Active layer material	...	GaP	...	Si	...	...
Pair creation energy	E_{e-h}	5.4	[274]	3.65	[276]	eV
Space charge thickness	t_s	0.5	[274]	10	[274]	µm
Diffusion length	L_{diff}	2.7	[274]	100	[276]	µm

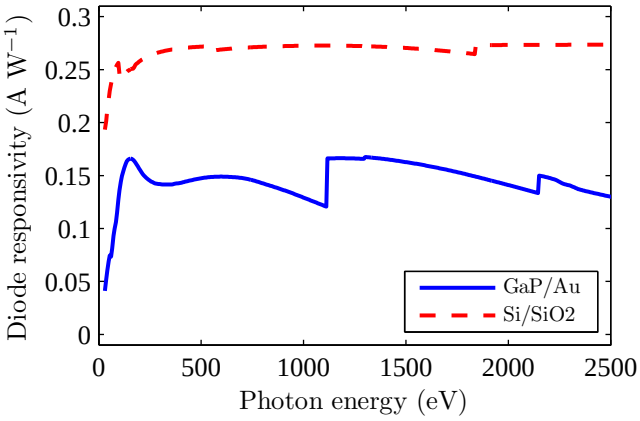

Figure 7.9: Responsivity of GaP/Au and Si/SiO_2 photodiodes, calculated using Equation 7.10 and data in Table 7.2 [274]. Over the photon energy range of interest $E_\gamma = 800 - 2000$ eV, the Si/SIO_2 is linear to within $\pm 2\%$ [274, 277]. Over the same photon energy range, the responsivity of the GaP/Au diode has a linearity of $\pm 14\%$. The silicon K absorption edge is at $E_\gamma = 1839$ eV [275].

Preliminary measurements were made using a Hamamatsu G1963 GaP/Au Schottky photodiode [172,278]. The photodiode is designed and optimised for detection of ultraviolet radiation; it is not manufactured as an X-ray detector. Over the desired photon energy range of $E_\gamma = 800 - 2000$ eV, the responsivity of the GaP/Au diode has a linearity of $\pm 14\%$, with large discontinuities at absorption edges. Crucially, the measurement of emittance in this technique depends on the ratio of photon flux at different photon energies. To simplify interpretation of photon fluxes at different photon energies, an International Radiation Detectors AXUV100 silicon photodiode was used for experimental results presented in this thesis [276, 279]. Within an uncertainty of $\pm 2\%$, these silicon photodiodes have been demonstrated to exhibit a linear responsivity over the photon energy range of interest; 800–2000 eV [274, 277].

7.5.5 Simulation of Apparatus

The measured profile of undulator radiation was compared to simulations. Initially, the magnetic model of the undulator assumed an ideal sinusoidal vertical electron beam trajectory though the magnet. An improved model is presented which accounts for the effect of undulator phase errors on the electron beam trajectory, using the measured magnetic field of the insertion device.

At the time of manufacture of this APPLE-II insertion device, the magnetic field profile was measured at the design magnetic gap of 16.0 mm [271]. The magnetic field was measured along the device centreline with a three-axis Hall probe. Direct measurement of the ID magnetic field was impossible, because the only priority of this ID is as the photon source for the soft X-ray user beamline [269].

As outlined in Section 7.5.1, for the purposes of safe clearance of the electron beam vacuum chamber, the minimum operating insertion device gap was limited to 17.0 mm. These experiments were conducted with a gap of 17.1 mm. To compensate for this in our model, the magnitude of the magnetic field components measured at a gap of 16.0 mm were scaled down. The field was scaled down until the measured and simulated photon energies of the on-axis undulator spectrum agreed. This scaled field is presented for the horizontal (B_x) and vertical (B_y) components in Figure 7.10.

Using the magnetic field illustrated in Figure 7.10, the trajectory of a 3 GeV electron was calculated and is shown in Figure 7.11.

Figure 7.11 shows the trajectory of a single electron through the ID. This single-electron trajectory is convolved with the beam ensemble passing through the ID. The Courant-Snyder optical functions are plotted in Figure 7.12, for the insertion in which this ID is installed at the AS storage ring. Ideally, insertion devices are

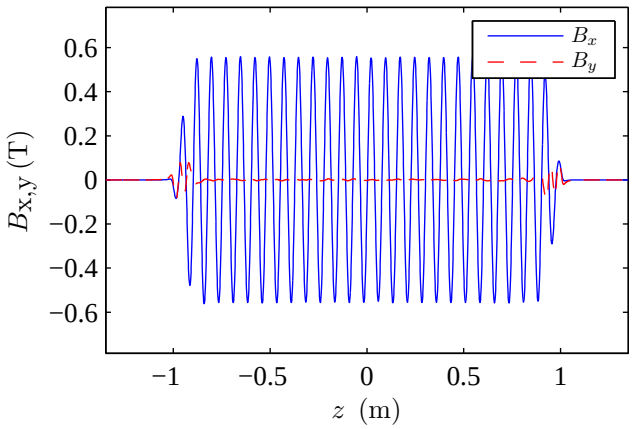

Figure 7.10: Magnetic field of APPLE-II insertion device in vertical polarisation mode, scaled from Hall probe measurements [271]. Undulators usually have the main field in the vertical (y) plane, but in this case the main field is in the horizontal (x) plane.

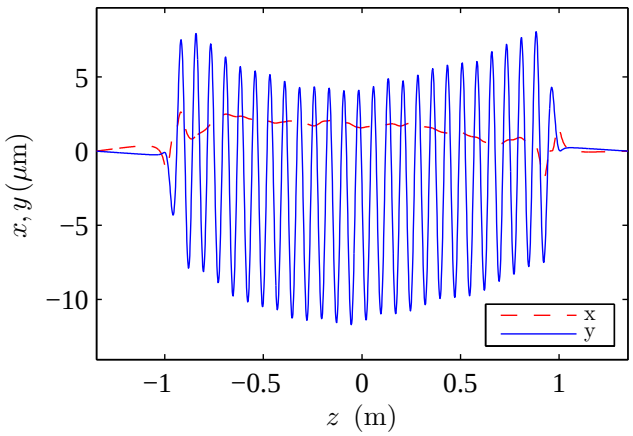

Figure 7.11: Horizontal and vertical trajectory of a 3 GeV electron beam through measured magnetic field map of Figure 7.10 [271], calculated using SPECTRA [250]. The horizontal field B_x (vertical field B_y) of Figure 7.10 results in a vertical (horizontal) electron beam trajectory.

centred in the insertion straight. However, the soft X-ray insertion device (ID14) is positioned asymmetrically in sector 14 of the storage ring, to accommodate one of the four storage ring injection kickers.

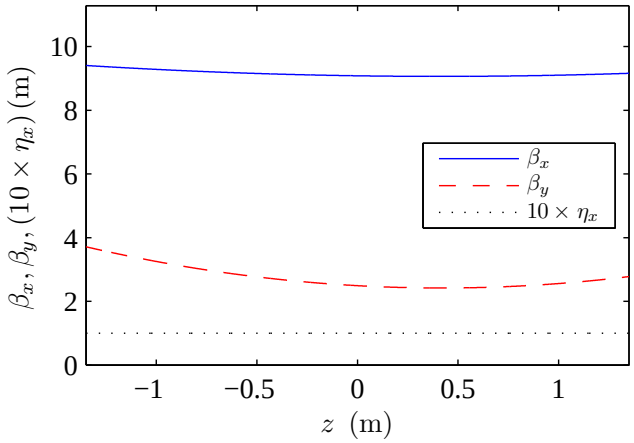

Figure 7.12: Optical functions through APPLE-II insertion device. It can be seen that the optical functions are asymmetric about the centre of the insertion device in z. For clarity, the horizontal dispersion η_x is multiplied by a factor of 10.

The synchrotron radiation code SPECTRA was used to simulate light produced by the insertion device [250]. At a longitudinal distance of $z = 15$ m from the centre of the insertion device, the radiation field is sampled in the (x, y) plane. This distance corresponds to the distance of the white beam slits from the insertion device.

As outlined in Section 7.5.3, all other beamline optical elements (toroidal and spheroidal mirrors, monochromator) are downstream of the white-beam slits, and serve to deliver a monochromatic photon beam to the photodiode detector. These elements are not simulated. The photodiode responsivity and beamline reflectivities presented in Section 7.5.3–7.5.4 are used to correct the photon fluxes measured at the photodiode. Hence the measured and simulated photon fluxes can be compared at the pinhole formed by the white-beam slits.

7.6 Discussion

The major finding of this work was that the pinhole photon flux from a vertical undulator is an appropriate vertical emittance diagnostic of ultralow vertical emittance storage rings. Several factors are identified as to why vertical undulators have not been previously used to measure vertical electron beam emittance.

7.6.1 Diffraction-Limited Insertion Device Radiation

As outlined in Section 7.4, undulators have been used in the measurement of horizontal electron beam emittance. However, the horizontal emittances of nm rad are orders of magnitude greater than the pm rad vertical emittances produced in current storage rings.

Working at these ultralow vertical emittances is qualitatively different to previous undulator measurements of beam emittance. For spontaneous undulator sources of length L and photon wavelength λ, the diffraction-limited source size σ_r is given by [40],

$$\sigma_r = \frac{1}{2\pi}\sqrt{\lambda L}. \tag{7.11}$$

The vertical electron beam size σ_y is given by Equation 3.65, and in the limit $\eta_y(s) = 0$ [40],

$$\sigma_y = \sqrt{\beta_y(s)\,\varepsilon_y}. \tag{7.12}$$

For the parameters given in Table 7.3, Equation 7.11 gives a diffraction-limited source size of $\sigma_r = 5.0$ μm. Using Equation 7.12, the beam size of an electron beam of ultralow vertical emittance $\varepsilon_y = 1$ pm rad is $\sigma_y = 1.7$ μm.

Table 7.3: Diffraction limited source parameters

Parameter		Value	Units
Photon energy	E_γ	2500	eV
Photon wavelength	λ	0.5	nm
Undulator length	L	2	m
Vertical beta function	$\beta_y(s)$	3	m
Vertical emittance	ε_y	1	pm rad

This comparison highlights a particular point of difference with previous undulator measurements of emittance: this work is with beams of significantly lower emittance than the insertion device diffraction limit. As highlighted in Section 7.4.1, the usual 'Gaussian' experimental approximations for the angular distribution of undulator radiation break down at these small electron beam emittances, and particularly these high undulator harmonics.

7.6.2 High Deflection Parameter Vertical Undulators

It was proposed in literature that radiation from a vertical undulator could be used to measure electron beam vertical emittance [261]. As stated in Section 7.5, vertical

undulators are exceptionally rare in laboratories around the world. High deflection parameter vertical undulators ($K_u > 1$) are rarer still.

Emittance measurements based on undulator radiation typically assume the weak undulator limit ($K_u \leq 1$), with undulators producing photon beams within a central cone of radius $\theta_{\max} \approx 0.3\,(K_u/\gamma)$ [265]. In the strong undulator limit ($K_u > 1$), the cone approximation breaks down, giving rise to a narrow angular interference pattern as illustrated in Figure 7.1. With odd harmonic number $n > 3$ and $n \geq (N_u/3)$, where N_u is the number of undulator periods, the half angle of the first interference minima is given by [280, 281]

$$\theta_{\max} = \frac{K_u}{\gamma}\frac{\pi}{2n}\frac{(1 + K_u^2/2)}{(1 + 2K_u^2)}. \tag{7.13}$$

For horizontal undulators at existing storage ring light sources, this pattern of interference fringes is normally convolved with a Gaussian electron beam distribution of large horizontal emittance. Hence for beamlines at present third-generation light-sources using horizontal undulators, this pattern is not normally observed. However with vertical emittances of the order of 10^3 smaller than the horizontal, the diffraction limit is reached with vertical undulators.

This narrow interference pattern imposes practical limits on the pinhole size for this measurement. Using Equation 7.13 for $n = 15$ and parameters presented in Table 7.1, an upper limit is placed on the pinhole half angle radius of $\theta_{max} = 0.029\,(K_u/\gamma)$. This corresponds in Figure 7.13 to the maximum in ratio F_{14}/F_{15} for pinhole offset. Pinhole half-apertures greater than this exhibit no sensitivity to vertical emittance, because a large pinhole has the effect of spatially averaging across the interference pattern.

7.6.3 Counter-intuitive introduction of vertical dispersion

It is well-known that the vertical dispersion of a lattice increases the equilibrium vertical emittance. Vertical emittance optimisation routines seek to minimise coupling and dispersion terms simultaneously. The inclusion of a vertical insertion device in a lattice has the well-known effect of increasing vertical emittance, which several lattice designs have exploited with the intent of creating round beams [73]. This suggests that designs for ultralow vertical emittance must avoid introducing vertical dispersion.

Vertical emittance growth due to undulator self-dispersion was calculated according to the method of Ref. [73], for the APPLE-II undulator and the normal AS

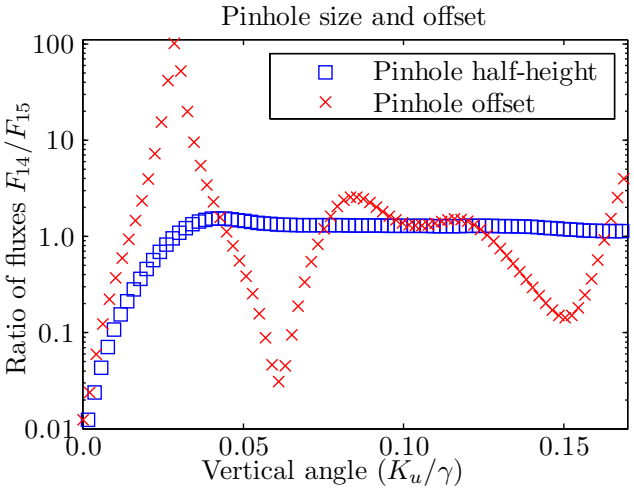

Figure 7.13: Flux ratio dependence for vertical emittance 0 pm rad, harmonics 14 and 15, and beam parameters of Table 7.1. A centered pinhole of half-height is illustrated in blue, and vertical offset of a pinhole of 50 μm in red. An angle of $0.10\,(K_u/\gamma) \equiv 1.0$ mm vertical position at 15 m, c.f. Figure 7.3 (g) & (h). [K.P. Wootton, et al., *Phys. Rev. Lett.*, **109** (19), 194801 (2012). © 2012 American Physical Society.]

user lattice with 0.1 m distributed horizontal dispersion in the insertion straights. A similar approach is presented in Ref. [282]. The vertical emittance growth in a ring from self-dispersion in a vertical wiggler is given by [73],

$$\frac{\Delta\varepsilon_y}{\varepsilon_{x0}} = \frac{\dfrac{5\pi}{6}\dfrac{\beta_y(s)}{\langle\mathcal{H}_0\rangle}\dfrac{\rho_0}{R}\left(\dfrac{\rho_0}{\rho_w}\right)^2 N_w\theta_w^3}{1+\dfrac{2}{\pi}\dfrac{\rho_0}{\rho_w}N_w\theta_w}. \tag{7.14}$$

For a ring, the curly-$\mathcal{H}$ function is given by Equation 3.37 and its mean can be approximated by [73],

$$\langle\mathcal{H}_0\rangle = \frac{\varepsilon_{x0}\rho_0}{C_a E^2}\frac{\rho_0}{R}\mathcal{J}_x. \tag{7.15}$$

Using the parameters in Table 7.4 for this experiment at the AS, the curly-$\mathcal{H}$ function was evaluated as $\langle\mathcal{H}_0\rangle = 0.0027$ m rad. Evaluating the curly-$\mathcal{H}$ function using the numerical model of Section D.2 gives $\langle\mathcal{H}_0\rangle = 0.0023$ m rad.

For the parameters of the storage ring and undulator at the AS given in Table 7.4, the vertical emittance increase due to self-dispersion of Equation 7.14 is presented in Figure 7.14 for an increasing number of vertical undulator poles.

The APPLE-II undulator used at the AS has a total of 50 poles, giving a calculated increase in vertical emittance due to self-dispersion of $\Delta\varepsilon_y = 0.012$ pm rad.

Table 7.4: Parameters used in the calculation of vertical undulator self-dispersion.

Parameter		Value	Units
Beam			
Energy	E_0	3.0	GeV
Energy spread	σ_E	0.11	%
Horizontal emittance	ε_x	10	nm rad
Undulator			
Period length	λ_u	75	mm
Peak field	B_u	0.55	T
Deflection parameter	K_u	3.8	...
Number of full periods	N_u	25	...
Number of poles	N_w	50	...
Wiggler deflection angle	θ_w	6.5×10^{-4}	rad
Wiggler bending radius	ρ_w	29.0	m
Storage ring			
Damping decrement – horizontal	$\mathcal{J}_x$	1.37	...
Bending radius	ρ_0	8.5	m
Ring radius	R	34.4	m
Curly-$\mathcal{H}$ function	$\langle \mathcal{H}_0 \rangle$	2.3×10^{-3}	m rad

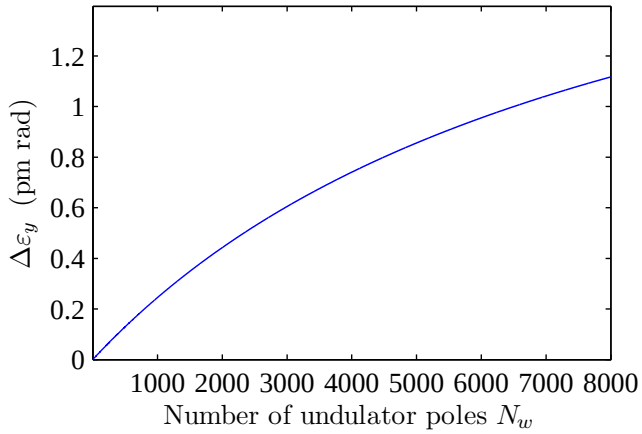

Figure 7.14: Increase in vertical emittance due to vertical undulator self-dispersion for an undulator of N_w poles. Calculated using Equation 7.14, and the parameters of Table 7.4. The APPLE-II undulator at the AS has 50 poles.

This is well below achievable vertical emittances of $\varepsilon_y \approx 1 - 2$ pm rad [95], and indeed below the quantum limit of vertical emittance[2].

It is possible that magnetic multipole errors of the insertion device introduce an additional skew quadrupole term, resulting in betatron coupling of the horizontal and vertical emittances. As will be outlined in Section 8.2, the vertical emittance optimisation including betatron coupling was performed on the storage lattice measured with the insertion device closed. Skew quadrupoles distributed around the ring were then optimised to compensate for the betatron coupling introduced by the undulator and other coupling sources.

7.7 Summary

As part of the low vertical emittance studies at the AS, a technique for direct measurement of ultralow vertical emittances was needed. Simulations demonstrated that undulator radiation from a vertical undulator was especially sensitive to ultralow vertical emittances.

A particular point of difference between this work and previous undulator measurements of emittance was that this work was with beams of lower emittance than the insertion device diffraction limit. The usual experimental assumptions about the angular distribution of undulator radiation break down at these ultralow electron beam emittances.

It was demonstrated that the counter-intuitive inclusion of a single vertical undulator in the lattice to measure the vertical emittance does not measurably increase the equilibrium ultralow vertical emittance due to vertical dispersion.

With this apparatus immediately available at most existing electron storage ring light sources, this novel technique can be used to observe ultralow vertical emittance.

[2]As presented in Figure 7.14, increasing the vertical emittance to $\varepsilon_y \approx 1$ pm rad by self-dispersion requires approximately 6500 undulator poles. At a total undulator length of 240 m, this exceeds the AS storage ring circumference of 216 m.

Chapter 8

Measurement of Ultralow Vertical Emittance Beams using a Vertical Undulator

8.1 Motivation

The world-record low vertical emittance of the AS storage ring makes the facility an important test bed for future collider damping rings. The aim of this work is to directly observe the minimum achievable vertical emittance in the AS storage ring, when an vertical emittance minimisation algorithm is employed [95]. Using the vertical undulator technique described in Chapter 7, direct measurements of vertical emittance are presented for the AS storage ring.

Based on the results of these measurements, the ideal apparatus to measure vertical emittance using this vertical undulator technique is discussed.

8.2 Results of Different Approaches

Various experimental approaches were investigated to measure vertical electron beam emittance from vertical undulator radiation. This process identified variables of the accelerator and beamline which were the most difficult to reproducibly control or quantify. Variables of interest in these measurements were the monochromator (photon energy), the size and position of the pinhole aperture formed by the white beam slits, and the electron beam orbit (position and pointing stability).

The goal of this work was to identify the experimental technique with greatest sensitivity to ultralow electron beam vertical emittance. To test this, the vertical

emittance of the electron beam was varied. After closing the undulator to its operating gap, the storage ring skew quadrupole lattice was measured using orbit response matrices and fitted using the LOCO algorithm [199]. Storage ring skew quadrupole magnets were optimised for a range of vertical emittances using a least-squares minimisation procedure [95].

8.2.1 Photon Energy Spectrum

As outlined in Section 7.4.2, the initial experimental approach was to evaluate vertical emittance from measurements of the on-axis undulator radiation spectrum.

The photon flux was measured passing an on-axis pinhole. The pinhole used was four blades of the white-beam slits, closed to form a rectangular pinhole aperture of approximately 250×250 μm. The aperture was small in both the horizontal and vertical dimensions, to minimise any contribution from the horizontal emittance. At a longitudinal distance of 15.0 m from the undulator centre, the pinhole passes undulator radiation within an opening angle of $\theta = 1.7 \times 10^{-5}$ rad.

The measured undulator spectra are presented in Figure 8.1 for vertical emittances from $\varepsilon_y = 2.6 \pm 1.1$ pm rad in blue up to $\varepsilon_y = 1750 \pm 330$ pm rad in red.

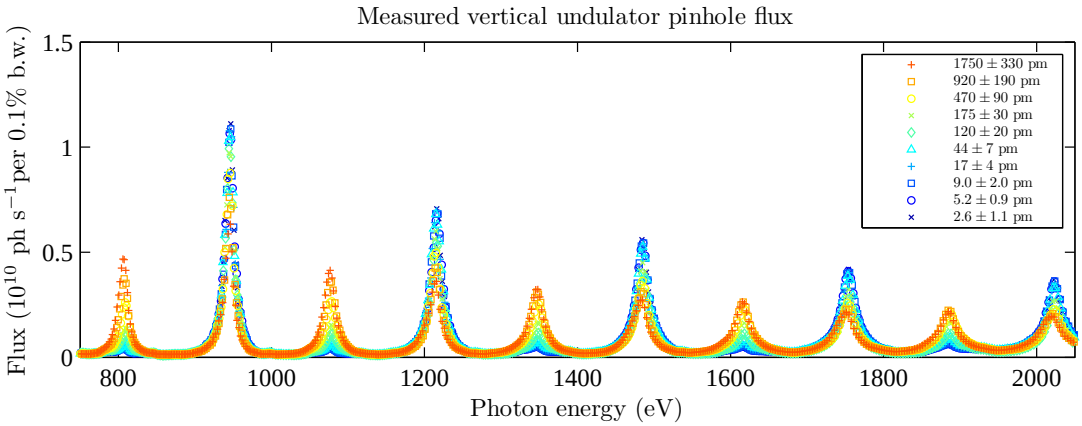

Figure 8.1: Measured undulator spectra for vertical emittances calibrated with LOCO [199], from minimum in blue up to maximum in red. Shown are undulator harmonics 6 – 15. [K.P. Wootton, et al., *Phys. Rev. Lett.*, **109** (19), 194801 (2012). © 2012 American Physical Society.]

Using the SPECTRA code [250], the flux of monochromated undulator radiation passing a pinhole was simulated. The simulated on-axis undulator radiation spectra are presented in Figure 8.2.

The greatest uncertainty in this technique was the size and vertical position of the pinhole. As outlined in Section 7.4.3, a pinhole of finite size or offset limits

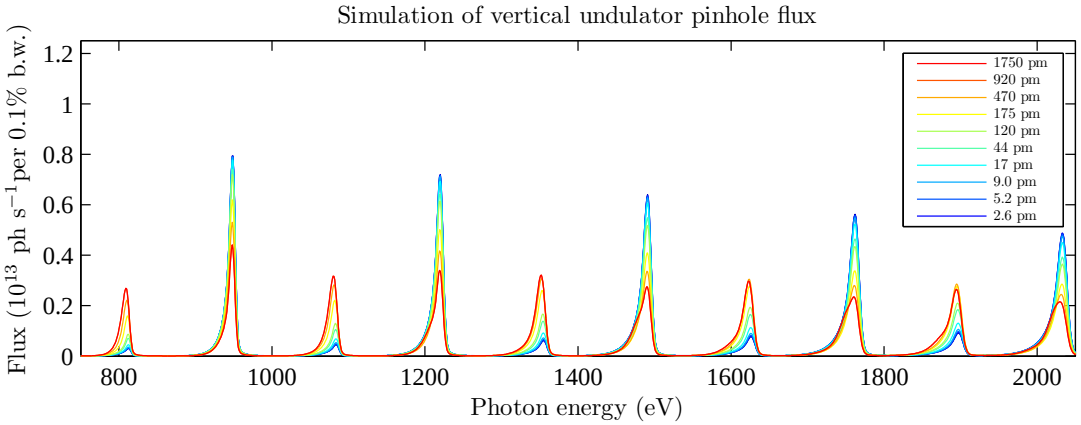

Figure 8.2: SPECTRA [250] simulation of pinhole undulator radiation, for the parameters of Figure 8.1. This simulation assumed an ideal sinusoidal undulator magnetic field, and a fitted on-axis pinhole of dimensions 261 × 261 μm.

the observation of smallest flux ratios. The uncertainty in the size of the pinhole arose from mechanical tolerances of linear stages used to actuate the white-beam slit positions. The white beam slits were intended as a coarse spatial filter of undulator radiation, to reduce the heat load incident upon beamline optical elements. Hence, the linear stage position resolution is approximately 10-20 μm. In addition, backlash of the linear stages meant that the linear stage motion was better when pushing the blades towards the photon beam, as opposed to retracting them. Hence, the dimension of the pinhole used in this spectral measurement was not assumed to be available, due to uncertainty in the positions of the four blades of the white-beam slits.

To extract the pinhole dimension from experimental data, the vertical dimension of the pinhole was fitted as a single free parameter using all datasets of Figure 8.1 simultaneously. Envelopes of beam emittance corresponding to LOCO measurements were fitted to the measured peak ratios, minimising the χ^2 test statistic. These peak ratios of F_{n-1}/F_n harmonics are presented in Figure 8.3.

The χ^2 test statistic was minimised for a pinhole of 261×261 μm. It was chosen to fit emittance contours based on the global emittance calculated from orbit response matrices fitted with LOCO, however this emittance monitor is intrinsically local to one point in the ring. Hence the apparent emittance measured may vary from the global projected emittance [283], for some contours of Figure 8.3.

Uncertainties are presented in Figure 8.3 corresponding to both the measured undulator spectra of Figure 8.1 and fitted emittance envelopes of Figure 8.2. The fitted envelopes and uncertainties correspond to the beam emittance evaluated us-

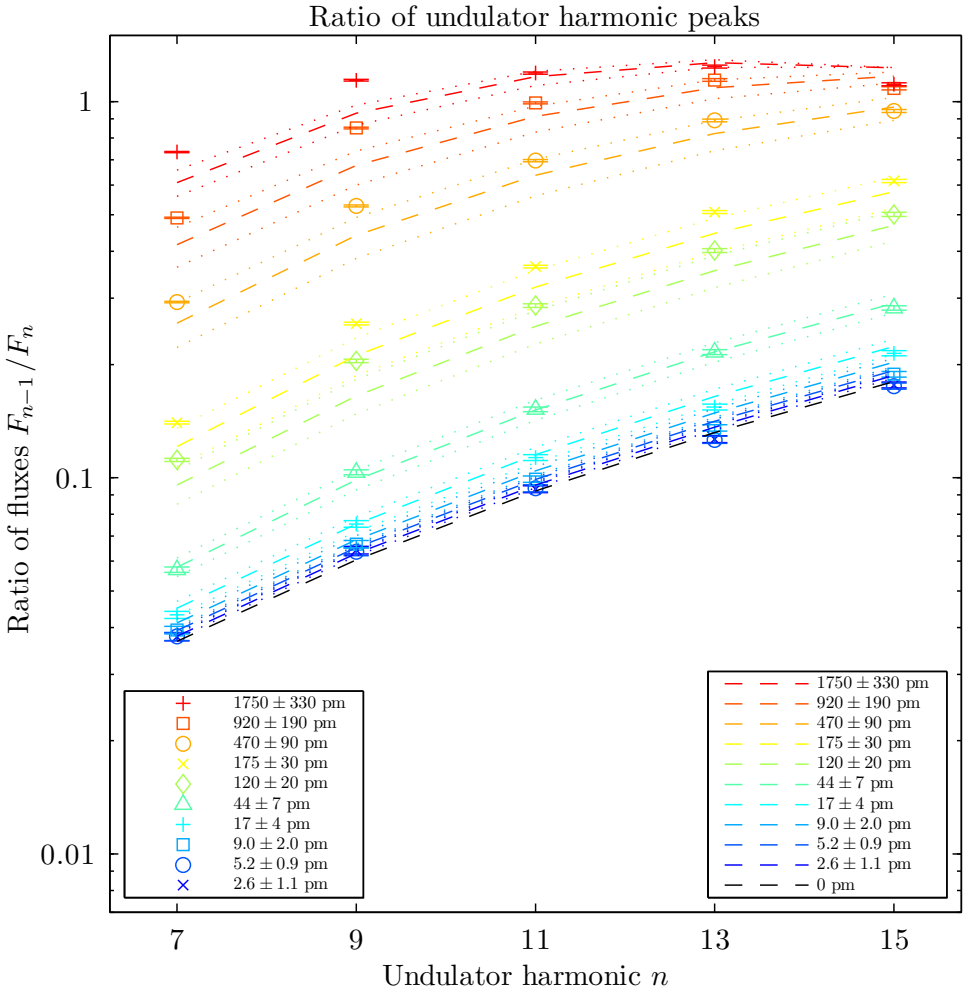

Figure 8.3: Model 261×261 μm pinhole spectrum of Figure 8.2 fitted to experimental data of Figure 8.1. Measured undulator peaks marked as squares, fitted SPECTRA [250] simulations denoted by dashed contours increasing from minimum in blue to maximum in red. The simulated contour of a beam with zero vertical emittance is shown in black. Uncertainties of measured ratios shown as error bars, and dotted contours for fitted model. [K.P. Wootton, et al., *Phys. Rev. Lett.*, **109** (19), 194801 (2012). © 2012 American Physical Society.]

ing LOCO. Uncertainties in measured ratios were evaluated from measurements of the photon flux with the undulator open to its maximum gap, nominally bending magnet edge radiation. This background was measured to be more than an order of magnitude lower than the minimum undulator flux.

8.2.2 Blade Profile Scans – Profile in One Dimension

The spatial profile of radiation was characterised in the vertical direction using blade scans. This is illustrated in Figure 8.4.

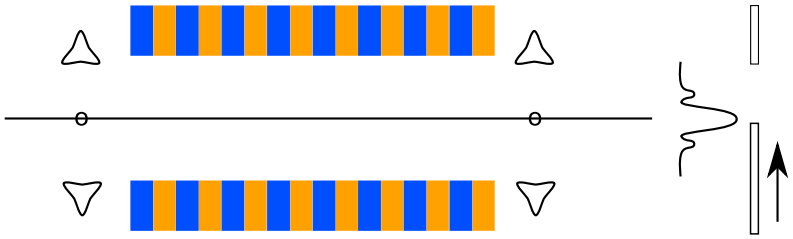

Figure 8.4: Schematic of blade scan through insertion device radiation, at a single photon energy corresponding to an odd undulator harmonic. The electron beam orbit is fixed through vertical positions denoted by ∘, and the lower vertical blade of the white-beam slits is stepped vertically upwards through the undulator radiation distribution.

With a horizontal aperture of 0.5 mm, the lower blade of the white beam slits was stepped vertically upwards through the radiation distribution. The photon flux measured through the aperture with blade position is plotted in Figure 8.5 (a–c). The derivative of this distribution with respect to the vertical position y of the blade recovers the intensity distribution of undulator radiation. The vertical distribution of undulator radiation is plotted in Figure 8.5 (d–f).

This measured undulator radiation profile confirms the non-Gaussian distribution of simulations presented in Figure 7.3. At this unusual parameter choice of low emittance, high deflection parameter and high undulator harmonic, the vertical distribution of undulator radiation is described by an inteferogram rather than usual approximations of the convolution of Gaussian electron beam and radiation distributions.

The sensitivity of blade scans to the vertical emittance was evaluated by varying the vertical emittance, as presented in Figure 8.6. Figure 8.6 demonstrates that blade scans are not sufficiently sensitive to measure smallest emittance beams.

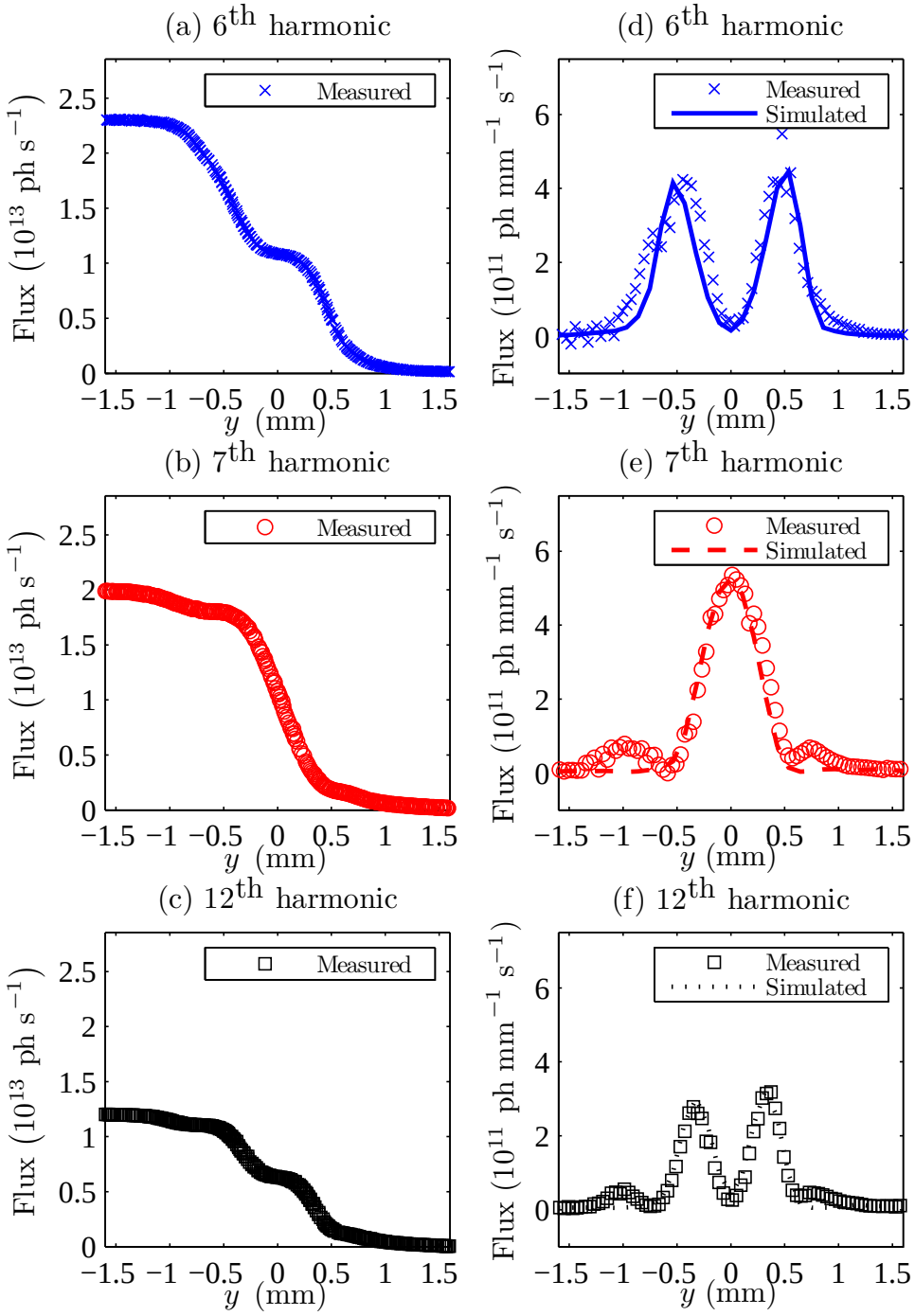

Figure 8.5: Photon flux measured from vertical blade scan, for three different undulator harmonics $\left(6^{\text{th}} = 808 \text{ eV}, 7^{\text{th}} = 941 \text{ eV}, 12^{\text{th}} = 1610 \text{ eV}\right)$. (a–c) The blade is pushed upwards in the positive direction of y through the photon beam, progressively extinguishing the number of photons passed. (d–f) The measured intensity distribution of undulator radiation is found by taking the derivative of photon flux with respect to blade position y. The measured radiation distribution is fitted by SPECTRA simulations [250] of the undulator radiation [284].

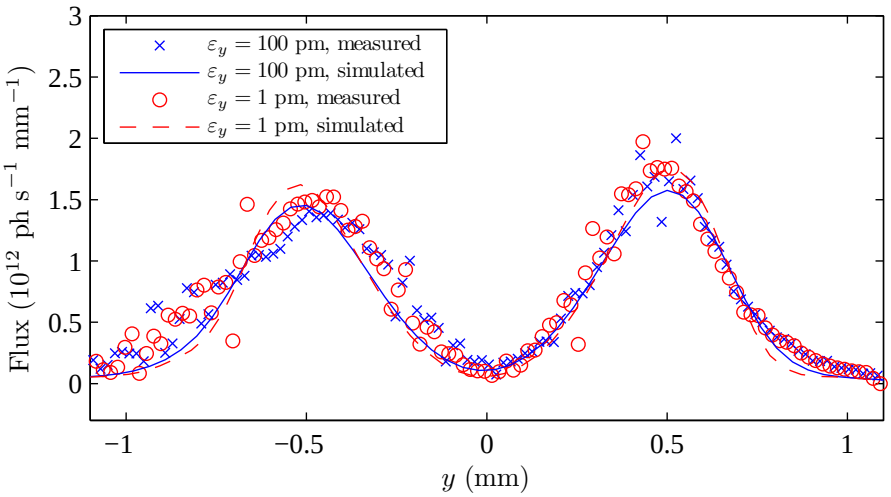

Figure 8.6: Blade scan sensitivity to vertical emittance. Measured and modelled undulator radiation profiles are shown for an emittance ratio of 1% ($\varepsilon_y \approx 100$ pm rad) and minimised vertical emittance ($\varepsilon_y \approx 1$ pm rad), at a photon energy of 808 eV (6^{th} harmonic).

8.2.3 Profile in Two Dimensions

To measure the spatial profile of undulator radiation, a pinhole aperture can be rastered across the distribution. This was demonstrated with a single, fixed pinhole in experiments at other laboratories [272]. In lieu of a pinhole of fixed size, the four blades of the white-beam slits were closed to form a rectangular pinhole aperture of size approximately 100 µm × 100 µm, which together were rastered horizontally and vertically to measure the spatial profile of undulator radiation. The measured and simulated profiles are presented in Figure 8.7.

The important features of Figure 8.7 are the central upper and lower lobes of the 6^{th} harmonic, and the outer ring of the 7^{th} harmonic. This narrow interference pattern is characteristic of undulator radiation, but is seldom observed. Storage ring light sources typically operate with very large horizontal emittances of order nm rad, convolving the narrow angular distribution of undulator radiation with the broad horizontal beam emittance. The interference pattern is observed here specifically because of the vertical deflection by the undulator and the low vertical emittance of order pm rad.

Integrating over the central 3 mm width of the distribution in Figure 8.7, the measured and simulated vertical profile of undulator radiation at 808 eV is presented in Figure 8.8. Figure 8.8 highlights that the measured vertical asymmetry in the distribution of undulator radiation is partially accounted for by using the scaled,

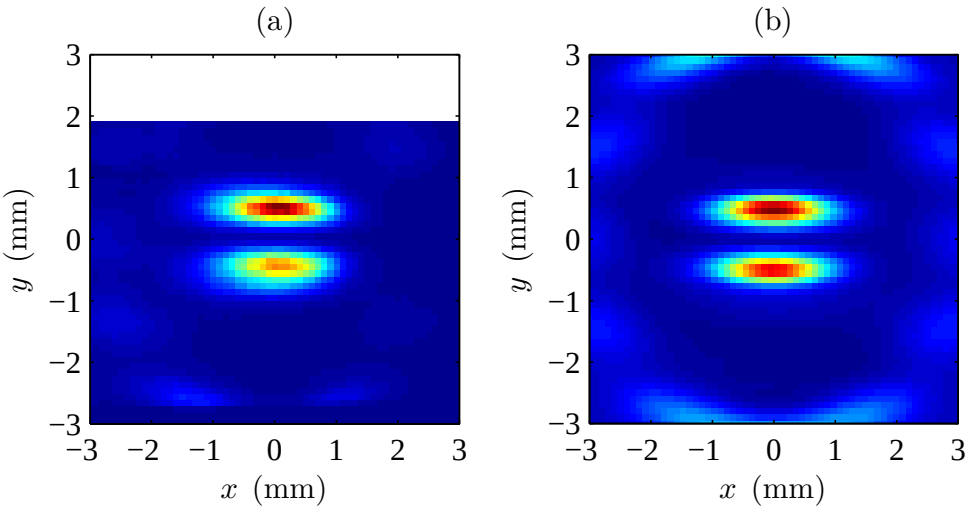

Figure 8.7: Spatial profile of undulator radiation 15 m downstream of a vertical undulator [284]. (a) Measured spatial profile of 6$^{\text{th}}$ undulator harmonic, at 808 eV. (b) SPECTRA [250] simulation of spatial profile of 6$^{\text{th}}$ undulator harmonic, at 808 eV. The measured magnetic field map of Figure 7.10 is used to represent the undulator in simulation [284].

measured magnetic field distribution in simulations.

Unfortunately, as stated in Section 7.5.5, at present the AS possesses no equipment with which to characterise insertion devices. In the absence of direct measurement of the magnetic field distribution at the operating insertion device gap and phase, this was the limit of applicability of the scaled, measured magnetic field model. An improved model of the radiation distribution would use the magnetic field distribution measured at the operating gap and phase of the insertion device.

8.2.4 Electron Beam Orbit Bumps

As outlined in Section 7.6.2, a significant systematic uncertainty in this flux measurement is the sensitivity to the size and transverse position of the pinhole mask. In particular, the technique is sensitive to vertical transverse offsets of the pinhole [263].

The photon energy scan technique employed in Section 8.2.1 aimed to simultaneously minimise the size and centring of the pinhole formed by closing four white beam blades. As an alternative, the pinhole size alone was minimised. The blades of the white-beam slits were closed to the minimum possible aperture. The photon energies of the desired odd and even undulator harmonics were determined from energy scans of the monochromator, as outlined in Section 8.2.1. At these photon energies, the centring of the pinhole on the undulator radiation distribution was

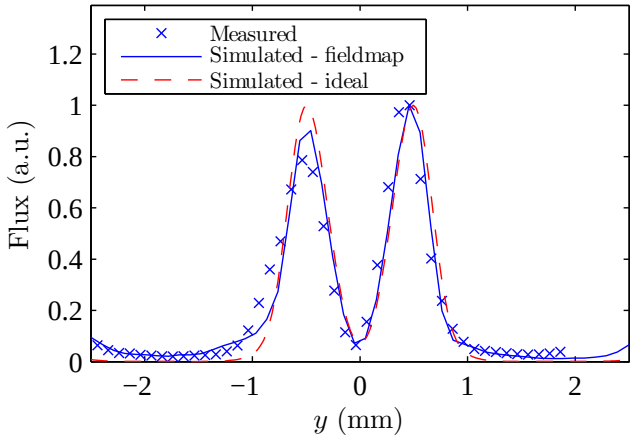

Figure 8.8: Vertical profile of undulator radiation in Figure 8.7, plotted on an arbitrary vertical intensity scale [284]. The intensity is integrated over $x = -1.5$ mm to 1.5 mm. Simulations of the insertion device are presented assuming an ideal sinusoidal field, and the measured field map of Figure 7.10.

achieved by vertical, angular electron beam closed orbit bumps through the insertion device straight. This is illustrated in Figure 8.9.

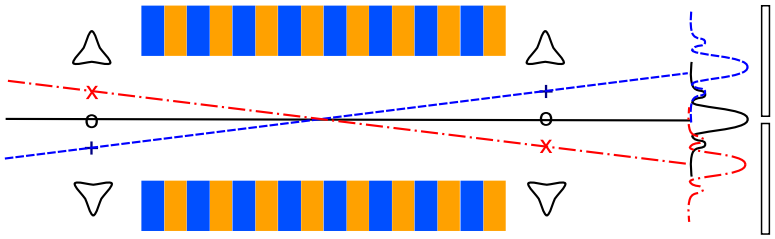

Figure 8.9: Schematic of vertical electron beam orbit bumps through an insertion device, illustrating an orbit bump at a single photon energy corresponding to an odd undulator harmonic. From an initial orbit through vertical positions denoted by ○, orbit correctors change the electron beam trajectory measured as positions at BPMs to × and +. This varies the angle of insertion device radiation measured passing the fixed pinhole aperture.

Closed orbit bumps were calculated using the AT code [285], and measured using storage ring electron beam position monitors adjacent to the insertion device. The pinhole flux measured in vertical angular bumps through the insertion device is illustrated in Figure 8.10, and for small amplitude bumps around the diffraction pattern central lobe in Figure 8.11.

The angle of the electron beam through the insertion device can be varied to recover the angular distribution of undulator radiation, illustrated for small angles in Figure 8.11.

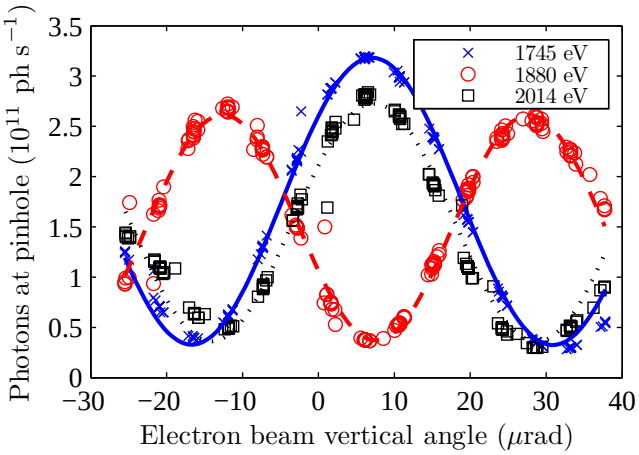

Figure 8.10: Pinhole photon flux measured and fitted for orbit bumps through the insertion device. Photon energies correspond to undulator harmonics 13, 14 and 15 [286].

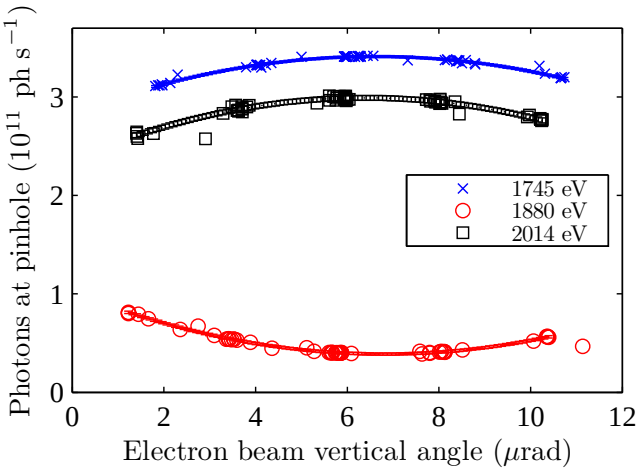

Figure 8.11: Pinhole photon flux measured and fitted for orbit bumps through the insertion device. These bumps are small bumps about the central lobe of the radiation distribution in Figure 8.10. Photon energies correspond to undulator harmonics 13, 14 and 15 [286].

The fitted distribution of undulator radiation plotted in Figure 8.11 was used to determine the maximum flux ratio between adjacent even and odd harmonics.

8.2.5 Time-Varying Magnetic Fields

A problem for many emittance monitors is the influence of time-varying magnetic fields on the measured electron beam distribution. This is addressed in Appendix E.

8.3 Measurements of Ultralow Vertical Emittance

As stated in Section 8.1, the goal of this work was the ability to directly measure picometre electron beam vertical emittance beams at the AS storage ring. Experiments conducted in 2010 using the AS storage ring demonstrated through indirect measurements a world-record low vertical emittance of $\varepsilon_y = 1.2^{+0.3}_{-0.2}$ pm rad [95].

In 2012, a new record low vertical emittance of $\varepsilon_y = 0.9 \pm 0.4$ pm rad was observed using the direct π-polarisation technique (Section 7.2.2) and the SLS storage ring [92].

With the goal of optimising the AS storage ring for even lower vertical emittance, a beam-based survey of storage ring magnets was undertaken in 2012 [287], culminating in the mechanical alignment of individual sextupole magnets within vertical tolerances of $\Delta y = \pm$ 25 µm [195]. Indirect measurements of the bunch volume by the Touschek lifetime demonstrated vertical emittances below 1 pm rad [195].

In this work, the new technique for vertical emittance measurement using a undulator was exploited for direct measurement of electron beam vertical emittances approaching the quantum limit in the AS storage ring.

8.3.1 Experimental Setup

The ID was closed to the nominal gap of 17.1 mm (close to minimum), and moved to a row phase of 37.5 mm corresponding to half an undulator period. Storage ring orbit response matrices were measured. Using the orbit response matrices fitted by LOCO [199], the skew quadrupole magnets of the AS storage ring were optimised for a range of vertical emittances, including the minimum emittance fitted by the routine [95]. To combat random bunch centroid motion, a bunch-by-bunch transverse feedback system was operated [288, 289].

The flux ratio of the 14^{th} to 15^{th} harmonics was measured using the approaches of energy scans, time-averaging and orbit bumps as described in Section 8.2. These

harmonics were selected as the highest harmonics (greatest sensitivity to vertical emittance) which were still lower in photon energy than the Au absorption edge cutoff of 2150 eV for the beamline.

8.3.2 Insertion Device Model

The magnetic field of the ID was modelled following the prescription of Section 7.5.5. This best model was based on magnetic measurements of the ID at a gap of 16.0 mm, the magnetic field was scaled to correspond to a magnetic gap of 17.1 mm.

Using this model, the flux in undulator harmonics 14 and 15 was calculated to determine the flux ratio of the adjacent harmonics. Estimates of uncertainty in the model correspond to uncertainty in setting the monochromator for the undulator harmonic of $\Delta E_\gamma = \pm 1$ eV.

8.3.3 Results

For vertical emittances $\varepsilon_y \leq 100$ pm rad, the flux ratio was measured using the techniques described in Section 8.2. Using each of those techniques, the measured and modelled flux ratio of the 14^{th} and 15^{th} harmonics are presented in Figure 8.12.

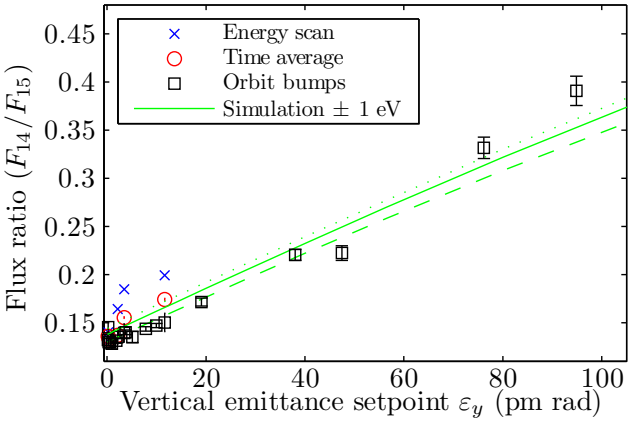

Figure 8.12: Measurement of low vertical emittances using the AS storage ring, and vertical undulator techniques of Section 8.2. This figure can be compared with undulator harmonic $n = 15$ of Figure 8.3.

Of the three measurement techniques used, the flux ratio measured using orbit bumps (Section 8.2.4) is in best agreement with the model. The orbit bumps technique minimises systematic uncertainties in the positioning of the pinhole: by scanning the beam, the maxima and minima are located and the flux ratio is min-

imised. Photon energy scans and time averaging did not have this minimisation goal.

Of particular interest are beams of lowest vertical emittance. Figure 8.13 shows a magnification of Figure 8.12 for smallest vertical emittances, $\varepsilon_y \leq 15$ pm rad.

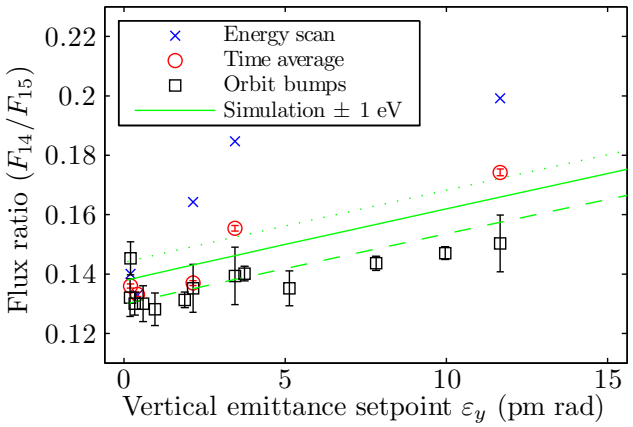

Figure 8.13: Magnification of Figure 8.12, for small vertical emittances. Measurement of lowest vertical emittances using the AS storage ring, and vertical undulator techniques of Section 8.2.

8.4 Analysis

8.4.1 The Quantum Limit of Vertical Emittance

Various contributions to electron beam equilibrium vertical emittance were considered in Section 3.4.7 and Chapter 6. The important contributions are typically vertical dispersion and vertical coupling, which typically produce vertical emittances orders of magnitude greater than the quantum limit of vertical emittance.

In this work, the vertical emittance is approaching the quantum limit of vertical emittance. For the AS storage ring, the quantum limit of vertical emittance given by Equation 3.62 is $\varepsilon_y = 0.35$ pm rad.

8.4.2 Comparison with Measured Orbit Response Matrices

Using the best-fitted model of Section 8.3.2, the vertical emittance was calculated from the measured flux ratio. For the setpoints of vertical emittance, the corresponding vertical emittance measured using orbit response matrices and vertical undulator orbit bumps through a vertical undulator are presented in Figure 8.14, and numerical values are presented in Table 8.1.

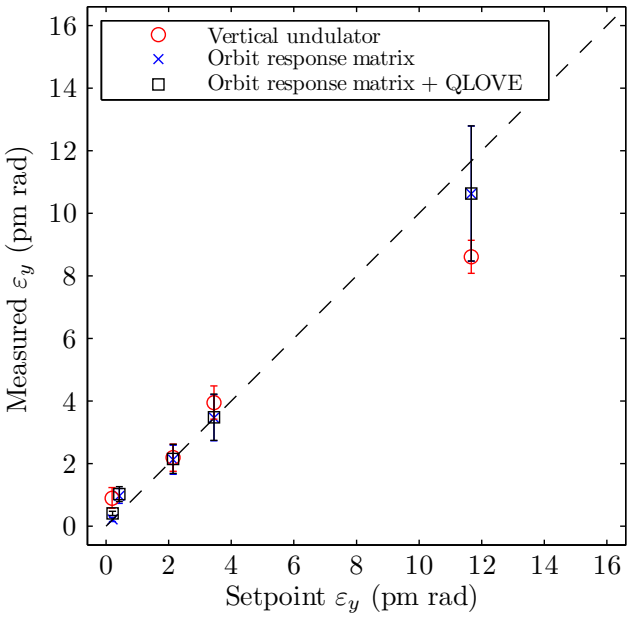

Figure 8.14: Measurement of vertical emittance. Orbit bumps and orbit response matrix fitting with LOCO [199]. The vertical emittance measured with orbit response matrices is also shown in quadrature with the quantum limit of vertical emittance, see Table 8.1. A dashed line −− is used to indicate measured vertical emittance equal to the setpoint.

The vertical emittances presented in Figure 8.14 were measured using different techniques. The vertical emittance measured using the vertical undulator technique measures directly the electron beam size, and so includes a contribution from the quantum limit of vertical emittance.

The vertical emittance fitted from measured orbit response matrices includes contributions from vertical dispersion and betatron coupling, but not from the quantum limit. Hence, the quantum limit of vertical emittance was added in quadrature to vertical emittances measured using orbit response matrices. This is presented in Table 8.1.

The smallest vertical emittance measured using the vertical undulator was $\varepsilon_y = 0.9 \pm 0.3$ pm rad. This is the smallest vertical emittance observed at the AS using a direct measurement technique, and is within a factor of π of the quantum limit for this ring of $\varepsilon_y = 0.35$ pm rad. This is equal to the present world-record for vertical emittance of the SLS [92]. This observed vertical emittance meets the design requirement of the CLIC damping rings.

Table 8.1: Vertical emittance measured with orbit response matrices and orbit bumps through a vertical undulator

Setpoint	QLOVE	Measured		
		Orbit response matrices		Vertical undulator
		$\eta_y, \varepsilon_y/\varepsilon_x$	$\eta_y, \varepsilon_y/\varepsilon_x$, QLOVE (quadrature)	
ε_y (pm rad)	ε_y (pm rad)	ε_y (pm rad)	ε_y (pm rad)	ε_y (pm rad)
0.2	0.35	0.2 ± 0.1	0.4 ± 0.1	$0.9^{+0.3}_{-0.3}$
0.4	0.35	1.0 ± 0.2	1.0 ± 0.2	...
2.1	0.35	2.1 ± 0.5	2.2 ± 0.5	$2.2^{+0.4}_{-0.4}$
3.4	0.35	3.5 ± 0.7	3.5 ± 0.7	$4.0^{+0.5}_{-0.5}$
11.7	0.35	10.6 ± 2.2	10.6 ± 2.2	$8.6^{+0.5}_{-0.5}$

8.4.3 Ideal Insertion Device Model

The utility of the magnetic model of this APPLE-II insertion device is reached. The model could be improved by measuring the ID field components $\vec{B}(x, y, z)$ at the operating magnetic gap of these experiments of 17.1 mm, in the phase used for vertical photon beam polarisation.

8.5 Discussion

The major finding of this work was that the ratios of undulator pinhole flux can be used to measure vertical emittance.

Advantages of the undulator technique and apparatus are the ability to exploit the linearity in detector response over a photon energy range spanning keV, and decades of intensity in photon flux. The measurement of a ratio – as opposed to absolute photon beam brilliance – absolves of the need for measurement of photon flux on an absolute scale, which is difficult to quantify.

These measurements confirm that the spatial and angular distribution of undulator radiation presented in Section 7.4.1 is sensitive to electron beam vertical emittance. The angular distribution of undulator radiation departs from usual Gaussian approximations, and at such low emittances resembles a narrow interference diffraction pattern. This is observed because the vertical emittance is so small relative to the transverse deflection of the undulator in the vertical direction.

Informed by results presented in Section 8.3.3, the ideal insertion device beamline for vertical emittance measurement is considered in terms of several contributing factors.

8.5.1 Electron Beam Energy Spread

The effect of energy spread on peak width has previously been quantified [254, 290]. In simulation we consider the effect of energy spread on peak height. Increasing the relative energy spread by 25%, we find that the measured peak height ratio does not exceed uncertainties in the measured peak ratios for beams with vertical emittance less than 200 pm rad (approximately 2% emittance ratio). The energy spread can be constrained within an uncertainty of 11% from measurements of the bunch length

σ_l which can be expressed by [64],

$$\sigma_l = \frac{c}{2\pi f_s}|\eta|\frac{\sigma_E}{E_0}, \tag{8.1}$$
$$\eta = \gamma^{-2} - \alpha_c.$$

The momentum compaction factor α_c and synchrotron frequency f_s can both be measured within 2% uncertainty using resonant spin depolarisation (Refs. [164, 263, 291], Chapter 5) and a spectrum analyser, respectively. The bunch length can be measured within 7% uncertainty using a calibrated streak camera and removing chromatic effects [292] with a band pass filter. Hence uncertainty in electron beam energy spread should not limit the application of this technique.

Interestingly, measurements of the spectrum of undulator radiation have been reported for an electron beam with very high energy spread ($\sigma_E \approx 5\%$) accelerated by a laser-plasma accelerator [257]. No features are discernible in the spectra presented.

8.5.2 Photon Beam Polarimetry to Extend Technique Sensitivity

One approach to minimise systematic uncertainties is by selective observation of the polarisation components of the photon beam flux. This was first outlined for a proposed SPring-8 vertical undulator measurement of vertical emittance [261]. For a photon beam, the intensities of horizontal I_x and vertical I_y linear polarised light can be described in terms of the Stokes parameters by [293]

$$I_x = 1 \times S_0 + 1 \times S_1 + 0 \times S_2 + 0 \times S_3, \tag{8.2}$$
$$I_y = 1 \times S_0 - 1 \times S_1 + 0 \times S_2 + 0 \times S_3, \tag{8.3}$$

where the Stokes parameters are defined in terms of the intensity of light with respect to polarisation orientations. S_1 denotes linear polarisation, S_2 linear at 45°, and S_3 circular polarisation [294],

$$S_0 = 2I_0, \tag{8.4}$$
$$S_1 = 2I_1 - 2I_0, \tag{8.5}$$
$$S_2 = 2I_2 - 2I_0, \tag{8.6}$$
$$S_3 = 2I_3 - 2I_0. \tag{8.7}$$

The brilliance of radiation from a vertical undulator was evaluated using the SPECTRA code [250]. This simulation is presented in Figure 8.15 in terms of the photon beam intensities I_x and I_y corresponding to horizontal and vertical linear polarisations, for an undulator with an ideal sinusoidal magnetic field and beam with parameters matching the experimental conditions given in Table 7.1.

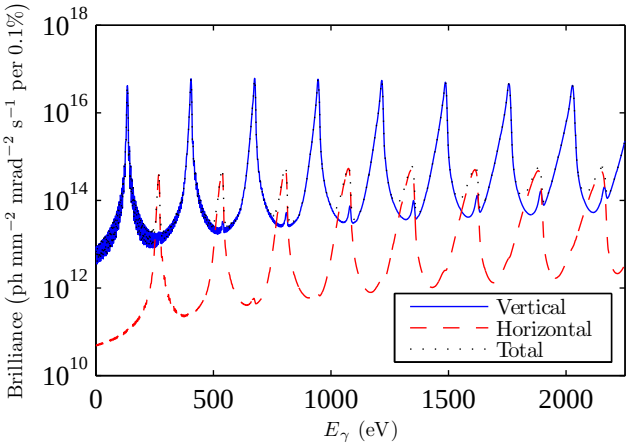

Figure 8.15: Undulator spectrum polarisation, assuming an ideal undulator trajectory and $\varepsilon_y = 1$ pm rad [286].

In this simulation of an ideal insertion device, it is seen that a significant contribution to the on-axis brilliance of even harmonics arises from horizontally polarised light I_x. The ratio of fluxes for the 14$^{\text{th}}$ and 15$^{\text{th}}$ undulator harmonics with varying emittance is presented in Figure 8.16.

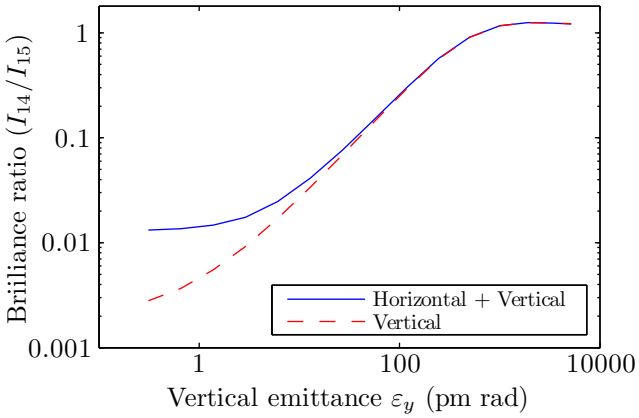

Figure 8.16: Undulator flux ratio I_{14}/I_{15}, for varying vertical emittance. Simulation assumes an ideal sinusoidal trajectory [286].

These results are in agreement with those in literature for an insertion device with an ideal sinusoidal magnetic field [261], and subsequent simulations using the SRW

simulation code for I05 and I06 at Diamond Light Source (DLS) [295]. Figure 8.16 in particular suggests that the rejection of horizontally polarised undulator radiation can extend the sensitivity of the vertical undulator technique to lowest vertical emittances by almost an order of magnitude. The linearity of the flux ratio is extended below 1 pm rad.

This simulation was extended to consider the potential benefit for a real emittance measurement. The simulation was repeated using the scaled, measured field map of Figure 7.10. The on-axis brilliance of the horizontal and vertical polarisations are plotted in Figure 7.10.

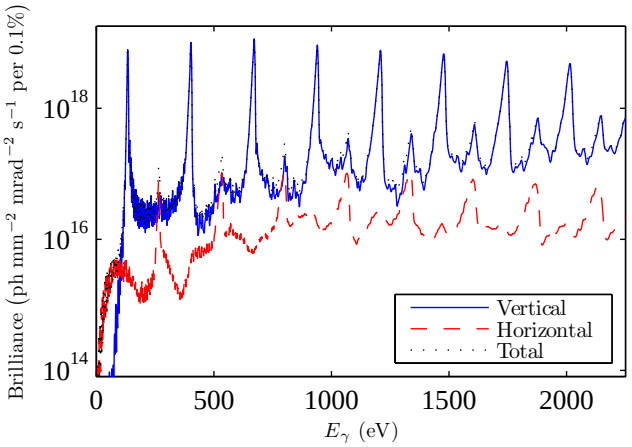

Figure 8.17: Undulator spectrum polarisation, assuming measured undulator magnetic field map and $\varepsilon_y = 1$ pm rad.

The corresponding brilliance ratio of high harmonics 14 and 15 is plotted for varying vertical emittance in Figure 8.18.

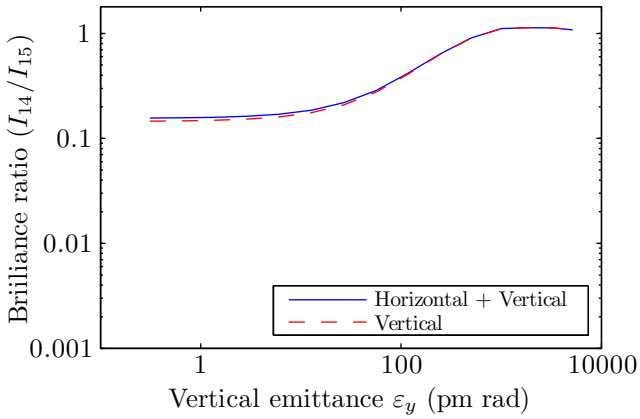

Figure 8.18: Undulator flux ratio I_{14}/I_{15}, for varying vertical emittance. Simulation assumes measured ID magnetic field map.

Unlike Figure 8.16 for an ideal undulator trajectory, Figure 8.18 demonstrates that using a measured magnetic field of a real insertion device that there is no significant benefit in rejecting the horizontal polarisation component in such a measurement. As illustrated in Figure 8.17, the brilliance of horizontal polarisation in high even harmonics is more than an order of magnitude lower than the brilliance of the vertical polarisation component.

8.5.3 Ideal Vertical Insertion Device

At the time of construction, the APPLE-II ID used was shimmed to correct multipole field errors while operating in the horizontal polarisation mode: operation as a usual horizontal undulator [271]. For operation principally as a vertical undulator, it would be beneficial to shim the ID for use in the vertical polarisation mode.

8.5.4 Ideal X-ray Detector for Undulator Measurement

As outlined in Section 7.6.2, the principal uncertainty in the vertical undulator technique is the uncertainty in the pinhole vertical dimension and position. For future experiments to measure vertical emittance, there are two complementary directions for an ideal detector – either a single pinhole of fixed dimensions, or a pixel detector for profile measurements of the undulator photon beam. Future experiments to measure vertical emittance should consider using a pinhole of known diameter, as in other work to characterise a tandem APPLE-II undulator [272].

Pixel detectors for direct observation of the diffraction pattern would also be very convenient. A candidate detector that would be particularly appropriate to this photon energy range would be the DiagOn device developed at SOLEIL. Recently, direct projections of undulator harmonics have been measured at SOLEIL [245]. Designed as a beam diagnostic for APPLE-II IDs, the reported device measures the distribution of horizontally-polarised undulator radiation at a fixed photon energy. As vertical undulators produce vertically-polarised radiation, the device would need to be rotated around the beam axis to pass photons of vertical polarisation. In much the same way as the orbit bump technique of Section 8.2.4, the interference pattern at a fixed photon energy could be observed to measure the vertical emittance.

8.6 Summary

Ultralow pm rad vertical emittance electron beams have been observed using a vertical undulator. Several variables were tested to optimise the sensitivity of the apparatus to electron beam vertical emittance. The variables tested included the X-ray monochromator, the electron beam orbit and the blades of the white beam slits. Comparison of the three techniques demonstrated that orbit bumps of the electron beam through the ID was the most robust technique.

The difference between pm rad ultralow vertical emittance electron beams was resolvable using this technique. Exploiting an existing photon beamline, the measured ratios of on-axis pinhole flux agree closely with a numerical model of radiation from the ID.

For a range of ultralow vertical emittances $\varepsilon_y < 15$ pm rad, the vertical emittance measured using a vertical undulator correlated with the vertical emittance measured using orbit response matrices, including a contribution from the quantum limit of vertical emittance.

Using a best-fitted model for the flux ratio of undulator radiation, the smallest vertical emittance measured was $\varepsilon_y = 0.9^{+0.3}_{-0.3}$ pm rad. This is the smallest vertical emittance observed at the AS using a direct measurement technique, is within a factor of π of the quantum limit for this ring of $\varepsilon_y = 0.35$ pm rad. This is equal to the present world-record for vertical emittance of the SLS [92]. This observed vertical emittance meets the design requirement of the CLIC damping rings.

Chapter 9

Opportunities of Low Vertical Emittance Beams

9.1 Motivation

Briefly, several speculative opportunities for experiments with polarised, low vertical emittance beams in electron storage rings are discussed.

9.2 Storage Ring Light Source Insertion Devices

As an aside to emittance measurement, vertical undulators may be used with existing storage rings to provide a more brilliant X-ray photon source. As shown in Figure 7.2 the brilliance of high, odd undulator harmonics is a factor of two greater for the undulator in the vertical rather than horizontal configuration, at vertical emittances of several pm rad. These small vertical emittances are achievable at many present and proposed storage ring light sources and could usefully improve photon beam brilliance of user beamlines when compared to horizontal insertion devices.

9.3 Ultimate Storage Ring Light Sources

As future ultimate storage rings and damping rings target lower horizontal emittances, it is likely that present techniques for the measurement of pm rad vertical emittances will be required even for the measurement of horizontal emittance. The vertical undulator emittance measurement technique presented in Chapter 7 was used in this work as a diagnostic for pm rad vertical emittances, and could be useful

for future pm rad horizontal emittances. It could similarly be used to measure the transverse emittance of free-electron laser beams.

Low emittance light sources are beginning to produce undulator radiation of interesting spatial distributions [272]. As electron beam light sources approach transverse diffraction limits, the spatial distribution of radiation may become a topic of interest. Diffraction-limited ultimate storage rings are currently proposed with horizontal emittance of order 100 pm rad [296–298]. Such proposals should be aware of the diffraction-limited spatial distribution of undulator radiation, and its departure from usual Gaussian-approximated, emittance dominated photon beams, as presented in Chapter 8.

9.4 Compton Backscattering of Undulator Virtual Photons

Accelerators providing polarised electron beams are envisaged for the proposed electron-ion colliders electron Relativistic Heavy Ion Collider (eRHIC) [299] and Large Hadron electron Collider (LHeC) [300, 301]. For the proposed machines, a rapid electron beam polarimeter could be provided using an elliptical insertion device.

Polarimetry in Chapter 5 was accomplished using Møller (electron-electron) scattering [155]. To similar effect, electron beam polarisation has been observed by measuring synchrotron radiation intensity [302]. Compton (electron-photon) scattering has often been used for absolute polarimetry of relativistic electron beams [303]. Using the Klein-Nishina formula [304, 305], the Compton cross-section was calculated [306] for combinations of incoming and outgoing electron and photon polarisation. Since the first proposal for Compton polarimetry of high energy electron beams [303], laser Compton scattering has been designed [169, 307] and used at SPEAR [147, 308] and LEP [309] among other rings.

One limitation of laser Compton backscattering experiments has been the angular resolution of the detector. Compton backscattered photons have very high energies (MeV), and the detectors used have no energy discrimination beyond thresholding. Undulator radiation polarimetry of proton beams was proposed using a planar undulator [310–312].

Instead, it is proposed to use a high deflection parameter circular undulator in place of a low deflection parameter laser beam with circular polarisation. Undulator radiation is qualitatively identical to laser Compton or Thomson scattering [82, 313,

314], scattering electrons with virtual rather than real photons. Using an undulator of moderate period ($\sim$ 30 mm) with beams of GeV energy, photon energies in the range of several keV are obtained. Such photon beams could be manipulated using existing light source photon beamlines.

This proposed insertion device polarimeter could be tested at existing storage ring lightsources.

9.5 Circular Unruh Effect

Since the seminal work of Sokolov and Ternov in 1963 [148], the maximum polarisation of electron beams in storage rings has remained with a stubborn upper limit of $P_{\mathrm{ST}} = 8/\left(5\sqrt{3}\right) \approx 0.924$. The goal of this work would be to grapple "with the minotaur, the mysterious and peculiar $8/\left(5\sqrt{3}\right)$" [149].

To serve the linear collider community, electron storage ring vertical emittances have advanced towards the quantum limit. At such low emittances, the Bell-Leinaas effect – the electromagnetic analogue of acceleration near a black hole – is predicted to yield electron beams of unprecedented high polarisation of $P_{\mathrm{BL}} = 0.992$, beating the Sokolov-Ternov equilibrium of $P_{\mathrm{ST}} = 0.924$ [150, 315–317].

Low vertical emittance electron rings offer the opportunity to observe the Bell-Leinaas effect. The effect has not been observed to date, owing to the very small transverse recoil of beam electrons due to spin flip photons. At such low vertical emittances, the equilibrium polarisation could exceed the Sokolov-Ternov equilibrium [318], as illustrated in Figure 9.1.

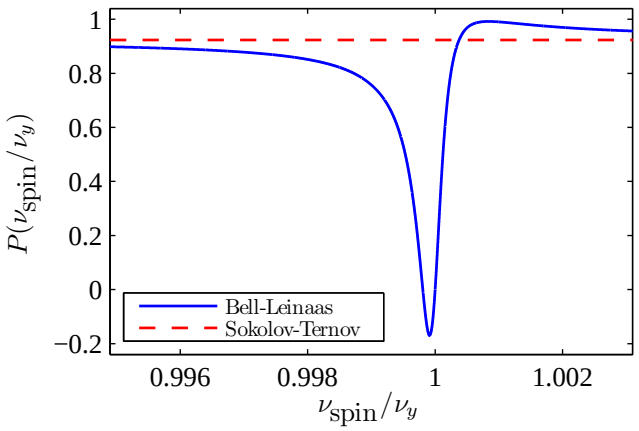

Figure 9.1: Predicted equilibrium polarisation in the vicinity of a spin tune of ν_{spin}, corresponding to a depolarisation by the vertical tune ν_y [150, 318].

The peak value in Bell-Leinaas polarisation is $P(1.001) = 0.992$. The Full Width

at Half Maximum (FWHM) of the peak is approximately 5×10^{-4} in tune space. For the AS storage ring, the FWHM of vertical betatron tune is approximately 5×10^{-4} in tune space [319]. For this reason, the vertical betatron tune is a poor probe for these studies. Instead, using a transverse kicker with field strength oscillating sinusoidally in time, it is possible to create an artificial resonance at that excitation frequency. Exciting the beam with a vertical kicker at frequencies around the spin tune, this effect would be observed if the maximum polarisation was observed above the Sokolov-Ternov limit.

The effect is expected to enhance the equilibrium polarisation in strong focussing electron rings [320, 321].

9.6 Summary

Briefly, several speculative opportunities for beam physics experiments exploiting polarised low vertical emittance beams in storage rings have been outlined.

Experiments with insertion devices operating with low emittance beams have highlighted features of undulator radiation that could be useful for the design of future light sources, and associated diagnostics.

Elliptically polarised insertion devices could be useful diagnostics of electron beam polarisation.

With beams of high transverse polarisation and ultralow vertical emittance, the opportunity exists to test the Bell-Leinaas theory of polarisation in electron storage rings. This may enable unprecedented high polarisation of electron beams in storage rings.

Chapter 10

Conclusions

The major findings of this thesis are:

- Within the uncertainty of the measurement, the momentum compaction factor measured at SPEAR3 and the AS was shown to agree with the numerical model of the trajectory within the bending magnet, and disagree with the hyperbolic cosine approximation.

- Simulations of the equilibrium vertical emittance in the proposed CLIC damping rings agree with analytical expectation values for the vertical emittance before correction of the linear lattice.

- For the proposed CLIC damping rings, the correction of orbit, tune and chromaticity is sufficient for quadrupole vertical, quadrupole roll and bending magnet roll misalignments. These lattice corrections are not satisfactory for sextupole vertical misalignments. In the absence of a skew quadrupole corrector scheme, a vertical emittance of $\varepsilon_y = 0.9$ pm rad was achieved with an RMS sextupole vertical misalignment of $Y_S = 6$ μm. For comparison, using beam-based alignment and individual shimming of the vertical offsets of sextupole magnets, sextupoles of the AS storage ring were aligned within tolerances of $Y_S = 25$ μm [195].

- A new vertical emittance measurement technique was developed, utilising a diffraction-limited vertical undulator.

- It was shown that the increase in vertical emittance due to self-dispersion from a vertical undulator is negligible for an ultralow vertical emittance measurement.

- Using the vertical undulator technique, several variables were tested to optimise experimental sensitivity to the vertical emittance. Comparing scans of the photon energy, orbit bumps through the ID and transverse blade scans demonstrated that orbit bumps of the electron beam through the ID reliably minimised the flux ratio for ultralow emittance beams.

- For a range of ultralow vertical emittances $\varepsilon_y < 15$ pm rad, the vertical emittance measured using a vertical undulator agreed within uncertainties with measurements of vertical emittance using orbit response matrices, including a contribution from the quantum limit of vertical emittance.

- Ultralow pm rad vertical emittance electron beams have been observed using a vertical undulator in a storage ring. Using a best-fitted model for the flux ratio of undulator radiation, the smallest vertical emittance measured was $\varepsilon_y = 0.9^{+0.3}_{-0.3}$ pm rad. This is the smallest direct measurement of vertical emittance at the AS storage ring. This is equal to the present world-record for vertical emittance of the SLS [92]. This observed vertical emittance meets the design requirement of the CLIC damping rings.

The most novel result in this thesis was that the self-dispersion introduced by a vertical undulator to an ultralow vertical emittance storage ring did not measurably increase the vertical emittance. This is counter-intuitive, because at pm rad vertical emittances in storage rings, spurious vertical dispersion is a significant contribution to the equilibrium vertical emittance.

Gradient Bending Magnet Measurements

There is very little published literature concerning the trajectory of beams through straight rectangular defocussing gradient bending magnets. Defocussing magnets are commonly used as part of a strategy to minimise horizontal emittance, and will be used for this purpose in the CLIC damping rings. This thesis contributes measurements to literature, and confirms the numerical modelling strategy of Ref. [104] as more accurate than analytical approximations of solutions for the equation of motion.

The characterisation of the gradient dipole using resonant spin depolarisation requires polarised beams in circular accelerators. This criterion is easily satisfied for ultrarelativistic electron beams, because of radiative polarisation by the Sokolov-Ternov effect. Beams of other species such as protons, ions or muons do not exhibit

significant radiative polarisation, and as such require dedicated spin-polarised acceleration and injection of beams. For many existing machines, such injection schemes are not available.

The implication of these measurements of defocussing gradient magnets is that numerical modelling of arbitrary magnetic fields is appropriate for novel bending magnet designs. This could be very relevant for the design of future low horizontal emittance storage ring light sources, employing longitudinal and transverse gradient bending magnets. It could also be useful in the design of fixed-field, alternating gradient accelerators, storage rings with large transverse gradients in bending magnets. Unlike the measurement technique which was applied to electron storage rings, the numerical trajectory modelling could be used for accelerators of other species such as protons.

Vertical Emittance Measurements

Using a best-fitted model for the flux ratio of undulator radiation, the smallest vertical emittance measured was $\varepsilon_y = 0.9^{+0.3}_{-0.3}$ pm rad. This is the smallest direct measurement of vertical emittance at the AS storage ring, and is within a factor of π of the quantum limit for this ring of $\varepsilon_y = 0.35$ pm rad. This is equal to the present world-record for vertical emittance of the SLS [92]. This observed vertical emittance meets the design requirement of the CLIC damping rings.

Presently the most common ultralow vertical emittance monitors are visible light diagnostics. As future electron beam sizes approach the visible light diffraction limit, soft and hard X-ray diagnostics will be required. For proposed ultimate storage rings, this undulator measurement of emittance may be required for the measurement of ultralow horizontal emittance beams.

The main limitation of the vertical undulator technique is the simulation of undulator radiation from the insertion device. A measured magnetic field map of the insertion device was the best input to modelling. A significant uncertainty was the size of the pinhole mask, formed by closing four white beam slits. Measurement of ultralow vertical emittances using a vertical undulator would significantly benefit from either a pinhole of fixed size, or an imaging detector.

Conclusion

In conclusion, this thesis describes the calibration of magnetic fields in a storage ring for low horizontal and ultralow vertical emittance. Measurements of beams of

the AS and SPEAR3 electron storage rings are used to demonstrate the feasibility of lowest emittance beams in damping rings.

Magnets used to minimise horizontal emittance have been calibrated using precision measurements of beams in electron storage rings. These measurements allow storage and damping ring design to confidently incorporate numerical modelling of combined function magnets in lattice designs for ultralow horizontal emittance.

Vertical emittance in storage rings depends primarily on the vertical alignment of multipole magnets. Using a calibrated electron storage ring, first measurements of ultralow vertical emittance using a new vertical emittance diagnostic are presented. The measured vertical emittance of $\varepsilon_y = 0.9^{+0.3}_{-0.3}$ pm rad satisfies the design vertical emittance of the CLIC damping rings.

Appendices

Appendix A

Parameter Reference Table

Parameters of the AS, SPEAR3 and CLIC storage and damping rings are summarised in Table A.1.

Table A.1: Storage ring parameters

Parameter		AS	SPEAR3	CLIC	units
Beam energy	E	3.01	3.00	2.86	GeV
Beam relativistic gamma	γ	5897	5871	5597	...
Circumference	C	215.99	234.14	420.56	m
Circumference - arcs	C_{arc}	...	...	263.26	m
Circumference - straights	C_{wig}	...	...	157.30	m
Betatron tune - horizontal	ν_x	13.29	14.13	55.46	...
Betatron tune - vertical	ν_y	5.21	6.19	11.61	...
Synchrotron tune	ν_s	0.01071	0.00849	0.00548	...
Chromaticity - horizontal	ξ_x	3.0	2	5.40	...
Chromaticity - vertical	ξ_y	13.0	2	5.43	...
Cavity voltage	V_{gap}	3.0	3.2	4.9	MV
Momentum compaction factor	α_c	0.00211	0.00165	7.6×10^{-5}	...
Damping partition - horizontal	$\mathcal{J}_x$	1.38	1.33	1.0	...
Damping partition - vertical	$\mathcal{J}_y$	1.0	1.0	1.0	...
Damping partition - longitudinal	$\mathcal{J}_s$	1.61	1.67	2.0	...
Synchrotron integral - 1	I_1	0.4601	0.4257	0.0324	m
Synchrotron integral - 2	I_2	0.7823	0.7714	4.4618	m^{-1}
Synchrotron integral - 3	I_3	0.0993	0.0944	0.8615	m^{-2}
Synchrotron integral - 4	I_4	-0.3014	-0.2559	0	m^{-1}
Synchrotron integral - 5	I_5	8.408×10^{-4}	1.52×10^{-3}	2.818×10^{-5}	m^{-1}

Appendix B

Physical Constants

Table B.1: Physical constants and derived quantities

	Parameter	Value	units
C_a	$\frac{cC_q}{C_D}$	1.463×10^{-6}	m GeV^{-2}
C_q	$\frac{55\hbar}{32\sqrt{3}mc}$	3.84×10^{-13}	m
$C_{\gamma e^-}$	$\frac{4\pi}{3}\frac{r_0}{(mc^2)^3}$	8.846×10^{-5}	m GeV^{-3}

Appendix C

Multipole Coefficient Definitions

Different definitions for the multipole coefficients are commonly used. Here, the different expansions are defined. The multipole coefficient k_n can be defined by [45],

$$k_n = \frac{e}{\vec{p_0}} \frac{\partial^n B_y}{\partial x^n}. \tag{C.1}$$

The multipole coefficient K_n is sometimes also defined including a factor of $n!$ [175, 322],

$$\begin{aligned} K_n &= \frac{1}{n!} \frac{e}{\vec{p_0}} \frac{\partial^n B_y}{\partial x^n} \\ &\equiv \frac{1}{n!} \frac{1}{B\rho} \frac{\partial^n B_y}{\partial x^n} \\ &= \frac{1}{n!} k_n. \end{aligned} \tag{C.2}$$

Appendix D

Models of Electron Beam Trajectory Through Straight Defocussing Bending Magnets

D.1 Motivation

The modelling of straight gradient bending magnets is considered. These magnets have been used at surprisingly few rings: the ALS [133, 134], SPEAR3 [103, 104], AS [98] and Fermilab Recycler ring [135].

Using the methods outlined for the SPEAR3 bending magnets [104], these models of the electron beam trajectory were first recorded for an AS bending magnet in an AS technical note [323]. These models were subsequently presented in Ref. [164].

D.2 Modelling Straight Rectangular Combined-Function Bending Magnets

In previous work, several analytical models as well as a numerical model were used to describe the trajectory of an electron beam through a straight rectangular gradient bending magnet [104]. Trajectories described by circular, analytical linear, analytical nonlinear and numerical models are quoted.

D.2.1 Coordinates and Parameters

In order to compare different modelling approaches, the coordinates of the beam trajectory are given with reference to the straight, rectangular gradient bending magnet as illustrated in Figure D.1 for the AS storage ring [164, 323].

This Cartesian coordinate system is right-handed in (x, y, z), with x pointing radially outward from the storage ring centre, y vertically upwards and z parallel to the gradient magnet centreline. The trajectory through a gradient bending magnet can be modelled as a beam travelling off-centre through a quadrupole magnet of very large aperture. A coordinate system is adopted [104], with $(x, y, z) = (0, 0, z)$

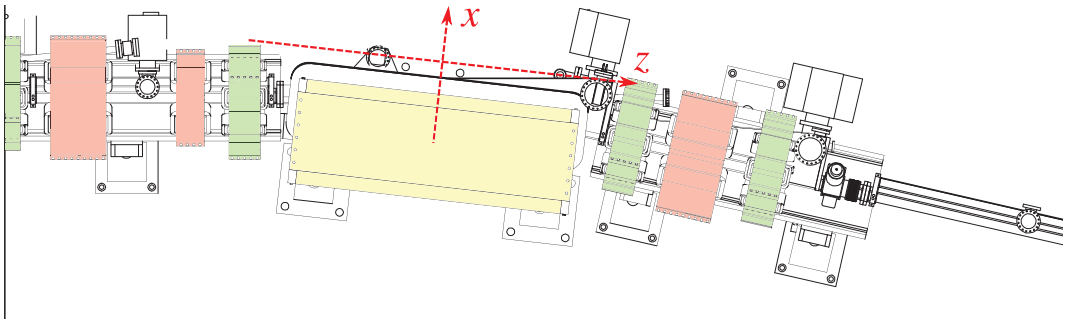

Figure D.1: Coordinate system used for modelling trajectory through a bending magnet. [K.P. Wootton, et al., *Phys. Rev. ST – Accel. Beams*, **16**, 074001 (2013). Published by the American Physical Society under the terms of the Creative Commons Attribution 3.0 License.]

defined as the straight line along the centre of this quadrupole magnet, with $z = 0$ at the longitudinal centre of the quadrupole as shown in Figure D.1. The real bending magnet will be considered to be centred at $(x, y, z) = (-x_{\mathrm{Q}}, 0, 0)$, where $x_{\mathrm{Q}} = B_0/B_1$ and,

$$B_{\mathrm{n}}(x, 0, z) = \frac{\partial^n B(x, z)}{\partial x^n}, \tag{D.1}$$

and n is the order of the transverse derivative of the magnetic field. In this definition, B_0 represents the design upright dipole field, B_1 the design quadrupole gradient, and higher order fields can also be defined. This transverse offset x_{Q} is further illustrated in Figure D.2. Corresponding design parameters of the AS and SPEAR3 bending magnets are summarised in Table D.1.

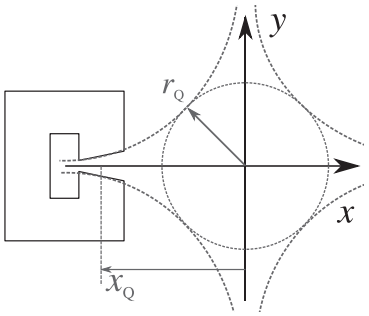

Figure D.2: Cross-section of AS gradient bending magnet, considered as a quadrupole magnet [104]. [K.P. Wootton, et al., *Phys. Rev. ST – Accel. Beams*, **16**, 074001 (2013). Published by the American Physical Society under the terms of the Creative Commons Attribution 3.0 License.]

D.2.2 Dipole Bending Magnet

At a lowest order approximation, the horizontal defocussing gradient is ignored, yielding a trajectory approximated by a circular arc [323]. This approximates the pole profile by a pure dipole as defined in Section 5.2.1.

Table D.1: Storage ring bending magnet parameters

Parameter	Symbol	AS	SPEAR3	units
Beam rigidity	$B\rho$	10	10	T m
Bending angle	θ	$2\pi/28$	$2\pi/34$	rad
Defocussing gradient	$\partial B/\partial x$	3.35	3.63	T m^{-1}
Iron length	L_{iron}	1.700	1.450	m
Effective length	L_{eff}	1.726	1.505	m

For the beam rigidity $B\rho$, bending angle θ and effective length L_{eff} given in Table D.1, the mean dipole field and bending radius are presented in Table D.2. Unless otherwise specified, only the vertical component (B_y) of the magnetic field on the mid-plane (B) is used in the following analysis and discussion, that is $B(x,z) \equiv B_y(x,0,z)$.

Table D.2: Circular radius approximation

Parameter	Symbol	AS	SPEAR3	units
Effective field	B_0	1.300	1.228	T
Bending radius	ρ	7.692	8.144	m

In the coordinate system given, the circular trajectory $x_{\text{circ}}(z)$ within the magnet is expressed by

$$x_{\text{circ}}(z) = \rho\sqrt{1-(z/\rho)^2} - x_{\text{Q}}. \tag{D.2}$$

Outside the effective length of the dipole L_{eff}, the trajectory is straight.

D.2.3 Linear Hyperbolic Cosine Approximation

The field profile of a straight gradient bending magnet (Section 5.2.3) can be considered as the field of a quadrupole of very large bore, laterally offset from the centreline of the bending magnet with a transverse gradient $k = B_1/(B\rho)$. The equation of motion of the beam through this quadrupole is given by [104, 323],

$$\frac{d^2x(z)}{dz^2} = \frac{B(x,z)}{B\rho}\left(1+\left(\frac{dx(z)}{dz}\right)^2\right)^{3/2}. \tag{D.3}$$

A linear solution to Eq. D.3 can be obtained in the approximation $dx(z)/dz \approx 0$. Using this linear approximation, the beam trajectory $x_{\text{L}}(z)$ from magnet centre to exit (and symmetrically, entrance) is expressed by [104, 323]

$$x_{\text{L}}(z) = x_{\text{L}}(0)\cosh(\sqrt{k}z), \tag{D.4}$$

$$x_{\text{L}}(0) = \frac{\tan(\theta/2)}{\sqrt{k}\sinh(\sqrt{k}L_{\text{eff}}/2)}. \tag{D.5}$$

D.2.4 Nonlinear Hyperbolic Cosine Approximation

A nonlinear analytic solution describing the horizontal trajectory of the electron through the bending magnet can be obtained on substitution of the linear solution given by Eq. D.4 into the equation of motion, Eq. D.3. This nonlinear analytic solution is given by [104, 323],

$$x_{\mathrm{NL}}(z) = x_{\mathrm{NL}}(0) - \frac{1}{\sqrt{k}}\left[\sin^{-1}\left(\frac{\cosh(\sqrt{k}z)}{\sqrt{1+1/[kx_{\mathrm{NL}}(0)^2)]}}\right) - \sin^{-1}\left(\frac{1}{\sqrt{1+1/[kx_{\mathrm{NL}}(0)^2]}}\right)\right], \tag{D.6}$$

where

$$x_{\mathrm{NL}}(0) = \frac{\tan(\theta/2)}{\sqrt{k}\sinh(\sqrt{k}L_{\mathrm{eff}}/2)\sqrt{1+\tan^2(\theta/2)}}. \tag{D.7}$$

D.2.5 Numerically Integrated Trajectory using Measured Magnetic Field

The difficulty in modelling the magnetic field of a straight rectangular bending magnet arises because the multipole components of the magnetic field change along the trajectory s. Hence to construct a numerical model of the bending magnet, a sequence of short magnetic elements are simulated with multipole components from dipole up to octupole in order. This modelling approach was implemented for both the AS and SPEAR3 bending magnets [104, 173, 323].

The distribution of the bending magnet magnetic field was measured using a three-axis Hall probe on the magnet mid-plane, $B_{x,y,z}(x, 0, z)$. The vertical component of the measured magnetic field $B_y(x, 0, z)$ is presented in Figure D.3 [323]. The trajectory of a 3 GeV electron beam through this field map (evaluated using this numerical approximation) is superimposed over the measured magnetic field.

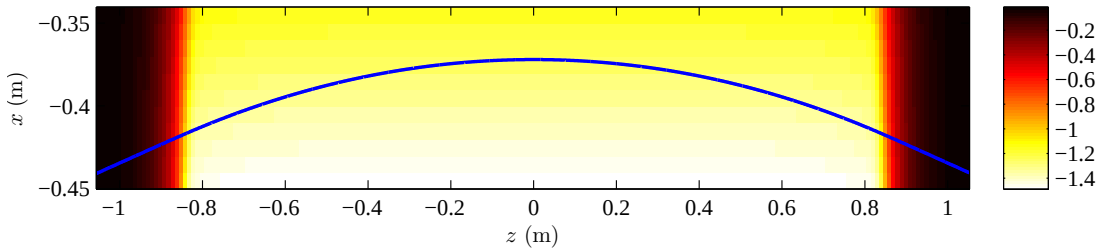

Figure D.3: Measured magnetic field map $B_y(x, 0, z)$ of AS defocussing gradient bending magnet. The trajectory of a 3 GeV model electron beam is superimposed over the map. The colour scale shows the magnitude of the magnetic field in units of Tesla [323]. [K.P. Wootton, et al., *Phys. Rev. ST – Accel. Beams*, **16**, 074001 (2013). Published by the American Physical Society under the terms of the Creative Commons Attribution 3.0 License.]

The electron beam trajectory was calculated by making Taylor expansions of the local vertical magnetic field [104,323]. The magnetic field map was measured in the $(x, 0, z)$ plane, but components of the numerically integrated magnetic field are specified in a curvilinear coordinate system (u, v, s) [323]. The curvilinear system is right-handed with s tangential to the trajectory of the beam, u perpendicular and radially outwards, and v perpendicular and vertically upwards. Using this curvilinear system, magnetic field components are evaluated as,

$$B_n(u, s) = \frac{\partial^n B(u, s)}{\partial u^n}. \tag{D.8}$$

The $n = 0, 1, 2, 3$ order coefficients are correspondingly referred to as the dipole, quadrupole, sextupole and octupole components of the magnetic field.

Solving for the trajectory and field is an iterative process. For a desired beam energy with corresponding rigidity $(B\rho)$ and nominated bending angle θ, the trajectory is solved for a deflection $\int B_0(s)ds = (B\rho)\,\theta$. The integration was performed using a fourth-order Runge-Kutta integrator [104, 323]. These field components given by Equation D.8 are then discretised into i slices along the trajectory s, with field components for the i^{th} slice given by [164],

$$m_n^i = \frac{1}{s_{i+1} - s_i} \int_{s_i}^{s_{i+1}} \frac{\partial^n B(0, s)}{\partial u^n} \partial s. \tag{D.9}$$

For increasing multipole order, the field components m_n are plotted along the curvilinear trajectory s in Figure D.4 for the AS bending magnet.

D.3 Comparison of all Trajectories

Figure D.5 shows the trajectory of a beam through the AS bending magnet, for the models considered in Section D.2.

D.4 Summary

Gradient bending magnets have been identified as useful in strategies to minimise the horizontal emittance of a storage ring lattice. In this appendix, various approximations to the modelling of trajectory through a straight rectangular gradient magnet are given for reference.

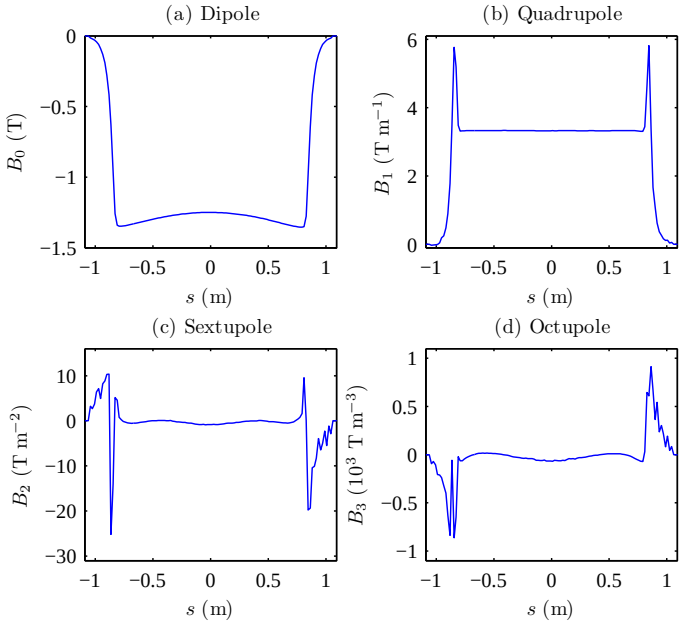

Figure D.4: Magnetic field components $B_n(u, s)$ along the evaluated trajectory [323]. [K.P. Wootton, et al., *Phys. Rev. ST – Accel. Beams*, **16**, 074001 (2013). Published by the American Physical Society under the terms of the Creative Commons Attribution 3.0 License.]

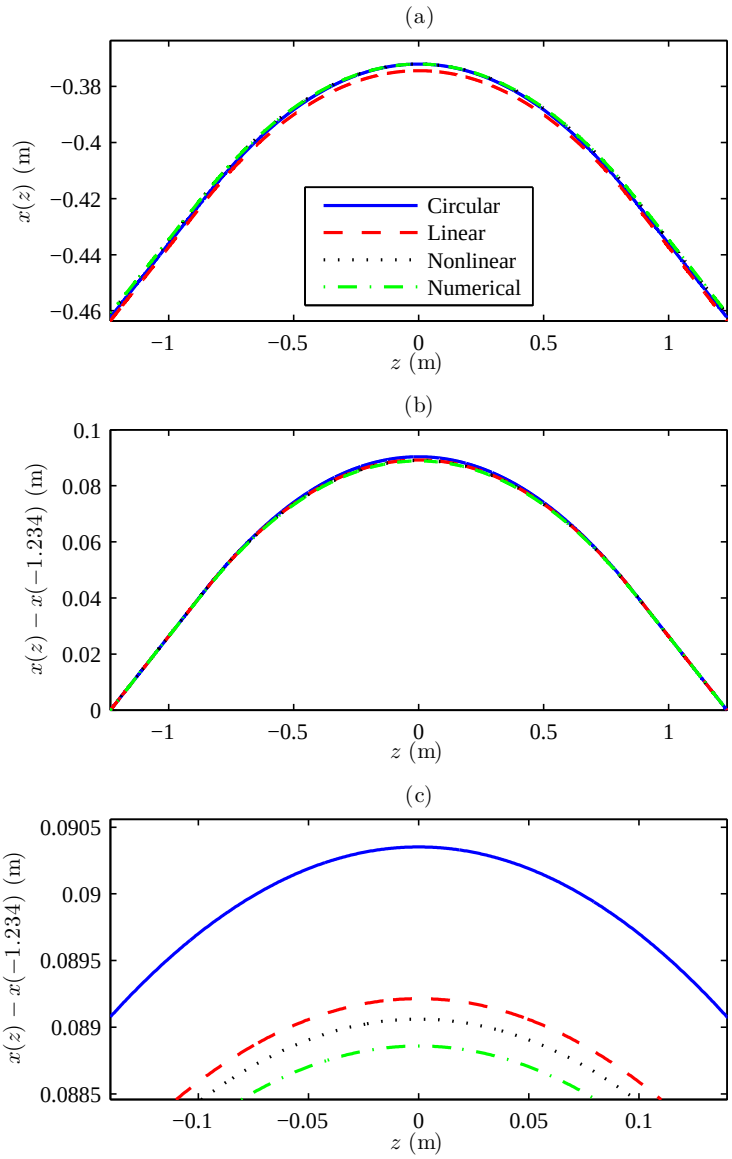

Figure D.5: Modelling of trajectory through AS gradient bending magnet. (a) Electron beam trajectories in coordinates (x, z) for each of the four models described in Appendix D, with equal entrance and exit angles. (b) Translation in x of trajectories in (a) by $x(z) - x(-1.234)$, to give equal entrance and exit positions and angles for each model. (c) Magnification of trajectories in (b). [K.P. Wootton, et al., *Phys. Rev. ST – Accel. Beams*, **16**, 074001 (2013). Published by the American Physical Society under the terms of the Creative Commons Attribution 3.0 License.]

Appendix E

Statistical Uncertainty

A problem for many emittance monitors is the influence of time-varying magnetic fields on the measured electron beam distribution. Time-varying beam motion can be classified either as random motion (noise or other instabilities) or coherent motion (periodic). To correct random bunch centroid motion, a bunch-by-bunch transverse feedback system was operated [288]. The coherent oscillation of electron beam position at known powerline frequencies of $f = 50$ Hz and harmonics was suspected to contribute to the measured electron beam size.

Statistical uncertainty in a measurement can be minimised by making repeated independent measurements of a single quantity [324]. The aim was to measure the photon flux passing through a pinhole, for a given stored electron beam current. To compensate for a decaying electron beam current, the photon flux measured from the photodiode drain current was normalised by the measured DCCT current to a nominal 200 mA stored beam current – the nominal stored electron beam current of the AS storage ring. For n repeat measurements of the photon flux Gaussian-distributed about some mean value μ, the standard uncertainty in the estimate of the mean $\delta\mu$ is given by [324]

$$\delta\mu = \frac{\sigma}{\sqrt{n}}, \tag{E.1}$$

where σ is the standard deviation of measured values. The interpretation of this statement is that as the number of samples n is increased, the mean of the sample (measured photon flux) converges toward the population mean (true photon flux). For comparison, in Figure E.1 and E.2 the measured relative standard deviation is shown for 12 and 80 acquisitions, over various acquisition ranges and times.

Figure E.1 and E.2 highlight that over appropriate choices of acquisition range, statistical uncertainty in the measured pinhole flux can be an insignificant contribution to the uncertainty in measured pinhole flux.

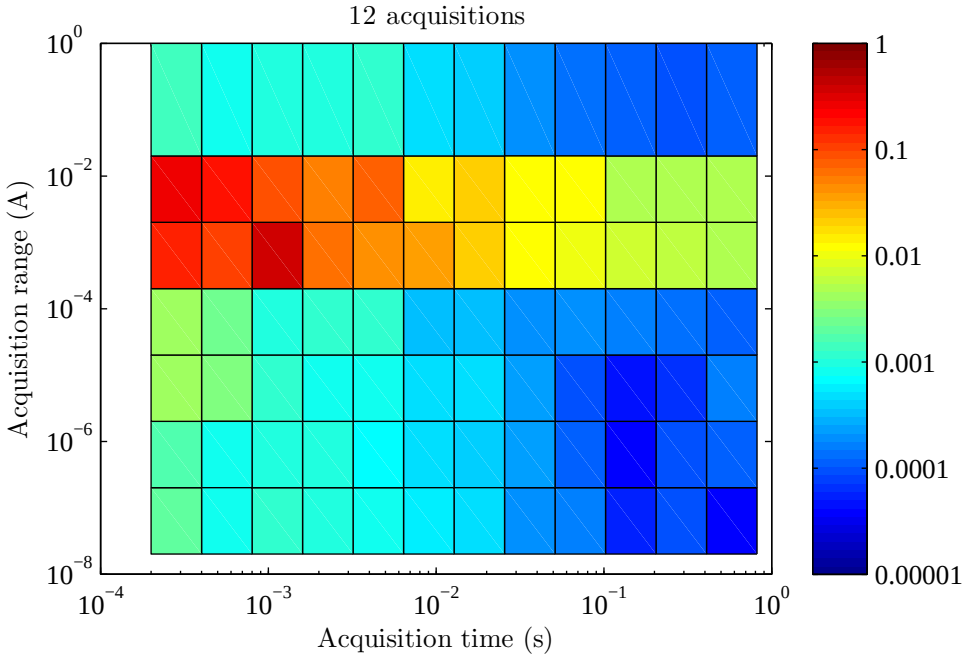

Figure E.1: Measured standard uncertainty $\delta\mu$ in 12 acquisitions, for various acquisition times and ranges [286].

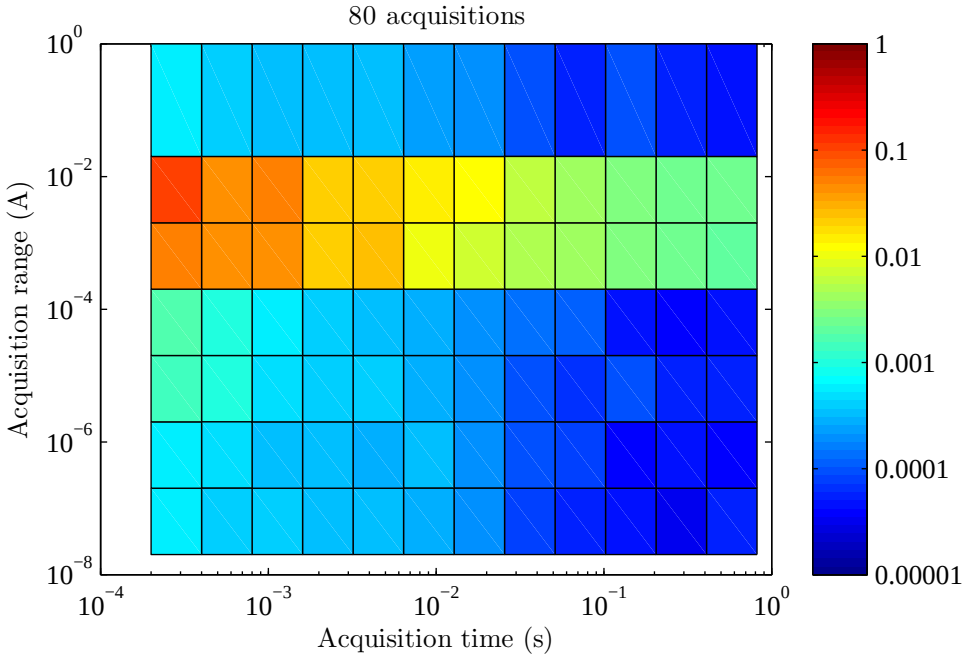

Figure E.2: Measured standard uncertainty $\delta\mu$ in 80 acquisitions, for various acquisition times and ranges [286].

Appendix F

Publications Arising from This Work

F.1 First Author

F.1.1 Refereed Journal Articles

1. K.P. Wootton, M.J. Boland, W.J. Corbett, X. Huang, G.S. LeBlanc, M. Lundin, H.P. Panopoulos, J.A. Safranek, Y.-R.E. Tan, G.N. Taylor, K. Tian and R.P. Rassool, Storage ring lattice calibration using resonant spin depolarization, *Physical Review Special Topics – Accelerators and Beams*, **16**, 074001, 2013. Published by the American Physical Society under the terms of the Creative Commons Attribution 3.0 License.

   doi: 10.1103/PhysRevSTAB.16.074001

2. K.P. Wootton, M.J. Boland, R. Dowd, Y.-R.E. Tan, B.C.C. Cowie, Y. Papaphilippou, G.N. Taylor, R.P. Rassool, Observation of Picometer Vertical Emittance with a Vertical Undulator, *Physical Review Letters*, **109** (19), 194801, 2012. Copyright 2012 by the American Physical Society.

   doi: 10.1103/PhysRevLett.109.194801

F.1.2 Non-refereed Conference Proceedings

1. K.P. Wootton, M.J. Boland, B.C.C. Cowie, R. Dowd and R.P. Rassool (2013) Vertical Undulator Emittance Measurement: A Statistical Approach, *Proc. Int. Beams Instrum. Conf. '13*, TUPF18, Oxford, United Kingdom, 16-19$^{\text{th}}$ September 2013.

2. K.P. Wootton, M.J. Boland, B.C.C. Cowie and R.P. Rassool (2013) APPLE-II Undulator Magnetic Fields Characterised from Undulator Radiation, *Proc. Int. Beams Instrum. Conf. '13*, TUPF19, Oxford, United Kingdom, 16-19$^{\text{th}}$ September 2013.

3. K.P. Wootton, M.J. Boland, G.N. Taylor, R.P. Rassool, B.C.C. Cowie, R. Dowd, Y.-R.E. Tan, Y. Papaphilippou (2012) Vertical Emittance Measurements Using a Vertical Undulator, *Proc. Int. Beams Instrum. Conf. '12*, MOCB04, Tsukuba, Japan, 1-4$^{\text{th}}$ October 2012.

4. K.P. Wootton, M.J. Boland, R.P. Rassool, Y.-R.E. Tan, W.J. Corbett, M. Donald, X. Huang, R.R. Ortiz, J.A. Safranek and K. Tian (2012) Resonant Spin Depolarisation Measurements at the SPEAR3 Electron Storage Ring, *Proc. Int. Particle Accelerator Conf. '12*, MOPPR001, New Orleans, USA, 20-25$^{\text{th}}$ May 2012.

5. K.P. Wootton, M.J. Boland, R.P. Rassool, Y. Papaphilippou, R. Dowd, Y.-R.E. Tan, G.S. LeBlanc, and G. Taylor (2011) Alignment Tolerances for Vertical Emittance, *Proc. Int. Particle Accelerator Conf. '11*, TUPC046, San Sebastian, Spain, 4-9$^{\text{th}}$ September 2011.

6. K.P. Wootton and M.J. Boland (2010), A Novel Synchrotron Radiation Interferometer for the Australian Synchrotron, *Proc. Int. Particle Accelerator Conf. '10*, MOPD079, Kyoto, Japan, 23-28$^{\text{th}}$ May 2010.

F.2 Other than First Author

F.2.1 Technical Reports

1. (The CLIC Detector and Physics Study), H. Abramowicz, *et al.* (2013) Physics at the CLIC e+e- Linear Collider, Input to the Snowmass process 2013, October 1, 2013 [arXiv:1307.5288].

2. A Multi-TeV linear collider based on CLIC technology: CLIC Conceptual Design Report (2012), edited by M. Aicheler, P. Burrows, M. Draper, T. Garvey, P. Lebrun, K. Peach, N. Phinney, H. Schmickler, D. Schulte and N. Toge, CERN-2012-007.

3. The CLIC Programme: towards a staged e+e– Linear Collider exploring the Terascale, CLIC Conceptual Design Report (2012), edited by P. Lebrun, L. Linssen, A. Lucaci-Timoce, D. Schulte, F. Simon, S. Stapnes, N. Toge, H. Weerts, J. Wells, CERN-2012-005.

4. Physics and Detectors at CLIC: CLIC Conceptual Design Report (2012), edited by L. Linssen, A. Miyamoto, M. Stanitzki, H. Weerts, CERN-2012-003.

F.2.2 Refereed Conference Proceedings

1. H.P. Panopoulos, K.P. Wootton, M.J. Boland and R.P. Rassool (2010), Electron Beam Energy Measurement by Resonant Spin Depolarisation at the Australian Synchrotron, *Proc. 19$^{\text{th}}$ AIP Congress*, Melbourne, December 2010.

2. R. Dowd, M.J. Boland, R.P. Rassool and K.P. Wootton (2010), Damping Ring Studies for Future Linear Colliders, *Proc. 19th AIP Congress*, Melbourne, December 2010.

F.2.3 Non-refereed Conference Proceedings

1. M.J. Boland, T. Mitsuhashi and K.P. Wootton (2013) Low Noise and High Dynamic Range Optical Interferometer Beamsize Measurements, *Proc. Int. Beams Instrum. Conf. '13*, TUPF20, Oxford, United Kingdom, 16-19th September 2013.

2. R. Dowd, G. LeBlanc, Y.-R.E. Tan and K. Wootton (2013) Beam Based Magnet Alignment for Emittance Coupling Minimization, *Proc. Int. Particle Accelerator Conf. '13*, TUPWA003, Shanghai, China, 12-17th May 2013.

3. R.B. Clarken, J.S. Hughes, K.P. Wootton, Y.-R.E. Tan and M.J. Boland (2013) 1.5GeV Low Energy Mode for the Australian Synchrotron, *Proc. Int. Particle Accelerator Conf. '13*, MOPEA002, Shanghai, China, 12-17th May 2013.

4. T.M. Mitsuhashi, M.J. Boland, K.P. Wootton (2012) Turn-by-turn Observation of the Injected Beam Profile at the Australian Synchrotron Storage Ring, *Proc. Int. Beams Instrum. Conf. '12*, MOPB83, Tsukuba, Japan, 1-4th October 2012.

5. M.J. Boland, T.M. Mitsuhashi, K.P. Wootton (2012) Injected Beam Profile Measurement during Top-up Operation, *Proc. Int. Beams Instrum. Conf. '12*, TUPB72, Tsukuba, Japan, 1-4th October 2012.

6. M.J. Boland, T.M. Mitsuhashi, T. Naito, K.P. Wootton (2012) Intensity Imbalance Optical Interferometer Beam Size Monitor, *Proc. Int. Beams Instrum. Conf. '12*, WECC03, Tsukuba, Japan, 1-4th October 2012.

7. Y. Papaphilippou, F. Antoniou, M.J. Barnes, S. Calatroni, P. Chiggiato, R. Corsini, A. Grudiev, J. Holma, E. Koukovini, T. Lefevre, M. Martini, M. Modena, N. Mounet, A. Perin, Y. Renier, L. Rinolfi, S. Russenschuck, G. Rumolo, D. Schoerling, D. Schulte, H. Schmickler, M. Taborelli, G. Vandoni, F. Zimmermann, P. Zisopoulos, M. Boland, M. Palmer, A. Bragin, E. Levichev, S. Syniatkin, K. Zolotarev, P. Vobly, M. Korostelev, A. Vivoli, C. Belver-Aguilar, A. Faus-Golfe, A. Bernhard, M. Pivi, S. Smith, R. Rassool, K. Wootton (2012) Conceptual Design of the CLIC Damping Rings, *Proc. Int. Particle Accelerator Conf. '12*, TUPPC086, New Orleans, USA, 20-25th May 2012.

8. D.J. Peake, K.P. Wootton, R.P. Rassool, M.J. Boland (2011) Operation and Storage Ring Calibration with the Transverse Bunch-by-Bunch Feedback System at the Australian Synchrotron, *Proc. Int. Particle Accelerator Conf. '11*, WEPC049, San Sebastian, Spain, 4-9th September 2011.

9. H.P. Panopoulos, K.P. Wootton, M.J. Boland, and R.P. Rassool (2011) Electron Beam Energy Measurement at the Australian Synchrotron Storage Ring, *Proc. Int. Particle Accelerator Conf. '11*, TUPC062, San Sebastian, Spain, 4-9$^{\text{th}}$ September 2011.

10. Y. Renier, F. Antoniou, H. Bartosik, Y. Papaphilippou, K.P. Wootton (2011) Non-Linear Dynamics Optimization of the CLIC Damping Rings, *Proc. Int. Particle Accelerator Conf. '11*, WEPC080, San Sebastian, Spain, 4-9$^{\text{th}}$ September 2011.

Storage ring lattice calibration using resonant spin depolarization

K. P. Wootton,[1,*] M. J. Boland,[1,2] W. J. Corbett,[3] X. Huang,[3] G. S. LeBlanc,[2] M. Lundin,[4] H. P. Panopoulos,[1,†] J. A. Safranek,[3] Y.-R. E. Tan,[2] G. N. Taylor,[1] K. Tian,[3] and R. P. Rassool[1]

[1]*School of Physics, The University of Melbourne, Melbourne, VIC, 3010, Australia*
[2]*Australian Synchrotron, 800 Blackburn Road, Clayton, VIC, 3168, Australia*
[3]*SLAC National Accelerator Laboratory, 2575 Sand Hill Road, Menlo Park, California 94025, USA*
[4]*MAX IV Laboratory, Lund University, P.O. Box 118, SE-221 00 Lund, Sweden*

(Received 22 February 2013; published 1 July 2013)

This paper presents measurements of the GeV-scale electron beam energy for the storage rings at the synchrotron light source facilities Australian Synchrotron (AS) and SPEAR3 at SLAC. Resonant spin depolarization was employed in the beam energy measurement, since it is presently the highest precision technique and an uncertainty of order 10^{-6} was achieved at SPEAR3 and AS. Using the resonant depolarization technique, the beam energy was measured at various rf frequencies to measure the linear momentum compaction factor. This measured linear momentum compaction factor was used to evaluate models of the beam trajectory through combined-function bending magnets. The main bending magnets of both lattices are rectangular, horizontally defocusing gradient bending magnets. Four modeling approaches are compared for the beam trajectory through the bending magnet: a circular trajectory, linear and nonlinear hyperbolic cosine trajectories, and numerical evaluation of the trajectory through the measured magnetic field map. Within the uncertainty of the measurement the momentum compaction factor is shown to agree with the numerical model of the trajectory within the bending magnet, and disagree with the hyperbolic cosine approximation.

DOI: 10.1103/PhysRevSTAB.16.074001 PACS numbers: 29.27.Hj, 29.40.Mc, 41.75.Ht

I. INTRODUCTION

This paper presents measurements of the momentum compaction factor using resonant spin depolarization, to calibrate the model of horizontal defocusing rectangular gradient bending magnets. We present experimental results in the storage rings of light sources SPEAR3 [1] and the Australian Synchrotron (AS) [2], which are modern light sources of intermediate energy with rectangular defocusing gradient dipoles in the double-bend achromat lattices [3]. In literature, there are very few measurements of the momentum compaction factor with rectangular gradient bending magnets. The momentum compaction factor was measured at ALS, with only a small departure from the model [4], however no details of the lattice model used in that study are available. At the time of that measurement, the bending magnets of the ALS lattice were all rectangular defocusing gradient magnets.

Electron beam energy measurements using resonant spin depolarization have been performed at storage rings for calibrating many aspects of the machine [4–8], most notably the absolute beam energy, beam energy stability, and momentum compaction factor. The technique is used because it is the highest precision energy measurement presently available, and the typical measurement accuracy is of order 10^{-5}–10^{-6}. This is one of very few methods for measurement of the momentum compaction factor, which can be calculated from measurements of the synchrotron frequency [9]. Pioneering work on polarization was performed on e^+–e^- collider rings such as ACO [10,11], VEPP-2M [12,13], SPEAR [14], and LEP [15]. Our method of polarizing and depolarizing the beam follows the technique used at BESSY I [5], BESSY II [6], ALS [4], SLS [7], and ANKA [8]. Independent recent measurements at Diamond [16] and SOLEIL [17,18] achieve the same high precision. However, of the above storage rings, the ALS alone employs rectangular gradient bending magnets.

Many existing [1,19–22], upgrading [23] and planned rings [24–28] incorporate defocusing gradients into the main bending magnets, as part of a strategy to reduce the horizontal equilibrium emittance. The trajectory through rectangular gradient magnets does not follow a circular arc as in the case of pure dipole magnets, and the modeling of gradient bending magnets is challenging. In this work, the electron trajectory through the gradient dipoles is modeled using trajectories that are circular, linear hyperbolic cosine, nonlinear hyperbolic cosine, or numerical integration of the measured magnetic field [21].

II. POLARIZATION THEORY

A familiar description of storage ring accelerators is that particles are deflected according to their electrical charge,

*k.wootton@student.unimelb.edu.au
†Present address: Centre for P.E.T., Austin Hospital, 145 Studley Road, Heidelberg, VIC 3084, Australia.

mass, and energy using electric and magnetic fields. These fields are arranged such that beams perform stable, oscillatory motion over many thousands of turns, which can be measured to great precision as a frequency spectrum. Measurement and control of resonances at the revolution and rf frequencies, betatron and synchrotron tunes, informs the global properties of the linear lattice [29]. Here, we exploit another property of the electron—its spin—to inform and calibrate our model of the dipole lattice of storage rings.

A thorough review of theory and experiments with polarized beams of protons, electrons, and muons was undertaken by Mane [30]. We will revisit the main theories of radiative polarization of electron beams, adiabatic resonant spin depolarization, and Møller scattering cross-section polarimetry in the following sections.

A. Radiative polarization

A beam of electrons in a storage ring with an initial random distribution of spin orientations (unpolarized) develops polarization over time, by the Sokolov-Ternov effect [31]. Under the action of emission of spin-flip photons, the population of beam electron spins aligns parallel or antiparallel with the main guide field of the bending magnets. The population of spin-up and spin-down particles is biased by the asymmetry of transition probabilities of spin-flip radiation [31], and the polarization $P(t)$ of the beam develops by [30]

$$P(t) \approx P_0(1 - e^{-t/\tau_{ST}}), \tag{1}$$

where time is denoted by t. The polarization $P(t)$ approaches an equilibrium [6]

$$P_0 = \frac{8}{5\sqrt{3}} \frac{\oint B_\perp^3 ds}{\oint |B_\perp^3| ds}. \tag{2}$$

Magnetic fields are considered in the directions perpendicular ($B_\perp$) and parallel ($B_\parallel$) to the curvilinear trajectory of the beam, s. In a storage ring, both vertical and radial magnetic fields are denoted here by $B_\perp$. To accommodate reverse bends and wiggler insertion devices, we integrate both $B_\perp$ and its absolute value $|B_\perp|$ around the trajectory s. By inspection, P_0 approaches a maximum for a storage ring without reverse bends or wiggler insertion devices, and for a beam of electron species with gyromagnetic factor $g_e \approx 2$, the theoretical maximum of polarization is $P_0 = 0.9238$ in an isomagnetic, planar ring [31]. The characteristic Sokolov-Ternov polarization time τ_{ST} is given by [31]

$$\tau_{ST}^{-1} = \frac{1}{4\pi\epsilon_0} \frac{5\sqrt{3}}{8} \frac{\hbar\gamma^5 r_e}{m_e} \frac{1}{\rho^3}, \tag{3}$$

where ρ is the local bending radius, m_e, r_e the classical electron mass and radius, ϵ_0 the permittivity of free space, $\hbar$ the reduced Planck's constant, and γ is the Lorentz factor of this relativistic electron beam. If the bending radius $\rho(s)$ varies around the ring circumference, rather than use the average value ρ we make the substitution of the third synchrotron radiation integral [30,32],

$$\frac{1}{\rho^3} \rightarrow I_3 = \frac{1}{2\pi R} \oint \frac{1}{|\rho(s)|^3} ds, \tag{4}$$

where R denotes the mean ring radius.

B. Resonant spin depolarization

Spin transport is described by the Thomas–Bargmann-Michel-Telegdi equation [33]. The electron spin precesses about the polarization axis at the spin precession frequency [15]

$$\vec{\Omega}_{BMT} = -\frac{q_e}{\gamma m_e}\Big[(1 + a_e\gamma)B_\perp + (1 + a_e)B_\parallel - \left(a_e\gamma + \frac{\gamma}{1+\gamma}\right)\frac{\vec{\beta}\times\vec{E}}{c}\Big], \tag{5}$$

where q_e is the electric charge and $a_e = (g_e - 2)/2$ the anomalous magnetic moment of the electron, and c the speed of light in vacuum. As defined for Eq. (2), the direction of electric fields $\vec{E}$ are considered with respect to the relativistic velocity of the electron $\vec{\beta} = \vec{v}/c$. Normally the storage rings of light sources do not include any significant solenoid magnetic fields nor transverse electric fields, that is $B_\parallel = 0$, $\vec{\beta}\times\vec{E} = 0$. Hence, we can make the simplifying assumption that the electron spin precesses about a polarization axis which is antiparallel to $B_\perp$ (for bending magnets of a ring, a vertical magnetic field), at a frequency given by Eq. (5) which can be simplified to the spin tune ν_{spin} [15]:

$$\nu_{spin} = a_e\gamma \equiv \left(\frac{g_e - 2}{2}\right)\frac{E}{m_e c^2}, \tag{6}$$

where E is the beam energy. If the beam is excited by a radial magnetic field f_{kick} resonant at any harmonic to the spin tune, the polarization axis of the beam can be coherently rotated away from its equilibrium vertical orientation. The beam is hence resonantly depolarized at the frequency $f_{kick} = f_{dep}$.

C. Current fundamental and experimental uncertainties

The gyromagnetic factor g_e for electrons has been measured to precision within the 12th significant figure [34]. We use the NIST CODATA values [35] for $a_e = 0.00115965218076(27)$ and $m_e = 0.510998928(11)\,\mathrm{MeV}$. As a point of interest, with a relative uncertainty of $\Delta a_e/a_e = 2.3\times10^{-10}$, $\Delta m_e/m_e = 2.2\times10^{-8}$, the uncertainty in the electron mass has improved by almost an order of magnitude since 1994 [15], and hence the theoretical fundamental limit of uncertainty in the resonant

TABLE I. Relative experimental uncertainties for AS and SPEAR3 experiments.

Parameter	Relative uncertainty
a_e	2.3×10^{-10}
m_e	2.2×10^{-8}
f_{rf}	1×10^{-10}
f_{kick}	1×10^{-7}
f_{dep}	1×10^{-6}

depolarization technique is reduced to approximately $\Delta E/E = 2.2 \times 10^{-8}$. In practice, this limit remains orders of magnitude lower than other experimental uncertainties, as detailed for these experiments in Table I.

As outlined in Table I, the rf frequency f_{rf} is calibrated to high precision and the excitation frequency f_{kick} can be calibrated against a reference clock. Hence from Eq. (6), measurement of the spin tune ν_{spin} gives a direct measurement of the beam energy, with experimental uncertainty dominated by uncertainty in fitting the depolarizing frequency f_{dep}.

D. Depolarizing effects

The effective polarization time τ_{eff} is given by [17,36]

$$\frac{1}{\tau_{\mathrm{eff}}} = \frac{1}{\tau_{\mathrm{ST}}} + \frac{1}{\tau_{\mathrm{dep}}}, \tag{7}$$

where τ_{ST} represents the Sokolov-Ternov polarization time [Eq. (3)], and τ_{dep} a depolarization time governed by radial magnetic field errors [17]. Storage rings of several GeV achieve Sokolov-Ternov polarization times on the order of 15–20 minutes, with depolarization times exceeding several hours [37]. Because the depolarization effects have a much longer characteristic time, the effective polarization time is dominated by the Sokolov-Ternov polarization time.

A strong depolarizing resonance to be avoided is the choice of stored beam energy corresponding to integer spin tune [Eq. (6)] [11]. Also depolarizing is the overlap of the spin tune with betatron or synchrotron tunes. The vertical betatron tune has been usefully employed for resonant spin depolarization [14]. In that experiment, the vertical betatron tune was swept as the depolarizer. The width of the vertical betatron tune resonance limited the uncertainty in the beam energy measurement to approximately $\Delta E/E = 10^{-4}$. In this experiment at the AS and SPEAR3, a feedback kicker is excited with a sinusoidal oscillation, because it can have a narrower frequency spread than the betatron tune.

E. Møller scattering polarimetry

Møller scattering is electron-electron scattering and occurs within a bunch in the storage ring. The polarimetry observable is the Møller scattering cross section of Touschek scattered electrons [38–40]: the intrabunch cross section resulting from betatron oscillations. The particle loss rate dN/dt is described in terms of the polarization $P(t)$ by [12,30,37]

$$\frac{dN}{dt} = -\frac{N(t)^2 c}{\sqrt{2}\gamma^2 \sigma_x \sigma_{x'} \sigma_y \sigma_{y'} \sigma_z}[f_1 + f_2 P(t)^2], \tag{8}$$

where the number of electrons per bunch is $N(t)$. For a stored beam of current $I(t)$ with equal current in several bunches, the bunch population $N(t) \propto I(t)$. The horizontal, vertical, and longitudinal beam dimensions are denoted by σ_x, σ_y, σ_z, and divergences denoted $\sigma_{x'}$, $\sigma_{y'}$ in the horizontal and vertical directions, respectively. The functions f_1 and f_2 can be treated for a given measurement as constants. Importantly, because $N(t) \propto I(t)$, an instantaneous normalized loss rate R_{norm} can be defined as

$$R_{\mathrm{norm}} = \frac{1}{I(t)^2}\frac{dN}{dt} \propto f_1 + f_2 P(t)^2. \tag{9}$$

The normalized loss rate is the figure of merit used to evaluate changes in the level of beam polarization.

III. DEPOLARIZATION EXPERIMENTS

A. Lattice and beam parameters

Depolarization experiments were conducted at both the AS and SPEAR3 storage rings [41,42]. The pertinent design parameters of the two rings are summarized in Table II.

Using Eq. (6), the spin tune of a 3 GeV electron beam was calculated as $\nu_{\mathrm{spin}} = 6.8081$, as presented in Table II. As outlined in Sec. II D, betatron tunes are depolarizing if overlapping with the spin tune. For the initial measurement of both rings, quadrupole strengths were changed to reduce the fractional vertical tune to approximately 0.1.

B. Polarization time

For both the AS and SPEAR3 storage rings, an unpolarized beam of electrons was injected into the storage ring, which was observed to polarize over time. The measured

TABLE II. Storage ring design parameters.

Parameter		AS	SPEAR3	
Beam energy	E	3.00	3.00	GeV
Lattice periodicity	...	14	18	...
Lorentz factor	γ	5871	5871	...
Spin tune	ν_{spin}	6.8081	6.8081	...
Betatron tunes	ν_x	13.290	14.130	...
	ν_y	5.216	6.194	...
Bending radius	ρ	7.69	7.86	m
Circumference	C	216.000	234.144	m
rf frequency	f_{rf}	499.671	476.300	MHz
Polarization time	τ_{ST}	807	1003	s

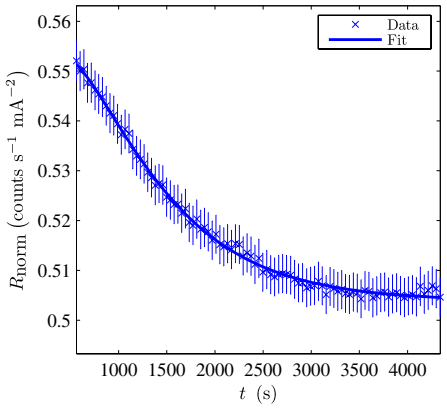

FIG. 1. Measurement of polarization time (AS). Fit to normalized count rate gives $\tau_{\mathrm{eff}} = 806 \pm 21$ s.

normalized loss rate R_{norm} was fitted by Eqs. (1) and (9) to determine the polarization time. This is shown for the AS in Fig. 1, and for SPEAR3 in Fig. 2.

Using Eq. (3) and design parameters in Table II the Sokolov-Ternov polarization time was calculated. The measured τ_{eff} and theoretical τ_{ST} are compared in Table III.

Importantly, for both rings a change in R_{norm} is observed, which can be sensibly attributed to a change in polarization $P(t)$ by the Sokolov-Ternov effect. Hence, with this apparatus we will be able to observe the depolarization of the beam at the spin tune. Additional detail about the detector apparatus is given in Appendix A.

C. Spin tune and beam energy measurement

With the stored electron beam polarized, a time-varying radial magnetic field was applied to the beam through a fast

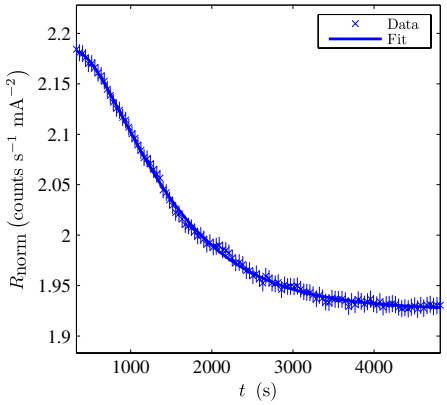

FIG. 2. Measurement of polarization time (SPEAR3). Fit to normalized count rate gives $\tau_{\mathrm{eff}} = 840 \pm 12$ s.

TABLE III. Polarization time in AS and SPEAR3.

Machine	Measured τ_{eff} (s)	τ_{ST} (s)
AS	806 ± 21	807
SPEAR3	840 ± 17	1003

kicker magnet and the oscillating frequency was scanned close to the predicted spin tune. Additional detail concerning the depolarizing kicker is given in Appendix B. As the magnetic field frequency crosses the spin tune the normalized loss rate increases indicating the beam is depolarized. Figure 3 shows a depolarizing event at AS where the change in the rate is clearly observable over and above the fluctuations due to counting statistics.

The uncertainty in the central frequency of the spin tune is not the same as the width of the spin tune resonance. The width of the spin tune resonance $\sigma_f/f_{\mathrm{dep}} \approx 5 \times 10^{-6}$ was observed to be much larger than the uncertainty in the central frequency of the spin tune resonance $\Delta f_{\mathrm{dep}}/f_{\mathrm{dep}} \approx 2 \times 10^{-6}$. In addition, the width of the spin tune resonance is much narrower than the energy spread of the beam, which for this lattice is $\sigma_E/E \approx 1 \times 10^{-3}$ [2].

The beam energy for AS and SPEAR3 were extracted from spin tune frequency measurements, and the results are presented in Table IV. The high precision which was achieved with this energy measurement technique is exploited to measure the momentum compaction factor of the storage rings.

D. Momentum compaction factor

The momentum compaction factor is the change in circumference with change in energy [29,43]. For a set of rf frequencies, the beam energy was measured using the

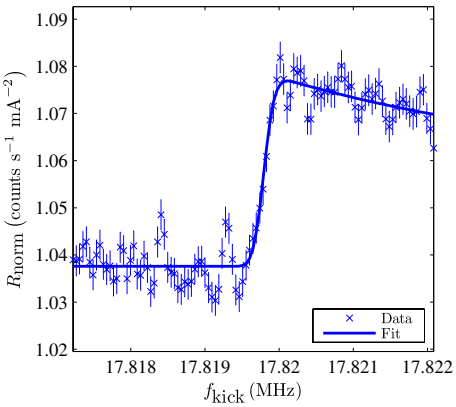

FIG. 3. Resonant spin depolarization (AS). A central frequency of $f_{\mathrm{dep}} = 17819790 \pm 30$ Hz is fitted with a width of $\sigma_f = 110 \pm 40$ Hz. An error function is fitted, allowing for the subsequent repolarization of the beam.

TABLE IV. Measured spin tune and beam energy.

Machine	f_{dep} (Hz)	$\nu_{\mathrm{spin}} = a_e\gamma$	E (eV)
AS	17819790 ± 30	6.83859 ± 0.00002	3013416 ± 9
SPEAR3	253620 ± 20	6.80192 ± 0.00002	2997251 ± 7

resonant spin depolarization technique. The rf frequency provides an accurate constraint on the circumference of the closed orbit, and resonant spin depolarization an accurate measurement of stored beam energy. In order to keep the beam energy stable, rf frequency feedback and fast-orbit feedback were turned off. The rf frequency was varied by small changes of 500 and 1000 Hz from the nominal frequency given in Table II, resulting in small changes to the stored beam energy. The corresponding change in beam energy was measured, as illustrated in Fig. 4 for AS. A similar measurement was implemented for SPEAR3. The measured momentum compaction factors of each ring are summarized in Table V. These values are later compared with calculated momentum compaction factor for the different models of the gradient dipoles in the rings as described in Sec. IV F.

IV. GRADIENT BENDING MAGNET MODELING

As demonstrated in Sec. III D, we can exploit resonant depolarization to measure the momentum compaction factor of a storage ring. The momentum compaction factor α_c of a lattice can be calculated by integrating around the curvilinear trajectory s as [44]

$$\alpha_c = \frac{1}{C}\oint_0^C \frac{\eta_x(s)}{\rho(s)}ds, \tag{10}$$

where C is the circumference, $\eta_x(s)$ the horizontal dispersion, and $\rho(s)$ the local bending radius. In previous work, several analytical models as well as a numerical model

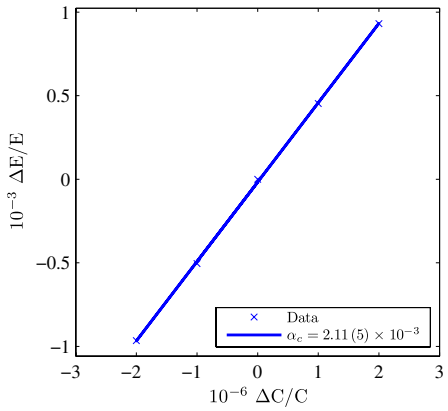

FIG. 4. Momentum compaction factor measurement (AS).

TABLE V. Momentum compaction factor measured using resonant spin depolarization.

Machine	α_c
AS	0.00211 ± 0.00005
SPEAR3	0.00164 ± 0.00001

were used to describe the trajectory of an electron beam through a rectangular gradient bending magnet [21], as used in the present experiments. Without a rigorous derivation, we quote the results of trajectories described by circular, analytical linear, analytical nonlinear, and numerical models. The model lattice optical functions and momentum compaction factor are analyzed and compared to measured values.

A. Coordinates and parameters

In this section of the paper, the coordinates of the beam trajectory will be given with reference to the straight, rectangular gradient bending magnet as illustrated in Fig. 5 for the AS storage ring.

This Cartesian coordinate system is right handed in (x, y, z), with x pointing radially outward from the storage ring center, y vertically upwards, and z parallel to the center line of the gradient magnet. The trajectory through a gradient bending magnet can be modeled as a beam traveling off center through a large quadrupole. We adopt a coordinate system [21], and define $(x, y, z) = (0, 0, z)$ as the straight line along the center of this quadrupole, with $z = 0$ at the longitudinal center of the quadrupole as shown in Fig. 5. The bending magnet will be considered to be centered at $(x, y, z) = (-x_{\mathrm{Q}}, 0, 0)$, where $x_{\mathrm{Q}} = B_0/B_1$ and

$$B_{\mathrm{n}}(x, 0, z) = \frac{\partial^n B(x, z)}{\partial x^n}, \tag{11}$$

and n is the order of the transverse derivative of the magnetic field. This is further illustrated in Fig. 6.

The numerically evaluated trajectory will be evaluated in terms of a magnetic field map measured in the $(x, 0, z)$ plane, but components of the numerically integrated magnetic field will subsequently be specified in a curvilinear coordinate system (u, v, s). The curvilinear system is right handed with s tangential to the trajectory of the beam, u perpendicular and radially outwards, and v perpendicular and vertically upwards. The curvilinear system is selected for the numerical trajectory because it is easy to implement curvilinear magnetic elements in existing accelerator tracking codes.

Parameters of the bending magnet are summarized in Table VI.

B. Circular arc trajectory

We make the simplifying assumption that the trajectory is approximated by a circular arc, as a base against which

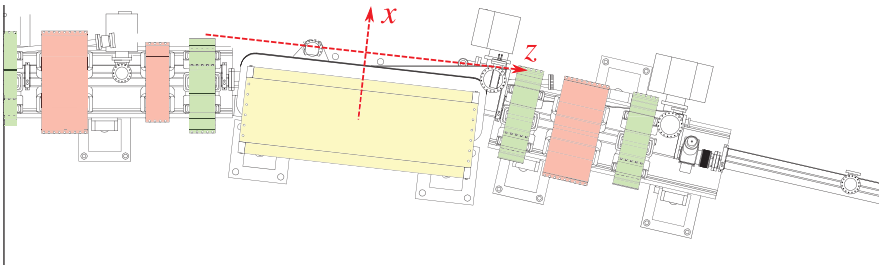

FIG. 5. Half sector of the AS storage ring [2]. The rectangular gradient bending magnet is shown in yellow, quadrupoles in red, and sextupoles in green.

to make comparisons. Ignoring the horizontal defocusing gradient, we approximate the pole profile as a pure dipole.

For the beam rigidity $B\rho$, bending angle θ, and effective length L_{eff} given in Table VI, the mean dipole field and bending radius are presented in Table VII. Unless otherwise specified only the vertical component of the magnetic field on the midplane will be used in the following analysis and discussion, i.e., $B(x, z) = B_y(x, 0, z)$.

In the coordinate system given, the circular trajectory $x_{\text{circ}}(z)$ within the magnet is expressed by

$$x_{\text{circ}}(z) = \rho\sqrt{1 - (z/\rho)^2} - x_{\text{Q}}. \tag{12}$$

Outside the effective length of the dipole L_{eff}, the trajectory is straight.

C. Linear hyperbolic cosine trajectory

The field profile of a gradient bending magnet can be considered to be the field of a quadrupole of very large bore, laterally offset from the center line of the bending magnet. This quadrupole is considered to have a strength, k, which is defined in terms of the defocusing gradient B_1 and beam rigidity $(B\rho)$ by $k = B_1/(B\rho)$. The equation of motion of the beam through this quadrupole is given by [21]

$$x''(z) = \frac{B(x, z)}{B\rho}[1 + x'(z)^2]^{3/2}, \tag{13}$$

where the prime denotes the derivative along z. A linear solution to Eq. (13) can be obtained by making the approximation $x'(z) = 0$. We quote the trajectory evaluated using this linear approximation, and direct the interested reader to its derivation [21]. The beam trajectory $x_{\text{L}}(z)$ from magnet center to exit (and symmetrically, entrance) is expressed by

$$x_{\text{L}}(z) = x_{\text{L}}(0)\cosh(\sqrt{k}z), \tag{14}$$

$$x_{\text{L}}(0) = \frac{\tan(\theta/2)}{\sqrt{k}\sinh(\sqrt{k}L_{\text{eff}}/2)}. \tag{15}$$

The deflection of the beam is chosen to be symmetric longitudinally about the magnet center $z = 0$ so that the magnet deflects the beam through a bending angle $\theta/2$ within the length $L_{\text{eff}}/2$, with maximum orbit amplitude at the magnet center.

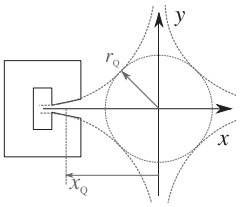

FIG. 6. Description of gradient bending magnet field by the field of a single quadrupole of radius r_{Q}, laterally offset from the nominal center line of the bending magnet by a distance x_{Q} [21].

D. Nonlinear hyperbolic cosine trajectory

A nonlinear analytic solution describing the horizontal trajectory of the electron through the bending magnet can be obtained on substitution of the linear solution given by Eq. (14) into the equation of motion, Eq. (13). This nonlinear analytic solution is given by [21]

TABLE VI. Storage ring bending magnet parameters.

Parameter	Symbol	AS	SPEAR3	units
Beam rigidity	$B\rho$	10	10	T m
Bending angle	θ	$2\pi/28$	$2\pi/34$	rad
Defocusing gradient	$\partial B/\partial x$	3.35	3.63	T m^{-1}
Iron length	L_{iron}	1.700	1.450	m
Effective length	L_{eff}	1.726	1.505	m

TABLE VII. Circular radius approximation.

Parameter	Symbol	AS	SPEAR3	
Effective field	B_0	1.300	1.228	T
Bending radius	ρ	7.692	8.144	m

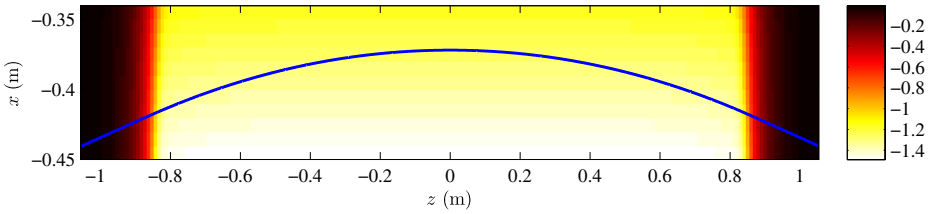

FIG. 7. Vertical component of magnetic field of AS horizontally defocusing gradient bending magnet, measured with a Hall probe. The x-z axes corresponds to the coordinate system of Fig. 5. The numerically evaluated trajectory is represented by a solid blue line. The color scale shows the vertical component of the magnetic field $B_y(x, 0, z)$ in units of Tesla.

$$x_{\mathrm{NL}}(z) = x_{\mathrm{NL}}(0) - \frac{1}{\sqrt{k}}\left[\sin^{-1}\left(\frac{\cosh(\sqrt{k}z)}{\sqrt{1 + 1/[kx_{\mathrm{NL}}(0)^2]}}\right) - \sin^{-1}\left(\frac{1}{\sqrt{1 + 1/[kx_{\mathrm{NL}}(0)^2]}}\right)\right], \tag{16}$$

where

$$x_{\mathrm{NL}}(0) = \frac{\tan(\theta/2)}{\sqrt{k}\sinh(\sqrt{k}L_{\mathrm{eff}}/2)\sqrt{1 + \tan^2(\theta/2)}}. \tag{17}$$

E. Numerically integrated trajectory using measured magnetic field data

A model of the AS bending magnet can be created by using a group of sector dipole elements with higher order multipole field components (quadrupole, sextupole, and octupole). This method has also been implemented for modeling the SPEAR3 ring [45], and has the benefit of ensuring that particle tracking is symplectic.

The magnetic field map of the defocusing gradient bending magnet was measured by a three-axis Hall probe on the horizontal midplane to give $B_{x,y,z}(x, 0, z)$. The vertical component of the magnetic field $B_y(x, 0, z)$ is presented in Fig. 7. Superimposed on the map is the trajectory of a 3 GeV electron passing through the magnet as calculated using the numerical integration method.

The vertical magnetic fields experienced by the electron while traversing the gradient magnet can be approximated by calculating the coefficients of the Taylor expansion of the local magnetic field relative to the trajectory. As outlined in Sec. IV A, this curvilinear system is selected for the numerical trajectory because it is easy to implement a sequence of curvilinear magnetic elements in existing accelerator tracking codes.

The first step in the calculation is a coordinate transformation from the Cartesian (x, y, z) coordinates to a curvilinear coordinate system (u, y, s), where s is tangential and u perpendicular to the reference trajectory. Therefore, all field components are evaluated as

$$B_n(u, s) = \frac{\partial^n B(u, s)}{\partial u^n}. \tag{18}$$

The $n = 0, 1, 2, 3$ order coefficients are correspondingly referred to as the dipole, quadrupole, sextupole, and octupole components of the magnetic field. The field components for the AS bending magnet are shown in Fig. 8.

The horizontal trajectory of the particle through the measured magnetic field (blue curve in Fig. 7) is calculated by numerically solving Eq. (13) with a fourth order Runge-Kutta integrator (with no variable step size). The trajectory is constrained to longitudinal symmetry, i.e. $x(-L_{\mathrm{eff}}/2) = x(L_{\mathrm{eff}}/2)$, $x'(-L_{\mathrm{eff}}/2) = x'(L_{\mathrm{eff}}/2)$, and a deflection of $\int B_0(s)ds = (B\rho)\theta$.

The numerical trajectory is modeled with field components given by Eq. (18). The bending magnet model is constructed by performing piecewise integration of the field map along the trajectory s at points s_i. For the ith slice, the integrated multipole component is given by

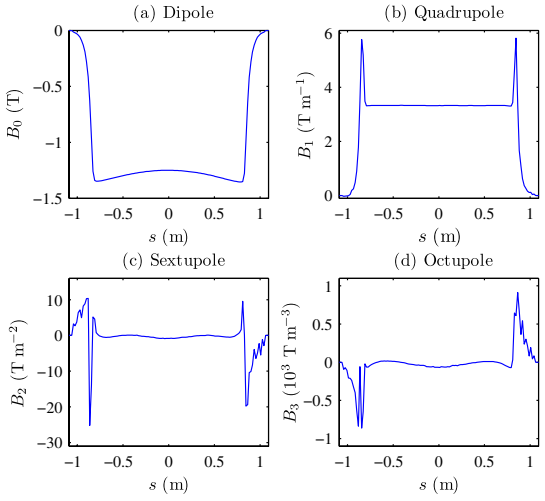

FIG. 8. Field components $B_n(u, s)$, along the curvilinear trajectory plotted in Fig. 7. (a) Dipole component. (b) Quadrupole component. The peaks at the ends of the bending magnet are due to edge focusing. (c) Sextupole component. (d) Octupole component.

$$m_n^i = \frac{1}{s_{i+1} - s_i} \int_{s_i}^{s_{i+1}} \frac{\partial^n B(0, s)}{\partial u^n} \partial s, \tag{19}$$

evaluated about the center of the trajectory $u = 0$. This sequence of sector elements describing the bending magnet model can readily be incorporated in an accelerator lattice model. Because the edge effects are encapsulated by the modeling approach, the individual segments are modeled with higher order multipole components m_n^i.

F. Evaluation of modeling approaches

In the preceding subsections, different analytical approaches were presented for the modeling of a straight, rectangular gradient bending magnet. We propose to compare the measured and modeled momentum compaction factor as an evaluation of these models. As defined in Eq. (10), the momentum compaction factor depends upon both the bending radius $\rho(s)$ and the horizontal dispersion $\eta_x(s)$. In this section, we will determine and evaluate both of these.

The trajectories of each of the four models are plotted in Fig. 9. As illustrated in Figs. 9(b) and 9(c), we compare the four trajectories relative to the initial position $x(z = -1.234)$. The circular trajectory approximation gives the greatest deviation from the numerically evaluated trajectory.

It is easier to see the local changes of the trajectory by inspecting the local bending radius of these four modeling approaches. The bending field $B_0(z)$ of the gradient bending magnet is described by a virtual quadrupole of transverse quadrupole gradient B_1, and hence the dipole field varies in the longitudinal coordinate z by $B_0(z) = B_1 x(z)$. As a result, the local bending radius $\rho(z)$ is given by

$$\rho(z) = p/(q_e B_0) = p/[q_e B_1 x(z)], \tag{20}$$

where p is the momentum of the beam electron. The local bending radii of each of the four models are plotted in Fig. 10. There is longitudinal variation in the bending radius $\rho(z)$, with the highest bending fields corresponding to lower bending radii at large z, as highlighted in Fig. 10(b). This results in a trajectory with greatest bending near the extrema of the bending magnet, and less bending in the center.

We can also compare the lattice parameters [29,43] with bending magnets modeled by the linear hyperbolic and

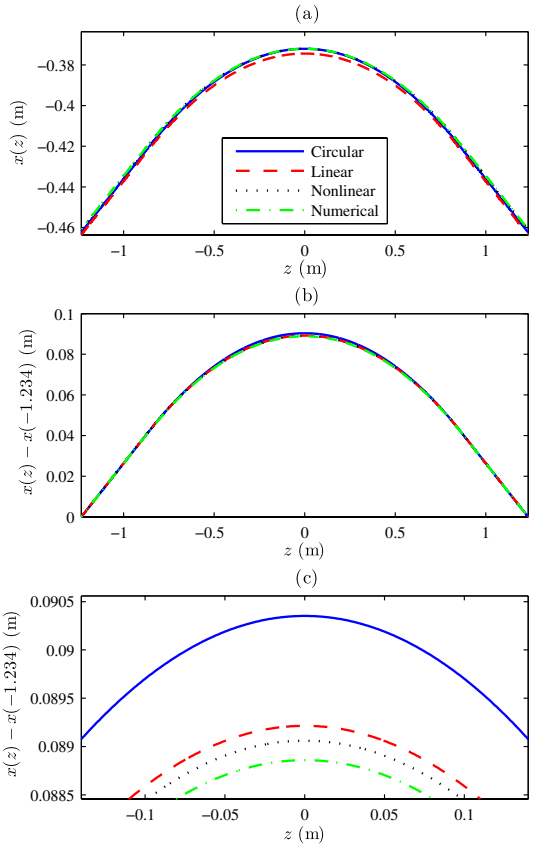

FIG. 9. (a) Electron beam trajectories in coordinates (x, z) for each of the four models described in Sec. IV, with equal entrance and exit angles. (b) Translation in x of trajectories in (a) by $x(z) - x(-1.234)$, to give equal entrance and exit positions and angles for each model. (c) Magnification of trajectories in (b).

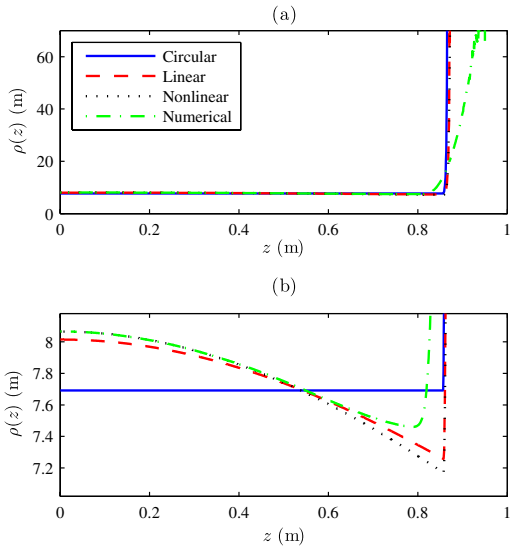

FIG. 10. Bending radius ρ as a function of the longitudinal coordinate z, for each of the four models described in Sec. IV. (a) Bending radius $\rho(z)$ with longitudinal position z, highlighting the longitudinal extent of the fringe field in the numerical model. (b) Magnification of (a), highlighting variation of bending radius within the iron length of the magnet.

numerical trajectories. The storage ring is simulated using the ACCELERATOR TOOLBOX (AT) code [46] for each of the analytical linear model given by Eq. (14), and numerically evaluated bending magnet fields given by Eq. (19). The equation for the path length of the trajectory using these models is given explicitly in Ref. [21]. Linear and numerical models of the trajectory are specifically compared, as the linear method is commonly implemented in accelerator tracking codes, and elements commonly included in accelerator tracking codes can be used to yield the numerically evaluated trajectory. For each model, the three families of storage ring quadrupoles are matched to give the same betatron tunes and horizontal dispersion in the straights. Figure 11 shows the difference between the betatron and dispersion functions for the AS lattice.

We observe in Fig. 11(b) that the solution of quadrupole strengths for matched tunes and dispersion in the center of the straights yields a significant difference in the dispersion and betatron functions. As an input to the momentum compaction factor, we focus on the change in the difference between the dispersion functions, which at the beam position monitor (BPM) in the center of the arc is a peak difference of $\eta_{x\mathrm{NUM}} - \eta_{x\mathrm{L}} = 4.8$ mm. The measured dispersion function $\eta_{x\mathrm{MEAS}}$ is compared to numerical and linear models in Fig. 12.

For the horizontal dispersion shown in Fig. 12, the mean and standard deviation of the difference between the measured and model dispersion of the BPMs in the center of the arcs is for the linear model $\eta_{x\mathrm{MEAS}} - \eta_{x\mathrm{L}} = 5.8 \pm 1.4$ mm, and for the numerical model $\eta_{x\mathrm{MEAS}} - \eta_{x\mathrm{NUM}} = -0.6 \pm 1.4$ mm. Hence, the measured dispersion function agrees with the numerical model to within the limits of this lattice calibration. The difference between the measured dispersion and linear model is attributable to the difference between the linear and numerical models.

As presented in Sec. III D, to evaluate which is a more accurate model of the bending magnet, we have measured the momentum compaction factor to high precision using resonant spin depolarization. Measured and modeled values of the momentum compaction factors of both lattices are compared in Table VIII.

Within the uncertainty of the measurement the momentum compaction factor is shown to agree with the numerical model of the trajectory within the bending magnet, and disagree with the linear hyperbolic cosine approximation. The accuracy of the numerical model comes from using the

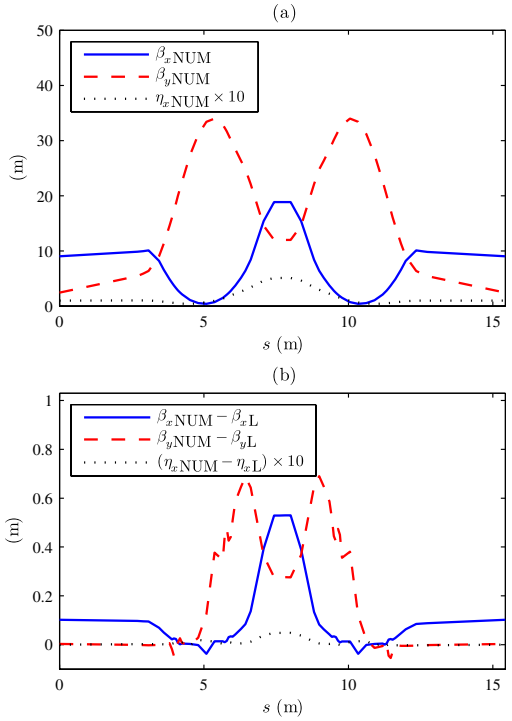

FIG. 11. (a) Lattice functions evaluated using numerical model for trajectory, fitting quadrupoles for the 0.1 m dispersion lattice of the AS [2]. (b) Difference between lattice functions of numerical and linear hyperbolic cosine trajectory.

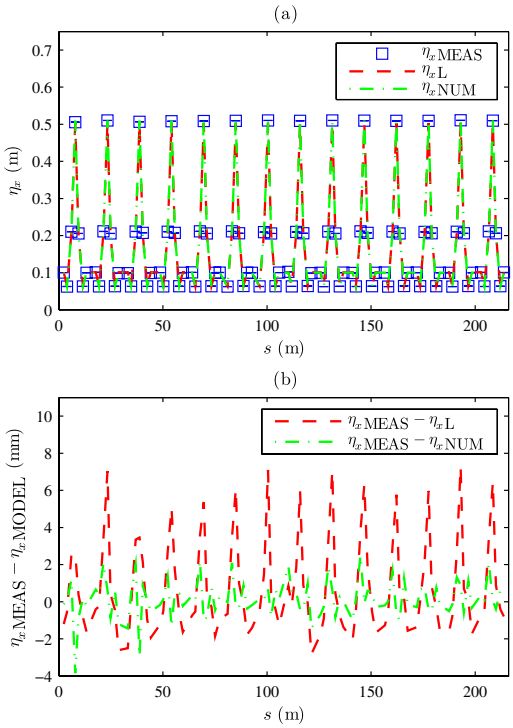

FIG. 12. (a) Measured and model dispersion functions for the AS. (b) Difference between measured dispersion, and dispersion evaluated using linear hyperbolic and numerical trajectory.

TABLE VIII. Momentum compaction factor.

	AS	SPEAR3
Linear hyperbolic cosine	0.00205	0.00162
Numerical	0.00211	0.00165
Measured	0.00211 ± 0.00005	0.00164 ± 0.00001

correct distribution of the dipole field component as illustrated in Figs. 8 and 10, subsequently giving a better model for the horizontal dispersion as illustrated in Fig. 12.

V. DISCUSSION

Resonant spin depolarization has been usefully employed previously at rings to confirm effects principally related to beam energy stability. In the present work, we benefit from the precision of the technique in the calibration of lattice models of gradient dipole magnets. We have compared the momentum compaction factor for analytic linear and numerically evaluated models, and measurements of storage ring lattices incorporating rectangular gradient bending magnets.

As a modeling technique, the numerical evaluation of trajectory could find potential application with various proposed accelerators. The design of present and future third-generation storage ring light sources already consider this approach [22,47]. Ultimate storage ring light sources [24–28] plan to employ gradient dipole magnets as part of a strategy to reduce the equilibrium horizontal emittance.

Fixed-field, alternating gradient accelerators are enjoying a recent resurgence in interest [48]. In particular, scaling lattices employing gradient dipoles [49,50] could find benefits to trajectory and focusing from numerical modeling, as well as nonscaling lattices with real quadrupoles at large transverse offsets [51]. Also, with beams of antiproton species, this modeling approach could prove useful to the Recycler ring at Fermilab [52]. For proton accelerators, this numerical evaluation of trajectory has been demonstrated to natively account for modeling of magnet fringe fields [53].

CONCLUSION

The beam energy was measured for two electron storage rings AS and SPEAR 3 with defocusing gradient bending magnets. Resonant spin depolarization was employed, achieving an uncertainty of order 10^{-6} in the beam energy. To measure the momentum compaction factor, the rf frequency provided an accurate constraint on the circumference of the closed orbit, and resonant spin depolarization an accurate measurement of stored beam energy. Measurements and models of the momentum compaction factor were compared to evaluate analytical and numerical models of the beam trajectory through a defocusing gradient dipole magnet.

Armed with precision measurements, we made a critical evaluation of the suitability of different modeling approaches of the electron beam trajectory. The trajectory through the gradient dipoles is modeled using circular, linear hyperbolic cosine, nonlinear hyperbolic cosine approximations, and numerical integration of the measured magnetic field. Within the uncertainty of the measurement the momentum compaction factor is shown to agree with the numerical model of the trajectory within the bending magnet, and disagree with the hyperbolic cosine approximation. Linear and numerical models of the trajectory are specifically compared, as the linear method is commonly implemented in accelerator tracking codes, and elements commonly included in accelerator tracking codes can be used to yield the numerically evaluated trajectory.

This is an extended article of measurements presented at recent International Particle Accelerator Conferences [41,42].

ACKNOWLEDGMENTS

Portions of this research were carried out at the Stanford Synchrotron Radiation Lightsource, a Directorate of SLAC National Accelerator Laboratory and an Office of Science User Facility operated for the U.S. Department of Energy Office of Science by Stanford University. Parts of this research were undertaken on the storage ring at the Australian Synchrotron, Victoria, Australia. K. P. W. thanks P. Kuske (BESSY), J. Zhang (LAL, Orsay), and I. P. S. Martin (Diamond) for useful discussions at and following IPAC'10 and IPAC'11.

APPENDIX A: DETECTOR CHOICE

The change in beam polarization is observed in the normalized loss rate R_{norm}, given by Eq. (9). Two main approaches are considered in literature: evaluation of the Touschek lifetime from the storage ring DC current

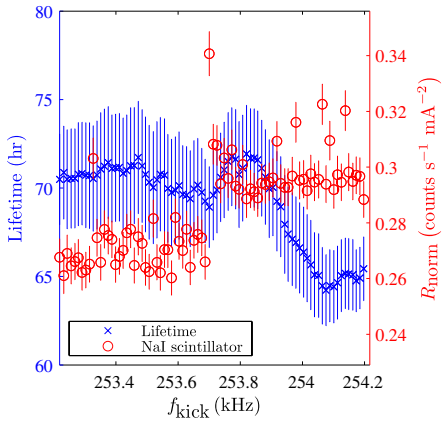

FIG. 13. Resonant depolarization measured for SPEAR3 using NaI scintillator and DCCT, increasing the excitation frequency in time. The lifetime is calculated from 30 samples of the DCCT.

transformer (DCCT), and detection of the electromagnetic shower from Touschek scattered beam particles striking the vacuum chamber when lost [5,54]. Figure 13 presents measurements of a depolarization using each of these techniques.

Figure 13 shows that both approaches could work in the identification of a depolarization. The measured NaI loss monitor count rate responds to the resonant depolarization within 1 s, while calculation of the lifetime with small uncertainty requires approximately 30 s of measurements of the stored beam current and the drop in lifetime is observed approximately 30 s after the depolarization. The beam lifetime is calculated from the time derivative of the stored beam current, while the loss monitor measures the absolute loss rate, which is the derivative of the beam current with respect to time.

For the technique of resonant spin depolarization it is best to have a beam lifetime dominated by Touschek scattering. One of the simplest ways to control this is to alter the fill pattern in the storage ring to maximize the single bunch current.

The beam loss monitor was a 75 mm diameter NaI scintillator and photomultiplier tube at AS, and 50 mm diameter at SPEAR3. For both experiments, the scintillator was installed in the orbit plane of the ring, on the inner side of the vacuum chamber. At SPEAR3, the detector was installed adjacent to the scraper defining the minimum energy aperture of the SPEAR3 storage ring, to maximize the count rate. This is immediately downstream of the central focusing quadrupole, which is the point of maximum horizontal dispersion in one of the double-bend achromat arc cells. At AS, the detector was installed at the upstream end of an insertion straight, where the horizontal dispersion is 0.1 m.

In summary, the change in polarization needs to be quite large to observe the depolarization using the beam lifetime. From a beam physics perspective, large changes of polarization are not necessary to measure the beam energy: one is interested in the precession frequency at which depolarization occurs. The time delay of 20–30 s observed in the beam lifetime measurement compromises this precision measurement of depolarization frequency.

APPENDIX B: DEPOLARIZATION KICKER

Resonant depolarization of the beam is achieved with a magnetic field which is radial in orientation (perpendicular to both the beam trajectory and main bending field), and oscillating sinusoidally in time. Presented in Fig. 14 is the measured loss rate while scanning the excitation frequency. Exciting the beam at a betatron resonance results in a decreased loss rate (increased lifetime) since the bunch vertical size increases, hence the scattering rate decreases. Crossing a spin resonance the count rate increases since the Møller scattering cross section increases when the polarization is reduced.

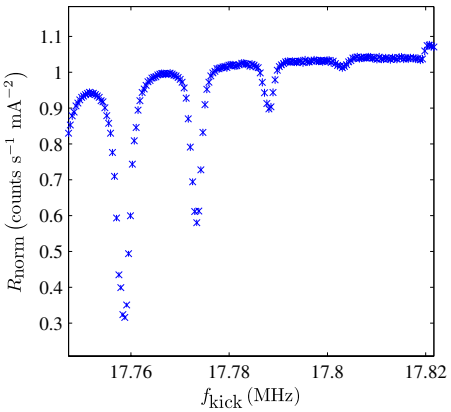

FIG. 14. Measured normalized loss rate resulting from excitation of the beam with a horizontal magnetic field, oscillating sinusoidally in time at the excitation frequency, using the AS storage ring. Large drops in counts correspond to exciting the beam at synchrotron sidebands of the vertical betatron tune. The spin tune was measured as a step increase in normalized loss rate at 17.82 MHz. The vertical axis R_{norm} is normalized according to Eq. (9): the value $R_{\mathrm{norm}} = 1$ has no special significance.

For both rings, the excitation frequency was swept at a rate of 10 Hz s^{-1}. Depolarization is a resonant effect—it is particularly important to scan slowly [6].

[1] J. Corbett, C. Limborg, Y. Nosochov, J. Safranek, and A. Garren, in *Proceedings of European Particle Accelerator Conference 1998* (JACoW, Stockholm, Sweden, 1998), pp. 574–576.
[2] J. W. Boldeman and D. Einfeld, Nucl. Instrum. Methods Phys. Res., Sect. A **521**, 306 (2004).
[3] R. Chasman, G. K. Green, and E. M. Rowe, IEEE Trans. Nucl. Sci. **22**, 1765 (1975).
[4] C. Steier, J. Byrd, and P. Kuske, in *Proceedings of the European Particle Accelerator Conference 2000* (JACoW, Vienna, Austria, 2000), p. MOP5B03.
[5] R. Thornagel, G. Ulm, P. Kuske, T. Mayer, and K. Ott, in *Proceedings of the European Particle Accelerator Conference 1994* (JACoW, London, England, 1994), pp. 1719–1721.
[6] P. Kuske, R. Goergen, J. Kuszynski, and P. Schmid, in *Proceedings of the International Particle Accelerator Conference 2010* (JACoW, Kyoto, Japan, 2010), p. MOPD083.
[7] S. C. Leemann, M. Böge, M. Dehler, V. Schlott, and A. Streun, in *Proceedings of the European Particle Accelerator Conference 2002* (JACoW, Paris, France, 2002), p. TUPRI011.
[8] A.-S. Müller, I. Birkel, E. Huttel, F. Pérez, M. Pont, and R. Rossmanith, in *Proceedings of the European Particle Accelerator Conference 2004* (JACoW, Lucerne, Switzerland, 2004), p. THPKF022.

[9] M. Attal, P. Brunelle, A. Loulergue, A. Nadji, L. Nadolski, and M.-A. Tordeux, Phys. Rev. ST Accel. Beams **16**, 054001 (2013).

[10] R. Belbéoch, M. Bergher, J. Le Duff, M. P. Level, P. Mann, C. Nguyen Ngoc, M. Sommer, and H. Zyngier, in *Proceedings of the Soviet Conference on Charged-Particle Accelerators, Moscow, Russia, 1968* (Israel Program for Scientific Translations, Jerusalem, Israel, 1972), pp. 130–134.

[11] The Orsay Storage Ring Group, in *Proceedings of the 8th International Conference on High-Energy Accelerators* (CERN, Geneva, Switzerland, 1971), pp. 127–131.

[12] S. I. Serednyakov, A. N. Skrinsky, G. M. Tumaikin, and Y. M. Shatunov, Zh. Eksp. Teor. Fiz. **71**, 2025 (1976) [Sov. Phys. JETP **44**, 1063 (1976)].

[13] Y. S. Derbenev, A. M. Kondratenko, S. I. Serednyakov, A. N. Skrinsky, G. M. Tumaikin, and Y. M. Shatunov, Part. Accel. **10**, 177 (1980).

[14] J. R. Johnson, R. Prepost, D. E. Wiser, J. J. Murray, R. F. Schwitters, and C. K. Sinclair, Nucl. Instrum. Methods **204**, 261 (1983).

[15] L. Arnaudon, B. Dehning, P. Grosse-Wiesmann, R. Jacobsen, M. Jonker, J. Koutchouk, J. Miles, R. Olsen, M. Placidi, R. Schmidt, J. Wenninger, R. Assmann, and A. Blondel, Z. Phys. C **66**, 45 (1995).

[16] I. P. S. Martin, M. Apollonio, R. T. Fielder, G. Rehm, and R. Bartolini, in *Proceedings of the International Particle Accelerator Conference 2011* (JACoW, San Sebastian, Spain, 2011), p. TUPC159.

[17] J. Zhang, L. Cassinari, M. Labat, A. Nadji, L. S. Nadolski, and D. Pédeau, in Proceedings of the International Particle Accelerator Conference 2011 (Ref. [16]), p. THPC006.

[18] J. Zhang, L. Cassinari, M. Labat, A. Nadji, L. S. Nadolski, and D. Pédeau, Nucl. Instrum. Methods Phys. Res., Sect. A **697**, 1 (2013).

[19] G. Vignola, Nucl. Instrum. Methods Phys. Res., Sect. A **246**, 12 (1986).

[20] A. Jackson, S. Chattopadhyay, R. Keller, C. Kim, H. Nishimura, F. Selph, and M. Zisman, in *Proceedings of European Particle Accelerator Conference 1988* (JACoW, Rome, Italy, 1988), pp. 359–361.

[21] M. Yoon, J. Corbett, M. Cornacchia, J. Tanabe, and A. Terebilo, Nucl. Instrum. Methods Phys. Res., Sect. A **523**, 9 (2004).

[22] D. Einfeld, M. Belgroune, G. Benedetti, M. D. Lima, J. Marcos, M. Munoz, and M. Pont, in *Proceedings of Particle Accelerator Conference 2007* (JACoW, Albuquerque, NM, 2007), p. TUPMN068.

[23] Y. Chen, D. E. Kim, W. Kang, F. S. Chen, M. Yang, Z. Zhang, B. G. Yin, and J. X. Zhou, Nucl. Instrum. Methods Phys. Res., Sect. A **682**, 85 (2012).

[24] S. C. Leemann, A. Andersson, M. Eriksson, L.-J. Lindgren, E. Wallén, J. Bengtsson, and A. Streun, Phys. Rev. ST Accel. Beams **12**, 120701 (2009).

[25] S. C. Leemann and A. Streun, Phys. Rev. ST Accel. Beams **14**, 030701 (2011).

[26] Y. Nosochkov, K. L. F. Bane, Y. Cai, R. Hettel, and M.-H. Wang, in Proceedings of the International Particle Accelerator Conference 2011 (Ref. [16]), p. THPC075.

[27] M.-H. Wang, Y. Nosochkov, K. Bane, Y. Cai, R. Hettel, and X. Huang, Nucl. Instrum. Methods Phys. Res., Sect. A **649**, 30 (2011).

[28] Y. Cai, K. Bane, R. Hettel, Y. Nosochkov, M.-H. Wang, and M. Borland, Phys. Rev. ST Accel. Beams **15**, 054002 (2012).

[29] E. D. Courant and H. S. Snyder, Ann. Phys. (N.Y.) **3**, 1 (1958).

[30] S. R. Mane, Y. M. Shatunov, and K. Yokoya, Rep. Prog. Phys. **68**, 1997 (2005).

[31] A. A. Sokolov and I. M. Ternov, Dokl. Akad. Nauk SSSR **153**, 1052 (1963) [Sov. Phys. Dokl. **8**, 1203 (1964)].

[32] R. H. Helm, M. J. Lee, P. L. Morton, and M. Sands, in *Proceedings of Particle Accelerator Conference 1973* (JACoW, San Francisco, CA, 1973), pp. 900–901.

[33] V. Bargmann, L. Michel, and V. L. Telegdi, Phys. Rev. Lett. **2**, 435 (1959).

[34] B. Odom, D. Hanneke, B. D'Urso, and G. Gabrielse, Phys. Rev. Lett. **97**, 030801 (2006).

[35] P. J. Mohr, B. N. Taylor, and D. B. Newell, Rev. Mod. Phys. **84**, 1527 (2012).

[36] A. W. Chao and M. Tigner, *Handbook of Accelerator Physics and Engineering* (World Scientific Publishing, Singapore, 1999).

[37] V. N. Baier and V. A. Khoze, At. Energ. **25**, 440 (1968) [Sov. J. At. En. **25**, 1256 (1968)].

[38] G. W. Ford and C. J. Mullin, Phys. Rev. **108**, 477 (1957).

[39] G. W. Ford and C. J. Mullin, Phys. Rev. **110**, 1485 (1958).

[40] C. Bernardini, G. F. Corazza, G. Di Giugno, G. Ghigo, J. Haissinski, P. Marin, R. Querzoli, and B. Touschek, Phys. Rev. Lett. **10**, 407 (1963).

[41] H. P. Panopoulos, K. P. Wootton, M. J. Boland, and R. P. Rassool, in Proceedings of the International Particle Accelerator Conference 2011 (Ref. [16]), p. TUPC062.

[42] K. P. Wootton, M. J. Boland, R. P. Rassool, Y.-R. E. Tan, W. J. Corbett, M. Donald, X. Huang, R. R. Ortiz, J. A. Safranek, and K. Tian, in *Proceedings of the International Particle Accelerator Conference 2012* (JACoW, New Orleans, 2012), p. MOPPR001.

[43] E. D. Courant, M. S. Livingston, and H. S. Snyder, Phys. Rev. **88**, 1190 (1952).

[44] H. Wiedemann, *Particle Accelerator Physics* (Springer-Verlag, Berlin, Germany, 2007), 3rd ed.

[45] X. Huang, J. A. Safranek, and D. Dell Orco, in Proceedings of the International Particle Accelerator Conference 2010 (Ref. [6]), p. THPE048.

[46] A. Terebilo, *Accelerator Toolbox for MATLAB* (Stanford Linear Accelerator Center, Stanford University, Stanford, CA, 2001).

[47] X. R. Resende, R. Basílio, L. Liu, P. P. Sanchez, and G. Tosin, in Proceedings of the International Particle Accelerator Conference 2012 (Ref. [42]), p. MOPPC053.

[48] S. Machida *et al.*, Nat. Phys. **8**, 243 (2012).

[49] G. H. Rees, D. J. Kelliher, S. Machida, C. R. Prior, and S. L. Sheehy, in Proceedings of the International

Particle Accelerator Conference 2012 (Ref. [42]), p. MOPPD020.
[50] S. L. Sheehy, K. J. Peach, H. Witte, D. J. Kelliher, and S. Machida, Phys. Rev. ST Accel. Beams **13**, 040101 (2010).
[51] K. J. Peach *et al.*, Phys. Rev. ST Accel. Beams **16**, 030101 (2013).
[52] M. Xiao, in Proceedings of the International Particle Accelerator Conference 2012 (Ref. [42]), p. TUPPR085.
[53] J. G. Wang, Nucl. Instrum. Methods Phys. Res., Sect. A **722**, 87 (2013).
[54] V. N. Baĭer, Usp. Fiz. Nauk **105**, 441 (1971) [Sov. Phys. Usp. **14**, 695 (1972)].

Observation of Picometer Vertical Emittance with a Vertical Undulator

K. P. Wootton,[1,*] M. J. Boland,[1,2] R. Dowd,[2] Y.-R. E. Tan,[2] B. C. C. Cowie,[2] Y. Papaphilippou,[3] G. N. Taylor,[1] and R. P. Rassool[1]

[1]*School of Physics, The University of Melbourne, Melbourne VIC 3010, Australia*
[2]*Australian Synchrotron, 800 Blackburn Road, Clayton VIC 3168, Australia*
[3]*European Organization for Nuclear Research (CERN), BE Department, 1211 Geneva 23, Switzerland*

(Received 11 July 2012; published 8 November 2012)

Using a vertical undulator, picometer vertical electron beam emittances have been observed at the Australian Synchrotron storage ring. An APPLE-II type undulator was phased to produce a horizontal magnetic field, which creates a synchrotron radiation field that is very sensitive to the vertical electron beam emittance. The measured ratios of undulator spectral peak heights are evaluated by fitting to simulations of the apparatus. With this apparatus immediately available at most existing electron and positron storage rings, we find this to be an appropriate and novel vertical emittance diagnostic.

DOI: 10.1103/PhysRevLett.109.194801 PACS numbers: 29.27.−a, 41.60.−m, 41.75.Ht, 41.85.Lc

In recent years, storage ring light sources and damping rings have produced electron and positron beams of diminishing vertical size [1–3]. Beams of unprecedented small size are demanded particularly for electron-positron colliders at both the energy [4] and intensity frontiers [5]. With vertical dimensions of several μm, direct measurement of beam size is approaching diffraction limits of visible light and hard x-ray diagnostics [6]. We report on the development of a new vertical electron beam size measurement technique which utilizes a vertical undulator. Vertical undulators are rare [7]—typically beams are deflected in the horizontal plane. In this work, an elliptically polarized undulator was phased as a vertical undulator. We present direct observation of μm vertical beam sizes corresponding to picometer radian (pm rad) vertical beam emittances, and remark that this technique is immediately achievable using existing photon beam lines of electron storage ring light sources.

The spectral and angular profile of undulator radiation is especially sensitive to the transverse emittance [8], defined as an envelope in position-angle phase space of the electron beam ensemble. Projections of the angular profile of undulator harmonics can be used to characterize the beam emittance. This has been demonstrated using a soft x-ray undulator producing a vertical field [9], referred to as a horizontal undulator because the beam is deflected in that transverse direction.

Previous analytical descriptions and modeling of undulator brilliance focused on determination of the absolute photon beam brilliance [8], and identified the brilliance of even harmonics as especially sensitive to the transverse emittance [10], using a horizontal undulator. The absolute photon beam brilliance is a difficult quantity to measure. A novel technique has been previously proposed, measuring the ratio of intensities of the first and second undulator harmonics and comparing with simulations of photon brilliance [11,12]. We present measurements of the stored electron beam size by expanding this idea and taking the ratios of many adjacent pairs of odd and even harmonics.

This technique shares similarities with another projection measurement of vertical emittance [1,13] but differs by passing, as opposed to masking, the on-axis null radiation field. Illustrated in Fig. 1 are simulated transverse profiles of the intensity of undulator radiation. Instead of trying to measure the absolute photon flux of the on-axis null field of the even harmonics, F_{n-1}, we calibrate this low flux against the high-flux peaks of the odd harmonics passing the same aperture, F_n. The ratio of fluxes of

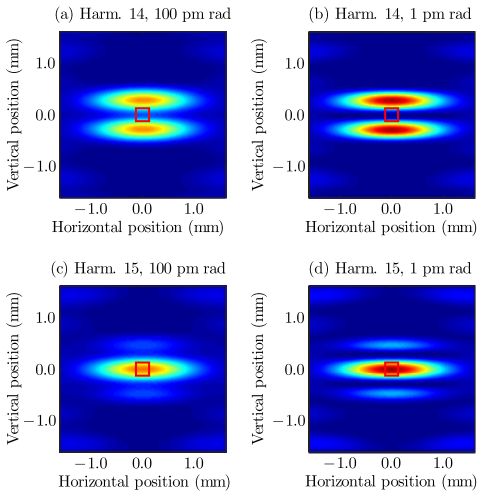

FIG. 1 (color online). SPECTRA [22] simulation of profile of undulator radiation 15 m from the undulator center, with the 250×250 μm rectangular pinhole aperture outline marked in red. (a) Harmonic 14, 100 pm emittance. (b) Harmonic 14, 1 pm emittance. (c) Harmonic 15, 100 pm emittance. (d) Harmonic 15, 1 pm emittance.

TABLE I. Electron beam and undulator properties used in simulation.

	Parameter	Value	Units
	Beam		
E_0	Energy	3.0	GeV
σ_E	Energy spread	0.11	%
ε_x	Horizontal emittance	10	nm rad
	Undulator		
λ_u	Period length	75	mm
B_u	Peak field	0.55	T
K_u	Deflection parameter	3.8	...
N_u	Number of full periods	25	...

adjacent undulator harmonics F_{n-1}/F_n is evaluated. For Fig. 1, the ratio of flux passing for the even 14th to odd 15th harmonics is $F_{n-1}/F_n = 0.42$ for a beam of 100 pm rad geometric vertical emittance shown in (a) and (c), and 0.17 for 1 pm rad shown in (b) and (d).

The undulator used was an Advanced Planar Polarized Light Emitter (APPLE-II) type undulator [14,15]. Properties of the electron beam and undulator are summarized in Table I below. The magnetic arrays of the undulator were phased to produce a horizontal field, deflecting the electron beam in the vertical plane. A gap of 17.1 mm was selected—close to the minimum gap—producing a peak horizontal field of 0.55 T. Magnetic measurements of the undulator during acceptance demonstrate that in the configuration for vertical polarization at minimum gap, the axis of the undulator field is within -6 ± 30 mrad of the nominal horizontal orientation [15].

Vertical emittance growth due to undulator self-dispersion was calculated [16], for the stated undulator and the normal Australian Synchrotron user lattice with 0.1 m distributed horizontal dispersion in the insertion straights. For a device of 2 m length, we calculate an emittance increase due to vertical self-dispersion of $\Delta\epsilon_y = 0.012$ pm rad, which is well below the lowest achieved vertical emittance in this ring of $\epsilon_y \approx 1$–2 pm rad [2], and indeed below the quantum limit of vertical emittance.

The APPLE-II undulator serves the soft x-ray user beam line of the Australian Synchrotron [17]. After closing the undulator to its operating gap, the storage ring skew quadrupoles were optimized for a range of emittance configurations using the linear optics from closed orbits (LOCO) routine [18]. The measured undulator spectra are presented in Fig. 2 for vertical emittances from 2.6 ± 1.1 pm rad in blue up to 1750 ± 330 pm rad in red.

We measure the photon flux passing an on-axis pinhole. The pinhole used is four blades of the white-beam slits, closed to form a rectangular pinhole aperture of approximately 250×250 μm. We choose an aperture which is small in both the horizontal and vertical dimensions, to minimize any contribution from the horizontal emittance. At a distance of 15.0 m from the undulator center, it passes undulator radiation within an opening angle of $\theta = 1.7 \times 10^{-5}$ rad.

Undulator measures of emittance typically assume the weak undulator limit $K_u \leq 1$, producing beams within a central cone of radius $\theta_{\max} \approx 0.3(K_u/\gamma)$ [10]. In the strong undulator limit $K_u > 1$, the cone approximation breaks down. With odd harmonic number $n > 3$ and $n \geq (N_u/3)$, the half angle of the first interference minima is given by [19,20]

$$\theta_{\max} = \frac{K_u}{\gamma}\frac{\pi}{2n}\frac{(1 + K_u^2/2)}{(1 + 2K_u^2)}. \quad (1)$$

Using Eq. (1) for $n = 15$ and parameters of Table I, we place an upper limit on the pinhole half angle radius of $\theta_{\max} = 0.029(K_u/\gamma)$. This corresponds in Fig. 3 to the maximum in ratio F_{14}/F_{15} for pinhole offset, and pinhole half-apertures greater than this exhibiting no sensitivity to vertical emittance. The ratio of fluxes is optimized by minimizing the vertical offset of the pinhole. This is achieved experimentally by scanning the pinhole vertically through the interference pattern for the unambiguous

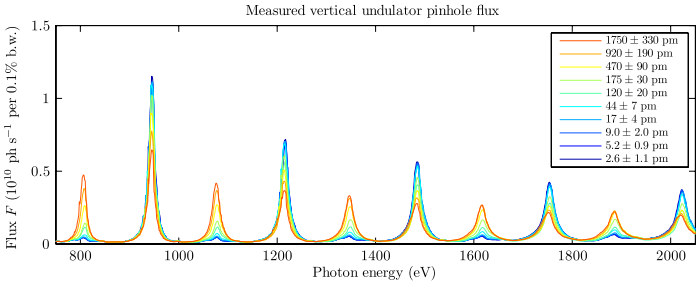

FIG. 2 (color online). Measured undulator spectra for vertical emittances calibrated with LOCO, from minimum in blue up to maximum in red. Shown in order of increasing photon energy are undulator harmonics 6–15. Small vertical emittances (blue) exhibit lowest intensity at even harmonics and highest intensity at odd harmonics. High vertical emittances (red) exhibit equal intensities at both even and odd harmonics.

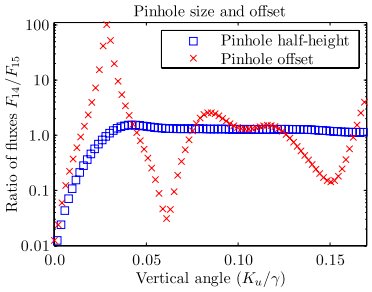

FIG. 3 (color online). Flux ratio dependence for vertical emittance 0 pm rad, harmonics 14 and 15, and beam parameters of Table I. A centered pinhole of half-height is illustrated in blue, and vertical offset of a pinhole of 50 μm in red. An angle of $0.10(K_u/\gamma) \equiv 1.0$ mm vertical position at 15 m, cf. Figs. 1(b) and 1(d).

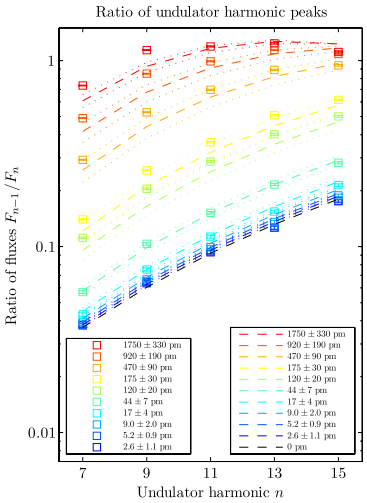

FIG. 4 (color online). Model 261×261 μm pinhole fitted to experimental data. Measured undulator peaks marked as squares, fitted SPECTRA simulations denoted by dashed contours increasing from lower flux ratios corresponding to lower emittances in blue, up to higher flux ratios in red. The simulated contour of a beam with zero vertical emittance is shown in black. Uncertainties of measured ratios shown as error bars, and dotted contours for fitted model.

intensity maximum of an odd undulator harmonic, as illustrated in Fig. 1(d).

The existing beam line optics were used for the spectrometer. The beam line employs a linear grating for the monochromator, and several gold-coated toroidal mirrors to focus the beam. The M absorption edges of the gold coatings restrict our studies to photon energies below 2200 eV. The spectrometer grating and all focussing mirrors are positioned downstream of the aperture. A second aperture was used to select a single grating diffraction order. Background was subtracted by measuring the photon flux with the undulator open to its maximum gap. The drain current of a silicon photodiode was detected, from which photon flux was calculated [21]. We calculate and present the photon flux on an absolute scale in Fig. 2; however, in the evaluation of the ratio arbitrary units would suffice.

Using the SPECTRA code [22], the flux of monochromated undulator radiation passing a pinhole was simulated. The dimensions of the pinhole used in measurements were not available due to inaccuracies in motor lash. To extract these dimensions from our data, we fit a single free parameter using all data sets simultaneously—the vertical dimension of the pinhole. Envelopes of beam emittance corresponding to LOCO measurements were fitted to the measured peak ratios, minimizing the χ^2 test statistic. These ratios of F_{n-1}/F_n harmonics are presented in Fig. 4. The χ^2 test statistic is minimized for a pinhole of 261×261 μm. We have chosen to fit emittance contours based on global LOCO emittances; however, this emittance monitor is intrinsically local to one point in the ring. Hence the apparent emittance measured may vary from the global projected emittance [23], for some contours of Fig. 4.

Uncertainties are presented in Fig. 4 corresponding to both the measured undulator spectra and fitted emittance envelopes. The fitted envelopes and uncertainties correspond to the beam emittance evaluated using LOCO. Uncertainties in measured ratios were evaluated from scans of the background flux with the undulator open to its maximum gap, nominally bending magnet edge radiation. This was measured more than an order of magnitude lower than the minimum undulator flux.

The major finding of this work is that the ratios of undulator pinhole flux can be used to measure vertical emittance. A vertical undulator appears to be an appropriate vertical emittance diagnostic in storage rings attempting to achieve lowest vertical emittance.

It is suggested in literature that such a technique should be possible for the measurement of horizontal emittance [11], but no published measurements have been found. It is also suggested that F_{n-1}/F_n should tend to zero for beams of zero transverse emittance [11]. Shown in Fig. 4 are envelopes of measured and simulated emittance ratios, including the envelope for zero vertical electron beam emittance. This envelope highlights the distinction between electron beam size and the size of the photon source, which in the limit of zero electron beam size is defined by the amplitude of undulator oscillations. The photon beam source size measured using this ratio technique is the convolution of the rms undulator deflection with the electron beam transverse dimension [24].

Advantages of the technique are the ability to exploit the linearity in detector response over a photon energy range spanning keV, and decades of intensity. The measurement of a ratio—as opposed to absolute photon beam

brilliance—absolves of the need for measurement of photon flux on an absolute scale.

The major uncertainty in the technique is the pinhole dimension. Future experiments to measure the vertical emittance should consider using a pinhole of known diameter. We fitted all spectra with a single free parameter being the pinhole dimension; however, with this fixed the free parameter becomes the electron beam size. The dependence of the flux ratio upon pinhole vertical offset and size is illustrated in Fig. 3 for a beam of 0 pm rad vertical emittance.

The effect of energy spread on peak width has previously been quantified [11,25]. In simulation, we consider the effect of energy spread on peak height. Increasing the relative energy spread by 25%, we find that the measured peak height ratio does not exceed uncertainties in the measured peak ratios for beams with vertical emittance less than 200 pm rad (approximately 2% emittance ratio). The energy spread can be constrained within an uncertainty of 11% from measurements of the bunch length σ_t,

$$\sigma_t = 2\pi f_s |\gamma^{-2} - \alpha_c| \sigma_E. \quad (2)$$

The momentum compaction factor α_c and synchrotron frequency f_s can both be measured within 2% uncertainty using resonant spin depolarization [26] and a spectrum analyzer, respectively. The bunch length can be measured within 7% uncertainty using a calibrated streak camera and removing chromatic effects [27] with a band pass filter. Hence uncertainty in electron beam energy spread should not limit the application of this technique.

Closing an undulator in the vertical direction has the effect of increasing the vertical dispersion of the electron beam. Our calculations, following [16], show that the increase is orders of magnitude lower than the quantum limit. It would be interesting to consider using the vertical undulator as a vertical emittance damping wiggler.

In conclusion, the observation of pm rad vertical emittance electron beams has been demonstrated using a vertical undulator. The difference between pm rad vertical emittance beams is resolvable using this technique. Exploiting a precision photon beam line, the measured ratios of on-axis pinhole flux agree closely with simulations. With a pinhole of fixed diameter, this technique should yield quantitative measurements of the electron beam vertical emittance.

This research was undertaken using the soft x-ray beam line and storage ring at the Australian Synchrotron, Victoria, Australia.

*k.wootton@student.unimelb.edu.au

[1] M. Aiba, M. Böge, N. Milas, and A. Streun, Nucl. Instrum. Methods Phys. Res., Sect. A **694**, 133 (2012).
[2] R. Dowd, M. Boland, G. LeBlanc, and Y.-R. E. Tan, Phys. Rev. ST Accel. Beams **14**, 012804 (2011).
[3] Y. Honda, *et al.*, Phys. Rev. Lett. **92**, 054802 (2004).
[4] Editorial, Nature (London) **456**, 422 (2008).
[5] A. Cho, Science **321**, 34 (2008).
[6] J. Flanagan, in *Proceedings of International Particle Accelerator Conference 2011* (JACoW, San Sebastian, Spain, 2011), p. WEYB01.
[7] T. Tanaka, X.-M. Maréchal, T. Hara, T. Tanabe, and H. Kitamura, J. Synchrotron Radiat. **5**, 414 (1998).
[8] G. Dattoli, G. K. Voykov, and M. Carpanese, Phys. Rev. E **52**, 6809 (1995).
[9] T. Moreno, E. Otero, and P. Ohresser, J. Synchrotron Radiat. **19**, 179 (2012).
[10] G. Dattoli and G. Voykov, Nuovo Cimento B **111**, 743 (1996).
[11] M. Bakeman, W. Leemans, K. Nakamura, K. Robinson, C. Schroeder, and C. Toth, in *Proceedings of Particle Accelerator Conference 2009* (JACoW, Vancouver, BC, Canada, 2009), p. WE6RFP074.
[12] M. Bakeman, E. Esarey, W. P. Leemans, K. Nakamura, J. Osterhoff, K. Robinson, C. B. Schroeder, J. van Tilborg, C. Toth, F. Gruner, and R. Weingartner, in *Proceedings of Particle Accelerator Conference 2011* (JACoW, New York, NY, USA, 2011), p. MOP161.
[13] Å. Andersson, M. Böge, A. Lüdeke, V. Schlott, and A. Streun, Nucl. Instrum. Methods Phys. Res., Sect. A **591**, 437 (2008).
[14] S. Sasaki, Nucl. Instrum. Methods Phys. Res., Sect. A **347**, 83 (1994).
[15] C. Ostenfeld, F. Bødker, M. Pedersen, E. Christensen, M. Bøttcher, and H. Bach, in *Proceedings of Particle Accelerator Conference 2007* (JACoW, Albuquerque, New Mexico, USA, 2007), p. TUPMN006.
[16] H. Wiedemann, Nucl. Instrum. Methods Phys. Res., Sect. A **266**, 24 (1988).
[17] B. C. Cowie, A. Tadich, and L. Thomsen, AIP Conf. Proc. **1234**, 307 (2010).
[18] J. Safranek, Nucl. Instrum. Methods Phys. Res., Sect. A **388**, 27 (1997).
[19] C. Leubner and P. Torggler, Opt. Commun. **48**, 362 (1984).
[20] R. Walker, Nucl. Instrum. Methods Phys. Res., Sect. A **335**, 328 (1993).
[21] M. Krumrey, L. Büermann, M. Hoffmann, P. Müller, F. Scholze, G. Ulm, and T. Warwick, AIP Conf. Proc. **705**, 861 (2004).
[22] T. Tanaka and H. Kitamura, J. Synchrotron Radiat. **8**, 1221 (2001).
[23] A. Franchi, L. Farvacque, J. Chavanne, F. Ewald, B. Nash, K. Scheidt, and R. Tomás, Phys. Rev. ST Accel. Beams **14**, 034002 (2011).
[24] K.-J. Kim, AIP Conf. Proc. **184**, 565 (1989).
[25] J. G. Gallacher, *et al.*, Phys. Plasmas **16**, 093102 (2009).
[26] H. Panopoulos, K. Wootton, M. Boland, and R. Rassool, in *Proceedings of International Particle Accelerator Conference 2011* (JACoW, San Sebastian, Spain, 2011), p. TUPC062.
[27] T. Obina and T. Mitsuhashi, in *Proceedings of Diagnostics and Instrumentation for Particle Accelerators 2007* (JACoW, Venice, Italy, 2007), p. WEPB12.

VERTICAL UNDULATOR EMITTANCE MEASUREMENT: A STATISTICAL APPROACH

K.P. Wootton*, R.P. Rassool, School of Physics, University of Melbourne, VIC, Australia
M.J. Boland, B.C.C. Cowie, R. Dowd, Australian Synchrotron, Clayton, VIC, Australia

Abstract

Direct measurement of low vertical emittance in storage rings is typically achieved via interferometric techniques. Proof of low vertical emittance is demonstrated by the measurement of a null radiation field, which is also the crux of the vertical undulator emittance measurement. Here we present strategies to improve the sensitivity to low vertical emittance beams. We move away from photon spectrum analysis to a statistical analysis of undulator radiation, showing the measured increase in signal-to-background. Reproducing simulations of previous work, we demonstrate that photon beam polarisation extends the linearity of the technique by several decades in emittance. These statistical and polarisation improvements to the signal-to-background allow realistic measurement of smallest vertical emittance.

INTRODUCTION

Measurements and simulations of vertical emittance using a vertical undulator are presented. In previous work, vertical undulators were observed as highly sensitive to the electron beam vertical emittance [1,2]. In order to measure beams of smallest vertical emittance, a concerted effort has been made to understand and minimise systematic and statistical uncertainties.

ORBIT BUMPS

One of the most significant systematic uncertainties in this flux measurement is the size and transverse position of the pinhole mask. In particular, the technique is sensitive to vertical transverse offsets of the pinhole [1].

The technique employed previously aimed to simultaneously minimise the size and centring of the pinhole formed by closing four white beam blades. Instead in this work the blades are closed to the minimum possible aperture, and transverse orbit bumps are performed of the electron beam through the insertion device to optimise centring. The pinhole flux measured in vertical angular bumps through the insertion device is illustrated in Fig. 1, and for small amplitude bumps around the diffraction pattern central lobe in Fig. 2. The small angular bumps through the insertion device are used to recover the angular distribution of undulator radiation. As an approximation, the angular distribution of undulator radiation can be fitted by the double-slit

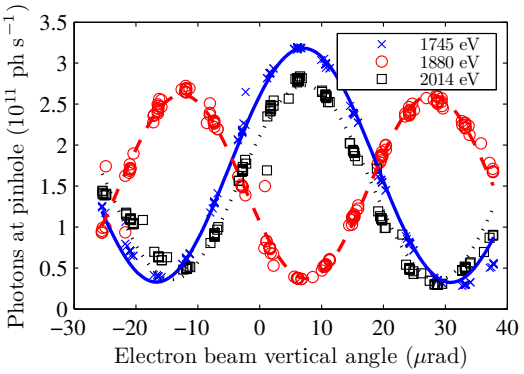

Figure 1: Insertion device photon flux measured and fitted for orbit bumps through the insertion device. Photon energies correspond to undulator harmonics 13, 14 and 15.

diffraction distribution [3]

$$I(\theta_y) = I(0)\,\mathrm{sinc}^2\left(\frac{2\pi\sigma_y\theta_y}{\lambda R_1}\right) \times \left[1+\gamma\cos\left(\frac{2\pi\sigma_r\theta_y}{\lambda R_1}+\phi\right)\right], \quad (1)$$

where λ is the photon beam wavelength, R_1 the distance between the undulator and pinhole, σ_y is the electron beam vertical size, σ_r the transverse deflected amplitude of the electron beam in the undulator, γ the magnitude of the complex degree of spatial coherence, θ_y the angle of the orbit bump (or angle of observation of the photon beam) and ϕ an arbitrary phase offset (odd harmonic, $\phi \approx 0$, even harmonic, $\phi \approx \pi$). The transverse oscillation amplitude of the electron beam in the undulator is approximated by a double slit.

Fitting for the undulator radiation distribution, the angle of the electron beam through the insertion device can be varied to recover the angular distribution of undulator radiation, illustrated for small angles in Fig. 2.

REPEATED ACQUISITIONS

Statistical uncertainty in a measurement can be minimised by making repeated independent measurements of a single quantity [4]. We aim to measure the photon flux passing through a pinhole, for a given stored electron beam current. To compensate for the decaying electron beam current, the quantity measured here is photodiode drain cur-

* k.wootton@student.unimelb.edu.au

ISBN 978-3-95450-127-4

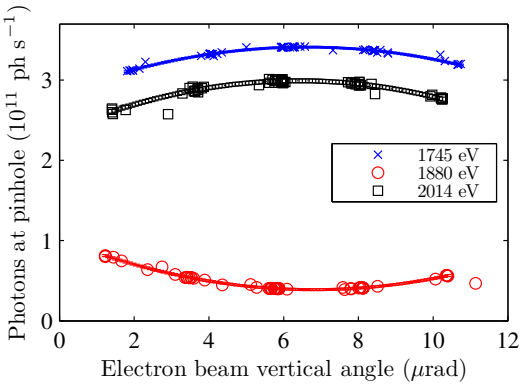

Figure 2: Measured and fitted vertical profile of undulator radiation through orbit bump. Photon energies correspond to undulator harmonics 13, 14 and 15.

rent, normalised to a nominal 200 mA stored beam current by the measured DCCT current. For n repeat measurements Gaussian-distributed about some mean value μ, the standard uncertainty in the estimate of the mean $\delta\mu$ is given by [4]

$$\delta\mu = \frac{\sigma}{\sqrt{n}}, \tag{2}$$

where σ is the standard deviation of measured values. The interpretation of this statement is that as the number of samples n is increased, the measured mean converges toward the true mean of the distribution. For comparison, in Figs. 3 and 4 the measured relative standard deviation is shown for 12 and 80 acquisitions, over various acquisition ranges and times. Figures 3 and 4 highlight that over appropriate

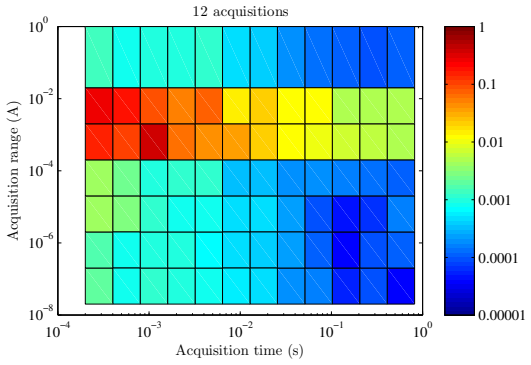

Figure 3: Relative standard uncertainty in diode current measured using a picoammeter over 12 acquisitions, for various acquisition times and current ranges. The mean diode current measured was approximately 1.1×10^{-7} A. The highest current range shown is the auto range. Colour scale shows measured $(\delta\mu/\mu)$.

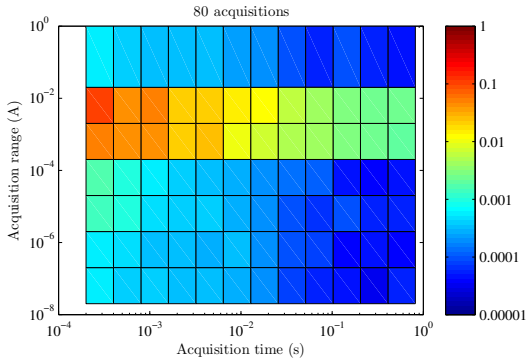

Figure 4: Relative standard uncertainty in diode current measured using a picoammeter over 80 acquisitions, for various acquisition times and current ranges. The mean diode current measured was approximately 1.1×10^{-7} A. The highest current range shown is the auto range. Colour scale shows measured $(\delta\mu/\mu)$.

choices of acquisition range, statistical uncertainty in the measured pinhole flux can be an insignificant contribution to the uncertainty in measured pinhole flux.

PHOTON POLARISATION

One approach in the minimisation of systematic uncertainties is by selective observation of the polarisation components of the photon beam flux. This was first outlined for a proposed SPring-8 vertical undulator measurement of vertical emittance [5]. The intensity of horizontal I_x and vertical I_y linear polarised light is described in terms of the Stokes parameters by [6]

$$I_x = 1 \times S_0 + 1 \times S_1 + 0 \times S_2 + 0 \times S_3, \tag{3}$$
$$I_y = 1 \times S_0 - 1 \times S_1 + 0 \times S_2 + 0 \times S_3, \tag{4}$$

where the Stokes parameters are defined in terms of the intensity of light with respect to polarisation orientations S_1 denotes linear polarisation, S_2 linear at 45°, and S_3 circular polarisation [7],

$$S_0 = 2I_0, \tag{5}$$
$$S_1 = 2I_1 - 2I_0, \tag{6}$$
$$S_2 = 2I_2 - 2I_0, \tag{7}$$
$$S_3 = 2I_3 - 2I_0. \tag{8}$$

We have undertaken simulations of the undulator brilliance using the SPECTRA code [8]. The code returns several polarisation parameters in the form,

$$I_0 = S_0, \tag{9}$$
$$PL = S_1/S_0, \tag{10}$$
$$PL45 = S_2/S_0, \tag{11}$$
$$PC = S_3/S_0. \tag{12}$$

ISBN 978-3-95450-127-4

Hence, we can calculate the intensities of horizontally and vertically polarised light as given by Eq. 3, 4 by

$$I_x = I_0(1 + S_1/S_0), \quad (13)$$
$$I_y = I_0(1 - S_1/S_0). \quad (14)$$

This simulation is presented in Fig. 5 for an ideal sinusoidal undulator and beam with parameters matching our experimental conditions [1]. It is seen that a significant contribution to the on-axis brilliance of even harmonics arises from horizontally polarised light. The ratio of fluxes for the 14^{th} and 15^{th} undulator harmonics with varying emittance is presented in Fig. 6. It can be seen that the measurement

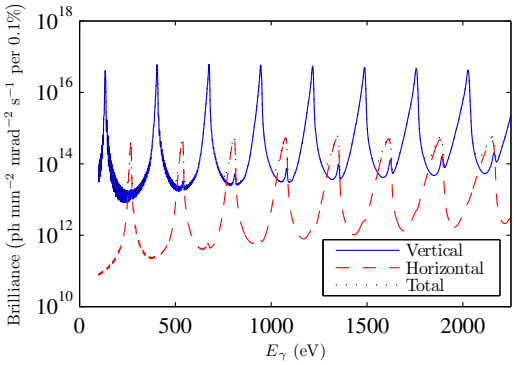

Figure 5: SPECTRA simulation [8] of spectral brilliance assuming an ideal undulator magnetic field, for horizontal and vertical photon polarisations. Vertical emittance $\varepsilon_y = 1$ pm rad.

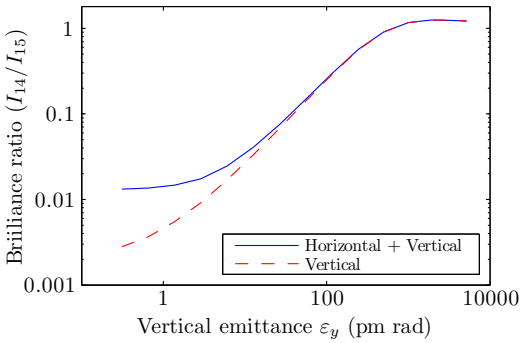

Figure 6: SPECTRA simulation [8] of the flux ratio of adjacent undulator harmonics, for total flux and vertical polarisation alone.

of the vertically polarised component of undulator radiation extends the linearity of the measurement technique to lowest vertical emittances. The next stage of investigation will be to repeat these brilliance calculations with measured magnetic fields of the insertion device, to account for phase errors of a real device.

CONCLUSION

The measurement of a null radiation field is the crux of this vertical emittance measurement. Techniques are presented to minimise sources of statistical and systematic uncertainty. To reconstruct the angular distribution of undulator radiation, transverse orbit bumps of the electron beam are promising, as is the rejection of horizontal polarised photons for the measurement of lowest vertical emittance.

ACKNOWLEDGEMENTS

KPW thanks S. Takano (SPring-8), C. Bloomer and E. Longhi (Diamond) for useful discussions at and following IBIC'12. This research was undertaken on the soft x-ray beamline on the storage ring at the Australian Synchrotron, Victoria, Australia.

REFERENCES

[1] K.P. Wootton, et al. Phys. Rev. Lett. **109** (19), 194801 (2012).

[2] K.P. Wootton, et al. Proceedings of IBIC 2012, Tsukuba, Japan, MOCB04 (2012).

[3] M. Katoh and T. Mitsuhashi, Proceedings of PAC 1999, New York, USA, WEP22, March, (1999).

[4] Evaluation of measurement data – Guide to the expression of uncertainty in measurement, Bureau International des Poids et Mesures, JCGM 100:2008, September (2008), http://www.bipm.org/en/publications/guides/gum.html.

[5] S. Takano, 'On emittance diagnostics of electron beam by observing synchrotron radiation from a vertical undulator', Proceedings of Workshop on Precise Measurements of Electron Beam Emittances, KEK Proceedings 97-20, 18-19 October, 1997 (1998).

[6] G. G. Stokes, Trans. Cambridge. Phil. Soc. **9** (3), 399–416 (1852).

[7] E. Hecht, *Optics, 4ed.*, Pearson Education, San Francisco, CA, USA (2002).

[8] T. Tanaka and H. Kitamura, J. Synch. Rad. **8**, 1221 (2001).

ISBN 978-3-95450-127-4

APPLE-II UNDULATOR MAGNETIC FIELDS CHARACTERISED FROM UNDULATOR RADIATION

K.P. Wootton*, R.P. Rassool, School of Physics, University of Melbourne, VIC, Australia
M.J. Boland, B.C.C. Cowie, Australian Synchrotron, Clayton, VIC, Australia

Abstract

The spatial profile of APPLE-II undulator radiation has been measured at high undulator deflection parameter, high harmonic and very small emittance. Undulators are typically designed to operate with small deflection parameter to push the fundamental mode to high photon energies. This unusual choice of parameters is desirable for measurement of vertical emittance with a vertical undulator.

We present 1-D and 2-D measured profiles of undulator radiation and show that this is reproduced in numerical models using the measured magnetic field of the insertion device. Importantly these measurements confirm that for these parameters, the spatial intensity distribution departs significantly from usual Gaussian approximations, instead resembling a double-slit diffraction pattern. This could be an important consideration for photon beamlines of ultimate storage ring light sources.

INTRODUCTION

Crucial to the vertical undulator emittance measurement technique we have developed is the availability of a high deflection parameter vertical undulator [1, 2]. At the Australian Synchrotron, we use an APPLE-II elliptically polarising undulator in a magnet phase configuration for vertically polarised light [3, 4]. The parameters of these experiments are summarised in Table 1.

Table 1: Undulator and Electron Beam Parameters for Experiment and Simulation

Parameter	Value
Electron beam energy	3.033 GeV
Beam energy spread	0.0011
Horizontal emittance	10 nm rad
Vertical emittance (nominal)	100 pm rad
Undulator K	3.85
Undulator period length	75 mm
Number of full periods	25
First harmonic photon energy	134.7 eV

UNDULATOR MAGNETIC FIELD

The model used in our previous analyses of the emittance measurements assumed an ideal horizontal, sinusoidal electron beam trajectory though the undulator. An improved model is presented which accounts for the deleterious effects of phase errors on the electron beam trajectory, using the measured magnetic field of the insertion device. The magnetic field profile of this APPLE-II insertion device was measured at the time of acceptance, at the design magnetic gap of 16.0 mm [4]. The magnetic field was measured along the device centreline with a three-axis Hall probe. Lamentably, at the time of writing we possess no equipment at the Australian Synchrotron with which to measure insertion device magnetic fields ourselves. For the purposes of safe clearance of the electron

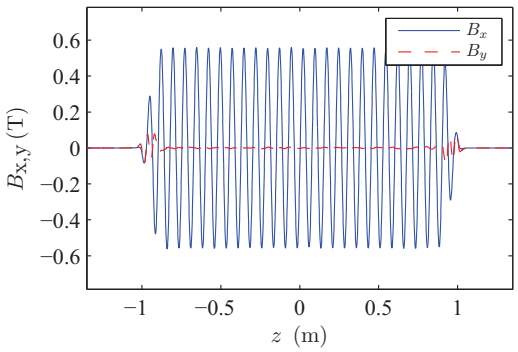

Figure 1: Magnetic field of APPLE-II insertion device in vertical polarisation mode, scaled from Hall probe measurements [4].

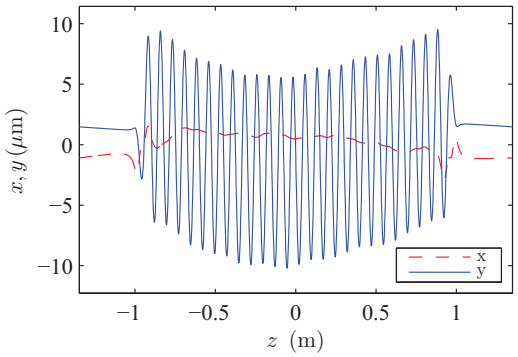

Figure 2: Trajectory of a 3 GeV electron beam through measured magnetic field map of Fig. 1 [4], calculated using SPECTRA [5].

* k.wootton@student.unimelb.edu.au

ISBN 978-3-95450-127-4

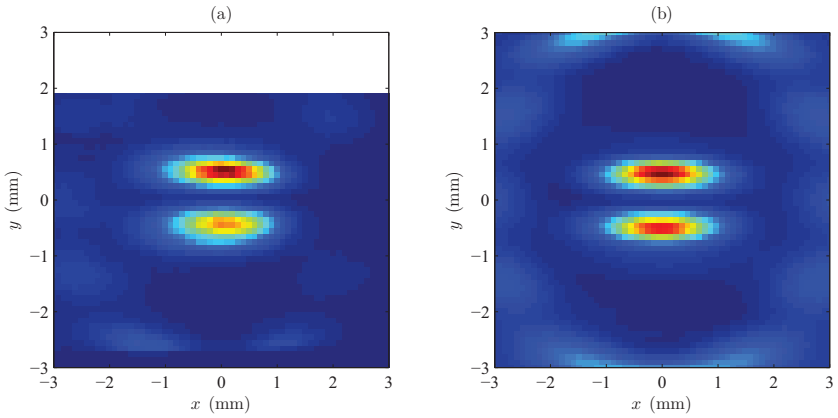

Figure 3: Spatial profile of undulator radiation from a vertical undulator, 15 m downstream of the insertion device. (a) Measured spatial profile of 6^{th} undulator harmonic, at 808 eV. (b) SPECTRA [5] simulation of spatial profile of 6^{th} undulator harmonic, at 808 eV. The magnetic field profile of Fig. 1 was used for the simulation of the insertion device.

beam vacuum chamber, we limit the minimum operating gap to 17.0 mm, and these experiments are conducted with a gap of 17.1 mm. To compensate for this in our model, the magnitude of the measured magnetic field components at a gap of 16.0 mm have been scaled down. The field was scaled down until the simulated on-axis peaks of the undulator harmonics were at the same photon energies as the measured spectrum. This scaled field is presented for the horizontal B_{x} and B_{y} components in Fig. 1.

The synchrotron radiation code SPECTRA was used to simulate light produced by the insertion device [5]. Using the field illustrated in Fig. 1, the trajectory of a 3 GeV electron was calculated and is shown in Fig. 2.

PINHOLE SCANS (2-D)

The angular distribution of spontaneous radiation from an undulator is theoretically described [6–8]. Devices of interest to storage ring lightsources typically employ undulators of small deflection parameter ($K \approx 1$), and prefer to use low undulator harmonics to achieve high photon beam brilliance. Figure 3 presents measurements and simulations of the projection of undulator radiation from this APPLE-II undulator.

The beamline used for these experiments does not have a pinhole for characterising the spatial profile of radiation [9]. Several other beamlines do, for this specific purpose [10]. Instead, we close four blades of the white-beam slits to form a rectangular pinhole aperture, which are scanned to measure the profile of Fig. 3. A photodiode which captures the full beam passed by the white-beam slits was used for this measurement.

The important features of Fig. 3 are the central two lobes of the 6^{th} harmonic, and the outer ring of the 7^{th} harmonic. This narrow interference pattern is characteristic of undulator radiation, but is seldom observed. Storage ring light sources typically operate with very large horizontal emittances of order nm rad, convolving the narrow angular distribution of undulator radiation with the broad horizontal beam emittance. The interference pattern is observed here specifically because of the vertical deflection by the undulator and the low vertical emittance of order pm rad.

Integrating over the central 3 mm width of the distribution in Fig. 3, the vertical profile of undulator radiation at 808 eV is presented in Fig. 4.

Figure 4 highlights that the measured vertical asymmetry in the distribution of undulator radiation is partially accounted for by using the measured magnetic field distribution in simulations. The central on-axis null at $y = 0$ mm is similarly well-described.

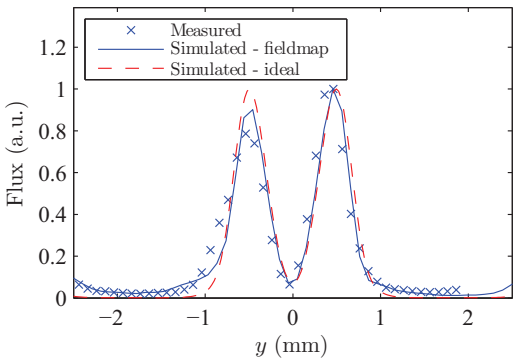

Figure 4: Vertical profile of undulator radiation in Fig. 3. The intensity is integrated over $x = -1.5$ mm to 1.5 mm.

ISBN 978-3-95450-127-4

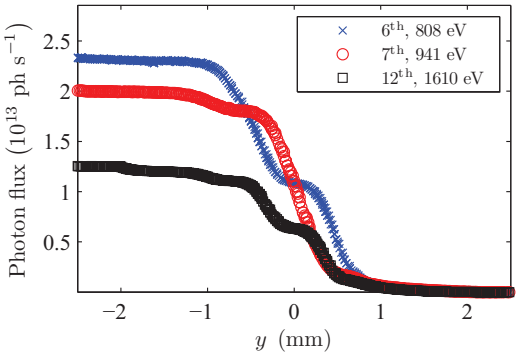

Figure 5: Measured undulator radiation intensity blade scans at different undulator harmonics. The lower white-beam slit is scanned vertically upwards from $y < 0$ to $y > 0$.

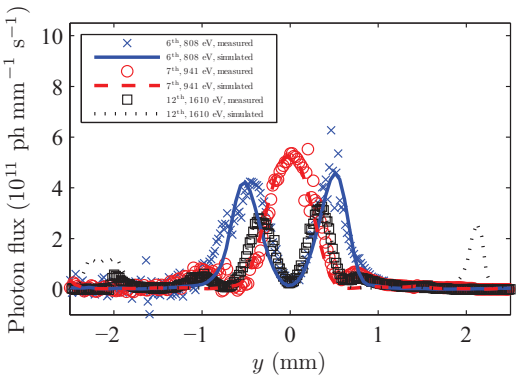

Figure 6: Gradient of Fig. 5 with respect to vertical blade scan direction. The vertical profile of undulator radiation is recovered and is compared to simulation. Compare also with Fig. 4.

BLADE SCANS (1-D)

The spatial profile of radiation was characterised in the vertical direction alone using blade scans. With a horizontal aperture of 0.5 mm, the lower blade of the white beam slits was stepped vertically upwards through the radiation distribution. The change in measured photon flux through the aperture with blade position is plotted in Fig. 5. Taking the derivative of this distribution with respect to the vertical position of the blade, the intensity distribution of undulator radiation is recovered. This is plotted in Fig. 6.

DISCUSSION

These measurements confirm assumptions regarding the spatial distribution of undulator radiation, which is sensitive to vertical emittance. The angular distribution of undulator radiation departs from usual Gaussian approximations, and at such low emittances resembles a narrow interference diffraction pattern. This is observed because the vertical emittance is so small relative to the transverse deflection of the undulator in the vertical direction.

Low emittance light sources are beginning to produce undulator radiation of interesting spatial distributions [10]. As electron beam light sources approach diffraction limits, the spatial distribution of radiation may become a topic of interest. Diffraction-limited ultimate storage rings are currently proposed with horizontal emittance of order 100 pm rad [11–13]. Such proposals should be aware of the diffraction-limited spatial distribution of undulator radiation, and its departure from usual Gaussian-approximated, emittance dominated photon beams.

CONCLUSION

The spatial distribution of radiation from a vertical insertion device has been characterised at very low vertical emittance. Both 2-D and 1-D spatial distributions of radiation have been measured, using a combination of blade scans. Simulations of the insertion device radiation are given, using a magnetic field distribution scaled from the measured field. It is shown that these simulations accurately reproduce the measured photon beam distribution. This close agreement between simulation and experiment is important both for the vertical emittance undulator technique, and potentially also for insertion devices at proposed ultimate storage ring light sources.

ACKNOWLEDGEMENTS

KPW is very grateful for useful discussions with Takashi Tanaka (SPring-8) in the implementation of measured magnetic field distributions within the SPECTRA code. This research was undertaken on the soft x-ray beamline on the storage ring at the Australian Synchrotron, Victoria, Australia.

REFERENCES

[1] K.P. Wootton, et al., Phys. Rev. Lett. **109** (19), 194801 (2012).

[2] K.P. Wootton, et al., Proceedings of IBIC 2012, Tsukuba, Japan, MOCB04 (2012).

[3] S. Sasaki, Nucl. Instrum. Methods A **347**, 83 (1994).

[4] C. Ostenfeld, et al., Proceedings of PAC 2007, Albuquerque, USA, TUPMN006, June (2007).

[5] T. Tanaka and H. Kitamura, J. Synch. Rad. **8**, 1221 (2001).

[6] H. Motz, J. Appl. Phys. **22**, 527 (1951).

[7] K.-J. Kim, Nucl. Instrum. Methods A, **246** 67 (1986).

[8] H. Wiedemann, Particle Accelerator Physics, 3rd ed., Springer-Verlag, Berlin, Germany (2007).

[9] B. C. Cowie, A. Tadich, and L. Thomsen, AIP Conf. Proc. **1234**, 307 (2010).

[10] J. Bahrdt, et al., Phys. Rev. Lett., **111**, 034801 (2013).

ISBN 978-3-95450-127-4

[11] M. Bei, et al., Nucl. Instrum. Methods A **622**, 518 (2010).

[12] Y. Shimosaki, et al. Proceedings of IPAC 2012, New Orleans, USA, TUPPC014, May (2012).

[13] L. Farvacque, et al. Proceedings of IPAC 2013, Shanghai, China, MOPEA008, May (2013).

ISBN 978-3-95450-127-4

VERTICAL EMITTANCE MEASUREMENTS USING A VERTICAL UNDULATOR

K.P. Wootton*, M.J. Boland, G.N. Taylor, R.P. Rassool,
School of Physics, University of Melbourne, VIC, Australia
M.J. Boland, B.C.C. Cowie, R. Dowd, Y.-R.E. Tan, Australian Synchrotron, Clayton, VIC, Australia
Y. Papaphilippou, CERN, BE Department, Geneva, Switzerland

Abstract

We have reported on initial work to measure vertical emittance using a vertical undulator. Using simulations, we motivate the important experimental subtleties in the application of this technique. Preliminary measurements of undulator spectra are presented that demonstrate the high sensitivity of vertical undulators to picometre vertical emittances. Finally, possible future applications of this technique are explored.

INTRODUCTION

Electron storage ring light sources and damping rings continue to produce beams of increasingly small vertical emittance. With the recent report of the minimum observed vertical emittance of $\varepsilon_y = 0.9 \pm 0.4$ pm rad at the SLS [1], we require techniques sensitive to sub-micrometre electron beam sizes. At the Australian Synchrotron, we have developed a technique for measuring the vertical emittance of electron beams that we call vertical undulator emittance measurement [2].

In these proceedings, we assess undulators as a beam diagnostic. In contrast to horizontal undulators being largely insensitive to picometre vertical emittance, we highlight the sensitivity of vertical undulators to the vertical emittance. We present preliminary results and simulations, as well as ideas for future vertical emittance diagnostics.

THEORY

Undulators have been used as diagnostics of storage ring emittance. Horizontal undulators – undulators that deflect the electron beam in the orbit plane of the ring – have been demonstrated to give excellent measurement of the horizontal beam size and energy spread [3–7]. Where the electron beam emittance is close to fully-coupled, the brilliance of horizontal undulators exhibits some sensitivity to the vertical emittance [4]. Electron storage and rings typically design for transverse emittance ratios less than a few percent, with damping ring designs aiming for minimum vertical emittance. In this low vertical emittance limit horizontal undulators are identified as particularly insensitive to vertical emittance, limited by the single-electron opening angle of undulator radiation [3].

* k.wootton@student.unimelb.edu.au

Photon Beam Brilliance

Modelled in SPECTRA [8], the sensitivity of horizontal and vertical undulators to vertical emittance is illustrated in Figure 1 below.

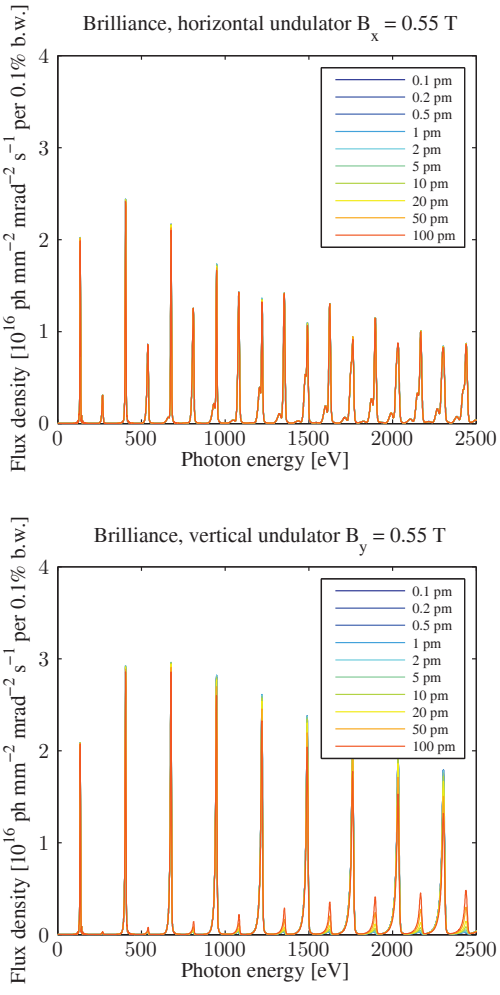

Figure 1: Photon beam brilliance, for horizontal undulator and vertical undulator of deflection parameter $K = 3.85$, for ASLS user lattice with $\eta_x = 0.1$ m in the insertion [9].

ISBN 978-3-95450-119-9

Figure 1 illustrates the photon beam brilliance for horizontal and vertical undulators of equal deflection parameter. Over a range of operational vertical emittances there is no measurable change in brilliance for a horizontal undulator. However we see that for a vertical undulator, at high even undulator harmonics, the photon beam brilliance changes by orders of magnitude. Hence, measurements of the photon beam brilliance at the even harmonics exhibit a strong dependence upon the electron beam emittance [10].

To measure the brilliance of these harmonics, we consider the angular distribution of undulator radiation. In Figure 2 we present simulations [8] of the vertical profile of a horizontal undulator, and a vertical undulator in Figure 3.

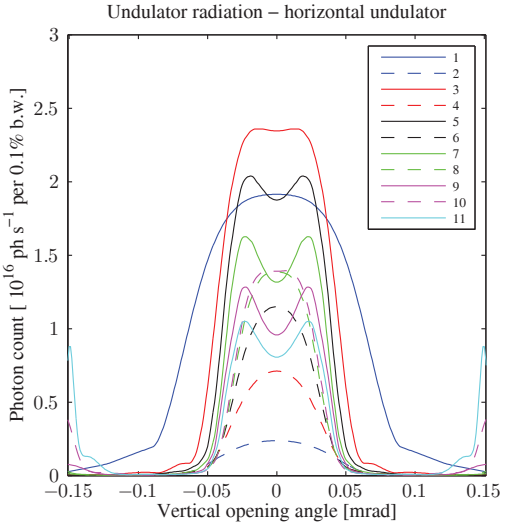

Figure 2: Simulated vertical profile of undulator harmonics, horizontal undulator. Vertical emittance $\varepsilon_y = 1$ pm rad.

For a fixed, low vertical emittance of $\varepsilon_y = 1$ pm rad and horizontal emittance $\varepsilon_x = 10$ nm rad, Figures 2–3 exemplify the difference between the horizontal and vertical direction of undulation. With undulations in the horizontal direction in Figure 2, we see the incoherent superposition of spontaneous undulator radiation from a beam with a comparatively large horizontal emittance.

In Figure 3 however, the small simulated vertical emittance of $\varepsilon_y = 1$ pm rad is indicative of the single-electron distribution of undulator radiation. The narrow spatial distribution of the interference pattern created at each undulator harmonic is of $\sin^2\theta$ distribution for odd harmonics, and $\cos^2\theta$ distribution for even harmonics. Hence an on-axis pinhole aperture passing a narrow angular distribution above and below the orbit plane of the undulator passes a maximum flux for odd undulator harmonics, and minimum for even harmonics, as illustrated in Figure 1.

The beam emittance is evaluated as a ratio of peak flux in the even harmonic to that of the adjacent odd harmonic.

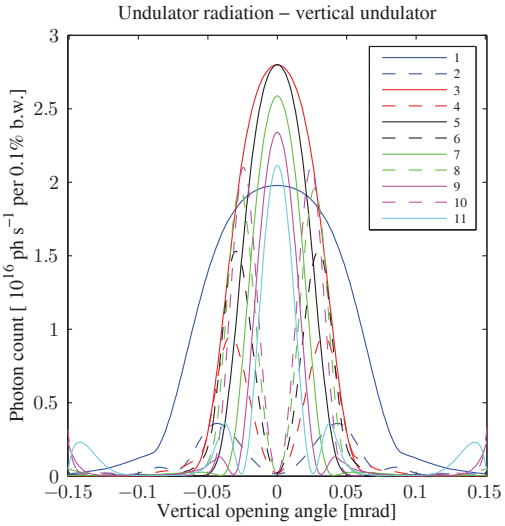

Figure 3: Simulated vertical profile of undulator harmonics, vertical undulator. Vertical emittance $\varepsilon_y = 1$ pm rad. Around $\theta_y \approx 0$, the narrow interference peaks of the even and odd harmonics are well-separated in amplitude.

This idea has also been proposed for measurement of horizontal beam emittance in plasma wakefield accelerated electron beams [6, 7].

METHOD

We measure the undulator flux passing an on-axis pinhole. The pinhole is formed by closing white-beam slits on the beamline. As a spectrometer, we utilise the soft x-ray user beamline [11, 12].

Vertical Emittance

A calibrated model of the storage ring lattice was measured using orbit response matrix analysis, and fitted using the LOCO technique [13]. The electron beam vertical emittance was adjusted by optimising skew quadrupole magnets in the lattice model [14].

Photodiode

The preliminary measurements presented in Figures 4 – 5 were made using a Hamamatsu G1963 GaP/Au Schottky photodiode. The diode was selected as it is installed on the beamline as a standard diagnostic of photon flux. The responsivity of the photodiode was calculated over the relevant range of photon energies [15]. Over the desired photon energy range, the responsivity for this type of diode exhibits large discontinuities at absorption edges. To avoid this, use of a doped silicon photodiode should be considered.

ISBN 978-3-95450-119-9

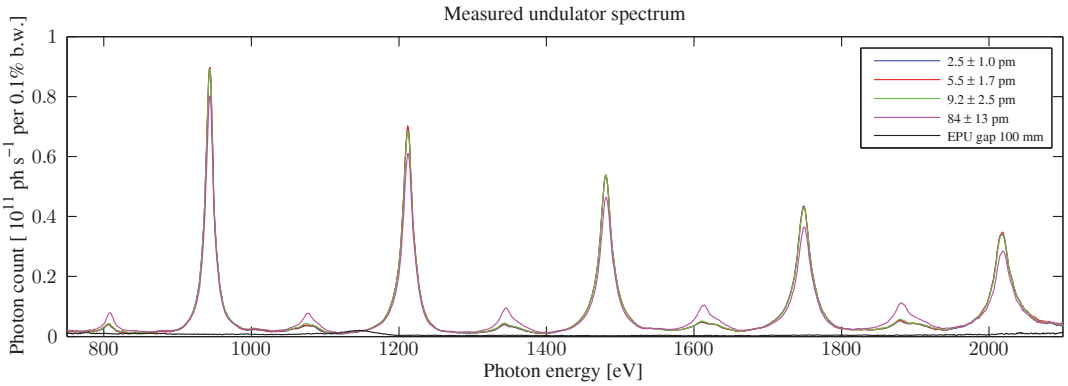

Figure 4: Measured vertical undulator flux passing an on-axis pinhole.

RESULTS

Measured Undulator Spectra

The measured undulator spectra are plotted in Figure 4 above. Four vertical emittance lattice configurations were considered, with the undulator closed to a gap of 17.1 mm, close to the minimum gap. This corresponds to an undulator deflection parameter of $K = 3.85$. The sensitivity of this technique to small vertical emittances is illustrated in Figure 5 below. The even undulator harmonics 6 – 14 are shown on an expanded vertical scale, to highlight the measurable separation in intensity of undulator spectra between beams of several picometre vertical emittance.

Background Flux

The background was estimated by measuring the photon flux with the undulator open to 100 mm, close to the maximum gap. This is shown in black on Figures 4 – 5. With the undulator open to 100 mm, the first undulator harmonic is shown in the measured spectrum at 1140 eV, and is not a background feature.

Measured Flux Ratio

The ratio of fluxes of adjacent harmonics is evaluated for 10 and 11. The results are summarised in Table 1 below. The vertical emittance and corresponding uncertainty was evaluated using orbit response matrix analysis. Uncertainty in the corresponding ratio of fluxes is estimated from systematics in measurement of the background flux, as well as statistical uncertainties. This measured ratio can be compared with simulation of the apparatus, however to extract a meaningful measurement of the emittance, the vertical dimension of the pinhole must be known. It can be seen that for this unknown pinhole dimension, that picometre beam emittances are resolvable at the level of a factor of two.

Table 1: Measured Flux Ratio F_{10}/F_{11}

ε_y [pm rad]	F_{10}/F_{11}
84 ± 13	0.204 ± 0.006
9.2 ± 2.5	0.083 ± 0.005
5.5 ± 1.7	0.078 ± 0.005
2.6 ± 1.0	0.074 ± 0.005

DISCUSSION

Future diagnostics and applications of vertical undulators to synchrotron light source storage rings are summarised.

SOLEIL DiagOn

Recently, direct of projections of undulator harmonics have been measured at SOLEIL [16]. Designed as a beam diagnostic for APPLE-II insertion devices, the reported DiagOn device measures the distribution of horizontally-polarised undulator radiation at a fixed photon energy. By rotating the device around the beam axis to pass photons of vertical polarisation, the inteference pattern at fixed energy could be measured to observe the vertical emittance.

Vertical Undulator

As an aside to emittance measurement, vertical undulators may be used with existing storage rings to provide a more brilliant photon source. As shown in Figure 1 the brilliance of high, odd undulator harmonics is a factor of two greater for the undulator in the vertical rather than horizontal configuration, at vertical emittances of several pm rad. These small vertical emittances are achievable at many storage ring light sources.

ISBN 978-3-95450-119-9

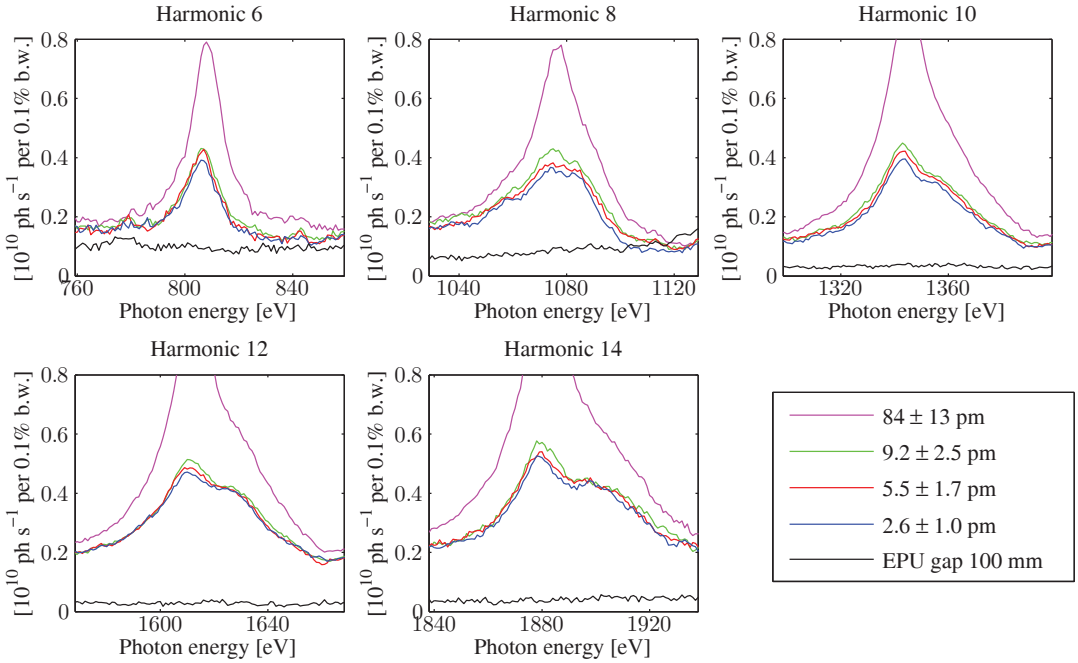

Figure 5: Even harmonics shown on expanded vertical scale, with background subtracted. The even harmonics 6 – 14 are illustrated for vertical emittances of 2.5, 5.2, 9.2 and 84 pm rad. Also shown in black is the undulator spectrum measured with the EPU open to 100 mm, for which the photon energy of the first harmonic is $E_{\mathrm{ph}} = 1140$ eV.

CONCLUSION

We have reported on initial work to measure vertical emittance using a vertical undulator. Using simulations, we demonstrate the usefulness of vertical undulators as a diagnostic for vertical emittance. Preliminary measurements of undulator spectra are presented that demonstrate the high sensitivity of vertical undulators to picometre vertical emittances. Future applications of this technique are explored, notably the possibility of imaging the interference pattern at a fixed photon energy.

ACKNOWLEDGEMENTS

This research was undertaken on the soft x-ray beamline on the storage ring at the Australian Synchrotron, Victoria, Australia.

REFERENCES

[1] M. Aiba, M. Böge, N. Milas, and A. Streun, Nucl. Instrum. Methods A **694**, 133 (2012)

[2] K.P. Wootton, M.J. Boland, R. Dowd, Y.-R.E. Tan, B.C.C. Cowie, Y. Papaphilippou, G.N. Taylor, and R.P. Rassool. Manuscript submitted for publication.

[3] E. Tarazona and P. Elleaume, Rev. Sci. Instrum. **67** (9), 3368-3368 (1996)

[4] Å. Andersson, et al., Proceedings of EPAC 1998, Stockholm, Sweden, WEP05J, June (1998)

[5] B.X. Yang and J.J. Xu, Proceedings of PAC 2001, Chicago, USA, WPAH108, June (2001)

[6] M. Bakeman, et al., Proceedings of PAC 2009, Vancouver, Canada, WE6RFP074, May (2009)

[7] M. Bakeman, et al., Proceedings of PAC 2011, New York, USA, MOP161, March (2011)

[8] T. Tanaka and H. Kitamura, J. Synch. Rad. **8**, 1221 (2001)

[9] G.S. LeBlanc, M.J. Boland and Y.-R.E. Tan, Proceedings of EPAC 2004, Lucerne, Switzerland, THPKF005, July (2004)

[10] G. Dattoli and G. Voykov, Il Nuovo Cimento B **111**, 743 (1996)

[11] B. C. Cowie, A. Tadich, and L. Thomsen, AIP Conf. Proc. **1234**, 307 (2010)

[12] C. Ostenfeld, et al., Proceedings of PAC 2007, Albuquerque, USA, TUPMN006, June (2007)

[13] J. Safranek, Nucl. Instrum. Methods A **388**, 27 (1997)

[14] R. Dowd, et al., Phys. Rev. ST Accel. Beams **14**, 012804 (2011)

[15] M. Krumrey and E. Tegeler, Rev. Sci. Instrum., **63** (1), 797 (1992)

[16] T. Moreno, E. Otero, and P. Ohresser, J. Synch. Rad. **19**, 179 (2012)

ISBN 978-3-95450-119-9

RESONANT SPIN DEPOLARISATION MEASUREMENTS AT THE SPEAR3 ELECTRON STORAGE RING

K.P. Wootton[1*], M.J. Boland[1,2], R.P. Rassool[1], Y.-R.E. Tan[2], W.J. Corbett[3], M. Donald[3], X. Huang[3], R.R. Ortiz[3], J.A. Safranek[3], K. Tian[3].
[1] School of Physics, University of Melbourne, VIC 3010, Australia
[2] Australian Synchrotron, Clayton, VIC, Australia
[3] SLAC National Accelerator Laboratory, Menlo Park, CA 94025, USA

Abstract

Accurate electron beam energy measurements are valuable for precision lattice modelling of high-brightness light sources. At SPEAR3 the beam energy was measured using the resonant spin depolarisation method with striplines to resonantly excite the spin tune and a sensitive NaI scintillator beam loss monitor to detect resulting changes in Touschek lifetime. Using the combined apparatus an electron beam energy of 2.997251 (7) GeV was measured, a relative uncertainty of 3×10^{-6}.

The measured momentum compaction factor was found to be in close agreement with the numerical model value using rectangular defocussing gradient dipoles with measured magnetic field map profiles. In this paper we outline the chosen experimental technique, with emphasis on its applicability to electron storage rings in general.

INTRODUCTION

Experimental verification of storage ring lattice models requires a very sensitive technique for beam energy measurement. As the highest available precision technique, resonant spin depolarisation was successfully employed for the beam energy measurement of the Australian Synchrotron storage ring [2]. We apply this measurement apparatus and technique to the SPEAR3 electron storage ring at SLAC.

THEORY

With specific reference to the literature review of Mane [1], much of the relevant theory for this resonant spin depolarisation experiment at SPEAR3 is the same as for the experiment at the Australian Synchrotron [2].

Serendipitously, the polarisation of electron beams in storage rings is a diagnostic tool we get for free. A beam of electrons with spins of random orientations develops polarisation under the Sokolov-Ternov effect [3]. The polarisation of the ensemble of spins develops with time, in addition to precession about the polarisation axis - normally in the direction of the main dipole field.

The polarisation time of electrons in an isomagnetic lattice is described in SI-units by [3]

$$(\tau_{ST})^{-1} = \frac{5\sqrt{3}}{8}\frac{1}{4\pi\epsilon_0}\frac{e^2\hbar}{m_e^2c^2}\frac{\gamma^5}{\rho^3}, \qquad (1)$$

where ρ is the bending radius, γ the relativistic gamma, m_e the electron rest mass, and all other symbols have their usual electromagnetic meanings [4]. The SPEAR3 racetrack lattice is configured with bending magnets of different bending radii, as well as reverse bends in a long canted-undulator straight. Integrating all bending fields over one turn of the non-isomagnetic ring [1],

$$\frac{1}{\rho^3} = \frac{1}{2\pi R}\oint \frac{1}{|\rho(s)^3|}ds. \qquad (2)$$

This is equivalent to the third synchrotron radiation integral divided by the circumference of the ring.

METHOD

Storage Ring Lattice and Beam

The SPEAR3 storage ring is a 3 GeV storage ring light source, with DBA lattice cells. The racetrack lattice is composed of 14 main arc cells, and 4 matching cells. Several important design parameters are summarised in Table 1. A normal user beam fill pattern was used, and all insertion devices were open for this measurement of the bare lattice.

Table 1: SPEAR3 Storage Ring Design Parameters

Parameter			Value	Units
Beam energy		E	3.00	GeV
Relativistic γ		γ	5871	-
Bending radius	- arc	ρ	8.14	m
	- match	ρ	8.25	m
Circumference		C	234.143	m
RF frequency		f_{RF}	476.30	MHz

Depolarisation Kicker and Polarimeter

Vertical betatron tune striplines were used to excite the spin tune resonance. Scanning over the baseband spin tune resonance, the excitation frequency was approximately 250 kHz.

The beam loss monitor was a 50 mm NaI scintillator and photomultiplier tube. The detector was installed adjacent to the scraper defining the minimum energy aperture of the SPEAR3 storage ring, to maximise the count rate. This is immediately downstream of the central focussing quadrupole, which is the point of maximum horizontal dispersion in one of the double-bend achromat arc cells. The

* k.wootton@student.unimelb.edu.au

ISBN 978-3-95450-115-1

scintillator was installed in the orbit plane of the ring, on the inner side of the vacuum chamber.

Data Acquisition System

The data acquisition system used at the Australian Synchrotron [2] was employed for this measurement. Using EPICS, the frequency of time-stamped data acquisition was approximately 1 record per second.

A Struck 3820 scaler was used to count the excitation frequency, as well as the counts from the beam loss monitor. The scaler features a 50 MHz internal reference clock, for accurate determination of the integration period (typically 1 s). The revolution frequency was determined from the RF frequency, and the stored beam current from the DCCT readback.

RESULTS

Polarisation Time

The beam loss apparatus was used to measure the polarisation time. The injected beam was initially unpolarised. The measured normalised loss rate illustrated in Figure 1 was fitted for the Sokolov-Ternov polarisation time given in Equation 1. Using Equation 1 and parameters in Table 1 we also calculated the model value. The results are summarised in Table 2 below.

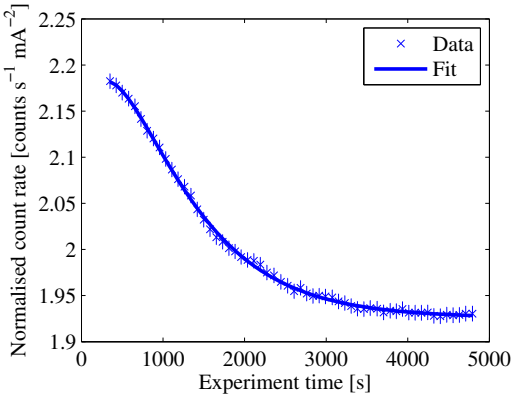

Figure 1: Measurement of polarisation time. Fit to normalised count rate gives $\tau_{pol} = 840 \pm 16$ s.

Table 2: Polarisation Time

Parameter		Value	Units
Measured	τ_{ST}	840 (16)	s
Model	τ_{ST}	1005	s

The 20% difference between the measured and model polarisation time has not yet been resolved.

Beam Energy

Resonant spin depolarisation of a stored, polarised electron beam can be achieved with excitation at any fractional spin tune sideband to the revolution harmonic. Designed for baseband tune excitation, the ampilifier and kicker were excited at frequencies of approximately 240-260 kHz. A radial field was used for the depolarisation.

Illustrated in Figure 2 below are resonant spin depolarisations of the measured beam energy. The real changes in beam energy during this measurement correspond to changes in the sum of horizontal corrector magnets, as fast-orbit feedback was operating. A change in the corrector sum of less than 2 A corresponded to a change in deflection angle of 0.1 mrad, and in depolarisation frequency of approximately 100 Hz.

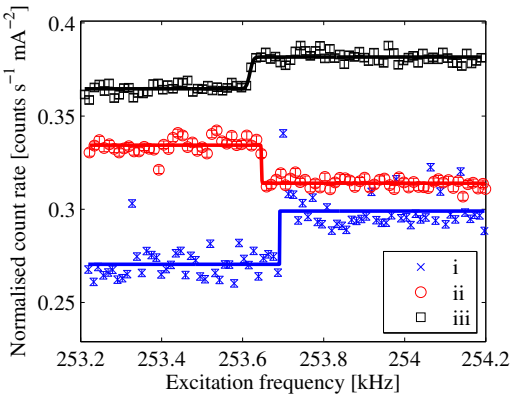

Figure 2: Three separate resonant spin depolarisations. Fast-orbit feedback was on during these measurements.

We can determine the beam energy from any single resonant spin depolarisation. For an RF frequency of 476,310,497 Hz and harmonic number 372, the resonant depolarisation shown in Figure 2 (iii) had a fitted mean depolarising frequency of 253.618 (7) kHz. This corresponded to a spin tune of 6.801923 (6), a beam energy of 2.997251 (7) GeV.

The measured beam energy was predicted in previous modelling [5]. Modelling the storage ring using field maps for the dipole and quadrupole magnets, it was postulated that the energy was 0.1 % lower than the design 3 GeV. Adding the contribution of the sum of horizontal corrector magnets as a net kick of -0.54 mrad at the time of measurement, the predicted energy at the time of measurement was 2.9971 GeV. The beam energy was measured to fluctuate within the range 2.9972-2.9973 GeV with the fast orbit feedback, during the time of measurement.

Spin Tune Synchrotron Sidebands

In locating the spin tune by scanning the excitation frequency, one can excite at the synchrotron sidebands to the spin tune and mistake this depolarisation for the spin tune.

The amplitude of synchrotron sidebands was observed to be lower than the central spin tune. Illustrated in Figure 3 are two excitation sweeps across the real spin tune harmonic at gap voltages of 2.65 and 2.45 MV. This reduction in gap voltage reduces the synchrotron frequency from 11.5 kHz to 11.0 kHz. As the measured depolarisation frequency does not change by 500 Hz with the change in gap voltage, this is a depolarisation of the spin tune and not a synchrotron sideband.

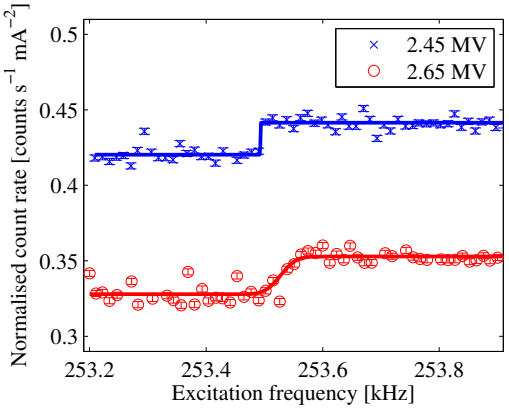

Figure 3: Resonant spin depolarisation at various gap voltages.

Momentum Compaction Factor

The momentum compaction factor – the change in circumference wchange in energy – was measured. The RF frequency provides an accurate constraint on the orbit circumference, and the spin tune an accurate measurement of beam energy. RF frequency feedback and fast-orbit feedback were turned off. Small changes in the RF frequency of 500 and 1000 Hz resulted in small changes to the stored beam energy. The corresponding change in spin tune was measured, as illustrated in Figure 4 below.

DISCUSSION

Measurement of the momentum compaction factor provides a precision calibration of the lattice dispersion. The momentum compaction factor fitted in Figure 4 was compared with different models of the SPEAR3 storage ring. Results are summarised in Table 3 below. This measurement of the momentum compaction factor demonstrates

Table 3: Momentum Compaction Factor

Momentum compaction factor, α_c	**Value**
Measured	0.001637(3)
Field-map model [5]	0.001650
Single-bend AT model	0.001621

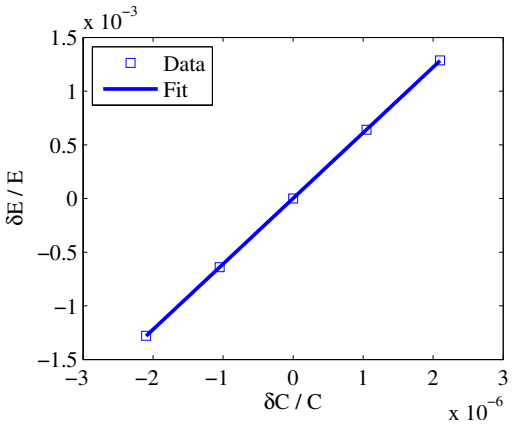

Figure 4: Measured momentum compaction factor.

that the more appropriate choice of model for the lattice dispersion is the numerical integration of simulated field maps.

CONCLUSION

Spin resonant depolarisation has been successfully used at the SPEAR3 electron storage ring. The beam energy has been measured as 2.997251 (7) GeV, representing a relative uncertainty of 3×10^{-6}. Beam energy and momentum compaction factor predictions from the field-map model are in excellent agreement with these measurements of the ring.

REFERENCES

[1] S.R. Mane, Y.M. Shatunov and K. Yokoya (2005), Reports on Progress in Physics, 68, pp. 1997-2265.

[2] H.P. Panopoulos, K.P. Wootton, M.J. Boland, R.P. Rassool (2011), IPAC'11, San Sebastian, Spain, TUPC062.

[3] A.A. Sokolov and I.M. Ternov (1964), (English translation) Soviet Physics Doklady, 8(12): 1203-5. (Originally published) Doklady Akademii Nauk SSSR. 153(5): 1052-4, 1963.

[4] P.J. Mohr, B.N. Taylor, and D.B. Newell (2011),"The 2010 CODATA Recommended Values of the Fundamental Physical Constants" http://physics.nist.gov/constants [Friday, 22-Jul-2011 10:04:27 EDT]. NIST, Gaithersburg, MD 20899, USA.

[5] X. Huang, J. Safranek, D. Dell'Orco (2010), IPAC'10, Kyoto, Japan, THPE048.

ISBN 978-3-95450-115-1

ALIGNMENT TOLERANCES FOR VERTICAL EMITTANCE

K.P. Wootton[1*], M.J. Boland[2], R.P. Rassool[1], Y. Papaphilippou[3], R. Dowd[2], Y.-R.E. Tan[2], G.S. LeBlanc[2], G. Taylor[1]
[1] University of Melbourne, VIC, Australia. [2] Australian Synchrotron, Clayton, VIC, Australia.
[3] CERN, Geneva, Switzerland.

Abstract

A sensitivity analysis of the CLIC main damping ring lattice to magnet misalignments is presented. Misalignments considered included quadrupole vertical offsets and rolls, sextupole vertical offsets, and main dipole rolls.

Expectation values for the vertical emittance were calculated from theory.

Simulations of magnet misalignments were made in MAD-X, for 200 machines at each RMS misalignment. The lattice was found to be sensitive to betatron coupling as a result of sextupole vertical offsets in the arcs.

INTRODUCTION

The design of the linear collider damping rings calls for design horizontal emittances more than an order of magnitude lower than measured in existing storage rings. The few new collider projects are keen to leverage the operational experience of the many constructed storage ring light sources. The design pm rad vertical emittance has been achieved at only a single accelerator; the Australian Synchrotron storage ring [1]. This measurement is not at the IBS bunch density required of the CLIC damping rings - further investigation will be required to achieve this.

The goal of this research is to demonstrate the feasibility of design extracted transverse emittances for the CLIC main damping rings. Table 1 presents a summary of extracted beam parameters.

Table 1: Main damping ring extracted beam requirements

Parameter		Value	Units
Energy	E_b	2.86	GeV
Bunch population	N	4.1	10^9
Emittance, horizontal (norm)	$\gamma\epsilon_x$	480	nm rad
Emittance, vertical (norm)	$\gamma\epsilon_y$	4.5	nm rad

The required emittances include growth due to intra-beam scattering (IBS). It has been demonstrated that a zero-population equilibrium vertical emittance, $\gamma\epsilon_y = 3.7$ nm rad will be required to allow for growth due to IBS [2]. With the quantum limit of vertical emittance for such a ring approximately 0.7 nm rad, the specification is demanding.

A sensitivity analysis of the CLIC main damping ring lattice to magnet misalignments is presented. Misalignments considered included quadrupole vertical offsets and rolls, sextupole vertical offsets, and main dipole rolls.

* k.wootton@student.unimelb.edu.au

LATTICE

The CLIC main damping ring lattice is a wiggler-dominated racetrack lattice [3], with two-fold superperiodicity. The lattice design has matured significantly since the last estimate of alignment tolerances for vertical emittance [4]. The arc TME cell has been optimised for IBS [5], with FODO wiggler straights to achieve the design horizontal emittance.

The compact lattice design necessitates the use of extra windings as orbit and skew quadrupole correctors. We consider first the most conservative corrector pattern: horizontal and vertical orbit correctors on each arc sextupole (three per TME cell), as well as alternating horizontal and vertical steering correctors adjacent to wiggler straight quadrupoles (two per FODO cell). Additional steering is included in the matching sections.

Beam position monitors (BPMs) are positioned in arc cells at points of alternating high and low dispersion, as well as high and low beta functions. We consider BPM buttons with both horizontal and vertical position measurement. A summary of correctors and BPMs introduced in this study is presented in Table 2 below.

Table 2: Correctors and position monitors considered

Component	Plane	Total number
BPM	H&V	358
Corr	H&V	282
Corr	H	28
Corr	V	30

The corrector and BPM pattern used in this study for the arc cells is illustrated in Figure 1 below. Skew quadrupole correctors will be required for local correction of skew quadrupole components. These will be implemented as additional windings on sextupole assemblies. The advantage of including steering and skew quadrupole correctors in this arrangement is the orthogonality to the main sextupole field.

ANALYTICAL EMITTANCE ESTIMATE

The formalism for estimation of flat-beam vertical emittance follows closely the work of Raubenheimer [6]. The mean square vertical dispersion arises from five main contributions:

- Vertical dipole kicks;

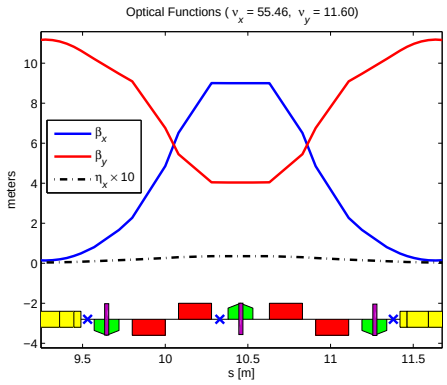

Figure 1: BPMs and correctors considered for TME arc cell. Steering correctors are shown in purple as additional windings on sextupoles, and BPMs indicated as blue crosses.

  - Main dipole rolls;
  - Quadrupole vertical offsets;

- Quadrupole transverse rolls;
- Sextupole vertical offsets;
- Function of the errors giving rise to a non-zero closed orbit;
- Orbit amplification factor (correlation function).

Contributions to the vertical emittance arising from betatron coupling are also considered.

- Quadrupole transverse rolls;
- Sextupole vertical offsets;
- Closed orbit.

The reader is referred to Raubenheimer's work for details of calculation of individual emittance contributions. In this work, the relevant individual contributions are evaluated, as presented in Figure 2. The sum of individual components is presented in Figure 5 as an analytical estimate of vertical emittance growth.

MISALIGNMENTS

Simulations of vertical emittance growth in the CLIC damping rings were made in MAD-X [7]. Lattice elements were seeded for RMS misalignments, in a Gaussian distribution truncated at 2.5 σ. For each misalignment magnitude considered, 200 machines were seeded. Vertical offsets were applied to quadrupoles and sextupoles, and longitudinal rolls were considered for quadrupoles and main dipoles. Misalignments were not considered for the damping wigglers.

Emittances were calculated using the method of Chao [8]. Vertical emittance growth was considered for both the uncorrected and corrected lattice. Results from the uncorrected lattice can represent the lattice sensitivity to misalignments.

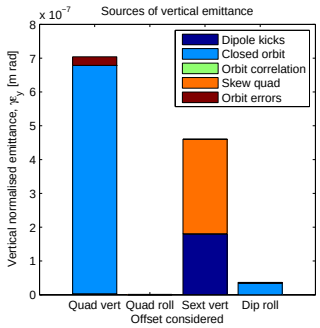

Figure 2: Contributions to vertical emittance. Uncorrected lattice, 100 μm, 100 μrad RMS misalignments.

CLOSED ORBIT

Figure 3 shows the RMS vertical closed orbit resulting from the four families of misalignments considered.

Orbit correction was undertaken using the MAD-X module. The correction algorithm used was singular value decomposition (SVD). All singular values were included in the correction.

Global corrections of tunes, chromaticity and energy were made. Beta-beating was uncorrected.

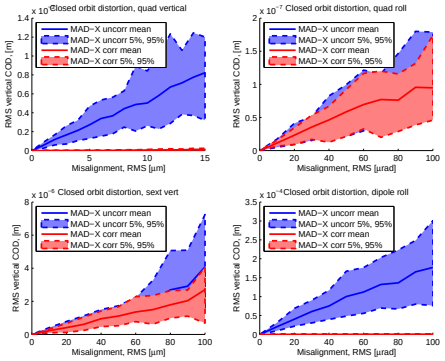

Figure 3: Closed orbit distortion under random misalignments. Uncorrected orbits shown in blue, corrected in red.

The closed orbit from quadrupole vertical displacements is seen to be orders of magnitude greater than the next leading contribution of dipole rolls. The uncorrected orbit amplification factor of 50 as shown in Figure 3 for quadrupole vertical misalignments, reduces to approximately 1 on orbit correction, as illustrated in Figure 4.

Orbit correction is seen to be effective in reducing emittance from quadrupole vertical displacements and dipole rolls, which represent vertical dipole kicks. Orbit correction is seen to be mildly detrimental for coupling from skew quadrupole terms.

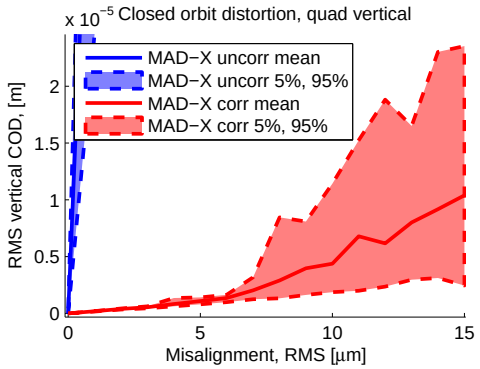

Figure 4: Closed orbit distortion (corrected), for quadrupole vertical displacements. Uncorrected (large) orbits shown in blue, corrected in red.

VERTICAL EMITTANCE

The equilibrium vertical emittance is summarised in Figure 5 below.

Orbit correction reduces the emittance contribution from random dipole kicks to acceptable levels. In the absence of a skew quadrupole corrector scheme, a vertical emittance of 5 nm rad is achieved with an RMS sextupole vertical misalignment of 6 μm. To allow realistic mechanical prealignment tolerances of approximately 50 μm, skew quadrupole correctors and an individual correction scheme will be required.

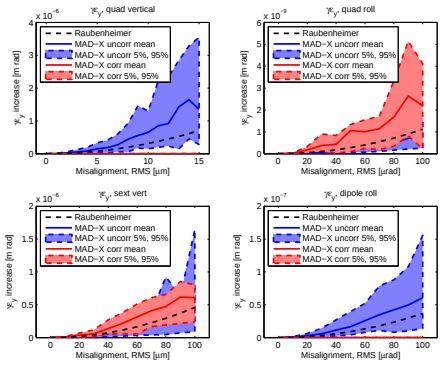

Figure 5: Normalised vertical emittance under random misalignments. Emittances of uncorrected orbits shown in blue, corrected in red, black curve shows analytical estimate of uncorrected emittance (not a quadratic fit).

DISCUSSION

Only relatively recently has low vertical emittance become a design specification of storage rings. The design emittance ratio of the Australian Synchrotron storage ring is and will remain 1%. Whilst many beam dynamics codes provide analysis of emittance growth arising from lattice imperfections, few codes provide a tool suitable for low vertical emittance correction requirements.

The benchmark code for storage ring lattice correction is LOCO [9] using orbit response matrices. MATLAB-based LOCO provides a convenient interface for iterative correction of a single ring. MAD-X features many useful modules for ring design and analysis, but as yet lacks a module for correction of coupling.

The author proposes to the community the inherent usefulness in implementing the LOCO algorithm as a MAD-X module, permitting analysis of many parallel seeded jobs.

CONCLUSION

In the absence of a skew quadrupole corrector scheme, a vertical emittance of 5 nm rad is achieved with an RMS sextupole vertical misalignment of 6 μm. This is not realistic, and an achievable sextupole distribution will require a skew quadrupole correction scheme. Large misalignments from dipole and quadrupole rolls of 100 μm are tolerable, and quadrupole misalignment of 50 μm acceptable.

REFERENCES

[1] R. Dowd, et al. (2011), Phys. Rev. ST: AB, 14, 012804.

[2] A. Vivoli and M. Martini (2010), , IPAC'10, Kyoto, Japan, WEPE090.

[3] Y. Papaphilippou, et al. (2011), IPAC'11, San Sebastian, Spain, TUPC051.

[4] M. Korostelev and F. Zimmermann (2006), EPAC'06, Edinburgh, Scotland, MOPLS135.

[5] E. Levichev et al. (2009), PAC'09, Vancouver, Canada, WE6PFP105.

[6] T. Raubenheimer (1991), "Tolerances to Limit the Vertical Emittance in Future Storage Rings", SLAC-PUB-4937.

[7] F. Schmidt (2005), PAC'05, Knoxville, USA, MPPE012.

[8] A.W. Chao (1979), J. of Applied Physics, 50(2), p. 595-8.

[9] J. Safranek et al. (2002), EPAC'02, Paris, France, WEPLE003.

ELECTRON BEAM ENERGY MEASUREMENT AT THE AUSTRALIAN SYNCHROTRON STORAGE RING

H.P. Panopoulos[1*], K.P. Wootton[1], M.J. Boland[2], R.P. Rassool[1]
[1] University of Melbourne, VIC, Australia [2]Australian Synchrotron, Clayton, VIC, Australia

Abstract

The technique of resonant spin depolarisation was used to precisely measure the electron beam energy in the storage ring at the Australian Synchrotron. A detector and data acquisition system dedicated to the measurement were developed. Using the system, the long term energy stability of the storage ring was monitored and a mechanical realignment of the ring was clearly seen in the energy measurement. Details of the parameters used to optimise the measurement are also discussed.

INTRODUCTION

The highest precision technique available for the measurement of the stored electron beam energy is that of resonant spin depolarisation. The technique was used to calibrate beam energy measurements for LEP [1]. Our method of polarising and observing the depolarisation follows the technique used at BESSY I [2], BESSY II [3], ALS [4], SLS [5], and ANKA [6].

THEORY

A thorough review of theory and experiments with polarised beams of protons, electrons and muons was undertaken by Mane [7]. We will consider the development of radiative polarisation of electron beams, adiabatic resonant spin depolarisation, and Møller scattering cross-section polarimetry.

Radiative Polarisation

Radiative polarisation develops in an initially unpolarised electron beam by the Sokolov-Ternov effect [8]. While travelling through a uniform magnetic field, such as a bending magnet of a storage ring, the spins of electrons will undergo both polarisation in the direction of the field, and precession about the polarisation axis. The polarisation of the beam develops with time approximately by [7],

$$P\left(t\right) = P_0\left(1 - exp\left(\frac{t}{\tau_{ST}}\right)\right) \tag{1}$$

$$\tau_{ST} = \frac{8}{5\sqrt{3}}\frac{m_e\rho^2 R}{\hbar\gamma^5 r_e} \tag{2}$$

where ρ is the mean bending radius, R the mean ring radius and m_e, r_e the classical electron mass and radius. The polarisation $P\left(t\right)$ approaches an equilibrium polarisation P_0 [3]:

$$P_0 = \frac{8}{5\sqrt{3}}\frac{\oint B^3 ds}{\oint |B^3| ds} \tag{3}$$

which approaches a maximum for a storage ring without reverse bends or wiggler insertion devices.

Resonant Spin Depolarisation

The number of spin precessions per revolution of the storage ring, the spin tune ν_{spin}, is given by [1],

$$\nu_{spin} = \left(\frac{g-2}{2}\right)\frac{E}{m_e c^2} \equiv a\gamma \tag{4}$$

where E is the beam energy, m_e the mass and g the gyromagnetic factor of the electron. The gyromagnetic factor g for electrons has been measured to precision within the 12^{th} significant figure [9]. Hence measurement of the spin tune ν_{spin} gives a direct measurement of the beam energy, with uncertainty corresponding to uncertainty in the measurement of the spin tune.

Spin transport and precession is described by the Thomas-BMT equation [7]. We remark that the spins initially polarised normal to the plane of the ring can be rotated away to random orientations, by a series of transverse magnetic kicks resonant at the spin tune.

Møller Scattering Polarimetry

Polarimetry is performed by investigation of the Møller scattering cross-section. The particle loss rate dN/dt is described in terms of the polarisation $P(t)$ by [7]:

$$\frac{dN}{dt} = -\frac{N^2 c}{\sqrt{2}\gamma^2\sigma_{x'}\sigma_{y'}}\left(f_1 + f_2 P(t)^2\right) \tag{5}$$

where f_1, f_2 are functions, which can be treated for this measurement as constants. Importantly, a normalised loss rate can be defined as:

$$R_{norm} = \frac{1}{I(t)^2}\frac{dN}{dt} \propto f_1 + f_2 P(t)^2 \tag{6}$$

where $I(t)$ is the stored beam current at time t.

METHOD

Storage Ring Lattice and Beam

The Australian Synchrotron is a 3 GeV storage ring light source, composed of modified Chasman-Green lattice

* harris.panopoulos@petnm.unimelb.edu.au
Now at Austin Hospital, Heidelberg, VIC

cells. Several important design parameters are summarised in Table 1. All results presented are for the bare storage ring lattice, with 0.1 m distributed dispersion, and high transverse chromaticities of $\xi_x = 3, \xi_y = 13$. The storage ring

Table 1: AS Storage Ring Design Parameters

Parameter		Value	Units
Beam energy	E	3.00	GeV
Relativistic gamma	γ	5871	-
Bending radius	ρ	7.69	m
Circumference	C	216.00	m
RF frequency	f_{RF}	499.67	MHz

was configured such that the Touschek lifetime dominated the beam lifetime. Skew quadrupoles normally used to increase betatron coupling (and accordingly lifetime) were unpowered, to give a beam with transverse emittance ratio of about 0.1% [10]. The fill pattern was reduced from a user fill of 300 bunches, to about 75 bunches in 360 buckets.

These optimisations improved the signal to noise ratio in the initial observation of the resonance. Once identified, the resonance was observable under normal user fill settings, with insertion devices closed.

Depolarisation Kicker and Polarimeter

Vertical betatron tune striplines were used to excite the resonance.

The beam loss monitor was a 75 mm NaI scintillator and photomultiplier tube. Various locations around the storage ring circumference were tested, but the observation of the depolarisation signal was largely insensitive to the circumferential positioning of the detector. The scintillator was installed in the orbit plane of the ring, on the inner side of the vacuum chamber.

Data Acquisition System

As Equation 4 highlights, the important parameter in this measurement is the accurate determination of the spin tune. Hence, the measurement of the depolarising excitation frequency and revolution frequency are the two important parameters.

A Struck 3820 scaler was used to count the excitation frequency, as well as the counts from the beam loss monitor. The scaler features a 50 MHz internal reference clock, for accurate determination of the integration period (typically 1 s). The revolution frequency was determined from the RF frequency, and the stored beam current from the DCCT readback records.

RESULTS

Polarisation Time

The polarisation time was measured. The beam was initially fully depolarised by resonant excitation at the spin tune. With the excitation switched off, the beam was allowed to develop radiative polarisation. The measured normalised loss rate was fitted by Equations 1 and 6. Using Equation 2 and parameters in Table 1 we calculate the model value. The results are summarised in Table 2 below.

Table 2: Polarisation Time

Parameter		Value	Units
Measured	τ_{ST}	806 (21)	s
Model	τ_{ST}	807	s

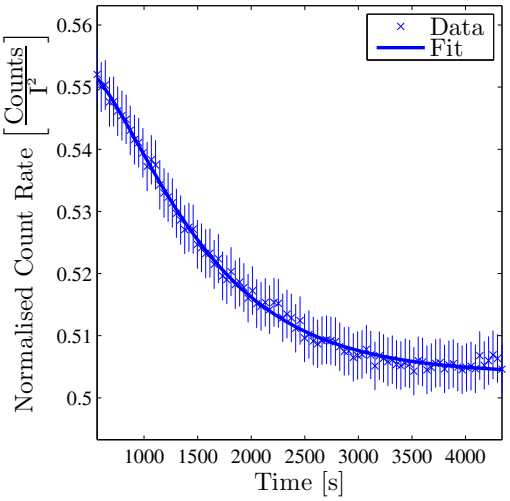

Figure 1: Measurement of polarisation time. Fit to normalised count rate gives $\tau_{pol} = 806 \pm 21$ s.

Beam Energy

A spin-polarised electron beam can be resonantly depolarised at any spin tune sideband to the orbit harmonic. The choice of sideband was determined by the bandwidth of the excitation system, particularly the amplifier and kickers. The resonance was excited at 17.81977(4) MHz. This corresponded to a beam energy of 3.013408(8) GeV.

Illustrated in Figure 2 are two excitation sweeps across the spin tune harmonic. Scanning from both above and below the spin tune places tight constraints on the uncertainty in beam energy fitted.

Spin Tune Synchrotron Sidebands

Resonant spin depolarisation is observed by exciting synchrotron tune sidebands of the spin tune. The amplitude of synchrotron sidebands was observed to be lower than the central spin tune. During this measurement, the cavity voltage was 2.873 MV.

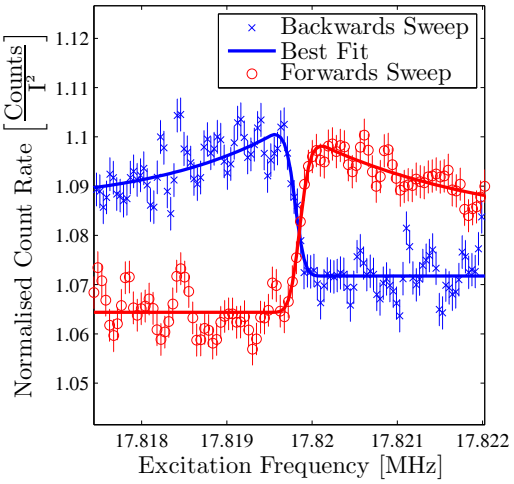

Figure 2: Resonant spin depolarisation at spin tune.

Table 3: Synchrotron Tune for $V_G = 2.873$ MV

Parameter		Value	Units
Measured	f_s	14.54(10)	kHz
Model	f_s	14.51	kHz

Momentum Compaction Factor

The momentum compaction factor was measured. Small changes in the RF frequency of 500 and 1000 Hz in 500 MHz resulted in small changes to the stored beam energy. The corresponding change in spin tune was measured. Results are summarised in Table 4 below.

Table 4: Momentum Compaction Factor

Parameter		Value
Measured	α_c	0.00211(5)
Model	α_c	0.00211

Energy Stability

Over the period of a shift, the beam energy was measured repeatedly. For a polarisation time of approximately 15 minutes, an interval of 30 minutes was appropriate for the radiative development of polarisation. Results are presented in Figure 3 below.

Long term energy stability is presented in Table 5 below.

DISCUSSION

The measurement of the beam energy has been a useful confirmation of the storage ring parameters. Several photon beamlines desire an online measurement of the beam energy, for calibration of absolute photon flux. We plan to provide this online measurement in anticipation of top-up operation.

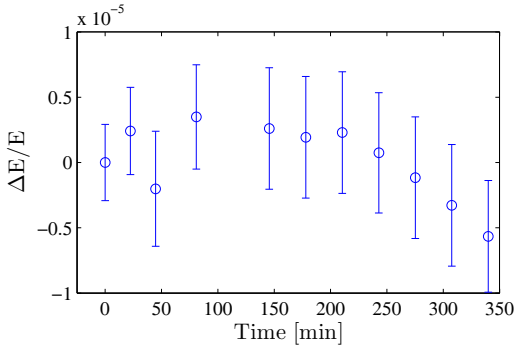

Figure 3: Energy drift with time.

Table 5: Long Term Energy Stability

Date (2010)	Mean energy [GeV]
20^{th} June	3.013418(4)
21^{st} June	3.013379(3)
28^{th} June	3.013171(3)
4^{th} July	3.013188(4)
18^{th} July	3.012996(5)
29^{th} August	3.012974(4)
17^{th} September	3.013332(5)
20^{th} September	3.013270(5)

CONCLUSION

Spin resonant depolarisation has been successfully used at the Australian Synchrotron storage ring. The beam energy has been measured within an uncertainty of 10^{-5}.

REFERENCES

[1] L. Arnaudon, et al. (1994), CERN Report SL/94-71, August 1994.
[2] R. Thornagel, et al. (1994), EPAC'94, London, pp. 1719-21.
[3] P. Kuske, et al. (2010), IPAC'10, Kyoto, MOPD083.
[4] C. Steier, et al. (2000), EPAC'00, Vienna, MOP5B03.
[5] S.C. Leemann, et al. (2002), EPAC'02, Paris, TUPRI011.
[6] A.-S. Müller, et al. (2004), EPAC'04, Lucerne, THPKF022.
[7] S.R. Mane, Y.M. Shatunov and K. Yokoya (2005), "Spin-polarized charged particle beams in high-energy accelerators", Reports on Progress in Physics, 68, pp. 1997-2265.
[8] A.A. Sokolov and I.M. Ternov (1964), (English translation) Soviet Physics Doklady, 8(12): 1203-5. (Originally published) Doklady Akademii Nauk SSSR. 153(5): 1052-4, 1963.
[9] B. Odom, et al. (2006), Phys. Rev. Lett., 97(3), 030801.
[10] R. Dowd et al. (2011), Phys. Rev. ST: AB, 14, 012804.

A NOVEL SYNCHROTRON RADIATION INTERFEROMETER FOR THE AUSTRALIAN SYNCHROTRON*

K.P. Wootton#, School of Physics, Monash University, Clayton 3800, VIC, Australia
M.J. Boland, Australian Synchrotron, Clayton 3168, VIC, Australia

Abstract

A new arrangement for the synchrotron radiation interferometer was proposed. The Young's-type interferometer is composed of two independent and optically identical paths, each with a single slit on a motorised translating stage. This arrangement permits rapid scanning of the profile of fringe visibility as a function of slit separation. The interferometer was used on two beamlines at the Australian Synchrotron, the optical diagnostic and infrared beamlines, to measure the coherence of the photon beam created by the electron beam source, for normal and low emittance couplings. A large change in fringe visibility was observed, proving the experimental arrangement. The interferometer was validated in the measurement of the width of a range of hard-edged single slits, ranging over an order of magnitude in diameter.

INTRODUCTION

The synchrotron radiation interferometer is an established optical diagnostic of many modern electron storage rings [1]. The technique leverages the partial spatial coherence of synchrotron radiation to determine the maximum size of the electron beam. The shape and size of the photon source produce a complementary profile (Fourier transform) of interference fringe visibilities.

The measured quantity of visibility of interference fringes with slit separation is typically determined by interchanging a series of double slits, at various separations. Thereafter, a single slit separation is fixed and the fringe visibility changes over time with electron beam size.

This work introduces an arrangement whereby two independent single slits – mounted on motorised translation stages – can be readily scanned transversely across the synchrotron radiation profile.

THEORY

Theory governing synchrotron radiation interferometers is well-documented, and will be outlined here briefly.

The experimental apparatus is essentially Young's double slit interferometer. Two singles slits are used, each of half-width a. The slits are at a transverse separation d, corresponding to a very large angular separation requiring a lens to form an image of the diffraction pattern at a distance of R_1 beyond the slits. The intensity distribution of the diffracted pattern $I(y)$ is described by the relationship [2]:

$$I(y) = I_0 \mathrm{sinc}^2\left(\frac{2\pi a}{\bar{\lambda}R_1}y\right)\left[1+|\gamma(\nu)|\cos\left(\frac{2\pi d}{\bar{\lambda}R_1}y+\varphi\right)\right], \quad (1)$$

where the photon beam is assumed quasi-monochromatic about some central wavelength $\bar{\lambda}$.

The magnitude of the complex degree of coherence $|\gamma(\nu)|$ is a function of the spatial frequency $\nu(d,\bar{\lambda})$ [2]. The slit separation d alone will be varied. For slits illuminated with light of equal intensity, $|\gamma(d)|$ is equivalent to the measured fringe visibility.

For a thermal Gaussian photon source, $|\gamma(d)|$ is given by [3]:

$$|\gamma(d)| = e^{-\frac{d^2}{2\sigma_d{}^2}}, \quad (2)$$

where σ_d denotes one standard deviation width of the measured profile of $|\gamma(d)|$ with slit separation. The size of the photon source σ_y is then given by [3]:

$$\sigma_y = \frac{\bar{\lambda}R_0}{2\pi\sigma_d}, \quad (3)$$

where R_0 is the propagation distance from the source to the double slit.

A hard-edged pinhole aperture was also imaged. The profile of visibility $|\gamma(d)|$ for such a source imaged by a double slit interferometer is described by [4]:

$$|\gamma(d)| = \frac{|\sin\xi|}{\xi}, \quad \xi = \frac{\pi\rho}{\bar{\lambda}R_0}d, \quad (4)$$

where the pinhole source is of diameter ρ.

INTERFEROMETER CONSTRUCTION

As far as is known, the interferometer as constructed is unique in the world. Theoretically, it measures the coherence of the photon beam in an identical manner to other SR interferometers. The feature of this arrangement is that with mechanisation, each of the single slits can be independently scanned across the photon beam to map the fringe visibility with increasing slit separation. Hence, this interferometer should be sensitive over a much larger range of electron beam size than interferometers with a fixed slit separation. The interferometer is illustrated schematically in Fig. 1 below.

The premise of this layout is to exert independent control over the two independent single slits, converging the two single slit diffraction patterns to form the image of a double slit pattern.

Two configurations for the lenses were explored. Initially, a lens was placed on each path, immediately following the single slit.

*Work supported by Australian Synchrotron studentship.
#kent.wootton@synchrotron.org.au

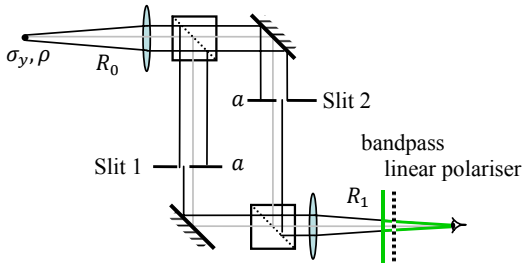

Figure 1: SR interferometer, illustrating two separate single slits, each offset by distance d / 2 from the central axis.

It was found to be more effective, and much simpler to position a lens before and after the beamsplitter arrangement, as illustrated in Fig. 1. The operation of the interferometer was largely insensitive to the centres or tilts of the lenses. The positioning of the two lenses resembles Thompson and Wolf's diffractometer [5].

Components

The beam is split and recombined equally in power using an unpolarised beamsplitter cube. Two planar mirrors of surface roughness λ/10 are used in steering the beam. Planoconvex lenses of diameter 25.4 mm and effective focal length 300 mm were selected. Variable aperture single slits were selected, with a typical aperture used between 200-300 µm.

A laser line bandpass filter of $\bar{\lambda}$ = 532 nm, 10 nm FWHM bandpass is optimised for the broadband visible antireflection coatings. Retrospectively, this is deemed too tight – a filter of up to 60 nm may not appreciably degrade the visibility of the central fringes [6]. A polarised beamsplitter cube was used for rejection of the π-mode polarisation of synchrotron radiation as it has a phase difference of π with the σ-mode, which would diminish the observed fringe visibility [1].

Linear translation stages were matched with actuators of a travel range of 12mm. The APT motor controllers feature USB connections and ActiveX control software, which was incorporated directly into MATLAB scripts.

Image acquisition was accomplished using a greyscale CCD flea camera, interfaced to EPICS.

The most difficult aspect of construction is alignment, especially minimising the path length difference to within the coherence length of the bandpass filter of only 28 µm. A streak camera could be very beneficial.

Beamlines

The optical diagnostic beamline (ODB) at the Australian Synchrotron is designed to cater principally to the longitudinal profile of the photon beam. It serves a suite of instruments, including a streak camera, bunch purity monitor and fill pattern monitor [7]. To deliver light to these instruments, a biconvex lens forms an image of the photon beam source over the optical table [8]. The distance between this virtual source and interferometer, R_0 is limited to at most 2-3 metres. Most SR interferometers have $R_0 \approx 10$ m.

The beamline front end has several apertures, with the crotch absorber the limiting aperture: 5 mm (2.8 mrad) vertical × 10 mm (5.6 mrad) horizontal. This is a standard crotch absorber used for bending magnet x-ray beamlines, but is too narrow to pass the vertical fan of optical synchrotron radiation, even at the VUV limit. Simulations made in Synchrotron Radiation Workshop demonstrate that passing the full vertical fan (3σ, 99.8% power) at 532 nm requires a vertical aperture of 15 mm (8.4 mrad).

The infrared beamline at the Australian Synchrotron has a much larger angular acceptance than the optical beamline. Bending magnet and edge radiation are extracted using a slotted mirror of 17.3 mrad vertical × 60.2 mrad horizontal [9]. A centrally positioned slot of 2.3 mrad (3 mm) passes the hot x-ray fan.

MEASUREMENTS

A goal of this interferometer is to directly confirm the vertical beam size, and hence the emittance coupling ratio of the storage ring beam. Indirect measurements using the Touschek lifetime have been made, giving a minimal emittance coupling of 0.009% [10].

Fringe visibilities were assigned for each slit separation by fitting Equation (1) to the measured visibility distribution, using a Levenberg-Marquhart technique. This is illustrated in Fig. 2 below.

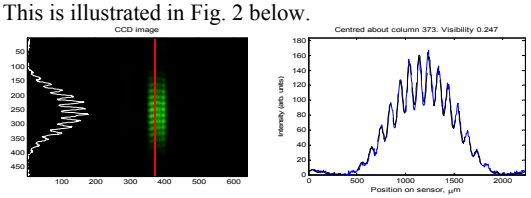

Figure 2: Fitting to determine fringe visibility. Blue: slice of measured interferogram, black: Equation (1), fitted for a visibility of 0.25.

Pinhole verification

The interferometer was arranged to image a selection of circular pinholes, the results of which are presented in Fig. 5. The propagation distance R_0 and separation of camera and objective R_1 were both 300 mm. The source pinhole was illuminated by a 600 µm diameter multimode optical fibre, positioned immediately behind the pinhole. To increase the measured intensity the integration time of the CCD was set as high as 1500 ms for pinhole 1.

Once aligned, each scan of approximately 20 slit separations was taken in less than five minutes.

The diameters of the pinholes were calibrated by single slit diffraction. A summary of the results is shown in Table 1 below.

Table 1: Measurement of Pinhole Diameter ρ

Pinhole -	Single Slit Diffraction [µm]	SR Interferometer [µm]
1	15 ± 2	15 ± 2
2	42 ± 3	38 ± 2
3	174 ± 10	171 ± 5

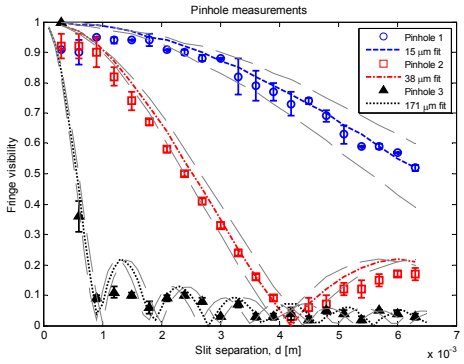

Figure 3: Measured profiles of fringe visibility for three pinhole sources. For uncertainties refer to Table 1.

Infrared Beamline

As the ODB mirror accepts light only above the orbit plane of the ring, measurements of the profile of synchrotron radiation were undertaken on the infrared microspectroscopy beamline. The beam emittance coupling was varied from nominal user coupling of 1% to a minimum coupling. The interferometer was at an effective distance R_0 of 1.00 m. At a single fixed slit separation of 3 mrad, the fringe visibility was seen to increase as the coupling was reduced. This is illustrated in Fig. 4 below.

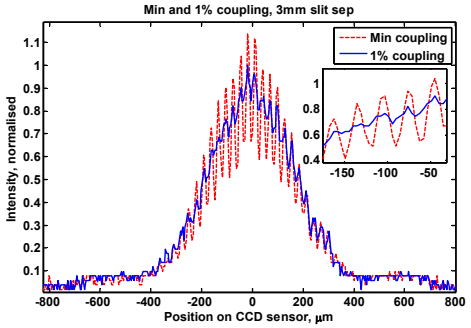

Figure 4: Observed increase in visibility with reduction of coupling. $|\gamma(3)_{1\%}| = 0.05, |\gamma(3)_{min}| = 0.35$.

Figure 5 below shows the profile of visibility with slit separation.

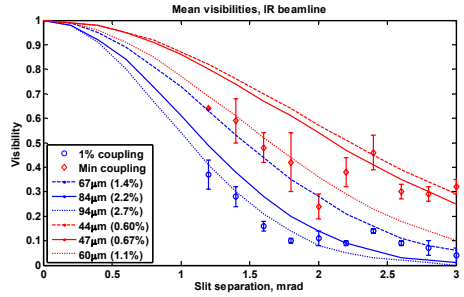

Figure 5: Fringe visibility profiles with variation in emittance coupling. (red: minimal, blue: 1% coupling).

DISCUSSION

The results of the pinhole measurement in Fig. 3 demonstrate the high dynamic range of the setup to measure source size, over at least an order of magnitude. A source size of 15 μm can be determined to ± 2 μm.

The results presented in Figs. 4 and 5 demonstrate qualitatively that the interferometer can image a synchrotron radiation bending magnet source. The couplings quoted in Fig. 5 compare poorly with other measurements. It is believed that the fringe visibility is degraded by the three infrared-transparent windows in the optical path, that are not optically flat at visible wavelengths.

The interferometer installed on the optical table is compact, with a footprint of approximately 0.2 m × 0.7 m. The dimensions would be scalable to suit larger transverse size, or greater propagation distance. Once aligned, scans require no user intervention to change slit separation. As such, a permanent diagnostic could be mounted near the photon source, within the accelerator tunnels.

CONCLUSION

The new arrangement for the synchrotron radiation interferometer has been demonstrated to give accurate measurements of three pinholes ranging in size over an order of magnitude. We have demonstrated a measurement of a pinhole source 15 ± 2 μm.

A measurement of the vertical size of the storage ring electron beam was made on the infrared beamline. The observed fringe visibility defined a source much larger than determined by other direct measurements.

We aim to implement the interferometer as a diagnostic in the future, on an accommodating beamline.

ACKNOWLEDGEMENT

This work was undertaken on the optical diagnostic, and infrared microspectroscopy beamlines at the Australian Synchrotron, Victoria, Australia.

REFERENCES

[1] T. Mitsuhashi, PAC'97, Vancouver, May 1997, 3V016, p. 766-68 (1997).
[2] M. Katoh and T. Mitsuhashi, PAC'99, New York, March 1999, WEP22, p. 2307-09 (1999).
[3] J. Corbett et al., PAC'09, Vancouver, May 2009, TH6REP033. (2009).
[4] D.M. Paganin, Coherent X-Ray Optics, Clarendon Press, Oxford, p. 34 (2006).
[5] M. Born and E. Wolf, Principles of Optics, 7th Ed., p. 578, (1999).
[6] L. Basano, et al., Applied Optics, (2003) 42 (31) 6239.
[7] D.J. Peake, et al., Nucl. Inst. and Methods A, 589 (2008) 143.
[8] M.J. Boland et al., EPAC'06, Edinburgh, June 2006, THPLS002, p. 3263 (2006).
[9] D. Creagh, J. McKinlay, and P. Dumas, Vibrational Spectroscopy, (2006) 41, 213.
[10] R. Dowd, et al., PAC'09, Vancouver, TH6PFP008 (2009).

Author's note: This page has deliberately been left blank in this electronic open-access version of the thesis. The copyright status of the following publication could not be determined, and as such only the citation is included.

- H.P. Panopoulos, K.P. Wootton, M.J. Boland and R.P. Rassool (2010), Electron Beam Energy Measurement by Resonant Spin Depolarisation at the Australian Synchrotron, *Proc. 19$^{\text{th}}$ AIP Congress*, Melbourne, December 2010.

The original page has been supplied for archival purposes to The University of Melbourne in a separate document.

Author's note: This page has deliberately been left blank in this electronic open-access version of the thesis. The copyright status of the following publication could not be determined, and as such only the citation is included.

- R. Dowd, M.J. Boland, R.P. Rassool and K.P. Wootton (2010), Damping Ring Studies for Future Linear Colliders, *Proc. 19$^{\text{th}}$ AIP Congress*, Melbourne, December 2010.

The original page has been supplied for archival purposes to The University of Melbourne in a separate document.

Acronyms

AdA Anello di Accumulazione.

ALS Advanced Light Source.

APPLE-II Advanced Planar Polarised Light Emitter–II.

AS Australian Synchrotron.

AT Accelerator Toolbox.

BPM Beam Position Monitor.

CDR Conceptual Design Report.

CERN European Organization for Nuclear Research.

CLIC Compact Linear Collider.

COD Closed Orbit Distortion.

DBA Double-Bend Achromat.

DCCT Direct-Current Current Transformer.

DLS Diamond Light Source.

eRHIC electron Relativistic Heavy Ion Collider.

FFAG Fixed-Field, Alternating Gradient.

FODO Focussing–Open–Defocussing–Open.

FWHM Full Width at Half Maximum.

IBS Intra-Beam Scattering.

ID Insertion Device.

ILC International Linear Collider.

KEK-ATF KEK Accelerator Test Facility.

LEP Large Electron Positron Collider.

LHC Large Hadron Collider.

LHeC Large Hadron electron Collider.

LOCO Linear Optics from Closed Orbits.

MAD-X Methodical Accelerator Design (version 10).

ODB Optical Diagnostic Beamline.

PSF Point-Spread Function.

RDR Reference Design Report.

rf radio frequency.

RMS Root Mean Square.

SI Système International d'Unités.

SLC SLAC Linear Collider.

SLS Swiss Light Source.

SPEAR Stanford Positron Electron Accelerating Ring.

SRW Synchrotron Radiation Workshop.

SVD singular value decomposition.

TDR Technical Design Report.

TME Theoretical Minimum Emittance.

USR Ultimate Storage Ring.

VUV Vacuum Ultra-Violet.

XDB X-ray Diagnostic Beamline.

Bibliography

[1] (D0 Collaboration), S. Abachi *et al.*, Physical Review Letters **74**, 2422 (1995), doi:10.1103/PhysRevLett.74.2422. (cited p. 1)

[2] (CDF Collaboration), F. Abe *et al.*, Physical Review Letters **74**, 2626 (1995), doi:10.1103/PhysRevLett.74.2626. (cited p. 1)

[3] (The ATLAS Collaboration), G. Aad *et al.*, Physics Letters B **716**, 1 (2012), doi:10.1016/j.physletb.2012.08.020. (cited p. 1)

[4] (The CMS Collaboration), S. Chatrchyan *et al.*, Physics Letters B **716**, 30 (2012), doi:10.1016/j.physletb.2012.08.021. (cited p. 1)

[5] P. W. Higgs, Physical Review Letters **13**, 508 (1964), doi:10.1103/PhysRevLett.13.508. (cited p. 1)

[6] F. Englert and R. Brout, Physical Review Letters **13**, 321 (1964), doi:10.1103/PhysRevLett.13.321. (cited p. 1)

[7] (Planck Collaboration), P. A. R. Ade *et al.*, (2013), arXiv:1303.5076 [astro-ph.CO]. (cited p. 1)

[8] G. Bertone, D. Hooper and J. Silk, Physics Reports **405**, 279 (2005), doi:10.1016/j.physrep.2004.08.031. (cited p. 1)

[9] D. Clowe *et al.*, The Astrophysical Journal **648**, L109 (2006), doi:10.1086/508162. (cited p. 1)

[10] R. Bernabei *et al.*, The European Physical Journal C **56**, 333 (2008), doi:10.1140/epjc/s10052-008-0662-y. (cited p. 1)

[11] (The CDMS II Collaboration), Z. Ahmed *et al.*, Science **327**, 1619 (2010), doi:10.1126/science.1186112. (cited p. 2)

[12] (XENON100 Collaboration), E. Aprile *et al.*, Physical Review Letters **109**, 181301 (2012), doi:10.1103/PhysRevLett.109.181301. (cited p. 2)

[13] (Particle Data Group), J. Beringer *et al.*, Physical Review D **86**, 010001 (2012), doi:10.1103/PhysRevD.86.010001. (cited p. 2)

[14] J. Goodman *et al.*, Physical Review D **82**, 116010 (2010), doi:10.1103/PhysRevD.82.116010. (cited p. 2)

[15] A. Einstein, Annalen der Physik **323**, 639 (1905), doi: 10.1002/andp.19053231314. (cited p. 5)

[16] M. Planck, Verhandlungen Deutsche Physikalische Gesellschaft **8**, 136 (1906). (cited p. 5)

[17] E. Rutherford, Philosophical Magazine Series 6 **21**, 669 (1911), doi: 10.1080/14786440508637080. (cited p. 6)

[18] K. Wille, *The Physics of Particle Accelerators* (Oxford University Press, New York, USA, 2000). (cited p. 6, 17)

[19] D. J. Tendam, School Science and Mathematics **59**, 175 (1959), doi: 10.1111/j.1949-8594.1959.tb08207.x. (cited p. 6)

[20] E. Fermi, Notes for a lecture on "What can we learn with High Energy Accelerators?" for the American Physical Society meeting in New York, January 29, 1954, in *The Enrico Fermi Collection*, The University of Chicago Library, Special Collections Research Center, Box 53, Folder 14, 1954. (cited p. 6)

[21] J. Orear, *Enrico Fermi – The Master Scientist* (The Internet-First University Press, 2004), http://hdl.handle.net/1813/74. (cited p. 6)

[22] G.-A. Voss, *Electron-Positron and Electron-Proton Storage Ring Colliders*, NATO ASI Series, Vol. 352 (Springer-Verlag, 1996), chap. 25, pp. 465–487, doi:10.1007/978-1-4613-1147-8_25. (cited p. 6)

[23] W. K. H. Panofsky, Beam Line **27**, 36 (1997). (cited p. 7)

[24] C. Bernardini *et al.*, Il Nuovo Cimento Series 10 **34**, 1473 (1964), doi: 10.1007/BF02750550. (cited p. 6, 7)

[25] R. Wideröe, Anordnung zur herbeiführung von kernreaktionen, 1953, German Patent 876279. Filed 6$^{\text{th}}$ September 1943, published 11$^{\text{th}}$ May 1953. (cited p. 6)

[26] D. W. Kerst *et al.*, Physical Review **102**, 590 (1956), doi: 10.1103/PhysRev.102.590. (cited p. 6)

[27] G. K. O'Neill, Physical Review **102**, 1418 (1956), doi: 10.1103/PhysRev.102.1418. (cited p. 6)

[28] C. Bernardini, G. F. Corazza, G. Ghigo and B. Touschek, Il Nuovo Cimento **18**, 1293 (1960), doi:10.1007/BF02733192. (cited p. 6)

[29] C. Bernardini *et al.*, Il Nuovo Cimento Series 10 **23**, 202 (1962), doi: 10.1007/BF02733556. (cited p. 6)

[30] (Particle Data Group), K. Nakamura *et al.*, Journal of Physics G: Nuclear and Particle Physics **37**, 075021 (2010), doi:10.1088/0954-3899/37/7A/075021. (cited p. 6)

[31] Stanford Linear Accelerator Center Report No. SLAC-R-229, 1980 (unpublished). (cited p. 7)

[32] J. S. Schwinger, Physical Review **70**, 798 (1946), doi: 10.1103/PhysRev.70.784.2. (cited p. 7, 21)

[33] (The LEP Energy Working Group), R. Assmann *et al.*, The European Physical Journal C - Particles and Fields **39**, 253 (2005), doi:10.1140/epjc/s2004-02108-8. (cited p. 7)

[34] J. Brau *et al.*, ILC Global Design Effort Report No. SLAC-R-857, 2007 (unpublished), doi:10.2172/914731. (cited p. 8)

[35] T. Behnke, J. E. Brau, B. Foster, J. Fuster and M. Harrison, ILC Global Design Effort Report No. ILC-REPORT-2013-040, 2013 (unpublished), arXiv:1306.6327 [physics.acc-ph]. (cited p. 8)

[36] P. Lebrun *et al.*, CERN Report No. CERN-2012-005, 2012 (unpublished), doi:10.5170/CERN-2012-005. (cited p. 9)

[37] M. Aicheler *et al.*, CERN Report No. CERN-2012-007, 2012 (unpublished), doi:10.5170/CERN-2012-007. (cited p. 9, 24, 32, 33, 61, 62, 68)

[38] L. Linssen, A. Miyamoto, M. Stanitzki and H. Weerts, CERN Report No. CERN-2012-003, 2012 (unpublished), doi:10.5170/CERN-2012-003. (cited p. 9)

[39] S. Y. Lee, *Accelerator Physics*, 2nd ed. (World Scientific, Singapore, 2004), doi:10.1142/5761. (cited p. 11, 16, 17, 22, 23, 24, 25, 36)

[40] H. Wiedemann, *Synchrotron Radiation* (Springer-Verlag, Berlin, Germany, 2003), doi:10.1007/978-3-662-05312-6. (cited p. 12, 20, 22, 23, 104)

[41] H. A. Lorentz, *Versuch einer Theorie der electrischen und optischen Erscheinungen in bewegten Körpern* (E. J. Brill, Leiden, 1895). (cited p. 12)

[42] J. D. Jackson, *Classical Electrodynamics*, 3rd ed. (John Wiley & Sons, Hoboken, NJ, USA, 1998). (cited p. 12)

[43] F. Frenet, Journal de Mathématiques Pures et Appliquées (1re série) **17**, 437 (1852). (cited p. 13)

[44] J.-A. Serret, Journal de Mathématiques Pures et Appliquées (1re série) **16**, 193 (1851). (cited p. 13)

[45] H. Wiedemann, *Particle Accelerator Physics*, 3rd ed. (Springer-Verlag, Berlin, Germany, 2007), doi:10.1007/978-3-540-49045-6. (cited p. 15, 17, 19, 20, 21, 23, 24, 49, 52, 88, 89, 91, 145)

[46] E. D. Courant, M. S. Livingston and H. S. Snyder, Physical Review **88**, 1190 (1952), doi:10.1103/PhysRev.88.1190. (cited p. 15, 18, 52)

[47] E. D. Courant and H. S. Snyder, Annals of Physics **3**, 1 (1958), doi: 10.1016/0003-4916(58)90012-5. (cited p. 15, 16, 17, 18, 19, 35, 51)

[48] R. Q. Twiss and N. H. Frank, Review of Scientific Instruments **20**, 1 (1949), doi:10.1063/1.1741343. (cited p. 16)

[49] E. D. Courant and H. S. Snyder, Annals of Physics **281**, 360 (2000), doi: 10.1006/aphy.2000.6012. (cited p. 16)

[50] M. Sands, Stanford Linear Accelerator Center Report No. SLAC-R-121, 1970 (unpublished). (cited p. 17, 26)

[51] E. M. McMillan, Physical Review **68**, 143 (1945), doi: 10.1103/PhysRev.68.143. (cited p. 18)

[52] M. Oliphant, The acceleration of particles to very high energies, http://hdl.handle.net/2440/48688, University of Adelaide Digital Library, 1943. (cited p. 18)

[53] V. I. Veksler, Comptes rendus de l'Académie des sciences de l'URSS **43**, 329 (1944). (cited p. 18)

[54] V. Veksler, Physical Review **69**, 244 (1946), doi:10.1103/PhysRev.69.244. (cited p. 18)

[55] E. M. McMillan, Physical Review **69**, 534 (1946), doi: 10.1103/PhysRev.69.534.2. (cited p. 18)

[56] M. L. Oliphant, J. S. Gooden and G. S. Hide, Proceedings of the Physical Society (London) **59**, 666 (1947), doi:10.1088/0959-5309/59/4/314. (cited p. 18)

[57] J. Liouville, Journal de Mathématiques Pures et Appliquées (1re série) **3**, 342 (1838). (cited p. 19)

[58] K. W. Robinson, Physical Review **111**, 373 (1958), doi: 10.1103/PhysRev.111.373. (cited p. 20, 22, 36)

[59] J. S. Schwinger, On radiation by electrons in a betatron, in *A Quantum Legacy: Seminal Papers of Julian Schwinger*, edited by K. A. Milton No. LBNL-39088, chap. 19, pp. 307–331, World Scientific, 2000, doi: 10.1142/9789812795694_0015. (cited p. 21)

[60] J. Schwinger, Physical Review **75**, 1912 (1949), doi:10.1103/PhysRev.75.1912. (cited p. 21)

[61] F. R. Elder, A. M. Gurewitsch, R. V. Langmuir and H. C. Pollock, Physical Review **71**, 829 (1947), doi:10.1103/PhysRev.71.829.5. (cited p. 21)

[62] R. H. Helm, M. J. Lee, P. L. Morton and M. Sands, Evaluation of synchrotron radiation integrals, in *Proceedings of the Particle Accelerator Conference 1973*, pp. 900–1, JACoW, San Francisco, CA, USA, 1973. (cited p. 21, 22, 36, 42)

[63] J. M. Jowett, AIP Conference Proceedings **153**, 864 (1987), doi: 10.1063/1.36374. (cited p. 21, 36)

[64] A. W. Chao and M. Tigner, *Handbook of Accelerator Physics and Engineering* (World Scientific Publishing, Singapore, 1999), doi:10.1142/3818. (cited p. 21, 23, 36, 43, 89, 125)

[65] H. Winick, G. Brown, K. Halbach and J. Harris, Physics Today **34**, 50 (1981), doi:10.1063/1.2914568. (cited p. 23)

[66] G. Brown, K. Halbach, J. Harris and H. Winick, Nuclear Instruments and Methods in Physics Research **208**, 65 (1983), doi:10.1016/0167-5087(83)91105-5. (cited p. 23)

[67] V. L. Ginzburg, Izvestiya Akademii Nauk SSSR, Seriya Fizicheskaya **11**, 165 (1947). (cited p. 24)

[68] G. N. Kulipanov, Uspekhi Fizicheskikh Nauk **177**, 384 (2007), doi: 10.1070/PU2007v050n04ABEH006237, [Physics-Uspekhi **50**, 368 (2007)]. (cited p. 24)

[69] A. Hofmann, Nuclear Instruments and Methods **152**, 17 (1978), doi: 10.1016/0029-554X(78)90231-8. (cited p. 24)

[70] H. Motz, Journal of Applied Physics **22**, 527 (1951), doi:10.1063/1.1700002. (cited p. 24, 88)

[71] H. Motz, Journal of Applied Physics **22**, 1217 (1951), doi:10.1063/1.1700144. (cited p. 24)

[72] H. Motz, W. Thon and R. N. Whitehurst, Journal of Applied Physics **24**, 826 (1953), doi:10.1063/1.1721389. (cited p. 24)

[73] H. Wiedemann, Nuclear Instruments and Methods in Physics Research Section A: Accelerators, Spectrometers, Detectors and Associated Equipment **266**, 24 (1988), doi:10.1016/0168-9002(88)90354-3. (cited p. 24, 105, 106)

[74] P. Emma and T. Raubenheimer, Stanford Linear Accelerator Center Report No. LCC-0037, 2000 (unpublished), doi:10.2172/826830. (cited p. 24)

[75] T. Naito *et al.*, Damping wiggler study at KEK-ATF, in *Proceedings of the Particle Accelerator Conference 2005*, p. MPPE044, JACoW, Knoxville, TN, USA, 2005. (cited p. 24)

[76] Y. Papaphilippou *et al.*, Conceptual design of the CLIC damping rings, in *Proceedings of the International Particle Accelerator Conference 2012*, p. TUPPC086, JACoW, New Orleans, USA, 2012. (cited p. 24, 32)

[77] K. Balewski and W. Decking, Beam dynamics study for PETRA III including damping wigglers, in *Proceedings of the European Particle Accelerator Conference 2004*, p. WEPLT066, JACoW, Lucerne, Switzerland, 2004. (cited p. 24)

[78] W. Guo *et al.*, NSLS-II lattice optimization with damping wigglers, in *Proceedings of the International Particle Accelerator Conference 2009*, p. TU5RFP008, JACoW, Vancouver, Canada, 2009. (cited p. 24)

[79] S. C. Leemann *et al.*, Physical Review Special Topics: Accelerators and Beams **12**, 120701 (2009), doi:10.1103/PhysRevSTAB.12.120701. (cited p. 24, 37, 58)

[80] M.-H. Wang *et al.*, Nuclear Instruments and Methods in Physics Research Section A: Accelerators, Spectrometers, Detectors and Associated Equipment **649**, 30 (2011), doi:10.1016/j.nima.2011.01.011. (cited p. 24, 37, 58)

[81] S. Doniach, K. Hodgson, I. Lindau, P. Pianetta and H. Winick, Journal of Synchrotron Radiation **4**, 380 (1997), doi:10.1107/S0909049597012235. (cited p. 24, 30)

[82] B. M. Kincaid, Journal of Applied Physics **48**, 2684 (1977), doi:10.1063/1.324138. (cited p. 24, 132)

[83] R. P. Walker, Wigglers, in *5th Advanced Accelerator Physics Course*, edited by S. Turner No. CERN-95-06, pp. 807–835, Geneva, Switzerland, 1995, CERN Accelerator School, doi:10.5170/CERN-1995-006. (cited p. 24, 25)

[84] T. O. Raubenheimer, Particle Accelerators **36**, 75 (1991), SLAC-PUB-4937. (cited p. 26, 62, 63, 64, 65, 66, 67, 68)

[85] H. Winick, Overview of synchrotron radiation facilities, in *Proceedings of the Particle Accelerator Conference 1989*, pp. 7–11, JACoW, Chicago, USA, 1989, doi:10.1109/PAC.1989.73018. (cited p. 29)

[86] A. Jackson, Synchrotron Radiation News **3**, 13 (1990), doi:10.1080/08940889008602558. (cited p. 29)

[87] P. Emma and T. Raubenheimer, Physical Review Special Topics: Accelerators and Beams **4**, 021001 (2001), doi:10.1103/PhysRevSTAB.4.021001. (cited p. 29)

[88] R. Bartolini, Review of lattice design for low emittance rings, in *ICFA Beam Dynamics newsletter*, edited by Y. Cai, Vol. 57, pp. 13–25, International Committee for Future Accelerators, 2012. (cited p. 30)

[89] J. Shanks, *Low-emittance tuning at CESRTA*, PhD thesis, Cornell University, Ithaca, NY, USA, 2013. (cited p. 30)

[90] J. Shanks, D. Rubin and D. Sagan, (2013), arXiv:1309.2247 [physics.acc-ph]. (cited p. 30)

[91] Y. Honda *et al.*, Physical Review Letters **92**, 054802 (2004), doi: 10.1103/PhysRevLett.92.054802. (cited p. 30, 86)

[92] M. Aiba, M. Böge, N. Milas and A. Streun, Nuclear Instruments and Methods in Physics Research Section A: Accelerators, Spectrometers, Detectors and Associated Equipment **694**, 133 (2012), doi:10.1016/j.nima.2012.08.012. (cited p. 29, 30, 83, 85, 94, 119, 122, 129, 136, 137)

[93] G. Kube *et al.*, PETRA III diagnostics beamline for emittance measurements, in *Proceedings of the International Particle Accelerator Conference 2010*, p. MOPD089, JACoW, Kyoto, Japan, 2010. (cited p. 30)

[94] R. Wanzenberg, Observation of collective effects during positron and electron operation at PETRA III, in *Presentation at Three-Way Meeting*, Argonne National Laboratory, IL, USA, 2013. (cited p. 29, 30)

[95] R. Dowd, M. Boland, G. LeBlanc and Y.-R. E. Tan, Physical Review Special Topics: Accelerators and Beams **14**, 012804 (2011), doi: 10.1103/PhysRevSTAB.14.012804. (cited p. 29, 30, 83, 84, 86, 108, 109, 110, 119)

[96] J. W. Boldeman, The Australian Synchrotron Light Source, in *Proceedings of the European Particle Accelerator Conference 2002*, p. TUPLE013, JACoW, Paris, France, 2002. (cited p. 30, 32)

[97] A. Jackson and H. Nishimura, Single-particle beam dynamics in Boomerang, in *Proceedings of the Particle Accelerator Conference 2003*, p. TOPA009, JACoW, Portland, OR, USA, 2003. (cited p. 30, 93)

[98] J. W. Boldeman and D. Einfeld, Nuclear Instruments and Methods in Physics Research Section A: Accelerators, Spectrometers, Detectors and Associated Equipment **521**, 306 (2004), doi:10.1016/j.nima.2003.11.191. (cited p. 30, 36, 38, 56, 86, 147)

[99] G. S. LeBlanc, M. J. Boland and Y.-R. E. Tan, The Australian Synchrotron Project storage ring and injection system overview, in *Proceedings of the European Particle Accelerator Conference 2004*, p. THPKF005, JACoW, Lucerne, Switzerland, 2004. (cited p. 31)

[100] B. Richter, *Nobel Lectures, Physics 1971-1980* (World Scientific Publishing Company, 1992), chap. From the Psi to Charm – The Experiments of 1975 and 1976, pp. 281–310. (cited p. 30)

[101] M. L. Perl, *Nobel Lectures in Physics 1991-1995* (World Scientific Publishing Co., Singapore, 1997), chap. Reflections on the Discovery of the Tau Lepton, pp. 168–195. (cited p. 30)

[102] I. Lindau, P. Pianetta, S. Doniach and W. E. Spicer, Nature **250**, 214 (1974), doi:10.1038/250214a0. (cited p. 32)

[103] J. Corbett, C. Limborg, Y. Nosochov, J. Safranek and A. Garren, Design of the SPEAR 3 magnet lattice, in *Proceedings of the European Particle Accelerator Conference 1998*, pp. 574–6, JACoW, Stockholm, Sweden, 1998. (cited p. 32, 36, 38, 147)

[104] M. Yoon, J. Corbett, M. Cornacchia, J. Tanabe and A. Terebilo, Nuclear Instruments and Methods in Physics Research Section A: Accelerators, Spectrometers, Detectors and Associated Equipment **523**, 9 (2004), doi: 10.1016/j.nima.2003.11.429. (cited p. 32, 38, 136, 147, 148, 149, 150, 151)

[105] P. Krejcik, Design for a practical, low-emittance damping ring, in *Proceedings of the European Particle Accelerator Conference 1988*, pp. 509–11, JACoW, Rome, Italy, 1988. (cited p. 32)

[106] Y. Papaphilippou, H. H. Braun and M. Korostelev, Parameter scan for the CLIC damping rings, in *Proceedings of the European Particle Accelerator Conference 2008*, p. MOPP060, JACoW, Genoa, Italy, 2008. (cited p. 32, 33)

[107] Y. Papaphilippou *et al.*, Design optimisation of the CLIC damping rings, in *Proceedings of the International Particle Accelerator Conference 2010*, p. WEPE089, JACoW, Kyoto, Japan, 2010. (cited p. 32, 33)

[108] J. P. Potier and L. Rivkin, A low emittance lattice for the CLIC damping ring, in *Proceedings of the Particle Accelerator Conference 1997*, p. 8W016, JACoW, Vancouver, Canada, 1997. (cited p. 33)

[109] F. Antoniou and Y. Papaphilippou, Optics design considerations for the CLIC pre-damping rings, in *Proceedings of the European Particle Accelerator Conference 2008*, p. MOPP062, JACoW, Genoa, Italy, 2008. (cited p. 33)

[110] M. Korostelev, *Optics design and performance of an ultra-low emittance damping ring for the Compact Linear Collider*, PhD thesis, University of Lausanne, Ecole Polytechnique Federale de Lausanne, CERN-THESIS-2007-008, 2006. (cited p. 33)

[111] M. Korostelev and F. Zimmermann, Optimization of CLIC damping ring design parameters, in *Prooceedings of the European Particle Accelerator Conference 2002*, p. MOPRI032, JACoW, Paris, France, 2002. (cited p. 33)

[112] M. Korostelev, J. Wenninger and F. Zimmermann, Flexibility, tolerances, and beam-based tuning of the CLIC damping ring, in *Proceedings of the European Particle Accelerator Conference 2004*, p. MOPLT024, JACoW, Lucerne, Switzerland, 2004. (cited p. 33)

[113] M. Korostelev and F. Zimmermann, Correction of vertical dispersion and betatron coupling for the CLIC damping ring, in *Proceedings of the European Particle Accelerator Conference 2006*, p. MOPLS135, JACoW, Edinburgh, Scotland, 2006. (cited p. 33, 62)

[114] C. Skokos and Y. Papaphilippou, Non linear dynamics study of the CLIC damping rings using symplectic integrators, in *Proceedings of the European Particle Accelerator Conference 2008*, p. MOPP061, JACoW, Genoa, Italy, 2008. (cited p. 33)

[115] E. Levichev, Lattice options for the CLIC damping rings, in *Proceedings of the Particle Accelerator Conference 2009*, p. WE6PFP105, JACoW, Vancouver, Canada, 2009. (cited p. 33)

[116] C. Steier, J. Byrd and P. Kuske, Energy calibration of the electron beam of the ALS using resonant depolarisation, in *Proceedings of the European Particle Accelerator Conference 2000*, p. MOP5B03, JACoW, Vienna, Austria, 2000. (cited p. 36, 39, 45)

[117] C. Steier *et al.*, Commissioning of the ALS with superbends, in *Proceedings of the European Particle Accelerator Conference 2002*, p. TUPRI033, JACoW, Paris, France, 2002. (cited p. 36)

[118] R. Chasman, G. K. Green and E. M. Rowe, Preliminary design of a dedicated synchrotron radiation facility, in *Proceedings of the Particle Accelerator Conference 1975*, pp. 1765 –1767, JACoW, Washnigton, DC, USA, 1975, doi: 10.1109/TNS.1975.4327987. (cited p. 36)

[119] G. Vignola, Nuclear Instruments and Methods in Physics Research Section A: Accelerators, Spectrometers, Detectors and Associated Equipment **246**, 12 (1986), doi:10.1016/0168-9002(86)90035-5. (cited p. 36)

[120] C.-x. Wang, Physical Review Special Topics: Accelerators and Beams **12**, 061001 (2009), doi:10.1103/PhysRevSTAB.12.061001. (cited p. 37)

[121] Y. Jiao, Y. Cai and A. W. Chao, Physical Review Special Topics: Accelerators and Beams **14**, 054002 (2011), doi:10.1103/PhysRevSTAB.14.054002. (cited p. 37)

[122] L. C. Teng, Fermilab Report No. TM-1269, 1984 (unpublished). (cited p. 37)

[123] S. Y. Lee and L. Teng, Theoretical minimum emittance lattice for an electron storage ring, in *Proceedings of the Particle Accelerator Conference 1991*, pp. 2679–2681, JACoW, San Francisco, CA, USA, 1991. (cited p. 37)

[124] J. T. Tanabe, *Iron Dominated Electromagnets: Design, Fabrication, Assembly and Measurements* (World Scientific, Singapore, 2005), doi:10.1142/5823, SLAC-R-754. (cited p. 37, 38, 53, 69)

[125] C. H. Chang *et al.*, The TBA prototype dipole magnet of SRRC, in *11th International Conference on Magnet Technology*, edited by T. Sekiguchi and S. Shimamoto, pp. 187–193, Tsukuba, Japan, 1990, Springer, doi:10.1007/978-94-009-0769-0_32. (cited p. 37)

[126] C. S. Hwang, C. H. Chang, P. K. Tseng, T. M. Uen and J. Le Duff, Nuclear Instruments and Methods in Physics Research Section A: Accelerators, Spectrometers, Detectors and Associated Equipment **383**, 301 (1996), doi: 10.1016/S0168-9002(96)00801-7. (cited p. 37)

[127] C. S. Hwang, C. H. Chang, G. J. Hwang, T. M. Uen and P. K. Tseng, Magnetics, IEEE Transactions on **32**, 3032 (1996), doi:10.1109/20.511515. (cited p. 37)

[128] D. Einfeld *et al.*, Modelling of gradient bending magnets for the beam dynamics studies at ALBA, in *Proceedings of the Particle Accelerator Conference 2007*, p. TUPMN068, JACoW, Albuquerque, NM, USA, 2007. (cited p. 37, 58)

[129] S. C. Leemann and A. Streun, Physical Review Special Topics: Accelerators and Beams **14**, 030701 (2011), doi:10.1103/PhysRevSTAB.14.030701. (cited p. 37, 58)

[130] Y. Nosochkov, K. L. F. Bane, Y. Cai, R. Hettel and M.-H. Wang, Lattice design for PEP-X ultimate storage ring light source, in *Proceedings of International Particle Accelerator Conference 2011*, p. THPC075, JACoW, San Sebastian, Spain, 2011. (cited p. 37, 58)

[131] Y. Cai *et al.*, Physical Review Special Topics: Accelerators and Beams **15**, 054002 (2012), doi:10.1103/PhysRevSTAB.15.054002. (cited p. 37, 58)

[132] Y. Chen *et al.*, Nuclear Instruments and Methods in Physics Research Section A: Accelerators, Spectrometers, Detectors and Associated Equipment **682**, 85 (2012), doi:10.1016/j.nima.2012.04.046. (cited p. 37)

[133] A. Jackson, The magnet lattice of the LBL, 1-2 GeV synchrotron radiation source, in *Proceedings of the Particle Accelerator Conference 1987*, pp. 476–478, JACoW, Washington, DC, USA, 1987. (cited p. 38, 147)

[134] A. Jackson *et al.*, The LBL Advanced Light Source, in *Proceedings of the European Particle Accelerator Conference 1988*, pp. 359–61, JACoW, Rome, Italy, 1988. (cited p. 38, 147)

[135] M. Xiao, Recycler chromaticities and end shims for NOVA at Fermilab, in *Proceedings of the International Particle Accelerator Conference 2012*, p. TUPPR085, JACoW, New Orleans, USA, 2012. (cited p. 38, 59, 147)

[136] J. P. Shan, S. G. Peggs and S. A. Bogacz, Particle Accelerators **45**, 1 (1994). (cited p. 39)

[137] L. Arnaudon *et al.*, European Laboratory for Particle Physics Report No. CERN SL/94-71, 1994 (unpublished). (cited p. 39, 42)

[138] R. Thornagel, G. Ulm, P. Kuske, T. Mayer and K. Ott, Monitoring the Beam Depolarization with a DC Current Transformer at BESSY I, in *Proceedings of the European Particle Accelerator Conference 1994*, pp. 1719–21, JACoW, London, England, 1994. (cited p. 39, 45, 47)

[139] L. Arnaudon *et al.*, Zeitschrift für Physik C Particles and Fields **66**, 45 (1995), doi:10.1007/BF01496579. (cited p. 39, 42, 43)

[140] P. Kuske, R. Goergen, J. Kuszynski and P. Schmid, Improvements of the set-up and procedures for beam energy measurements at BESSY II, in *Proceedings of the International Particle Accelerator Conference 2010*, p. MOPD083, JACoW, Kyoto, Japan, 2010. (cited p. 39, 41, 45, 46)

[141] S. C. Leemann, M. Böge, M. Dehler, V. Schlott and A. Streun, Precise beam energy calibration at the SLS storage ring, in *Proceedings of the European Particle Accelerator Conference 2002*, p. TUPRI011, JACoW, Paris, France, 2002. (cited p. 39, 45)

[142] A.-S. Müller *et al.*, Energy calibration of the ANKA storage ring, in *Proceedings of the European Particle Accelerator Conference 2004*, p. THPKF022, JACoW, Lucerne, Switzerland, 2004. (cited p. 39, 45)

[143] R. Belbéoch *et al.*, Recent Experiments with ACO, in *Proceedings of the Soviet Conference on Charged-Particle Accelerators: Moscow, 9-16 October, 1968*, edited by A. Vasilev, Vol. 1, pp. 130–134, Jerusalem, Israel, 1972, Israel Program for Scientific Translations. (cited p. 39)

[144] (The Orsay Storage Ring Group), G. Arzelier *et al.*, Status Report on ACO, in *Proceedings of the 8th International Conference on High-Energy Accelerators*, pp. 127–31, CERN, Geneva, Switzerland, 1971. (cited p. 39, 44)

[145] S. I. Serednyakov, A. N. Skrinsky, G. M. Tumaikin and Y. M. Shatunov, Zhurnal Eksperimentalnoi i Teoreticheskoi Fiziki **71**, 2025 (1976), [Sov. Phys. JETP **44**, 1063-7 (1976)]. (cited p. 39, 44)

[146] Y. S. Derbenev *et al.*, Particle Accelerators **10**, 177 (1980). (cited p. 39)

[147] J. R. Johnson *et al.*, Nuclear Instruments and Methods in Physics Research **204**, 261 (1983), doi:10.1016/0167-5087(83)90056-X. (cited p. 39, 44, 49, 132)

[148] A. A. Sokolov and I. M. Ternov, Doklady Akademii Nauk SSSR **153**, 1052 (1963), [Sov. Phys. Dokl. **8**, 1203-5 (1964)]. (cited p. 39, 41, 133)

[149] J. D. Jackson, Reviews of Modern Physics **48**, 417 (1976), doi: 10.1103/RevModPhys.48.417. (cited p. 39, 40, 133)

[150] S. R. Mane, Y. M. Shatunov and K. Yokoya, Reports on Progress in Physics **68**, 1997 (2005), doi:10.1088/0034-4885/68/9/R01. (cited p. 39, 41, 42, 44, 133)

[151] V. Bargmann, L. Michel and V. L. Telegdi, Physical Review Letters **2**, 435 (1959), doi:10.1103/PhysRevLett.2.435. (cited p. 42)

[152] B. Odom, D. Hanneke, B. D'Urso and G. Gabrielse, Physical Review Letters **97**, 030801 (2006), doi:10.1103/PhysRevLett.97.030801. (cited p. 43)

[153] P. J. Mohr, B. N. Taylor and D. B. Newell, Reviews of Modern Physics **84**, 1527 (2012), doi:10.1103/RevModPhys.84.1527. (cited p. 43)

[154] J. Zhang *et al.*, Experiments to measure electron beam energy using spin depolarization method on SOLEIL storage ring, in *Proceedings of the International Particle Accelerator Conference 2011*, p. THPC006, JACoW, San Sebastian, Spain, 2011. (cited p. 43, 44, 45)

[155] V. N. Baier and V. A. Khoze, Atomnaya Énergiya **25**, 440 (1968), doi: 10.1007/BF01239705, [Sov. J. At. Energy **25**, 1256 (1968)]. (cited p. 44, 132)

[156] G. W. Ford and C. J. Mullin, Physical Review **108**, 477 (1957), doi: 10.1103/PhysRev.108.477. (cited p. 44)

[157] A. Rączka and R. Rączka, Physical Review **110**, 1469 (1958), doi: 10.1103/PhysRev.110.1469. (cited p. 44)

[158] G. W. Ford and C. J. Mullin, Physical Review **110**, 1485 (1958), doi: 10.1103/PhysRev.110.1485.2. (cited p. 44)

[159] C. Bernardini *et al.*, Physical Review Letters **10**, 407 (1963), doi: 10.1103/PhysRevLett.10.407. (cited p. 44, 84)

[160] P. Kuske and T. Mayer, Set up for beam energy measurements at BESSY II, in *Proceedings of the European Particle Accelerator Conference 1996*, p. TUP005L, JACoW, Sitges, Spain, 1996. (cited p. 45)

[161] P. Kuske and R. Goergen, High precision determination of the energy at BESSY II, in *Proceedings of the European Particle Accelerator Conference 2000*, p. WEP3A09, JACoW, Vienna, Austria, 2000. (cited p. 45)

[162] I. P. S. Martin, M. Apollonio, R. T. Fielder, G. Rehm and R. Bartolini, Energy measurements with resonant spin depolarisation at Diamond, in *Proceedings of the International Particle Accelerator Conference 2011*, p. TUPC159, JACoW, San Sebastian, Spain, 2011. (cited p. 45)

[163] J. Zhang *et al.*, Nuclear Instruments and Methods in Physics Research Section A: Accelerators, Spectrometers, Detectors and Associated Equipment **697**, 1 (2013), doi:10.1016/j.nima.2012.09.003. (cited p. 45)

[164] K. P. Wootton *et al.*, Physical Review Special Topics: Accelerators and Beams **16**, 074001 (2013), doi:10.1103/PhysRevSTAB.16.074001. (cited p. 45, 50, 53, 58, 125, 147, 151)

[165] R. Hofstadter, Physical Review **74**, 100 (1948), doi:10.1103/PhysRev.74.100. (cited p. 46)

[166] A. Zhukov, Beam loss monitors (BLMs): Physics, simulations and applications in accelerators, in *Proceedings of Beams Instrumentation Workshop 2010*, p. THTNB01, JACoW, Santa Fe, NM, USA, 2010. (cited p. 46)

[167] C. Grupen and B. Shwartz, *Particle Detectors* (Cambridge University Press, Cambridge, United Kingdom, 2008), doi:10.1017/CBO9780511534966. (cited p. 46)

[168] G. M. Griffiths, Canadian Journal of Physics **33**, 209 (1955), doi:10.1139/p55-026. (cited p. 46)

[169] V. N. Baĭer, Uspekhi Fizicheskikh Nauk **105**, 441 (1971), doi:10.1070/PU1972v014n06ABEH004751, [Sov. Phys. Usp. **14**, 695 (1972)]. (cited p. 47, 132)

[170] S. R. Mane, AIP Conference Proceedings **187**, 959 (1989), doi:10.1063/1.38349. (cited p. 49)

[171] S. R. Mane, (private communication), 2013. (cited p. 49)

[172] K. P. Wootton *et al.*, Resonant spin depolarisation measurements at the SPEAR3 electron storage ring, in *Proceedings of the International Particle Accelerator Conference 2012*, p. MOPPR001, JACoW, New Orleans, USA, 2012, SLAC-PUB-15794. (cited p. 50, 51, 53, 101)

[173] X. Huang, J. A. Safranek and D. Dell Orco, Lattice modeling for SPEAR3, in *Proceedings of the International Particle Accelerator Conference 2010*, p. THPE048, JACoW, Kyoto, Japan, 2010. (cited p. 50, 53, 150)

[174] M. Attal *et al.*, Physical Review Special Topics: Accelerators and Beams **16**, 054001 (2013), doi:10.1103/PhysRevSTAB.16.054001. (cited p. 52)

[175] A. Terebilo, Stanford Linear Accelerator Center Report No. SLAC-PUB-8732, 2001 (unpublished). (cited p. 55, 145)

[176] X. R. Resende, L. L. R. Basílio, P. P. Sanchez and G. Tosin, Modeling of bending magnets for SIRIUS, in *Proceedings of the International Particle Accelerator Conference 2012*, p. MOPPC053, JACoW, New Orleans, USA, 2012. (cited p. 58)

[177] S. Machida *et al.*, Nature Physics **8**, 243 (2012), doi:10.1038/nphys2179. (cited p. 58)

[178] G. H. Rees, D. J. Kelliher, S. Machida, C. R. Prior and S. L. Sheehy, A model for a high-power scaling FFAG ring, in *Proceedings of the International Particle Accelerator Conference 2012*, p. MOPPD020, JACoW, New Orleans, USA, 2012. (cited p. 58)

[179] S. L. Sheehy, K. J. Peach, H. Witte, D. J. Kelliher and S. Machida, Physical Review Special Topics: Accelerators and Beams **13**, 040101 (2010), doi: 10.1103/PhysRevSTAB.13.040101. (cited p. 58)

[180] Y. Giboudot and A. Wolski, Physical Review Special Topics: Accelerators and Beams **15**, 044001 (2012), doi:10.1103/PhysRevSTAB.15.044001. (cited p. 58)

[181] K. J. Peach *et al.*, Physical Review Special Topics: Accelerators and Beams **16**, 030101 (2013), doi:10.1103/PhysRevSTAB.16.030101. (cited p. 58)

[182] J. P. Delahaye and J. P. Potier, Reverse bending magnets in a combined-function lattice for the CLIC damping ring, in *Proceedings of the Particle Accelerator Conference 1989*, pp. 1611–3, JACoW, Chicago, USA, 1989. (cited p. 59)

[183] A. Streun, Nuclear Instruments and Methods in Physics Research Section A: Accelerators, Spectrometers, Detectors and Associated Equipment **737**, 148 (2014), doi:10.1016/j.nima.2013.11.064. (cited p. 59)

[184] A. Vivoli and M. Martini, Intra-beam scattering in the CLIC damping rings, in *Proceedings of the International Particle Accelerator Conference 2010*, p. WEPE090, Kyoto, Japan, 2010. (cited p. 62)

[185] G. Vanbavinckhove, *Optics measurements and corrections for colliders and other storage rings*, PhD thesis, NIKHEF, Universiteit van Amsterdam, Amsterdam, Netherlands, 2013, CERN-THESIS-2013-022. (cited p. 62)

[186] K. G. Panagiotidis, *Low Emittance Tuning Studies for Future Linear Colliders: Design Issues and Practical Techniques*, PhD thesis, University of Liverpool, Liverpool, United Kingdon, 2010. (cited p. 63)

[187] T. Raubenheimer and R. Ruth, Analytic estimates of coupling in damping rings, in *Proceedings of the Particle Accelerator Conference 1989*, pp. 1435–7, JACoW, Chicago, USA, 1989. (cited p. 66)

[188] K. P. Wootton *et al.*, Alignment tolerances for vertical emittance, in *Proceedings of the International Particle Accelerator Conference 2011*, p. TUPC046, JACoW, San Sebastian, Spain, 2011. (cited p. 69, 74, 75, 76, 77)

[189] J. C. Nash, *Compact Numerical Methods for Computers: Linear Algebra and Function Minimisation*, 2nd ed. (Adam Hilger, Bristol, United Kingdom, 1990). (cited p. 70)

[190] A. W. Chao, Journal of Applied Physics **50**, 595 (1979), doi:10.1063/1.326070. (cited p. 70, 71)

[191] F. Schmidt, *MAD-X User's Guide*, European Organization for Nuclear Research, Geneva, Switzerland, 2007. (cited p. 70)

[192] P. Röjsel, Nuclear Instruments and Methods in Physics Research Section A: Accelerators, Spectrometers, Detectors and Associated Equipment **343**, 374 (1994), doi:10.1016/0168-9002(94)90214-3. (cited p. 73)

[193] I. Barnett *et al.*, Dynamic beam based alignment, in *Proceedings of the Beam Instrumentation Workshop 1994*, pp. 530–5, Vancouver, Canada, 1994, CERN-SL-94-84-BI. (cited p. 73)

[194] G. Portmann, D. Robin and L. Schachinger, Automated beam based alignment of the ALS quadrupoles, in *Proceedings of the Particle Accelerator Conference 1995*, p. RPQ13, JACoW, Dallas, Texas, USA, 1995. (cited p. 73)

[195] R. Dowd, G. S. LeBlanc, Y.-R. E. Tan and K. P. Wootton, Beam based magnet alignment for emittance coupling minimization, in *Proceedings of the International Particle Accelerator Conference 2013*, p. TUPWA003, JACoW, Shanghai, China, 2013. (cited p. 79, 81, 119, 135)

[196] M. Lee, Y. Zambre and W. Corbett, SLAC Report No. SLAC-PUB-5701, 1992 (unpublished). (cited p. 79)

[197] M. Aiba *et al.*, Physical Review Special Topics: Accelerators and Beams **16**, 012802 (2013), doi:10.1103/PhysRevSTAB.16.012802. (cited p. 79, 84)

[198] W. J. Corbett, M. J. Lee and V. Ziemann, A fast model-calibration procedure for storage rings, in *Proceedings of the Particle Accelerator Conference 1993*, pp. 108–110, JACoW, Washington, DC, USA, 1993. (cited p. 79)

[199] J. Safranek, Nuclear Instruments and Methods in Physics Research Section A: Accelerators, Spectrometers, Detectors and Associated Equipment **388**, 27 (1997), doi:10.1016/S0168-9002(97)00309-4. (cited p. 79, 110, 119, 122)

[200] J. Safranek, G. Portmann, A. Terebilo and C. Steier, MATLAB-based LOCO, in *Proceedings of the European Particle Accelerator Conference 2002*, p. WEPLE003, JACoW, Paris, France, 2002. (cited p. 79)

[201] J. Safranek and M. Lee, AIP Conference Proceedings **315**, 128 (1994), doi: 10.1063/1.46761. (cited p. 79)

[202] J. Safranek and S. Krinsky, Plans to increase source brightness of NSLS X-ray ring, in *Prooceedings of the Particle Accelerator Conference 1993*, pp. 1491–1493, JACoW, Washington, DC, USA, 1993. (cited p. 80)

[203] C. Steier, D. Robin, A. Wolski, G. Portmann and J. Safranek, Coupling correction and beam dynamics at ultralow vertical emittance in the ALS, in *Proceedings of the Particle Accelerator Conference 2003*, p. RPPG018, JACoW, Portland, OR, USA, 2003. (cited p. 80)

[204] Editorial, Nature **456**, 422 (2008), doi:10.1038/456422a. (cited p. 83)

[205] A. Cho, Science **321**, 34 (2008), doi:10.1126/science.321.5885.34. (cited p. 83)

[206] Y. Honda *et al.*, Nuclear Instruments and Methods in Physics Research Section A: Accelerators, Spectrometers, Detectors and Associated Equipment **538**, 100 (2005), doi:10.1016/j.nima.2004.08.122. (cited p. 83)

[207] J. Flanagan, Diagnostics for ultra-low emittance beams, in *Proceedings of the International Particle Accelerator Conference 2011*, p. WEYB01, JACoW, San Sebastian, Spain, 2011. (cited p. 83)

[208] A. Wolski, D. Rubin, D. Sagan and J. Shanks, Physical Review Special Topics: Accelerators and Beams **14**, 072804 (2011), doi: 10.1103/PhysRevSTAB.14.072804. (cited p. 84)

[209] A. Piwinski, DESY Report No. 98-179, 1999 (unpublished), arXiv:physics/9903034 [physics.acc-ph]. (cited p. 84)

[210] J. Camas, C. Fischer, J. J. Gras, R. Jung and J. Koopman, Observation of thermal effects on the LEP wire scanners, in *Proceedings of the Particle Accelerator Conference 1995*, p. TPC21, JACoW, Dallas, Texas, USA, 1995. (cited p. 85)

[211] H. Sakai *et al.*, Physical Review Special Topics: Accelerators and Beams **5**, 122801 (2002), doi:10.1103/PhysRevSTAB.5.122801. (cited p. 85)

[212] A. Bosco *et al.*, Nuclear Instruments and Methods in Physics Research Section A: Accelerators, Spectrometers, Detectors and Associated Equipment **592**, 162 (2008), doi:10.1016/j.nima.2008.04.012. (cited p. 85)

[213] S. T. Boogert *et al.*, Physical Review Special Topics: Accelerators and Beams **13**, 122801 (2010), doi:10.1103/PhysRevSTAB.13.122801. (cited p. 85)

[214] (ATF Collaboration), K. Kubo *et al.*, Physical Review Letters **88**, 194801 (2002), doi:10.1103/PhysRevLett.88.194801. (cited p. 85)

[215] T. Shintake, Nuclear Instruments and Methods in Physics Research Section A: Accelerators, Spectrometers, Detectors and Associated Equipment **311**, 453 (1992), doi:10.1016/0168-9002(92)90641-G. (cited p. 85)

[216] Y. Yamaguchi *et al.*, Physics Procedia **37**, 1983 (2012), doi: 10.1016/j.phpro.2012.02.520, Proceedings of the 2nd International Conference on Technology and Instrumentation in Particle Physics (TIPP 2011). (cited p. 85)

[217] J. Yan *et al.*, Physics Procedia **37**, 1989 (2012), doi: 10.1016/j.phpro.2012.02.522, Proceedings of the 2nd International Conference on Technology and Instrumentation in Particle Physics (TIPP 2011). (cited p. 85)

[218] J. Yan, Nuclear Instruments and Methods in Physics Research Section A: Accelerators, Spectrometers, Detectors and Associated Equipment **740**, 131 (2014), doi:10.1016/j.nima.2013.11.041. (cited p. 85)

[219] P. Elleaume, C. Fortgang, C. Penel and E. Tarazona, Journal of Synchrotron Radiation **2**, 209 (1995), doi:10.1107/S0909049595008685. (cited p. 85)

[220] C. Thomas, G. Rehm, I. Martin and R. Bartolini, Physical Review Special Topics: Accelerators and Beams **13**, 022805 (2010), doi: 10.1103/PhysRevSTAB.13.022805. (cited p. 85)

[221] H. Sakai *et al.*, Physical Review Special Topics: Accelerators and Beams **10**, 042801 (2007), doi:10.1103/PhysRevSTAB.10.042801. (cited p. 85)

[222] B. K. Scheidt, Detection of hard X-rays in air for precise monitoring of vertical position & emittance in the ESRF dipoles, in *Proceedings of the Workshop on Beam Diagnostics and Instrumentation for Particle Accelerators 2005*, p. CTWM01, JACoW, Lyon, France, 2005. (cited p. 85)

[223] Å. Andersson, M. Böge, A. Lüdeke, V. Schlott and A. Streun, Nuclear Instruments and Methods in Physics Research Section A: Accelerators, Spectrometers, Detectors and Associated Equipment **591**, 437 (2008), doi: 10.1016/j.nima.2008.02.095. (cited p. 85, 94)

[224] N. Milas *et al.*, Design and expected performance of the new SLS beam size monitor, in *Proceedings of the International Beams Instrumentation Conference 2012*, p. TUCC03, JACoW, Tsukuba, Japan, 2012. (cited p. 85)

[225] V. Schlott *et al.*, Commissioning experience and first results from the new SLS beam size monitor, in *Proceedings of the International Beams Instrumentation Conference 2013*, p. TUPF09, JACoW, Oxford, United Kingdom, 2013. (cited p. 85)

[226] T. Mitsuhashi, Spatial coherency of the synchrotron radiation at the visible light region and its application for the electron beam profile measurement, in *Proceedings of the Particle Accelerator Conference 1997*, p. 3V016, JACoW, Vancouver, Canada, 1997. (cited p. 85)

[227] T. Mitsuhashi, *Beam Measurement: Proceedings of the Joint US–CERN–Japan–Russia School on Particle Accelerators* (World Scientific, 1998), chap. Beam Profile and Size Measurement by SR Interferometers, pp. 399–427, doi: 10.1142/9789812818003_0018. (cited p. 85)

[228] T. Naito and T. Mitsuhashi, Physical Review Special Topics: Accelerators and Beams **9**, 122802 (2006), doi:10.1103/PhysRevSTAB.9.122802. (cited p. 85)

[229] A. A. Michelson, The Astrophysical Journal **51**, 257 (1920), doi: 10.1086/142550. (cited p. 85)

[230] P. H. van Cittert, Physica **1**, 201 (1934), doi:10.1016/S0031-8914(34)90026-4. (cited p. 85)

[231] F. Zernike, Physica **5**, 785 (1938), doi:10.1016/S0031-8914(38)80203-2. (cited p. 85)

[232] P. H. van Cittert, Physica **24**, 505 (1958), doi:10.1016/S0031-8914(58)96209-8. (cited p. 85)

[233] T. Naito and T. M. Mitsuhashi, Improvement of the resolution of SR interferometer at KEK-ATF damping ring, in *Proceedings of the International Particle Accelerator Conference 2010*, p. MOPE009, JACoW, Kyoto, Japan, 2010. (cited p. 86)

[234] T. Mitsuhashi, Recent progess in SR interferometer, in *Proceedings of the International Beams Instrumentation Conference 2012*, p. WEIC02, JACoW, Tsukuba, Japan, 2012. (cited p. 86)

[235] M. J. Boland, T. M. Mitsuhashi, T. Naito and K. P. Wootton, Intensity imbalance optical interferometer beam size monitor, in *Proceedings of the International Beams Instrumentation Conference 2012*, p. WECC03, JACoW, Tsukuba, Japan, 2012. (cited p. 86, 88)

[236] M. J. Boland, T. Mitsuhashi and K. P. Wootton, Low noise and high dynamic range optical interferometer beamsize measurements, in *Proceedings of the International Beams Instrumentation Conference 2013*, p. TUPF20, JACoW, Oxford, United Kingdom, 2013. (cited p. 86, 88)

[237] M. J. Boland *et al.*, X-ray and optical diagnostic beamlines at the Australian Synchrotron storage ring, in *Proceedings of the European Particle Accelerator Conference 2006*, p. THPLS002, JACoW, Edinburgh, Scotland, 2006. (cited p. 86, 87)

[238] G. LeBlanc, M. Boland and E. Tan, Australian Synchrotron Report No. AS-200309-02, 2003 (unpublished). (cited p. 86)

[239] M. J. Boland and M. Spencer, Vertical beam profile measurement and analysis with an X-ray pinhole, in *Proceedings of the European Particle Accelerator Conference 2008*, p. TUPC009, JACoW, Genoa, Italy, 2008. (cited p. 86)

[240] K. Wootton, Electron beam emittance measurements using optical interferometry, Honours thesis, School of Physics, Monash University, Australia, 2009. (cited p. 87)

[241] K. P. Wootton and M. J. Boland, A novel synchrotron radiation interferometer for the Australian Synchrotron, in *Proceedings of the International Particle Accelerator Conference 2010*, p. MOPD079, JACoW, Kyoto, Japan, 2010. (cited p. 87, 88)

[242] O. Chubar and P. Elleaume, Accurate and efficient computation of synchrotron radiation in the near field region, in *Proceedings of the European Particle Accelerator Conference 1998*, p. THP01G, JACoW, Stockholm, Sweden, 1998. (cited p. 87)

[243] D. Creagh, J. McKinlay and P. Dumas, Vibrational Spectroscopy **41**, 213 (2006), doi:10.1016/j.vibspec.2006.02.009. (cited p. 87)

[244] G. Dattoli, G. K. Voykov and M. Carpanese, Physical Review E **52**, 6809 (1995), doi:10.1103/PhysRevE.52.6809. (cited p. 88, 93)

[245] T. Moreno, E. Otero and P. Ohresser, Journal of Synchrotron Radiation **19**, 179 (2012), doi:10.1107/S0909049511052873. (cited p. 88, 128)

[246] M. Borland, Calculating emittance from images of undulator radiation, in *Proceedings of the Particle Accelerator Conference 1989*, pp. 1228–1230, JACoW, Chicago, USA, 1989. (cited p. 88)

[247] E. Tarazona and P. Elleaume, Review of Scientific Instruments **66**, 1974 (1995), doi:10.1063/1.1145774. (cited p. 88)

[248] U. Hahn *et al.*, Journal of Synchrotron Radiation **4**, 1 (1997), doi:10.1107/S0909049596010734. (cited p. 88)

[249] K.-J. Kim, Nuclear Instruments and Methods in Physics Research Section A: Accelerators, Spectrometers, Detectors and Associated Equipment **246**, 71 (1986), doi:10.1016/0168-9002(86)90048-3. (cited p. 88)

[250] T. Tanaka and H. Kitamura, Journal of Synchrotron Radiation **8**, 1221 (2001), doi:10.1107/S090904950101425X. (cited p. 88, 92, 94, 95, 102, 103, 110, 111, 112, 114, 116, 126)

[251] D. F. Alferov, Y. A. Bashmakov and E. G. Bessenov, Zhurnal Tekhnicheskoi Fiziki **43**, 2126 (1973), [Soviet Physics – Technical Physics (1974) **18**, 1336]. (cited p. 88)

[252] K. P. Wootton *et al.*, Vertical emittance measurements using a vertical undulator, in *Proceedings of the International Beams Instrumentation Conference 2012*, p. MOCB04, JACoW, Tsukuba, Japan, 2012. (cited p. 92, 93)

[253] M. S. Bakeman *et al.*, AIP Conference Proceedings **1086**, 643 (2009), doi:10.1063/1.3080983. (cited p. 93, 94)

[254] M. S. Bakeman *et al.*, Undulator-based laser wakefield accelerator electron beam diagnostic, in *Proceedings of the Particle Accelerator Conference 2009*, p. WE6RFP074, JACoW, Vancouver, Canada, 2009. (cited p. 93, 94, 124)

[255] M. S. Bakeman *et al.*, AIP Conference Proceedings **1299**, 133 (2010), doi:10.1063/1.3520301. (cited p. 93, 94)

[256] M. S. Bakeman *et al.*, Undulator-based laser wakefield accelerator electron beam diagnostic, in *Proceedings of the Particle Accelerator Conference 2011*, p. MOP161, JACoW, New York, NY, USA, 2011. (cited p. 93, 94)

[257] B. Shaw *et al.*, AIP Conference Proceedings **1507**, 310 (2012), doi: 10.1063/1.4773713. (cited p. 93, 125)

[258] E. Tarazona and P. Elleaume, Review of Scientific Instruments **67**, 3368 (1996), doi:10.1063/1.1147371. (cited p. 93)

[259] Å. Andersson *et al.*, Electron beam characterisation by undulator radiation, in *Proceedings of the European Particle Accelerator Conference 1998*, p. WEP05J, JACoW, Stockholm, Sweden, 1998. (cited p. 93)

[260] B. Yang and J. Xu, Measurement of the APS storage ring electron beam energy spread using undulator spectra, in *Proceedings of the Particle Accelerator Conference 2001*, p. WPAH108, JACoW, Chicago, IL, USA, 2001. (cited p. 93)

[261] S. Takano, On emittance diagnostics of electron beam by observing synchrotron radiation from a vertical undulator (transparencies), in *Proceedings of the workshop on 'Precise measurements of electron beam emittances'*, edited by J. Urakawa, S. Kamada, K. Nakajima and T. Mitsuhashi, Vol. 97-20, p. 20, Tsukuba, Ibaraki, Japan, 1997. (cited p. 93, 94, 104, 125, 126)

[262] S. Takano, (private communication), 2012. (cited p. 93)

[263] K. P. Wootton *et al.*, Physical Review Letters **109**, 194801 (2012), doi: 10.1103/PhysRevLett.109.194801. (cited p. 93, 116, 125)

[264] C. Wang *et al.*, Calculation of undulator radiation from measured magnetic fields and comparison with measured spectra, in *Proceedings of the European Particle Accelerator Conference 1992*, pp. 928–31, JACoW, Berlin, Germany, 1992. (cited p. 93, 96)

[265] G. Dattoli and G. Voykov, Il Nuovo Cimento B **111**, 743 (1996), doi: 10.1007/BF02743404. (cited p. 93, 94, 105)

[266] M. Bazin, Y. Farge, M. Lemonnier, J. Perot and Y. Petroff, Nuclear Instruments and Methods **172**, 61 (1980), doi:10.1016/0029-554X(80)90608-4. (cited p. 96)

[267] T. Mitsuhashi, T. Shioya, M. Ando and T. Yamakawa, Nuclear Instruments and Methods in Physics Research Section A: Accelerators, Spectrometers, Detectors and Associated Equipment **246**, 54 (1986), doi:10.1016/0168-9002(86)90044-6. (cited p. 96)

[268] T. Tanaka, X.-M. Maréchal, T. Hara, T. Tanabe and H. Kitamura, Journal of Synchrotron Radiation **5**, 414 (1998), doi:10.1107/S0909049597013745. (cited p. 96)

[269] B. C. C. Cowie, A. Tadich and L. Thomsen, AIP Conference Proceedings **1234**, 307 (2010), doi:10.1063/1.3463197. (cited p. 96, 98, 99, 101)

[270] S. Sasaki, T. Shimada, K. Yanagida, H. Kobayashi and Y. Miyahara, Nuclear Instruments and Methods in Physics Research Section A: Accelerators, Spectrometers, Detectors and Associated Equipment **347**, 87 (1994), doi: 10.1016/0168-9002(94)91860-0. (cited p. 97)

[271] C. W. Ostenfeld *et al.*, APPLE-II and TESLA FEL undulators at Danfysik A/S, in *Proceedings of the Particle Accelerator Conference 2007*, p. TUPMN006, JACoW, Albuquerque, New Mexico, USA, 2007. (cited p. 97, 101, 102, 128)

[272] J. Bahrdt *et al.*, Physical Review Letters **111**, 034801 (2013), doi: 10.1103/PhysRevLett.111.034801. (cited p. 98, 115, 128, 132)

[273] B. C. C. Cowie, (private communication), 2012. (cited p. 99)

[274] M. Krumrey and E. Tegeler, Review of Scientific Instruments **63**, 797 (1992), doi:10.1063/1.1143800. (cited p. 99, 100, 101)

[275] B. L. Henke, E. M. Gullikson and J. C. Davis, Atomic Data and Nuclear Data Tables **54**, 181 (1993), doi:10.1006/adnd.1993.1013. (cited p. 99, 100)

[276] Opto Diode Corporation, *IRD UV Photodiodes – Absolute UV Silicon Photodiodes – AXUV Series*, Newbury Park, CA, USA, 2012. (cited p. 100, 101)

[277] M. Krumrey *et al.*, AIP Conference Proceedings **705**, 861 (2004), doi: 10.1063/1.1757931. (cited p. 100, 101)

[278] Hamamatsu Photonics K.K., *GaP photodiode, Schottky type – G1961, G1962, G1963*, Hamamatsu City, Japan, 2001. (cited p. 101)

[279] Opto Diode Corporation, *IRD Photodiode – AXUV 100G*, Newbury Park, CA, USA, 2013. (cited p. 101)

[280] C. Leubner and P. Torggler, Optics Communications **48**, 362 (1984), doi: 10.1016/0030-4018(84)90316-X. (cited p. 105)

[281] R. P. Walker, Nuclear Instruments and Methods in Physics Research Section A: Accelerators, Spectrometers, Detectors and Associated Equipment **335**, 328 (1993), doi:10.1016/0168-9002(93)90288-S. (cited p. 105)

[282] R. Talman, Nuclear Instruments and Methods in Physics Research Section A: Accelerators, Spectrometers, Detectors and Associated Equipment **489**, 519 (2002), doi:10.1016/S0168-9002(02)00898-7. (cited p. 106)

[283] A. Franchi *et al.*, Physical Review Special Topics: Accelerators and Beams **14**, 034002 (2011), doi:10.1103/PhysRevSTAB.14.034002. (cited p. 111)

[284] K. P. Wootton, M. J. Boland, B. C. C. Cowie and R. P. Rassool, APPLE-II undulator magnetic fields characterised from undulator radiation, in *Proceedings of the International Beams Instrumentation Conference 2013*, p. TUPF19, JACoW, Oxford, United Kingdom, 2013. (cited p. 114, 116, 117)

[285] J. Corbett, G. Portmann and A. Terebilo, Accelerator control middle layer, in *Proceedings of the Particle Accelerator Conference 2003*, p. WPPE020, JACoW, Portland, Oregon, USA, 2003. (cited p. 117)

[286] K. P. Wootton, M. J. Boland, B. C. C. Cowie, R. Dowd and R. P. Rassool, Vertical undulator emittance measurement: A statistical approach, in *Proceedings of the International Beams Instrumentation Conference 2013*, p. TUPF18, JACoW, Oxford, United Kingdom, 2013. (cited p. 118, 126, 156)

[287] R. Dowd and Y.-R. E. Tan, Beam based sextupole alignment studies for coupling control at the ASLS, in *Proceedings of the International Particle Accelerator Conference 2011*, p. WEPC001, JACoW, San Sebastian, Spain, 2011. (cited p. 119)

[288] D. J. Peake, K. P. Wootton, R. P. Rassool, M. J. Boland and Y.-R. Tan, Operation and storage ring calibration with the transverse bunch-by-bunch feedback system at the Australian Synchrotron, in *Proceedings of the International Particle Accelerator Conference 2011*, p. WEPC049, JACoW, San Sebastian, Spain, 2011. (cited p. 119, 155)

[289] D. J. Peake, *Diagnostics and Control of Transverse Coupled-Bunch Instabilities in Third Generation Electron Storage Rings*, PhD thesis, School of Physics, The University of Melbourne, 2011. (cited p. 119)

[290] J. G. Gallacher *et al.*, Physics of Plasmas **16**, 093102 (2009), doi: 10.1063/1.3216549. (cited p. 124)

[291] H. P. Panopoulos, K. P. Wootton, M. J. Boland and R. P. Rassool, Electron beam energy measurement at the Australian Synchrotron storage ring, in *Proceedings of the International Particle Accelerator Conference 2011*, p. TUPC062, JACoW, San Sebastian, Spain, 2011. (cited p. 125)

[292] T. Obina and T. Mitsuhashi, Measurement of bunch lengthening effects using a streak camera with reflective optics, in *Proceedings of the Workshop on Beam Diagnostics and Instrumentation for Particle Accelerators 2007*, p. WEPB12, JACoW, Venice, Italy, 2007. (cited p. 125)

[293] G. G. Stokes, Transactions of the Cambridge Philosophical Society **9**, 399 (1852). (cited p. 125)

[294] E. Hecht, *Optics*, 4$^{\text{th}}$ ed. (Pearson Education, San Francisco, CA, USA, 2002). (cited p. 125)

[295] C. Bloomer, (private communication), 2013. (cited p. 127)

[296] M. Bei *et al.*, Nuclear Instruments and Methods in Physics Research Section A: Accelerators, Spectrometers, Detectors and Associated Equipment **622**, 518 (2010), doi:10.1016/j.nima.2010.01.045. (cited p. 132)

[297] Y. Shimosaki *et al.*, Design study of nonlinear optics for a very low-emittance lattice of the SPring-8 II, in *Proceedings of the International Particle Accelerator Conference 2012*, p. TUPPC014, JACoW, New Orleans, USA, 2012. (cited p. 132)

[298] L. Farvacque *et al.*, A low emittance lattice for the ESRF, in *Proceedings of the International Particle Accelerator Conference 2013*, p. MOPEA008, JACoW, Shanghai, China, 2013. (cited p. 132)

[299] V. Ptitsyn *et al.*, High luminosity electron-hadron collider erhic, in *Proceedings of the International Particle Accelerator Conference 2011*, p. THPZ019, JACoW, San Sebastian, Spain, 2011. (cited p. 132)

[300] (LHeC Study Group), J. L. Abelleira Fernandez *et al.*, Journal of Physics G: Nuclear and Particle Physics **39**, 075001 (2012), doi:10.1088/0954-3899/39/7/075001. (cited p. 132)

[301] O. Brüning and M. Klein, Modern Physics Letters A **28**, 1330011 (2013), doi:10.1142/S0217732313300115. (cited p. 132)

[302] S. A. Belomesthnykh *et al.*, Nuclear Instruments and Methods in Physics Research Section A: Accelerators, Spectrometers, Detectors and Associated Equipment **227**, 173 (1984), doi:10.1016/0168-9002(84)90119-0. (cited p. 132)

[303] V. N. Baĭer and V. A. Khoze, Yadernaya Fizika **9**, 409 (1969), [Sov. J. Nucl. Phys. **9**, 238 (1969)]. (cited p. 132)

[304] O. Klein and Y. Nishina, Nature **122**, 398 (1928), doi:10.1038/122398b0. (cited p. 132)

[305] O. Klein and Y. Nishina, Zeitschrift für Physik **52**, 853 (1929), doi:10.1007/BF01366453. (cited p. 132)

[306] F. W. Lipps and H. A. Tolhoek, Physica **20**, 385 (1954), doi:10.1016/S0031-8914(54)80054-1. (cited p. 132)

[307] R. Zimmermann and W. Hillert, Investigation of techniques for precise compton polarimetry at ELSA, in *Proceedings of the International Particle Accelerator Conference 2012*, p. MOPPR007, JACoW, New Orleans, USA, 2012. (cited p. 132)

[308] D. B. Gustavson *et al.*, Nuclear Instruments and Methods **165**, 177 (1979), doi:10.1016/0029-554X(79)90268-4. (cited p. 132)

[309] M. Placidi and R. Rossmanith, Nuclear Instruments and Methods in Physics Research Section A: Accelerators, Spectrometers, Detectors and Associated Equipment **274**, 79 (1989), doi:10.1016/0168-9002(89)90367-7. (cited p. 132)

[310] A. Luccio, Brookhaven National Laboratory Report No. BNL-52348, 1992 (unpublished), doi:10.2172/10105046. (cited p. 132)

[311] A. Luccio, Measurement of the spin of a particle using undulator radiation, in *Prooceedings of the Particle Accelerator Conference 1993*, pp. 2175–2177, JACoW, Washington, D.C., USA, 1993. (cited p. 132)

[312] A. Luccio and L. Miceli, Journal of X-Ray Science and Technology **4**, 247 (1994), doi:10.1016/S0895-3996(05)80043-6. (cited p. 132)

[313] K. Y. Ng, Fermilab Report No. FERMILAB-FN-0840-AD, 2009 (unpublished). (cited p. 132)

[314] G. Geloni, V. Kocharyan and E. Saldin, On quantum effects in spontaneous emission by a relativistic electron beam in an undulator, in *Proceedings of Free Electron Laser 2012*, p. MOOC03, JACoW, Nara, Japan, 2012. (cited p. 132)

[315] J. S. Bell and J. M. Leinaas, Nuclear Physics B **212**, 131 (1983), doi: 10.1016/0550-3213(83)90601-6. (cited p. 133)

[316] Y. S. Derbenev and A. M. Kondratenko, Zhurnal Eksperimentalnoi i Teoreticheskoi Fiziki **64**, 1918 (1973), [Sov. Phys. JETP, **6**, 968-973 (1973)]. (cited p. 133)

[317] S. R. Mane, Physical Review A **36**, 105 (1987), doi:10.1103/PhysRevA.36.105. (cited p. 133)

[318] J. S. Bell and J. M. Leinaas, Nuclear Physics B **284**, 488 (1987), doi: 10.1016/0550-3213(87)90047-2. (cited p. 133)

[319] S. Dawson, D. J. Peake, R. P. Rassool, R. J. Steinhagen and M. J. Boland, Storage ring tune measurements using high-speed metal-semiconductor-metal photodetector, in *Proceedings of the International Beams Instrumentation Conference 2012*, p. TUPB84, JACoW, Tsukuba, Japan, 2012. (cited p. 134)

[320] S. R. Mane, Fermilab Report No. FN-467, 1987 (unpublished). (cited p. 134)

[321] D. P. Barber and S. R. Mane, Physical Review A **37**, 456 (1988), doi: 10.1103/PhysRevA.37.456. (cited p. 134)

[322] E. J. N. Wilson, *An Introduction to Particle Accelerators* (Oxford University Press, Oxford, United Kingdom, 2001), doi: 10.1093/acprof:oso/9780198508298.001.0001. (cited p. 145)

[323] E. Tan, Australian Synchrotron Report No. AS-200604-02, 2005 (unpublished). (cited p. 147, 148, 149, 150, 151, 152)

[324] Joint Committee for Guides in Metrology, Bureau International des Poids et Mesures Report No. JCGM 100:2008, 2008 (unpublished). (cited p. 155)

Author/s:
Wootton, Kent Peter

Title:
Demonstrating beams for a future linear collider using electron storage rings

Date:
2014

Persistent Link:
http://hdl.handle.net/11343/39616

File Description:
Demonstrating beams for a future linear collider using electron storage rings